High Areal-capacity and Durable Aqueous Rechargeable Zinc Li-ion Battery

by

Sepehr Khazraei

A thesis

presented to the University of Waterloo

in fulfillment of the

thesis requirement for the degree of

Doctor of Philosophy

in

Chemical Engineering

Waterloo, Ontario, Canada, 2021

Examining Committee Membership

The following served on the Examining Committee for this thesis. The decision of the Examining Committee is by majority vote.

External Examiner	Dr. Sen Zhang Assistant Professor Chemistry, University of Virginia
Supervisor	Dr. Zhongwei Chen Professor Chemical Engineering, University of Waterloo
Internal Members	Dr. Eric Croiset Professor Chemical Engineering, University of Waterloo
	Dr. William A. Anderson Professor Chemical Engineering, University of Waterloo
Internal-external Member	Dr. Xianguo Li Professor Mechanical and Mechatronics Engineering, University of Waterloo

Author's Declaration

This thesis consists of material all of which I authored or co-authored: see Statement of Contributions included in the thesis. This is a true copy of the thesis, including any required final revisions, as accepted by my examiners.

I understand that my thesis may be made electronically available to the public.

Statement of Contributions

The body of this thesis is based upon a combination of patents and unpublished works.

Chapter 3

Sepehr Khazraei, Ali Ghorbani Kashkooli, and Zhongwei Chen. "Design and feasibility of thick dough-like cathodes for high areal-capacity zinc/$LiFePO_4$ battery"

"AQUEOUS ZINC LITHIUM-ION BATTERY AND METHOD FOR MAKING SAME", PCT/CA2019/051096, W0/2020/061677.

I designed and carried out the experiments, collected and analyzed the data, and wrote the manuscript. Dr. Chen and Dr. Ghorbani assisted with analyzing the data, discussion, and manuscript reviewing.

Chapter 4

Sepehr Khazraei, Hao Liu, Gaopeng Jiang, and Zhongwei Chen. "Design of thick cathode enabled by 3D carbon nanotube networks for high areal-capacity zinc/$LiMn_2O_4$ battery."

I designed and carried out the experiments, collected and analyzed the data, and wrote the manuscript. Dr. Chen and Mr. Liu assisted with analyzing the data and discussion. Dr. Jiang reviewed the manuscript.

Chapter 5

Sepehr Khazraei, Hao Liu, Gaopeng Jiang, and Zhongwei Chen. "Development of porous zinc paste composite anode for high areal-capacity zinc/$LiMn_2O_4$ battery."

"POROUS ZINC PASTE ELECTRODE FOR AQUEOUS ZINC LITHIUM-ION BATTERY", (The patent application is being filed)

I designed and carried out the lab experiments, collected and analyzed the data, and wrote the manuscript. Dr. Chen, Dr. Jiang, and Mr. Liu assisted with analyzing the data, discussion, and manuscript reviewing.

Chapter 6

Sepehr Khazraei, Gaopeng Jiang, Ali Ghorbani Kashkooli, and Zhongwei Chen. "Development of gel electrolyte for high areal-capacity zinc/$LiMn_2O_4$ battery."

I designed and performed the experiments, collected and analyzed the data, and wrote all parts of the chapter. Dr. Chen, Dr. Jiang, and Dr. Ghorbani contributed to data analysis and discussion.

Abstract

Rapid deployment of renewable energy sources around the world is crucial to lessen energy shortage and environmental pollution. As the contribution of renewable energy rises, energy storage with different battery systems is an increasingly important solution to balance generation and loads of energy due to the intermittent nature of sustainable energy sources. Among modern battery systems, lithium-ion (Li-ion) batteries have a combination of high energy density and power density with a wide range of applications from portable electronic devices to large stationary storage systems. However, safety concerns, environmental threats, and costly manufacturing processes stemming from the implementation of toxic and flammable organic electrolytes are the key public arguments against their widespread application. Accordingly, aqueous rechargeable zinc Li-ion batteries (ARZLBs) were proposed and developed as an alternative safe, environmentally benign, and economically viable technology for electrical energy storage. Nevertheless, an ARZLB with high energy density and sufficient cycle life has not yet been introduced to the market. The limited energy density of this type of battery is mainly due to the inferior areal capacity corresponding to a low ratio of active material to inactive components in the battery. Moreover, the zinc dendrite formation on the anode surface and hydrogen evolution-induced corrosion reaction in the aqueous electrolyte restrict the cycle life of the battery. In an effort to fill this research gap, this thesis intends to i) introduce a flexible thick cathode design with superb areal capacity and active material loading for zinc/$LiFePO_4$ battery, ii) propose a novel conductive thick cathode architecture with unprecedented active material loading and areal capacity for zinc/$LiMn_2O_4$ battery, iii) design a porous zinc anode with high surface area to suppress the zinc dendrite growth and prolong the cycle life of high areal-capacity zinc/$LiMn_2O_4$ battery, and iv) develop a gel-type electrolyte with the ability to mitigate the hydrogen evolution-induced corrosion and further extend the cycle life.

This work begins with enhancing the areal capacity of the zinc/$LiFePO_4$ battery. To achieve a high areal-capacity battery, the electrode was designed with a thick, flexible, and binder-less architecture called a dough-like cathode. In this innovative method, organic solvent processing is replaced by aqueous processing and thus the electrode fabrication is more straightforward, faster, cheaper, and safer than conventional electrodes. The dough-like cathodes are fabricated up to an extremely high thickness of 1000 μm with decent consistency and without any crack formation. Moreover, the electrolyte-based and binder-less electrode structure lowers the tortuosity and elevates the electronic/ionic conductivity of the cathode, leading to a near-theoretical specific capacity performance. As a result of this novel electrode design, the areal capacity and active material loading of the zinc/$LiFePO_4$ battery manufactured with thick dough-like cathodes reach extremely high values of 10.5 mAh cm^{-2} and 74.5 mg cm^{-2}, respectively. Consequently, the energy density of the zinc/$LiFePO_4$ battery with a 700 μm thick dough-like cathode is 190% higher than that of the battery with a 100 μm conventional cathode design. Furthermore, the battery assembled with the dough-like cathode maintains 80% of its capacity compared to only 50% with the conventional cathode after 200 cycles and at the same cathode thickness.

To further improve the energy density, $LiFePO_4$ cathode active material was replaced by $LiMn_2O_4$ that has a higher electrochemical potential. Therefore, in the next step, a newly thick cathode architecture was redesigned for $LiMn_2O_4$ cathode with three-dimensional (3D) conductive networks of carbon nanotubes (CNTs). This unique electrode structure allows the manufacturing of crack-free and reinforced thick cathodes up to 900 μm with high structural stability during battery cycling. Similar to the dough-like cathode, eco-friendly and cost-effective aqueous processing is employed for electrode manufacturing. The zinc/$LiMn_2O_4$ batteries assembled with 3D-CNT cathodes manifest an unprecedented areal capacity of 13.5 mAh cm^{-2}, which is at least 10 times greater than that of the battery with the conventional cathode design. More importantly,

the energy density of the zinc/$LiMn_2O_4$ battery with a thick 3D-CNT cathode is 140% higher than the energy density of the zinc/$LiFePO_4$ battery with a thick dough-like cathode at the same electrode thickness.

To extend the lifespan of the zinc/$LiMn_2O_4$ battery with the thick 3D-CNT cathode over 100 cycles, a novel porous zinc paste composite (PZPC) is proposed. The PZPC provides a high surface area for zinc deposition, facilitates the homogenous current distribution, and improves the corrosion resistance of the electrode. Hence, the cycle life of the zinc/$LiMn_2O_4$ battery with the PZPC anode and a thick 3D-CNT cathode is prolonged by as much as 5 times the cycle life of the battery with the conventional zinc anode. Moreover, the PZPC promotes the rate capability and voltage efficiency of the battery due to the conductive porous structure and high electrode-electrolyte contact area.

Finally, to further extend the lifespan of the high areal-capacity zinc/$LiMn_2O_4$ battery, a low-cost gel electrolyte was developed by using fumed silica thickening agent inside the aqueous electrolyte to mitigate the destructive effect of hydrogen evolution-induced corrosion. The fumed silica gel electrolyte immobilizes the water molecules through hydrogen bonding and thus reduces the corrosion current of the zinc by at least 50% of its value in the aqueous electrolyte. Furthermore, the fumed silica gel electrolyte improves the reversibility of redox reactions on both cathode and anode sides. Consequently, the cycle life of zinc/$LiMn_2O_4$ battery with a thick 3D-CNT cathode, fumed silica gel electrolyte, and PZPC anode is extended to 600 cycles.

Taken together, these findings suggest the ability of thick 3D-CNT cathode, PZPC anode, and fumed silica gel electrolyte in promoting the areal capacity and durability of ARZLBs. The high areal-capacity and durable zinc/$LiMn_2O_4$ battery enable the manufacturing of high energy density and cost-effective ARZLBs that can compete with state-of-the-art aqueous batteries.

Acknowledgments

First of all, I would like to express my sincere gratitude to my supervisor, Professor Zhongwei Chen, for his support and valuable input during my Ph.D. work. His continued mentorship and enthusiasm enlightened me for pursuing my doctoral degree.

I would also like to extend my appreciation to my Ph.D. examining committee: Professor Sen Zhang, Professor Eric Croiset, Professor William Anderson, and Professor Xianguo Li for their time in reviewing my thesis and for the valuable comments they gave me.

I want to thank all my colleagues in Dr. Zhongwei Chen's group for providing feedback, sharing ideas, and helping me with setting up experiments, especially Dr. Ali Ghorbani, Dr. Gaopeng Jiang, Hao Liu, and Dr. Zachary Cano. I wish to acknowledge the financial assistance provided by the Natural Sciences and Engineering Research Council and the University of Waterloo. I would also like to acknowledge Pro-Flange Ltd. for providing additional financial support.

Finally, my special thanks to my loving family and dear friends for all their patience and encouragement, especially during difficult times. Most of all, I would like to thank my dear wife, Mina, from bottom of my heart. I am eternally grateful for all her endurance, countless support, and encouragement. None of this would have been possible without you, my darling.

Dedication

To my beloved parents, Teimour and Mahvash, who gave me everything and I am grateful for their love and support forever.

Table of Contents

List of Figures

List of Tables

List of Abbreviations

3D	Three dimensional
AGM	Absorbent Glass Mat
ARLB	Aqueous rechargeable lithium-ion battery
ARZLB	Aqueous rechargeable zinc lithium-ion battery
BET	Brunauer-Emmett-Teller
CA	Chronoamperometry
CE	Coulombic efficiency
CV	Cyclic voltammetry
CF	Carbon fiber
CMC	Carboxymethyl cellulose
CNT	Carbon nanotube
DDI	Distilled de-ionized
EES	Electrical energy storage
EIS	Electrochemical impedance spectroscopy
FS	Fumed silica
GCE	Glassy carbon electrode
HER	Hydrogen evolution reaction
LFP	$LiFePO_4$
Li-ion	Lithium-ion
LMO	$LiMn_2O_4$
LiTFSI	Lithium bis(trifluoromethanesulfonyl)imide
Ni-Cd	Nickel-cadmium
Ni-MH	Nickel-metal hydride
NMP	1-Methyl-2-pyrrolidone
OCV	Open circuit voltage
OER	Oxygen evolution reaction
PVDF	Polyvinylidene fluoride
PTFE	Polytetrafluoroethylene
PZPC	Porous zinc paste composite
SCE	Standard calomel electrode
SEI	Solid electrolyte interface
SEM	Scanning electron microscopy
SHE	Standard hydrogen electrode
SP-C	Super P carbon
SOC	State of charge
SWCNT	Single-wall carbon nanotube
VE	Voltage efficiency
XRD	X-ray diffraction

1. Introduction

1.1. Motivation

With skyrocketing energy demands and the increased awareness of the negative impacts of climate change, addressing the sustained growth of the world's energy and electricity sectors without overwhelming reliance on fossil fuels has become a top priority. Global energy consumption is projected to increase by 60% over the period of 2018-2050 [1]. This rapidly increasing energy demand is driving the search for viable solutions to integrate sustainable and clean energy resources, which are prone to inconsistency over varying times and weather patterns, into power systems. Electrical energy storage (EES) is an established approach to facilitate full integration of sustainable energy sources and improve the reliability, capacitance, and resilience of power grids by storing electricity during off-peak periods and delivering it during peak-demand times to meet varying time-dependent energy supplies and consumption [1–4]. With the widespread adoption of renewable resources, the requirement for safe, environmentally benign, and inexpensive EES devices to incorporate intermittent energy resources such as wind and solar into existing energy infrastructure is imperative.

Among various types of EES devices, rechargeable batteries are the most promising technology to provide service to the electric grid because of high energy density and efficiency, great installation speed, and flexibility [5]. Many types of rechargeable batteries are commercially available for relatively large-scale EES including lead-acid, nickel-metal hydride (Ni-MH), nickel-cadmium (Ni-Cd), redox flow cells, and lithium-ion (Li-ion) batteries [5,6]. However, significant challenges exist for the utilization of each of these batteries. Despite the fact that lead-acid batteries

are a low-cost and mature technology, their use is limited due to their short lifetime, low energy density, and serious impact on the environment [7]. Redox flow batteries can be flexibly scaled up to match various energy and power needs, but they require expensive ion-exchange membranes which account for 30-40% of battery-stack cost [8,9]. Ni-Cd batteries cause serious environmental threats due to the use of extremely toxic cadmium metal, and Ni-MH batteries are prone to high self-discharge and are relatively expensive considering the rare-earth precursor materials used in the anode [10–12]. Li-ion batteries with organic electrolytes provide superior electrochemical properties with high cell voltage, high energy density, and decent cycle stability and undoubtedly dominate the current market from portable electronic devices to large stationary grid energy storage [13,14]. Despite the tremendous achievements in their commercialization, safety concerns due to the flammability of organic electrolytes and relatively high production cost, primarily related to expensive electrolyte components and the strict manufacturing process, are the main critical issues for the widespread deployment of Li-ion batteries in large-scale EES [15,16]. In 1994, Dahn and co-workers [17] proposed a new battery system by replacing the flammable organic electrolyte in Li-ion batteries with an aqueous electrolyte. Incorporation of aqueous electrolyte instead of organic electrolyte can resolve several intrinsic disadvantages of commercial Li-ion batteries including 1) higher safety via eliminating the thermal runaway problem in organic electrolytes, 2) lower manufacturing price via cheaper electrolyte components and an open-air manufacturing process, 3) higher ionic conductivity (about two orders of magnitude) compared to organic electrolytes due to the lower viscosity of solvent at the same salt concentration, and 4) better eco-friendliness via the deployment of non-toxic aqueous media and electrolyte salts [18,19]. Owing to these advantages, the use of aqueous rechargeable Li-ion batteries (ARLBs) has been recommended as a promising system for large-scale EES. However, suitable Li-ion intercalation anode host materials by their

potentials in ARLBs have relatively low thermodynamic stability in aqueous electrolytes and inadequate specific capacity [20]. Therefore, the investigation for an electrochemically stable anode material for ARLBs with high specific capacity is necessary.

Aqueous rechargeable zinc Li-ion batteries (ARZLBs) as the hybrid-type of ARLBs were developed by replacing Li-ion intercalation anode with zinc metal and using a hybrid solution of Zn^{2+} and Li^{+} ions [10]. The metallic zinc has been considered as an ideal anode for ARLBs since it is an earth-abundant and low-cost material with high theoretical specific capacity and low electrochemical potential [21]. Accordingly, the use of ARZLBs has been recommended as a promising alternative for large-scale EES. Despite their compelling advantages over Li-ion batteries, ARZLBs suffer from poor energy density and relatively low cycle life. The energy density of ARZLBs is limited due to the low output voltage and extremely low areal capacity. Moreover, the zinc anode is susceptible to the growth of needle-like structure, called dendrite, upon cycling that would affect the cycle life of the battery by causing short-circuiting. Therefore, the end-goal of this work lies in the contribution to the development of high-performance ARZLBs in terms of improved energy density and cycle life to make them a suitable candidate for large-scale EES.

1.2. Thesis objectives and structure

Despite the significant progress of ARZLBs in recent years, there are still some remaining gaps and scientific challenges that should be addressed for this type of battery, notably in terms of energy density and cycle life. A feasible strategy to increase the energy density of ARZLBs is through optimizing the battery design which necessitates maximization of their areal capacity and thus increasing the thickness of the cathode. However, increasing the thickness of the cathode via

current conventional electrode manufacturing is challenging due to mechanical instability, poor electronic/ionic conductivity, and inferior specific capacity at high electrode thicknesses, normally greater than 200 μm. As to the anode, the deep-seated issues of dendrite formation and hydrogen evolution-induced corrosion reaction, specifically at high areal capacities, worsen the lifespan of the battery. The zinc dendrites, which are sharp and needle-like protrusions, can grow during charging and penetrate through the separator and contact the cathode, causing short-circuiting and failure of the battery. Besides, zinc can be corroded by the water-zinc reactions and deteriorate the zinc metal plating/stripping efficiency. Accordingly, the main objectives of this thesis are to design and develop an ARZLB with improved electrochemical performance in terms of:

I) enhanced energy density by optimizing the battery design with high areal capacity battery cathode and low inactive to active component ratio,

II) prolonged cycle life via suppressing the zinc dendrite growth and mitigating the hydrogen evolution-induced corrosion reaction.

The structure of this thesis is organized as illustrated in Figure 1.1. **Chapter 2** provides a detailed overview of current challenges, scientific mechanisms, and recent strategies for the advancement of ARZLBs. **Chapters 3** and **4** aim to fill the gap in the literature by proposing innovative fabrication methods for the cathode with high active material loading to enhance the energy density of ARZLBs. The proposed methods for the cathode enable the manufacturing of crack-free and conductive thick electrode design while maintaining a high specific capacity. **Chapter 3** designs a novel binder-less and flexible thick cathode structure for zinc/$LiFePO_4$ battery with superb active material loading and areal capacity to compensate for the low energy density of ARZLBs. **Chapter 4** reveals a 3D conductive thick $LiMn_2O_4$ cathode with the assistance of carbon nanotube (CNT) networks with unprecedented areal capacity and active material loading

for ARZLBs. In this chapter, $LiFePO_4$ active material is replaced by $LiMn_2O_4$ to further enhance the energy density of ARZLBs.

Chapters 5 and **6** propose strategies to increase the cycle life of high areal-capacity ARZLBs via effectively suppressing the zinc dendrite formation and mitigating the hydrogen evolution-induced corrosion. **Chapter 5** replaces the conventional zinc metal with a novel porous structure zinc anode to prolong the lifespan of the high areal-capacity zinc/$LiMn_2O_4$ battery. The highly porous zinc anode facilitates the homogenous current distribution, provides more space for zinc deposition, improves the corrosion resistance of the electrode, and thus extends the lifespan of the battery. **Chapter 6** develops a gel-type electrolyte for the current system to mitigate the hydrogen evolution-induced corrosion reaction and thus further extends the durability of the battery. Therefore, these strategies are considerable advancements that resolve the current issues associated with ARZLBs in the literature. Finally, **Chapter 7** summarizes the major results and findings obtained from the present research work and outlines some suggestions for future research that can be considered for further improvement in the electrochemical performance of the current system.

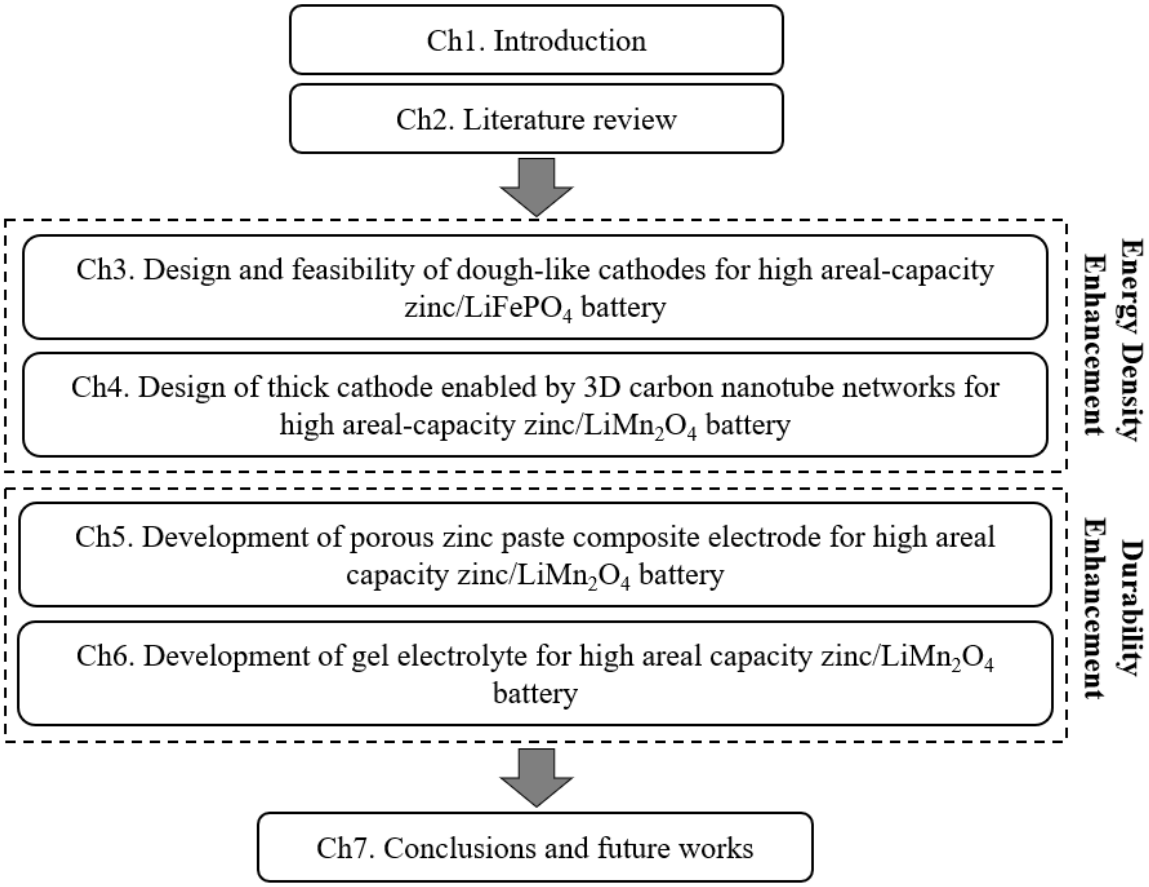

Figure 1.1 Thesis layout

2. Literature Review

2.1. Introduction of ARZLBs

The total energy storage market is undergoing rapid expansion and thus researchers are investigating new types of rechargeable batteries with high energy density, low cost, high safety, and environmentally friendly characteristics to meet a diverse set of demands. Current commercial batteries are generally made with toxic and hazardous components, e.g., toxic lead and cadmium in lead-acid and Ni-Cd batteries and flammable organic electrolytes in Li-ion batteries. To fill the need for non-hazardous materials in rechargeable batteries, ARLBs have emerged as a promising candidate for the large-scale energy storage market, since aqueous electrolytes resolve the safety concerns of flammable and toxic organic electrolytes. Moreover, the low cost of aqueous components and non-moisture-sensitive production and packaging lower the overall cost of battery manufacturing. Furthermore, the ionic conductivity of aqueous electrolytes is greater than organic electrolytes by at least two orders of magnitude [10,20].

ARLBs can be divided into two main categories: rocking-chair (intercalation cathode and anode with Li^+ ion solution) and hybrid-type (intercalation cathode and metal anode with mixed ions solution) batteries. Accordingly, ARZLBs with a mixed solution of Li^+ and Zn^{2+} ions are classified as the hybrid type of ARLBs. The zinc metal in this type of battery is a promising anode for ARLBs owing to its 1) high theoretical capacity (820 mAh g^{-1}), 2) low electrochemical potential (-0.762 V vs. standard hydrogen electrode (SHE)), 3) natural abundance on earth, 4) low cost, and 5) non-toxicity [21,22]. The first ARZLB was introduced by Chen's group in 2012 by employing $LiMn_2O_4$ as the cathode and zinc metal as the anode [10]. In their proposed system, two distinct reversible electrochemical redox reactions occurred based on Li-ion

intercalation/deintercalation into/from spinel $LiMn_2O_4$ at the cathode and zinc deposition/dissolution at the anode.

A typical schematic of an ARZLB is illustrated in Figure 2.1. The main components of the battery include a Li-ion intercalation compound cathode, zinc anode, separator, current collectors, and ionically conductive aqueous electrolyte that carries a hybrid solution of Li^+ and Zn^{2+} ions. The common Li-ion intercalation compounds used in ARZLBs are $LiFePO_4$ and $LiMn_2O_4$ since their operating voltages situate in the safe zone of the electrochemical stability windows of aqueous electrolytes, specifically in a mild acidic electrolyte. The electrochemical reactions at the cathode side of aqueous rechargeable zinc/$LiFePO_4$ and zinc/$LiMn_2O_4$ batteries can be expressed as follows:

$$LiFePO_4 \rightleftharpoons Li_{1-x}FePO_4 + xLi^+ + xe^- \quad (2.1)$$

$$LiMn_2O_4 \rightleftharpoons Li_{1-x}Mn_2O_4 + xLi^+ + xe^- \quad (2.2)$$

At the anode side, the electrochemical reaction can be written as follows:

$$Zn^{2+} + 2e^- \rightleftharpoons Zn \quad (2.3)$$

The forward/backward reaction occurs during the charge/discharge process, respectively. During discharge, the zinc electrode is oxidized and releases a flow of electrons to the external circuit. After traveling across the external circuit, the electrons are consumed at the cathode when the dissolved Li^+ ions intercalate inside the host crystal structure. During charge, Li^+ ions are extracted from the crystal structure and dissolved into the electrolyte. On the other side, Zn^{2+} ions in the electrolyte accept electrons and deposit on the zinc surface. Although zinc metal offers significant advantages for ARZLBs, zinc anode problems such as dendrite growth and hydrogen evolution-induced corrosion shorten the cycle-life of the battery. The major research directions for

ARZLBs are thus aimed at developing dendrite-free zinc anodes and suppressing parasitic side reactions to prolong their lifespan.

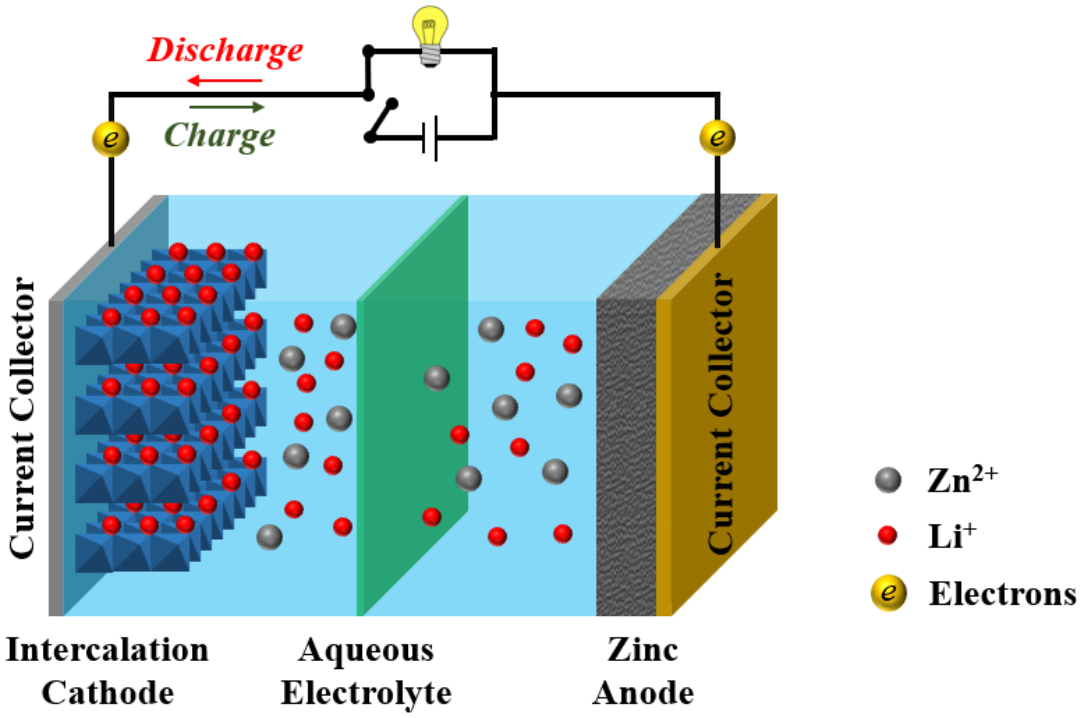

Figure 2.1 Schematic of battery configuration and operating mechanism of an ARZLB. Red and green arrows represent the direction of movement of electrons during discharge and charge, respectively.

In this chapter, the challenges and fundamental basics of ARZLBs including narrow electrochemical stability window of water, chemical/electrochemical instability of Li-ion intercalation compounds, and the zinc electrode performance-limiting phenomena will be discussed. Then, the recent advances and strategies reported in the literature for addressing the current challenges in ARZLBs will be reviewed. The up-to-date strategies are presented in three main categories including the development of cathode material, zinc anode engineering, and electrolyte engineering.

2.2. Current challenges of ARZLBs and their corresponding mechanisms

State-of-the-art ARZLBs have undergone significant improvements with corresponding approaches to tackle their limitations and challenges. The main obstacles that hinder the success of ARZLBs are the water-splitting reactions, chemical/electrochemical instability of Li-ion intercalation compounds, and zinc performance-limiting phenomena. These drawbacks have provided the motivation for several studies in the literature which elucidate details of their mechanisms. In this section, these challenges and limitations of ARZLBs are discussed and the fundamental basics and corresponding mechanisms behind them are provided.

2.2.1 Water-splitting reactions and limited output voltage

Water emerged as a natural replacement for expensive and flammable organic solvents due to its ability to cut the manufacturing price and improve the safety of Li-ion batteries, but at the cost of inferior energy density. The energy density of ARZLBs is usually below 70 Wh kg^{-1} due to the narrow electrochemical stability of water, which is 1.23 V. This limitation is caused by the thermodynamic oxidation and reduction potential of the water known as oxygen evolution reaction (OER) and hydrogen evolution reaction (HER). The low electrochemical potential windows of aqueous electrolytes also narrow down the list of specific cathodes and anodes that can be utilized, with an assembled cell voltage typically below 1.5 V. The slightly higher cell voltage of aqueous batteries is attainable due to the kinetic overpotential of HER and OER and is effective when the battery cells are operated at high rates. At low C-rates, parasitic side reactions, specifically HER at the anode side, intensify and affect the coulombic efficiency (CE) of the battery cell [18,23,24]. Moreover, electrolyte additives play a decisive role in controlling the rate of parasitic side reactions by increasing the overpotential of the HER and OER. Metal element additives such as bismuth,

indium, lead, and tin are effective inhibitors for hydrogen generation by imposing high overpotentials for the HER [25].

The cell voltage of common Li-ion intercalation couples used as cathodes and anodes in non-aqueous Li-ion batteries are usually more than 3 V, and thus the use of these active materials in aqueous media is not feasible because of water-splitting reactions. The reduction of organic electrolyte components constructs a protective solid electrolyte interface (SEI) layer on the surface of the anode and prevents further decomposition of the electrolyte. In contrast to organic electrolytes, the water-splitting reactions continuously generate hydrogen and oxygen gases that can escape from the anode and cathode surfaces [26]. Strategies such as highly concentrated electrolyte salts [24] and artificial SEI layers [27] have been introduced to transplant the SEI layer to aqueous electrolytes and broaden the electrochemical stability limits of water.

In aqueous electrolytes, the following HER and OER occur with respect to acidic or alkaline environments.

$$2H^+ + 2e^- \rightarrow H_2 \qquad \textit{Acidic} \qquad (2.4)$$

$$2H_2O \rightarrow O_2 + 4H^+ + 4e^- \qquad (2.5)$$

$$2H_2O + 2e^- \rightarrow H_2 + 2OH^- \qquad \textit{Alkaline} \qquad (2.6)$$

$$4OH^- \rightarrow O_2 + 2H_2O + 4e^- \qquad (2.7)$$

For example, in an acidic electrolyte, protons gain electrons and produce hydrogen gas in the vicinity of the anode surface and water molecules decompose and produce oxygen gas on the cathode side. Thereupon, the electrons participate in these unwanted side reactions rather than in the main electrochemical reactions and thus the CE of the aqueous battery is lowered to less than 100%. Moreover, the produced hydrogen and oxygen gases on the electrode surface increase the

resistance of the battery and bring serious safety issues in a sealed battery package due to the pressure build-up.

The electrochemical potential of HER and OER depends strongly on electrolyte pH, which affects the selection of cathode and anode materials. The electrochemical potentials of some cathode and anode Li-ion intercalation materials and their comparisons with the thermodynamic stability of water (vs. SHE) are illustrated in Figure 2.2. Shifting from an acidic media to a very strong alkaline electrolyte will allow the use of more anodic materials with lower electrochemical potentials while restricting the use of cathode materials due to the simultaneous downward shift of the oxygen evolution potential, since the gap between anodic and cathodic limits remains constant at 1.23 V [18,23,24]. Therefore, suitable cathode active materials in ARZLBs should be selected based on the position of their electrochemical potentials in the safe region of the thermodynamic stability window of water in a certain pH value.

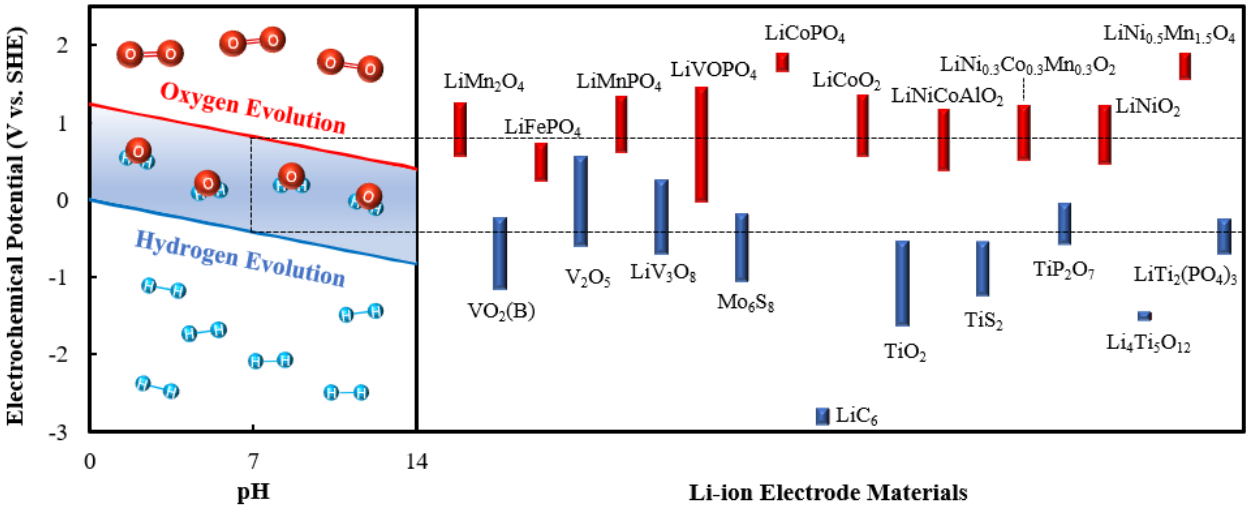

Figure 2.2 Working potentials of Li-ion intercalation electrode materials vs. SHE and their comparisons with the stability window of water. Red and blue columns represent active materials for cathode and anode, respectively.

In addition to electrolyte pH, the water-splitting reactions are expedited in the presence of electrode materials with potential catalytic functionality. For example, de-lithiated $LiMn_2O_4$ can

provide active sites for water oxidation reactions. Robinson et al. reported that nanosized λ-MnO_2 obtained by the citrate route has a much higher catalytic rate for water oxidation than synthesized microsized $LiMn_2O_4$ materials from solid-state reaction [28]. Hence, the synthesizing method and active material particle size may affect the catalyst activity for the OER.

2.2.2 Chemical/electrochemical instability of Li-ion intercalation compounds

In addition to parasitic side reactions such as HER and OER, an important aspect that should be considered is the chemical/electrochemical stability of the electrode materials in aqueous electrolytes. The chemical and electrochemical reactions of the Li-ion intercalation compounds in aqueous electrolytes are much more complicated than those in organic electrolytes. Aside from HER and OER, many other side reactions may occur in aqueous solutions such as the interaction of water and dissolved oxygen molecules with the electrode materials, co-insertion of protons concurrently with intercalation of Li-ions, and dissolution of the electrode material components. Lithium does not bond strongly enough in some intercalation compounds to prevent it from deintercalation and direct reaction with water and oxygen molecules in the aqueous electrolyte. Subsequently, the formation of various complexes, e.g., LiOH and Li_2O is possible. A good measure of the binding energy of lithium in a Li-ion transition metal oxide is the working potential; generally, a higher potential indicates more tightly bonded lithium in the structure [29–33]. Li and co-workers [30] showed that Li-ion transition metal oxide materials as cathodes and anodes with an electrochemical potential of more than 3.3 V vs. Li/Li^+ are stable in aqueous electrolytes. They discussed the stability of electrode materials at thermodynamic equilibrium in aqueous electrolytes in the absence of oxygen molecules based on the following reaction:

$$Li\ (intercalated) + H_2O \rightarrow Li^+ + OH^- + (^1/_2)\ H_2 \qquad (2.8)$$

The minimum electrochemical stability potential of a Li-ion intercalation compound, V(x), without the presence of dissolved oxygen as a function of pH in 1 mol L^{-1} LiOH solution was derived as follows:

$$V(x) = 3.885 - 0.118\,pH \quad (V\ vs.\ Li/Li^{+}) \tag{2.9}$$

Equation 2.9 gives valuable information about the stability of the Li-ion intercalation compound in an aqueous solution. From this equation, the appropriate range of pH in which the Li-ion intercalation material is stable as a cathode or anode in the aqueous electrolyte can be theoretically determined. The electrode is theoretically stable in the aqueous electrolyte when the potential of the Li-ion intercalation electrode is higher than V(x). For instance, $Li_2Mn_2O_4$ with V=2.97 V vs. Li/Li^{+} is expected to be stable in LiOH aqueous electrolyte at pH greater than about 8 when there is no oxygen inside the electrolyte [18].

Since aqueous electrolytes naturally contain dissolved oxygen, Luo and co-workers [31] examined the stability of the electrode materials by considering the presence of dissolved oxygen. Based on the presence of both oxygen and water molecules, the following reaction may occur:

$$Li\ (intercalated) + (^1/_4)O_2 + (^1/_2)\,H_2O \rightleftharpoons Li^{+} + OH^{-} \tag{2.10}$$

In this case, the minimum electrochemical stability potential of a Li-ion intercalation compound, V(x), in equilibrium with oxygen and water as a function of pH and assuming 2 mol L^{-1} Li^{+} was calculated as follows:

$$V(x) = 4.268 - 0.059\,pH \quad (V\ vs.\ Li/Li^{+}) \tag{2.11}$$

According to Equation 2.11, no stable active materials in the presence of O_2 can be found for the anodes in ARLBs, regardless of the electrolyte pH. For instance, based on this equation, the electrochemical stability potential is 3.5 V vs. Li/Li^{+} at a pH of 13, whereas the electrochemical

potential of Li-ion intercalation anode materials is generally lower than 3.0 V vs. Li/Li^+. Therefore, all Li-ion intercalation anode materials could be theoretically oxidized by water and oxygen molecules at any pH value rather than undergoing the main electrochemical redox process [31]. The reactions of Li-ion intercalation compounds with water and dissolved oxygen molecules result in severe capacity fading upon cycling. Accordingly, it is highly challenging for ARLBs with Li-ion intercalation anode materials in the presence of oxygen to sustain acceptable capacity during long-term charge/discharge cycling. On the other hand, materials with long-lasting stability and specific working potentials within the electrolysis limits of water can be used in ARLBs. For instance, cathodes with working potentials between 3 and 4 V vs. Li/Li^+ such as $LiCoO_2$, $LiMn_2O_4$, and $LiFePO_4$ can be used in ARLBs. On the anode side, vanadium-based oxide compounds such as VO_2(B) and $V_2O_5.nH_2O$ can be utilized in aqueous electrolytes [18]. Therefore, anodes with a high electrochemical potential combined with the limited choice of cathode active materials tend to cause ARLBs to have a low cell voltage and inferior energy density. For example, graphite, which is extensively used in non-aqueous Li-ion batteries as the anode active material, does not suit aqueous solutions because of the very low redox potential (0 - 0.25 V vs. Li/Li^+).

As an example of the practical consequences of Li-ion electrode instability in water-based solutions, Pei and co-workers [34] studied the electrochemical performance of $LiMn_2O_4$ in aqueous $LiNO_3/HNO_3$ electrolyte and observed a sudden capacity degradation after 20 cycles. This quick capacity loss was due to proton co-intercalation and manganese dissolution as a result of the Jahn-Teller distortion effect. Unwanted side reactions may also occur in $LiFePO_4$ electrode as the common cathode active material in ARLBs. Olivine structured $LiFePO_4$ compound, which is first reported by Manickam and co-workers [35], suffers from irreversible reduction because of the formation of a mixture of $LiFePO_4$ and Fe_3O_4 during the discharge process [18,35]. He et al. [36]

investigated the adverse effect of OH^- and oxygen on the stability of $LiFePO_4$ in 0.5 mol L^{-1} Li_2SO_4 aqueous electrolyte and found a capacity loss of 37% after 10 cycles due to chemical/electrochemical instability with the presence of oxygen and water molecules as possible reactants. Fast capacity degradation indicates that $LiFePO_4$ cycling may proceed with different reactions. For instance, equation 2.10 may occur in the presence of oxygen and water [36]. In another experiment, they evaluated the cyclability of $LiFePO_4$ in the absence of oxygen and at different pH values. Increasing the pH value caused the cycling stability to deteriorate; after 10 cycles, the capacity retention at a pH of 13 was only 5% of the initial value. In this case, the capacity fading of $LiFePO_4$ is due to the participation of OH^- in a side reaction with intercalated lithium and the dissolution of active material in the strong basic solution [36]. Therefore, optimizing the pH and eliminating oxygen could enhance the cycling behavior of $LiFePO_4$ in ARLBs. While eliminating oxygen is not a practical option, alternative strategies such as carbon coating have been found to be effective. A carbon layer on $LiFePO_4$ electrode materials can mitigate the attack of dissolved oxygen and OH^- in aqueous electrolytes [36].

To conclude, capacity degradation in ARLB intercalation electrode materials (either cathode or anode) is mostly due to 1) water decomposition at high voltages, 2) water, OH^-, and oxygen side reactions with intercalated lithium, 3) dissolution of active material into aqueous electrolyte systems, and 4) H^+ co-intercalation into the electrode material host. To address these issues and enhance the electrochemical performance and stability of Li-ion intercalation compounds in aqueous electrolytes, many studies have focused on optimizing the electrolyte pH, eliminating the residual O_2, developing new long-lasting active materials, and modifying the structure of existing active materials using additives, dopants, and surface coating. Moreover, adjusting the cut-off

voltage for high voltage aqueous battery cells can prevent water decomposition reactions but at the cost of losing a portion of available capacity.

2.2.3 Zinc electrode performance-limiting problems

Zinc metal provides outstanding advantages as an anode for ARZLBs including low material cost, high theoretical capacity (820 mAh g^{-1}), high discharge voltage due to its low electrochemical potential (-0.762 V vs. SHE), and environmental friendliness. However, despite these numerous merits, zinc suffers from low plating/stripping efficiency (i.e. low CE) and potentially severe problems during cycling such as dendrite growth, shape change, and passivation in aqueous systems, particularly in alkaline environments [21,37]. The CE of zinc is defined as the ratio of zinc ions removed off the surface of the substrate during discharging to those that can be deposited on the surface during charging for each cycle; in other words, it is the zinc plating/stripping efficiency. CE also acts as a metric to report the reversibility of the zinc electrode. The CE of zinc is typically less than 50% in alkaline systems, while in acidic electrolytes such as zinc sulfate it is much higher, around 80% [21]. Any attempt to increase the CE of zinc results in higher utilization and reversibility of the zinc metal and consequently improves the energy density of aqueous zinc-based batteries. The term utilization refers to the percentage of the theoretical capacity of a given zinc mass that is extracted during the full discharge process. The reversibility and utilization of the zinc electrode and the corresponding performance of zinc-based batteries are affected by four major phenomena that may occur during battery cycling. These detrimental phenomena include zinc dendrite formation, shape change, passivation, and hydrogen evolution (Figure 2.3a). Each of these phenomena will be discussed in the following sections.

2.2.3.1 Zinc dendrite

The most visible problem of using zinc metal in rechargeable aqueous batteries is the formation of dendrites, which are sharp and needle-like protrusions that can grow during charging and penetrate through the separator and contact the cathode, causing short-circuiting and failure of the battery. Dendrites form due to the presence of zinc ion concentration gradients that occur during zinc electrodeposition, which cause deposition preferably on top of screw dislocations and consequently progressive intensification of the zinc surface heterogeneities. The zinc dendrites propagate faster at higher current densities as a consequence of the lack of zinc ions close to the electrode surface due to more pronounced concentration gradients [38–40].

2.2.3.2 Shape change

Shape change of the zinc electrode is another detrimental phenomenon in zinc-based batteries, which is the direct effect of unequal current distribution within the zinc anode or breakage of zinc dendrites during the discharge process. During repeated battery cycling, zinc ions dissolve into the electrolyte and redeposit on a different site, causing shape change and densification of the original zinc electrode. The electrode densification increases overpotentials and may intensify the growth of zinc dendrites. Dendrite breakage and shape change can also lead to a loss of active material and a sudden drop in the zinc plating/stripping efficiency [39].

2.2.3.3 Passivation

Another serious performance-limiting phenomenon is the formation of a passivation layer on the zinc surface in alkaline solutions, which restricts the zinc utilization to 60-80%. During the discharge process in an alkaline electrolyte, the concentration of zincate ions can surpass the solubility limit, resulting in the precipitation of insoluble ZnO or $Zn(OH)_2$ on the surface of the

electrode which can block the migration of zinc ions and OH^-. Aside from its harmful effect on electrode utilization, the non-conductive passivation layer can also escalate the internal resistance of the electrode and lower the energy efficiency of the battery. This insulating layer also reduces the active surface area or the zinc electrode, which may trigger enhanced dendrite growth and shape change as a consequence of inhomogeneous current distribution [39,41]. In contrast, the zinc surface oxide layer in acidic electrolytes is not stable and tends to form dissolved Zn^{2+} ions due to their high solubility. In mildly acidic conditions, some porous oxide films which do not act as a passivation layer can form.

2.2.3.4 Hydrogen evolution

The Pourbaix diagram of zinc species based on a low concentration of zinc ions (10^{-3} mol L^{-1}) is plotted in Figure 2.3b. It is evident that the redox potential and thermodynamically stable species of zinc are both dependent on the pH value. The Nernst equation was used for the corresponding reaction in each region to calculate the electrochemical potential of the zinc as a function of pH and zinc species concentration. In acidic and neutral solutions with a pH of less than about 8, Zn^{2+} ions are soluble in the solution with constant electrochemical redox potential. At 8<pH<13, zinc ions are not soluble and form $Zn(OH)_2$. In a very strong alkaline solution with a pH above 13, soluble zincate ions ($Zn(OH)_4^{2-}$) are the stable species in the aqueous system [42]. The following equations are presented to describe the effect of the pH value on electrochemical potential of the zinc species.

$$Zn^{2+} + 2e^- \leftrightarrow Zn \qquad E^0 = -0.762\,V \qquad (2.12)$$
$$E = -0.762 + 0.0296log[Zn^{2+}]$$

$$Zn(OH)_2(s) + 2e^- \leftrightarrow Zn + 2OH^- \qquad E^0 = -1.249\,V \qquad (2.13)$$
$$E = -0.420 - 0.0592pH$$

$$Zn(OH)_4^{2-} + 2e^- \leftrightarrow Zn + 4OH^- \qquad E^0 = -1.199\,V \tag{2.14}$$

$$E = 0.4586 - 0.1184pH + 0.0296log[Zn(OH)_4^{2-}]$$

From Figure 2.3b, it is noticeable that the electrochemical redox potential of zinc is lower than the hydrogen evolution equilibrium potential at all pH values. Hence, the HER is thermodynamically favorable in aqueous systems when zinc is being used as the anode. This means that the zinc electrode can be corroded and consumed by the HER, worsening the zinc metal plating/stripping efficiency and reversibility of the zinc electrode. The competitive HER can occur during zinc deposition/dissolution processes or even at rest periods (referred to as self-discharge). The problem is more profound in acidic solutions because of a higher gap between the hydrogen evolution and Zn/Zn^{2+} equilibrium potentials compared to alkaline solutions. The production of hydrogen gas from hydrolysis of water also leads to the consumption of protons and a rise in electrolyte pH, altering the suitable environment for certain electrodes. Consumption of water molecules could ultimately lead to water depletion, notably in open-cell configurations, and thus inflate the battery maintenance cost. Moreover, the production of hydrogen gas can build up resistance and amplify internal pressure in a sealed battery pack, causing swelling and blow-out in the worst-case scenario [43].

The following pairs of reactions are examples of water-zinc reactions and the production of hydrogen gas in acidic and alkaline environments.

$$Zn \leftrightarrow Zn^{2+} + 2e^- \qquad \textit{Acidic} \tag{2.15}$$
$$2H^+ + 2e^- \leftrightarrow H_2$$

$$Zn + 4OH^- \leftrightarrow Zn(OH)_4^{2-} + 2e^- \qquad \textit{Alkaline} \qquad (2.16)$$
$$2H_2O + 2e^- \leftrightarrow H_2 \uparrow + 2OH^-$$

In an acidic solution, the zinc is transformed to Zn^{2+} by losing two electrons, which combine with available protons in aqueous media to form hydrogen gas. In an alkaline solution, the species of zinc are dependent on pH value as shown in Figure 2.3b. For instance, in a very strong alkaline solution, zinc dissolves in the form of zincate ions and donates the electrons to decompose the water. Although the HER is thermodynamically favorable, its rate is controlled by its slow kinetics. Therefore, the relative rate of hydrogen evolution (as a percentage of total current) is curtailed as the zinc deposition current density increases. Any strategies that raise the hydrogen evolution overpotential contribute to cutting down the rate of unwanted HER [38,39].

All four of the above-mentioned detrimental phenomena can weaken the reversibility of the zinc deposition/dissolution reactions and thus the electrochemical performance of aqueous zinc-based batteries. To compensate for the low reversibility and underutilization of the zinc metal, its capacity in aqueous systems is often designed to be in excess of the cathode.

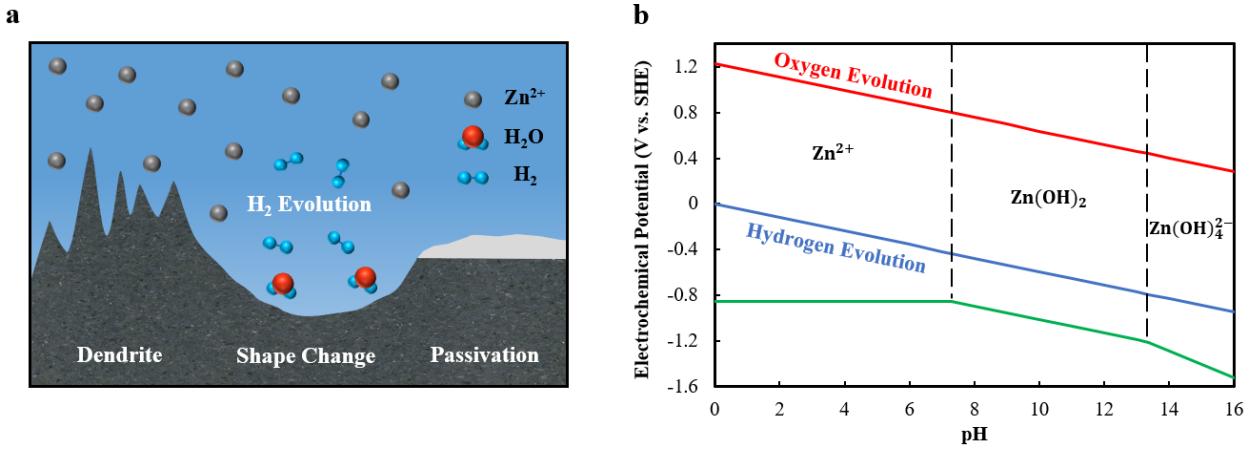

Figure 2.3 a) Schematic illustration of the performance-limiting phenomena that may happen on the zinc electrode including dendrite formation, shape change, passivation, and hydrogen evolution. b) Pourbaix diagram of water and zinc at a low concentration of zinc ions (10^{-3} mol L^{-1}). Blue and red lines represent the hydrogen and oxygen evolution potentials, respectively. The green line is the electrochemical potential of zinc as a function of pH.

2.3. State-of-the-art strategies toward high-performance ARZLBs

Motivated by the promising potential and current challenges and limitations of ARZLBs, researchers have developed strategies and made significant progress to improve their electrochemical performance. State-of-the-art strategies for ARZLBs including cathode material development, zinc anode engineering (porous zinc electrode, surface coating, electrode additives), and electrolyte engineering (pH adjustment, electrolyte additives, highly concentrated electrolyte, and gel-type electrolytes) are discussed here.

2.3.1 Cathode material development

Improving the electrochemical performance and structural stability of Li-ion intercalation materials in aqueous media are important factors to further develop aqueous Li-ion batteries. For this reason, some strategies include surface coating, metal doping, optimization of electrode morphology, and SEI layers are found to improve the electrochemical performance of the electrode. Several Li-ion intercalation compounds have been studied as cathode active materials for ARLBs, including $LiMn_2O_4$ [44], $LiFePO_4$ [36], $LiMnPO_4$ [45], $LiCoO_2$ [46], $LiNi_{1/3}Co_{1/3}Mn_{1/3}O_2$ [47], V_2O_5 [48], and most recently $LiVOPO_4$ [49] and silicate-based Li_2MnSiO_4 [50].

Spinel $LiMn_2O_4$ is considered a promising cathode active material in ARLBs due to its high safety, low cost, high voltage, and structural stability in aqueous electrolytes. However, pristine $LiMn_2O_4$ particles suffer from dissolution of Mn^{3+} in acidic electrolytes, phase transition, and relatively low Li-ion diffusion rate [51,52]. Tang et al. optimized the morphology of $LiMn_2O_4$ by synthesizing novel nanostructured materials like nanochains [53] and nanotubes [54]. The optimized morphology boosted the rate capability and cyclability of $LiMn_2O_4$ in ARLBs. The nanochain structure showed rapid charging capability and no evidence of capacity fading at 4.5 C-rate after

200 cycles [53]. The $LiMn_2O_4$ with nanotube structure (Figure 2.4a) presented superior rate capability with about 50% of its theoretical capacity at a high current of 600 C-rate (6 s) as observed in Figure 2.4b. It also exhibited excellent cycling performance after 1200 cycles due to the porous structure that could buffer the stress of Jahn-Teller effects [54]. Chen et al. [55] synthesized nanocomposite $LiMn_2O_4$/graphene/CNTs with ultrafast lithium diffusion, making it an ideal choice for hybrid supercapacitors. Qu and co-workers [56] prepared porous $LiMn_2O_4$ by using polystyrene as a template for the cathode active material, which demonstrated excellent rate capability in aqueous 0.5 M Li_2SO_4 electrolyte; its discharge capacity at 1 Ah gr^{-1} current density was around 95% of its total capacity. The exceptional rate performance of nanostructured $LiMn_2O_4$ in ARLBs is attributed to the short Li^+ diffusion length and the minimal strain from Jahn-Teller distortion, leading to long cycle life.

Zhi et al. [27] demonstrated a unique coating strategy by introducing graphene films as an artificial SEI with a controllable thickness of about 10 nm, which they claimed can prevent the structural distortion of $LiMn_2O_4$ in aqueous electrolyte. By constructing the SEI layer, the accumulation of Li^+ and formation of Mn^{3+} rich regions around the $LiMn_2O_4$ particles, which both are responsible for Jahn-Teller distortion, can be avoided (Figure 2.4c). As a further example, Zhi et al. [57] recently coated the top surface of $LiMn_2O_4$ with acrylonitrile copolymer and graphene using air-spraying as a fully scalable method with controllable thicknesses of 200 nm up to 1 μm. The Li^+ penetrable acrylonitrile copolymer coating is capable of suppressing undesirable side reactions while graphene accelerates the ion diffusion rate, resulting in improved electrochemical performance in aqueous Li-ion batteries.

Layered metal-oxide materials such as $LiCoO_2$ and $LiNi_{1/3}Co_{1/3}Mn_{1/3}O_2$ are also commonly employed as cathode active materials in ARLBs. $LiCoO_2$ has a high electrochemical potential,

meaning that it can show stable performance only with the use of reduced cut-off voltages. Raising the cut-off voltage to the values of more than 1.4 V vs. SHE normally results in lowered CE and capacity retention; using the $LiCoO_2$ at higher cut-off potentials to benefit from a higher specific capacity (up to 135 mAh g^{-1}) could lead to serious capacity fading as a result of side reactions like water oxidation [46].

An ARLB based on $LiNi_{0.81}Co_{0.19}O_2$ as the cathode was first proposed by Kohler et al. [58] with a 1 mol L^{-1} Li_2SO_4 solution and LiV_3O_8 as the anode. However, only 15-20% of the cathode's theoretical capacity was achievable, cutting down the effective energy density of the battery to a trivial value of 10-15 Wh kg^{-1} (about half the energy density of common nickel-cadmium batteries). Furthermore, only about 40% of the initial discharge capacity was maintained after 100 cycles with a 1.3 V cut-off charge voltage, and a further lowered 25% retention after 100 cycles with a 1.9 V cut-off charge voltage (Figure 2.4d). It was concluded that the bare LiV_3O_8 and $LiNi_{0.81}Co_{0.19}O_2$ electrodes are not stable in aqueous electrolyte [58].

Vanadium oxide (V_2O_5) has a high theoretical capacity of 238 mAh g^{-1}; however, as the cathode active material, it exhibits poor stability and low electronic conductivity in aqueous electrolyte. To address this issue, Han et al. [48] proposed a surface modification strategy to form an artificial SEI layer on the V_2O_5 electrode, which could prevent direct contact of the water molecules with the active material particles and provide thermal stability under elevated temperature. Lithium vanadium phosphate ($Li_3V_2(PO_4)_3$) is also an attractive candidate as the cathode active material for aqueous batteries owing to its low cost, high safety, and strong structural stability. Recently, Ding et al. [59] developed a $Li_3V_2(PO_4)_3$ material coated with both carbon-citric acid and polyvinylpyrrolidone with a 125 mAh g^{-1} discharge capacity at 1 C-rate and excellent rate performance up to 100 C-rate, making it a logical choice for high power applications.

Olivine-structured $LiFePO_4$ is considered as a suitable cathode active material for ARLBs owing to its high theoretical capacity, robust chemical stability in water, low cost, safety, and environmental advantages [60]. The relatively low electrochemical potential of $LiFePO_4$ can theoretically inhibit the OER. However, pristine $LiFePO_4$ suffers from accelerated degradation when it is in direct contact with OH^- and dissolved oxygen in aqueous media [36] and when it is exposed to mechanical agitation during electrode processing [60]. In addition, $LiFePO_4$ materials suffer from poor electronic conductivity (about 10^{-9} S cm^{-1} at 30 °C) and a low Li-ion diffusion rate [61,62]. Modification of $LiFePO_4$ via surface coating with carbon [63] or AlF_3 [64] can hinder unfavorable side reactions between $LiFePO_4$ and aqueous electrolytes and prevent detrimental surface passivation. In addition to improved surface stability, surface coating strategies on $LiFePO_4$ active materials can also lower the charge transfer resistance, leading to generally enhanced electrochemical performance of ARLBs including cycle life, capacity retention, and rate capability [64]. Recently developed high surface area and electronically conductive additives such as graphene [62] and CNTs [65] have been further introduced to enhance the electron migration rate in the $LiFePO_4$ cathode. Duan et al. [65] prepared a $LiFePO_4$ material covered with flocculent carbon layers and wrapped with CNTs by the sol-gel method. The assembled battery with the prepared carbon-nanotube composite $LiFePO_4$ cathode and a zinc anode delivered a high discharge capacity of 158 mAh g^{-1} at 1 C-rate and 110 mAh g^{-1} at 50 C-rate [65].

Recently, the use of highly concentrated electrolytes has expanded the electrochemical stability limit of water to more than 3 V, making it possible to incorporate a wider range of cathode materials for aqueous Li-ion batteries. For example, water-in-salt electrolytes have enabled stable cycling performance of $LiNi_{0.5}Mn_{1.5}O_4$ and halogen-conversion-intercalation compound in graphite with more than 2.5 V cell voltage [66,67]. Wang et al. [66] synthesized $LiNi_{0.5}Mn_{1.5}O_4$ with an

expanded lattice structure to facilitate Li^+ diffusion, showing that almost the full theoretical capacity of $LiNi_{0.5}Mn_{1.5}O_4$ could be realized in a mild acidic concentrated electrolyte with an assembled cell voltage of 2.5 V. Yang et al. [67] reported a halogen-conversion-intercalation compound in graphite as the cathode with a high specific capacity of 243 mAh g^{-1} and a 4.0 V discharge voltage using a highly concentrated electrolyte.

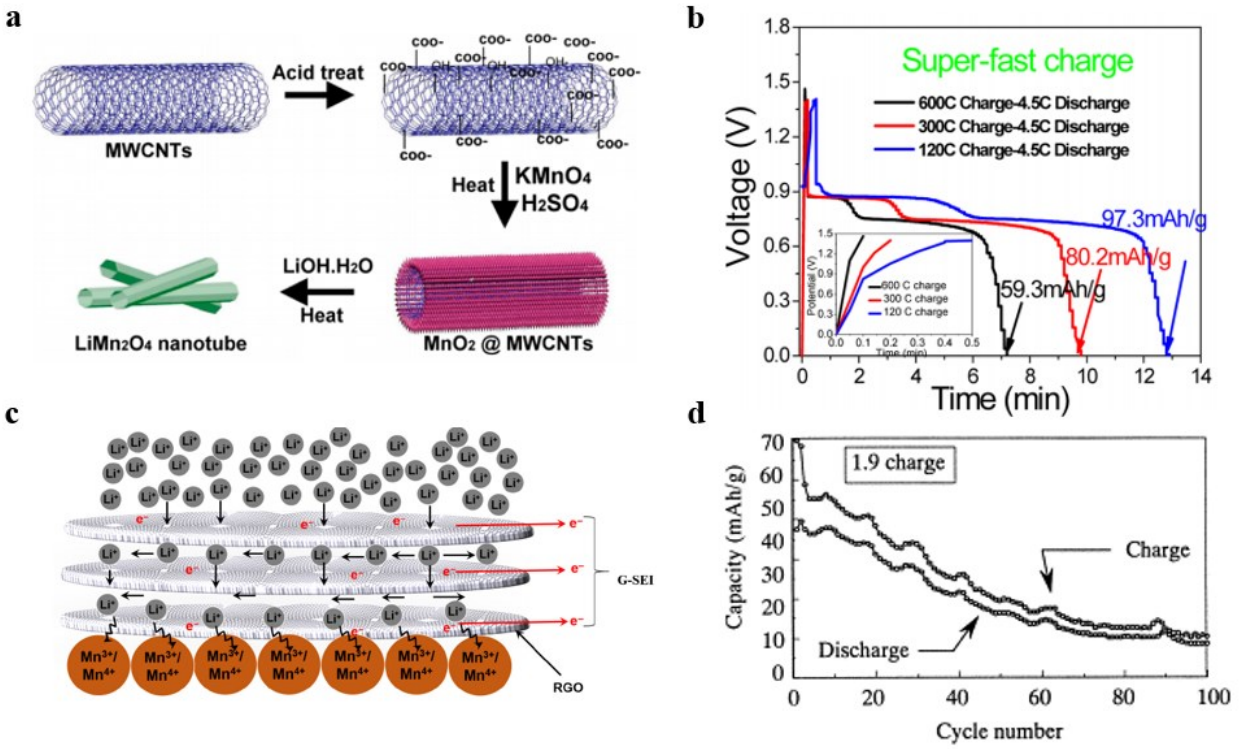

Figure 2.4 a) Schematic of the $LiMn_2O_4$ nanotube preparation. b) Super-fast charge and discharge curves of the $LiMn_2O_4$ nanotube vs. time tested by nickel as the counter electrode and the saturated calomel electrode (SCE) as the reference electrode. Reproduced with permission from ref. [54], Copyright 2013 American Chemical Society. c) Permeation-based mechanism illustration for $LiMn_2O_4$ cathode with the SEI layer, showing Li^+ diffusion and electron movement. Reproduced with permission from ref. [27], Copyright 2017 American Association for the Advancement of Science. d) Cycling behavior of $LiNiCoO_2/LiV_3O_8$ cell at 1.9 V charge cut-off voltage. Reproduced with permission from ref. [58], Copyright 2000 Elsevier.

2.3.2 Zinc anode engineering

The geometry and morphology of the zinc electrode are fundamental factors for achieving high-performance zinc-based batteries. Increasing the surface area of the zinc electrode can optimize the current distribution, minimize the local current density, and provide more void space for zinc deposition, thus lowering the likelihood of zinc dendrite growth and shape change problems. However, a higher surface area activates a higher rate of HER and corrosion of the zinc [39]. Any effective strategies such as surface coating and deployment of additives to mitigate the water activity reactions and corrosion rate of the zinc can improve the CE and reversibility of the zinc.

2.3.2.1 Porous zinc electrode

Previous investigations demonstrated that zinc electrodeposition on a highly porous open-structure current collector such as copper foam [68] and the design of highly porous zinc composites such as 3D sponge zinc [69] can enhance the electrochemical performance of the zinc electrode. Local current densities can be diminished on a higher surface area compared to a planer and flat surface, which assists in applying higher planar current densities in porous zinc-based batteries [38].

In a series of works by Parker and co-workers [69–72], the authors designed porous sponge-like three-dimensional (3D) zinc electrodes with applications in alkaline zinc batteries such as zinc-air, nickel-zinc, and silver-zinc batteries. The sponge form-factor zinc can deliver dendrite-free operation, though the costly and complicated fabrication process and low rate performance may hinder its development and scalable manufacturing for next-generation zinc-based batteries. One practical approach to manufacturing highly porous and high-surface-area zinc anodes is achieved by electrodeposition on a 3D open-structure current collector as a host material. Wang et al. [73] synthesized conventional metal-organic framework ZIF-8 as a porous host material for

dendrite-free zinc deposition. The 3D structure was attained by ZnN_4 tetrahydrate units that were connected through imidazolate linkers with large void spaces, and its inherent porous structure was maintained intact upon frequent cycling. Kang et al. [74] reported a 3D zinc anode by electrodeposition on a porous and open-structure copper skeleton. The 3D structure of the copper host ensured uniform and reversible zinc plating/stripping at near 100% CE which provides a pathway for developing high-cycle life zinc-based batteries. The large pores of the 3D copper skeleton could accommodate the volume change during zinc plating/stripping and its structure maintained high electrical conductivity. In contrast, since zinc foil acts simultaneously as the current collector and active material, the electrical properties and volume of planner zinc foil change adversely during cycling, resulting in an unstable performance (Figure 2.5a).

The 3D architecture has not yet been adopted in ARZLBs, and further research is needed to develop a specialized 3D structured zinc electrode for this type of battery. As a first step to developing a dendrite-free zinc electrode, Molkenova and co-workers investigated porous zinc as an anode for aqueous rechargeable zinc/$LiFePO_4$ batteries [75]. The porous zinc was prepared by electrodeposition of zinc ions onto carbon paper which was attached to a 0.13 mm backing-plate graphite. As potential separators and coating layers for the porous zinc anode, the effect of poly (p-phenylene oxide) (PPO) polymer [75] or a gel-like composite polymer [76] were investigated and demonstrated better cyclability than the uncoated zinc. However, the initial capacity of the battery with a PPO-coated anode was lower than the uncoated zinc. Ahmed et al. [77] employed a scalable supersonic cold spraying technique to manufacture a highly porous zinc anode with 40% higher surface area than a zinc plate. The slurry mixture, consisting of zinc powder, lead oxide, and bismuth oxide, was carried by a gas stream at supersonic speed and then sprayed on a brass substrate. The sprayed zinc anode showed improved cycle life and rate performance in an ARZLB

due to the high surface area and suppressed dendrite growth. The authors noted that this strategy is fully scalable for any size of battery manufacturing and can be employed for large-scale energy storage systems [77].

To further improve the electrochemical performance of the porous zinc anode, Tao and his colleagues [78] investigated the effect of different types of carbon additives including acetylene black, CNTs, and activated carbon which were added to the porous zinc anode. The cycling performance of the porous zinc anode composite in a zinc/$ZnSO_4$-Li_2SO_4/$LiMn_2O_4$ hybrid aqueous battery is illustrated in Figure 2.5b. The results show that carbon additives increase the discharge capacity and cycling performance of the zinc/$LiMn_2O_4$ battery; the battery with activated carbon additive maintained an initial capacity of 140 mAh g^{-1} and 210 cycles compared to 114 mAh g^{-1} and 36 cycles in the pure zinc anode [78].

2.3.2.2 Surface coating

Surface coating is a rational strategy that serves as an inert physical barrier to protect the zinc surface from direct contact with aqueous media, thus reducing the water activity corrosion reactions and dendrite formation. However, coating layers may increase electrode resistance and weaken electronic/ionic conductivity. The selection of an ideal coating layer depends crucially on various factors including high ionic conductivity for Zn^{2+} ions, low electronic resistivity, insolubility and stability in acidic or alkaline environments, and high mechanical properties [79].

Various types of surface coatings containing activated carbon [80], $CaCO_3$ [81], TiO_2 [82], ZrO_2 [83], and polyamide [79] have been investigated in aqueous zinc-based batteries. Zhao et al. [79] presented a strategy to solve common zinc electrode issues in advanced zinc-based batteries by introducing a multifunctional polymeric interface that has a strong capability to coordinate with metal ions and form hydrogen bonds. The coated layer consisted of polyamide and zinc trifluoromethane

sulfonate ($Zn(TfO)_2$) with the ability to suppress water-induced corrosion reactions, evenly distribute current, and restrict Zn^{2+} two-dimensional diffusion. Li et al. [80] developed a facile and scalable strategy by coating carbon on the zinc foil surface to suppress dendrite generation. To keep the coating layer protective while maintaining effective Zn^{2+} ion migration, the thickness was optimized at 90 μm. The coated carbon layer featured a rough surface and abundant void space for zinc deposition that could facilitate homogeneous current distribution and zinc deposition [80]. In another study, Kang et al. [81] proposed a porous nano-$CaCO_3$ coating on zinc metal to promote zinc plating/stripping efficiency and stability of the electrode. The high porosity of the coating confined the zinc nucleation within the nanopores, which could assist in promoting uniform and bottom-up zinc deposition and constrained the augmentation of protrusions (Figure 2.5c). The pristine nano-$CaCO_3$ coated zinc is much more porous than the bare zinc and its morphology remained intact after 100 repeated plating/stripping cycles without any detectable protrusions. The effectiveness of the porous surface-coating strategy was also confirmed with acetylene black and nano-SiO_2 coatings, which demonstrated similar functionality [81].

2.3.2.3 Electrode additives

The main purpose of the electrode additives, which can be applied whether inside the zinc anode structure or into the plating solution, is to prevent the growth of zinc dendrites by regulating current distribution and facilitating smooth deposition of zinc. Sun et al. [84] investigated the effect of various additives including cetyltrimethylammonium bromide (CTAB), sodium dodecyl sulfate (SDS), polyethylene glycol (PEG-8000), and thiourea (TU) on electrochemical performance of a zinc/$LiMn_2O_4$ battery. The zinc anodes were prepared by electrodeposition in the plating solution with these organic additives, which affected their crystallographic properties and morphology. The zinc/$LiMn_2O_4$ batteries with zinc-PEG, zinc-SDS, and zinc-TU anodes showed 76%, 79%, and

80% capacity retention for 1000 cycles at 4 C-rate compared to 67% for the same battery with a commercial zinc foil. In another study [85], they also synthesized zinc electrodes by electroplating in aqueous electrolytes with selected inorganic additives including tin oxide, indium sulfate, and boric acid. They showed that the corrosion rate of the synthesized zinc anode decreased up to eleven times compared to the conventional zinc foil, which was attributed to the enhanced crystallography and surface texture of the deposited zinc. The morphologies of electroplated zinc anodes with indium sulfate and tin oxide additives and their comparison with commercial zinc foil can be observed in the scanning electron microscopy (SEM) images in Figure 2.5d. The commercial zinc foil has a flat and shiny surface, while the electrodeposited zinc electrodes have chunks of zinc deposits with thin fiber-like zinc on top; the higher surface areas of the latter morphologies are claimed to minimize the possibility of dendrite growth [85].

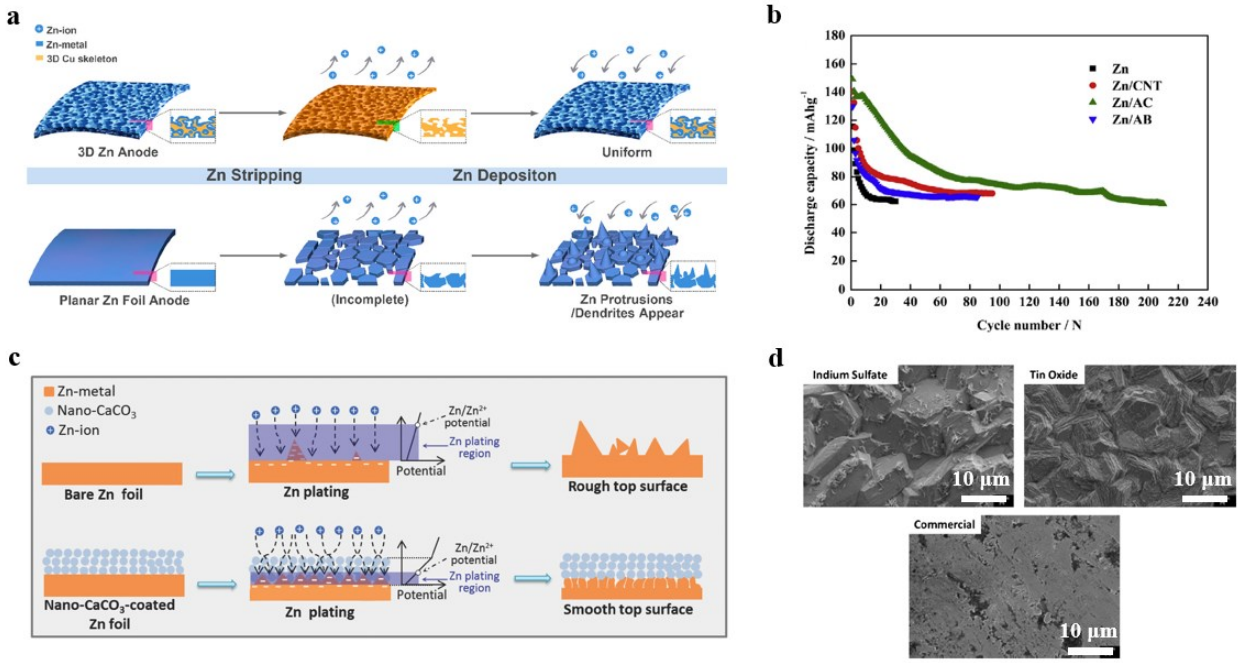

Figure 2.5 a) Schematic diagrams of zinc plating/stripping processes on 3D zinc electrodes and planar zinc foil electrodes. Reproduced with permission from ref. [74], Copyright 2019 American Chemical Society. b) Cycle stability of the zinc/$LiMn_2O_4$ battery at 240 mA g^{-1} current density with pristine porous zinc, zinc/CNTs, zinc/active carbon, and zinc/acetylene black anode. Reproduced with permission from ref. [78], Copyright 2016 Elsevier. c) Schematic of the morphology evolution mechanism for bare and nano-$CaCO_3$-coated zinc foils during zinc deposition/dissolution cycling. Reproduced with permission from ref. [81], Copyright 2018 Wiley-VCH. d) Surface SEM images of electrodeposited zinc with additives and of commercial zinc foil. Reproduced with permission from ref. [85], Copyright 2018 Wiley-VCH.

2.3.3 Electrolyte engineering

2.3.3.1 Electrolyte pH adjustment

The electrolyte pH is a crucial factor that dictates the solubility and form of oxidized zinc species, and most importantly alters the redox potential of parasitic side reactions in aqueous solutions. As observed in the Pourbaix diagram of water (Figure 2.2), the HER and OER can be suppressed in alkaline and acidic solutions, respectively. The oxygen evolution potential shifts downward at high pH values and limits the selection of cathode active materials, while the hydrogen evolution potential shifts upward at low pH values and restricts the anode options. For instance, high voltage cathode materials such as $LiNi_{1/3}Co_{1/3}Mn_{1/3}O_2$ and $LiMn_2O_4$ should not be used in alkaline electrolytes since their working potential is higher than the oxygen evolution potential. Many studies in the literature have reported adjusting the electrolyte pH to accommodate more cathode and anode active materials with extreme electrochemical potentials. Although regulating the electrolyte pH alters the hydrogen and oxygen evolution potential, it should be noted the gap between them remains constant and does not expand the thermodynamic stability limits of water. Optimization of the electrolyte pH can also result in several benefits including higher utilization of active material, higher reversibility, and more stable cycling performance [13].

Pei et al. studied the effect of pH on the electrochemical performance of a zinc/$LiMn_2O_4$ battery. They used 5 mol L^{-1} $LiNO_3$ aqueous electrolyte and investigated the effect of pH over a wide range from 2.0 to 12.3 via cyclic voltammetry (CV). At high pH values, they observed that the oxidation peaks of water are heightened which can be attributed to the decreased oxygen evolution potential. At lower pH values, the reduction peaks for the initial and subsequent cycles are relatively overlapped which indicates a negligible capacity loss; however, the co-intercalation of protons can take place in electrolytes with very low pH [34]. Another aspect of electrolyte pH to

consider is its crucial impact on the zinc speciation and redox potential of zinc ions. As shown in Figure 2.3b, zinc species can be in the form of Zn^{2+} ions in acidic and neutral solutions and in the form of insoluble $Zn(OH)_2$ and soluble zincate in basic solutions. Due to the high availability of OH^- ions in alkaline electrolyte, the formation of insulating $Zn(OH)_2$ and ZnO by-products is favorable and thereby leads to inferior CE and capacity fading. Accordingly, when alkaline electrolytes are chosen, the concentration of KOH electrolyte should be high enough to dissolve the discharged zinc products and convert them to zincate ions. On the other hand, as the concentration of KOH exceeds 6 mol L^{-1}, the conductivity of the electrolyte weakens. To balance the conductivity and solubility of the electrolyte, the concentration of KOH is often optimized at 6 mol L^{-1} which can dissolve 1 mol L^{-1} of zinc oxide. The relatively low solubility of zincates can limit the amount of zinc that can be employed, leading to low energy density for alkaline zinc-based batteries [86,87]. In contrast to alkaline electrolytes, neutral and acidic electrolytes tend to have high solubility in the form of Zn^{2+} ions and also render high ionic conductivity.

Since the Zn^{2+} ions in ARZLBs can also be the source of the zinc electrode capacity, the concentration of Zn^{2+} ions should be high enough to provide sufficient energy density and maintain an adequate amount of capacity during battery cycling due to zinc reversibility challenges. However, the concentration of zinc ions is limited by zinc solubility, which is affected by electrolyte pH. Yesibolati et al. [20] developed a rechargeable aqueous zinc/$LiFePO_4$ battery with high performance and high rate capability in an acidic electrolyte. In their system, a binary solution of 3 mol L^{-1} LiCl and 4 mol L^{-1} $ZnCl_2$ was suggested, which provided high conductivity and sufficient zinc concentration. Since $LiFePO_4$ and zinc materials are not stable in strongly acidic electrolytes, the pH of the electrolyte was optimized at 4 (Figure 2.6a). The assembled

zinc/$LiFePO_4$ battery showed relatively stable performance over 400 charge-discharge cycles at 6 C-rate in the optimized mildly acidic electrolyte with 99% CE [20].

Yan et al. [10] verified that a $LiMn_2O_4$ cathode is not stable in strongly acidic aqueous electrolytes; the electrolyte concentration of manganese ions was about 180 mg L^{-1} at pH=1 compared to only 1.7 mg L^{-1} at pH=4, indicating much higher manganese dissolution in the former electrolyte. Furthermore, in very strong acidic solutions, hydrogen evolution is more profound and co-insertion of proton ions along with Li^+ intercalation is possible. While Wang et al. [88] showed that olivine $FePO_4$ and amorphous $FePO_4.2H_2O$ anodes are stable at any pH value, the optimal electrolyte pH was found to be 5 to avoid the HER and thus fully utilize their capacity. They also reported that traditional Li-ion cathode active materials such as $LiMn_2O_4$, $LiCoO_2$, and $LiNi_{1/3}Co_{1/3}Mn_{1/3}O_2$, which are not completely stable in alkaline electrolytes, can operate with full utilization in acidic solutions to effectively suppress the OER [88].

As discussed before, the HER and OER change linearly with pH value, but the electrochemical stability window of water remains constant. From Figure 2.2, it is obvious that the maximum redox voltage difference between potential cathode and anode materials in extremely acidic and alkaline solutions could be theoretically up to roughly 2 V, and the kinetic overpotential of HER and OER can further extend this value. This expanded voltage window is feasible when hybrid electrolyte solutions with a maximal difference in pH values between the cathode and anode sides are used. To our knowledge, only one study [89] has incorporated electrolytes with different pH values in ARZLBs, but there are more reports [90,91] in other types of aqueous batteries. Zhang et al. [91] developed a hybrid alkaline zinc iodine flow battery with a 0.497 V voltage enhancement by tuning an acid-alkaline electrolyte. The redox potential of zinc drops from -0.763 V (vs. SHE) in acids to -1.260 V (vs. SHE) in basic solutions. This strategy could expand the working potential

of zinc Li-ion batteries up to 0.497 V, which ultimately can increase energy density. Yuan et al. [89] proposed a zinc/$LiMn_2O_4$ battery with a hybrid electrolyte system containing alkaline (1 mol L^{-1} LiOH and 1 mol L^{-1} $Li_2Zn(OH)_4$) and neutral (5 mol L^{-1} $LiNO_3$) electrolytes on the anode and cathode sides, respectively. The average discharge voltage of the battery was enhanced up to 2.31 V and it exhibited 300 cycles at 1.69 C-rate. However, utilizing expensive membranes to retard electrolyte crossover could prevent the success of this strategy. Hence, there is still room for further development of hybrid acidic-basic electrolyte battery designs.

2.3.3.2 Electrolyte additives

Electrolyte additives have been extensively utilized in aqueous batteries to suppress side reactions and mitigate zinc dendrite growth. Electrolyte additives explored in literature can be categorized into organic additives including polymers and surfactants and inorganic additives such as metal oxides and metal salts.

Organic electrolyte additives can cause higher deposition overpotentials by blocking the growth sites of zinc dendrites, resulting in increased nucleation rates and smooth electrodeposits. Organic additives can also selectively adsorb on the zinc electrode surface and cover some active hydrogen evolution sites, thus preventing the HER [38,92,93]. Wu et al. [94] utilized thiourea as an organic electrolyte additive in zinc/$LiMn_2O_4$ battery to increase the cycling performance by decreasing the float charge current density. The float charge can be used to evaluate the side reactions in an aqueous battery. It is believed that the lower float current density can reduce self-discharge and improve energy efficiency. Hao et al. [93] further proposed sodium dodecylbenzene sulfonate as an effective additive to improve the electrochemical performance of zinc/$LiFePO_4$ battery. They reported that this additive upgraded the surface wettability of the electrode and regulated the zinc plating pattern. The diffusion of Li-ions at the electrode-electrolyte interface

was also accelerated and the resulting cycling stability of the battery was boosted via dendrite-free operation.

Tron and co-workers [95] studied the anti-freeze effect of PEG on the electrochemical performance of an ARLB with $LiFePO_4$ cathode in 1 mol L^{-1} Li_2SO_4 aqueous solution. 40 wt.% and even 20 wt.% of the PEG additive to the electrolyte solution extended the operational range of ARLBs to sub-zero temperatures down to -20 °C with improved cycling performance (Figure 2.6b) [95]. The aqueous battery with this anti-freeze additive could therefore have applications in high-altitude drones, aerospace, and extreme weather conditions. Mitha et al. [43] proposed an interaction mechanism (Figure 2.6c) to explain the effect of PEG on the nucleation sites of the zinc surface. They showed that PEG molecules preferably occupy the nucleation sites via adsorption on the electrode surface, retarding the further adsorption of zinc ions and dendrite growth. Moreover, the PEG molecules restrict the lateral diffusion of zinc ions to existing nucleation sites, facilitating the formation of many nucleation sites instead, leading to much smaller particles and smoother electrodeposits. The authors also reported that corrosion and deposition current densities decreased in the presence of PEG to one-fourth of the non-additive values.

Inorganic additives have not been used extensively in ARZLBs; however, they have been utilized in other types of zinc-based aqueous batteries. The mechanism of the beneficial zinc electrode behavior offered by inorganic additives is based on the so-called substrate effect, and they function analogous to alloying strategies for zinc-based batteries. Metal oxide and metal salt electrolyte additives such as TiO_2, $SnSO_4$, Pb_3O_4, In_2O_3, $BiCl_3$ can deposit prior to zinc ions due to having higher reduction potentials [85,96,97]. The additives can raise the conductivity of the zinc electrode, optimize current distribution, and suppress hydrogen evolution by raising this reaction's overpotential.

2.3.3.3 Highly concentrated electrolyte

The concept of highly concentrated electrolyte salts emerged in Wang's group in 2015 to enable the formation of a protective SEI layer in aqueous media to expand the narrow electrochemical stability of water in ARLBs [24]. Highly concentrated electrolyte solutions are also deployed in ARZLBs such as the zinc/$LiMn_2O_4$ battery, but not for the purpose of expanding the cell voltage, since the battery voltage is already mostly fixed by the selection of the zinc anode. The main goal of using highly concentrated electrolytes in ARZLBs is to resolve the low CE of zinc metal plating/stripping and suppress zinc dendrite growth [21,98,99]. Wang et al. [21] proposed a zinc/$LiMn_2O_4$ battery in water-in-salt electrolyte (1 mol kg^{-1} $Zn(TFSI)_2$ and 20 mol kg^{-1} LiTFSI) that delivered 4000 cycles with 85% capacity retention and 99.9% CE. Their assembled zinc/$LiMn_2O_4$ battery started with a very low discharge capacity of 30 mAh g^{-1} (based on the cathode active material mass) compared to the 120 mAh g^{-1} practical specific capacity of $LiMn_2O_4$, as a consequence of the low ionic conductivity of the supersaturated solution. However, they observed great reversibility and CE (>99%) during CV testing of zinc metal plating/stripping in the water-in-salt electrolyte. They revealed that at high concentrations of $TFSI^-$, the Zn^{2+} solvation sheath structure was reshaped and surrounded by $TFSI^-$ anions (Figure 2.6d), resulting in inhibition of the HER, high reversibility, and dendrite-free zinc operation [21]. Zhao et al. [98] employed a zinc/$LiMn_{0.8}Fe_{0.2}PO_4$ electrochemical couple for the first time with a water-in-salt electrolyte (0.5 mol kg^{-1} $ZnSO_4$ and 21 mol kg^{-1} LiTFSI), demonstrating a discharge voltage exceeding 1.8 V and having high discharge capacity at an optimized pH of 4. As an endeavor for finding cheaper electrolyte salts than $Zn(TFSI)_2$, Wang et al. recently utilized $Zn(ClO_4)_2$ [100] which has the ability to limit the side reactions by reduction of ClO_4^- and construction of a Cl^- containing layer on the zinc surface. The $Zn(ClO_4)_2$ aqueous electrolyte showed reversible zinc plating/stripping for over

3000 hours at a 1 mA cm^{-2} current density. Also, Zhong et al. utilized a low-cost water-in-salt electrolyte (15 mol kg^{-1} $ZnCl_2$ and 1 mol kg^{-1} LiCl) in zinc/$LiFePO_4$ battery to enhance CE and reversibility of the zinc. The assembled zinc/$LiFePO_4$ showed 1000 cycles under 3 C-rate with roughly 100% CE and 70% capacity retention [99].

Highly concentrated electrolyte solutions open a viable route to the development of a series of high voltage/energy-density aqueous Li-ion batteries and reversible zinc anodes without compromising safety. Notwithstanding all these merits, the high cost and potential toxicity of imide-based anions and low ionic conductivity need to be addressed to facilitate the manufacturing of low-cost, high energy-density, and high power ARZLBs. Therefore, further investigation and exploration of cheap and effective anions to expand the stability limits and protect the zinc anode are required.

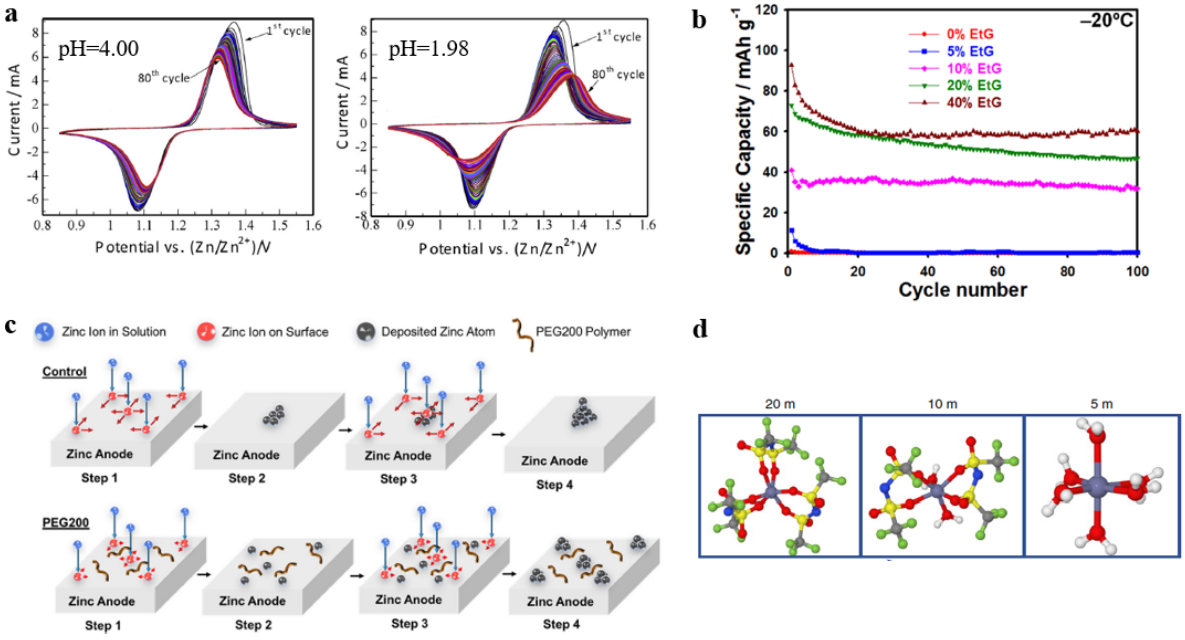

Figure 2.6 a) CV profile of zinc/$LiFePO_4$ at 0.5 mV s^{-1} scan rate at different pH values. Reproduced with permission from ref. [20], Copyright 2015 Elsevier. b) Cyclic performance of the $LiFePO_4$ material in a 1 mol L^{-1} Li_2SO_4 aqueous electrolyte with different wt.% of ethylene glycol (EtG) antifreeze additive at -20 °C. Reproduced with permission from ref. [95], Copyright 2019 American Chemical Society. c) Schematics of the zinc deposition mechanism in the presence and absence of PEG200 additive on the zinc electrode. Reproduced with permission from ref. [43], Copyright 2018 Wiley-VCH. d) Solvation sheath structures of Zn^{2+} in the electrolytes with 1 mol kg^{-1} $Zn(TFSI)_2$ and three different concentrations of LiTFSI. Reproduced with permission from ref. [21], Copyright 2018 Springer Nature.

2.3.3.4 Gel-type electrolyte

The use of liquid electrolytes entails risks of loss or leakage during battery operation, as well as zinc dendrite formation in conventional aqueous electrolytes during the charging process of zinc-based batteries. Free water molecules can also react with zinc metal to induce corrosion. One feasible strategy to restrain the water activity reactions is by taking advantage of gel-type electrolytes, which is analogous to one aspect of highly concentrated electrolyte systems in that the number of free water molecules is reduced [40,101]. Compared to the conventional electrolyte, gel-type electrolytes can offer better water retention capability in an open-air atmosphere [102]. Moreover, gel-type electrolytes render outstanding abilities to the batteries including stretchability, flexibility, self-healing, and mechanical strength [102]. The increased mechanical strength of the gel-type electrolyte can diminish the chance of dendrite growth occurring.

In one of the pioneering works in gel-type electrolytes for ARZLBs, Lu et al. [103] used a silica gelling agent in the range of 4-15 wt.%. Different formats of silica agents such as fumed silica, nano silica, and silica aerogel were added to a conventional 1 mol L^{-1} $ZnSO_4$ and 2 mol L^{-1} Li_2SO_4 electrolyte system, and the prepared gel electrolytes could reduce the self-discharge and capacity retention of the assembled battery cells [103]. Studies have shown that PEG is also very helpful to control the crystallography and morphology of zinc depositions in zinc-based batteries [104,105]. Xiong et al. [106] introduced PEG in a fumed silica gel-based electrolyte having $ZnSO_4$ and Li_2SO_4 aqueous salts, resulting in improved battery performance. The addition of PEG lowered the corrosion current density by 37%, meaning that the hydrogen evolution-induced corrosion is substantially reduced. Some other corrosion inhibitors and homogenizing agents such as pyrazole [107], Pb^{2+} [108], lignin [109], fatty methyl ester ethoxylate [110] have also been introduced in silica gel-based electrolytes. Hoang et al. [111] utilized thixotropic fumed silica and non-thixotropic B-

cyclodextrin gelling agent in an aqueous zinc/$LiMn_2O_4$ battery, resulting in higher thermal tolerance. The water retention capability of the electrolyte was confirmed by thermal gravimetric analysis; for comparison, the water in a conventional aqueous electrolyte inside an AGM separator evaporated at 64 ºC, while the gel electrolyte having 3 wt.% fumed silica and 2 wt. % B-cyclodextrin dehydrated only when the temperature reached 110 °C (Figure 2.7a). In another study, Hoang et al. [108] revealed that a thixotropic gel electrolyte containing $PbSO_4$ could result in a 20% lower corrosion current density and significantly higher shelf-life. The same group also proved that adding an optimized amount of pyrazole (0.2 wt.%) in the fumed silica gel electrolyte can significantly reduce the corrosion current density by 83% and enhance the battery performance in terms of higher open-circuit voltage (OCV) retention and lower float charge current (Figure 2.7b) [107]. In addition to its crucial role in preventing zinc dendrite formation, it has also been reported that fumed silica gel improved the stability of $LiFePO_4$ by preventing Iron dissolution and lithium loss [112].

Lowering the freezing point of gel electrolytes without sacrificing their principal merits such as low cost and high mechanical durability is challenging. Zhu et al. [113] disclosed that cooperative hydration of Zn^{2+} and Li^+ ions in a polyacrylamide hydrogel (PAAm) electrolyte can drop the freezing point of a hydrogel electrolyte to subzero temperatures while maintaining the major criteria of gel electrolytes such as toughness and sufficient ion transportation rates. Additionally, the cooperative adsorption of Li^+ can effectively inhibit the HER and prohibit the resulting local rise of pH. Henceforth, the formation of $Zn(OH)_2$ and ZnO upon cycling can be averted with this solution.

Some specific gel electrolytes can act as a separator that prevents water molecules from contacting the anode. Wang et al. [114] fabricated a unique electrode by coating a gel-polymer

membrane and LISICON on lithium metal. In this system, the lithium electrode is first covered with a gel-polymer electrolyte consisting of polyvinylidene fluoride and nonwoven fabrics, and the LISICON film comprising Li_2O-Al_2O_3-SiO_2-P_2O_5-TiO_2-GeO_2 was then covered on top of the gel-polymer electrolyte and served as a solid separator to keep water molecules away from the anode. Despite the absence of water molecules, the Li-ions can move through the coating and access the electrode due to the cross-over effect. This novel design was a big leap toward 4 V class ARLBs [114]. In another study, Chang et al. [19] employed the same concept by coating the gel-polymer membrane and LISICON on a graphite electrode (Figure 2.7c) to avoid sudden failure from dendrite formation on lithium metal, since this could not be completely prevented with the coating system. This design enabled the operation of an ARLB with a high average discharge voltage of 3.1 V and thus increased energy density relative to using a conventional electrolyte. Considering the high cost and low ionic conductivity of solid-state electrolytes with LISICON at room temperature, their application in ARLBs is restricted and the aforementioned coating strategy offers a more practical solution that extracts the advantages of both solid-state and conventional aqueous electrolytes [19].

As mentioned previously, gel-type electrolytes can revamp the safety and flexibility of aqueous batteries. Batteries may break during mechanical abuse such as twisting and cutting, leading to failure and/or serious safety problems. Zhao et al. [115] offered a new class of flexible all-solid-state aqueous Li-ion batteries with a self-healing property. In their system, a gel electrolyte composed of Li_2SO_4 and cross-linked sodium carboxymethylcellulose (CMC) which can act simultaneously as separator and electrolyte was designed and exhibited 0.12 S cm^{-1} ionic conductivity at room temperature. Additionally, electrodes composed of aligned CNT sheets loaded in $LiMn_2O_4$ and $LiTi_2(PO_4)_3$ active materials on polymer-based substrates displayed self-

healing properties. The self-healing aqueous Li-ion batteries exhibited high flexibility and good recovery of electrochemical storage even after several deformation procedures such as cutting (Figure 2.7d). The revised design of ARLBs with self-healing gel electrolytes is promising for wearable electronic devices due to its flexibility and resistance to mechanical deformation.

The use of gel electrolytes in ARZLBs is restricted to only a few types of gel electrolytes and thus exploration of additional kinds of gel electrolytes is warranted. There are many different types of gel-type electrolytes including, among others, xanthan gum [116], polyvinyl alcohol [117,118], gelatin [119], hydrogel sheets [120], pluronic hydrogel electrolyte (PHE) [121], all of which showed promising results in other types of aqueous batteries such as zinc-ion and zinc-MnO_2 batteries. In one of very few works examining the aforementioned gel-type electrolytes in ARZLBs, Chen et al. [122] proposed an oversaturated-gel electrolyte system with expanded electrochemical stability. The gel was prepared by adding 10 wt.% polyvinyl alcohol in an oversaturated 1 mol kg^{-1} $Zn(ClO_4)_2$ and 10 mol kg^{-1} $LiClO_4$ electrolyte system, which could assist the homogenous dispersion of $LiClO_4$ with the electrolyte. The zinc/$LiMn_2O_4$ assembled with the oversaturated gel electrolyte delivered 300 cycles with 99% CE and roughly 90 mAh g^{-1} discharge capacity under 1 C-rate [122]. Han et al. [123] reported a gelatin-based hydrogel electrolyte in a zinc/$LiMn_2O_4$ battery that could resist mechanical abuse such as bending, twisting, and cutting, thus having potential applications in flexible and wearable devices. The gelatin electrolyte was prepared by mixing gelatin powder in a Li_2SO_4 and $ZnSO_4$ solution, followed by cooling. A sudden decrease in the cooling temperature can reinforce the mechanical strength of the gelatin electrolyte and hence suppress zinc dendrite growth [123].

Despite countless advantages of gel-type electrolytes in aqueous batteries such as flexibility, self-healing, water retention, and thermal tolerance, the use of gel electrolytes in ARZLBs is still

in early development and needs more investigation. Specifically, their effect on the lifespan of ARZLBs needs to be further studied.

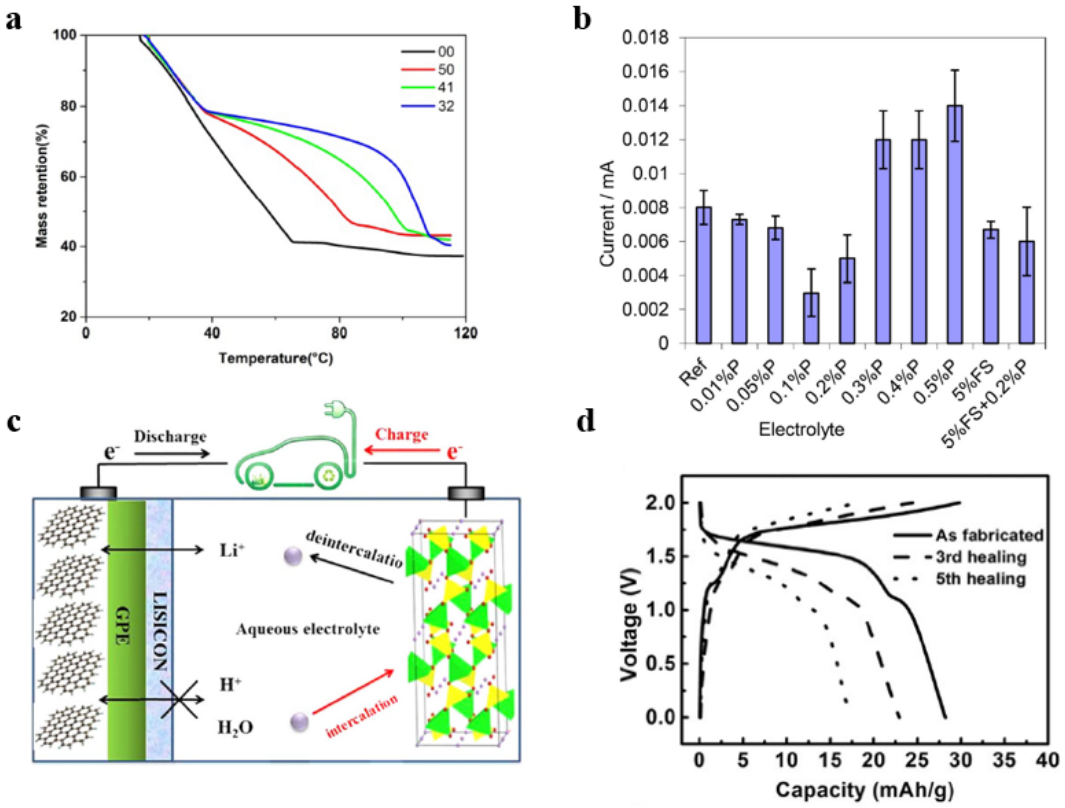

Figure 2.7 a) Thermogravimetric analysis of conventional, 5% fumed silica, 4% fumed silica + 1% cyclodextrin, and 3% fumed silica + 2% cyclodextrin electrolytes denoted as 00, 50, 41, and 32, respectively. Reproduced with permission from ref. [111], Copyright 2016 American Chemical Society. b) Float charge currents of an ARZLB with various electrolyte compositions. Reproduced with permission from ref. [107], Copyright 2017 Wiley-VCH. c) Schematic illustration of a specifically designed ARLB using graphite covered by gel-polymer and LISICON as the anode and $LiFePO_4$ as the cathode in 0.5 mol L^{-1} Li_2SO_4 electrolyte. Reproduced with permission from ref. [19], Copyright 2016 Springer Nature. d) Galvanostatic measurements of charge-discharge curves for an ARLB after various self-healing cycle numbers at 0.5 A g^{-1} current density. Reproduced with permission from ref. [115], Copyright 2016 Wiley-VCH.

3. Design and feasibility of thick dough-like cathodes for high areal-capacity zinc/$LiFePO_4$ battery

3.1. Introduction

Although recent years have witnessed impressive progress in ARZLBs in terms of electrolyte design and suppressing zinc dendrite growth as reviewed in Chapter 2, the low energy density as a result of limited output voltage and inferior areal capacity is still a barrier for the development of ARZLBs. Since the operating voltage of ARZLBs is fixed by the redox potential differences between Zn/Zn^{2+} and Li-ion active material and limited by the electrochemical stability window of water, increasing the operating voltage is not a preferred strategy to improve energy density. On the other hand, the energy density of ARZLBs is also restricted by the low specific capacity of the cathode active materials ($LiMn_2O_4$: 148 mAh g^{-1}, $LiFePO_4$: 170 mAh g^{-1}) instead of the high specific capacity of the zinc (820 mAh g^{-1}) anode. This huge difference, wherein the capacity of zinc is about 5 times higher than the capacity of the cathode, is one of the primary technical challenges in achieving high energy density ARZLBs. Therefore, to enhance the energy density, cathode loading and hence the areal capacity must be extremely high to match with the high specific-capacity zinc anode. However, the current reported areal capacity and active material loading of ARZLBs in literature are only in the range of 0.3-2.4 mAh cm^{-2} and 2.4-10 mg cm^{-2}, respectively. [10,20,21,85,107,111,122].

Despite the lack of research in increasing the areal capacity and improving the energy density of ARZLBs, several methods have been applied to enhance the energy density of commercial non-aqueous Li-ion batteries [124–126]. Among the published methods, optimizing the

cell design is a promising approach to effectively increase the energy density of the cell and reduce the battery cost. The cell design can be optimized by reducing the ratio of electrochemically inactive components in the battery cell such as separator, current collector, conductive additive, and binder [124,125,127]. With respect to the optimization of the cell design, thickening the electrode is a simple but effective strategy to increase the volume ratio of active to inactive materials and to achieve high energy density and low-cost Li-ion batteries [124,128]. However, increasing the thickness and energy density of ARZLBs with the current electrode processing for the cathode, i.e., conventional slurry-cast method, still encounters some barriers. First, the electrode thickness in conventional slurry-cast electrode manufacturing is typically less than 200 μm due to mechanical integrity limitations and the formation of cracks in thick electrodes (more than 200 μm) [129–131]. Second, electrodes thicker than 100 μm in ARZLBs and Li-ion batteries suffer from poor rate capability due to Li-ion diffusivity limitations. A study by Zheng et al. showed that by increasing the thickness of $LiFePO_4$ cathode from 10 μm to 108 μm in Li-ion batteries, the rate capability performance was reduced from 100 C to 2 C [128]. Third, the binders inside the electrode structure increase tortuosity by blocking the active material surface and isolating the particles, resulting in low electronic/ionic conductivity, active material underutilization, and thus inferior specific capacity [132–134].

To resolve the above-mentioned challenges, a first-ever approach for the thick cathode fabrication in ARZLBs is introduced. It is called dough-like cathode fabrication. Compared to the traditional slurry-cast electrode manufacturing, the proposed method is more straightforwardly, less costly, and utilizing less equipment, making the system more commercially appealing. The novel dough-like cathode design brings several advantages for the fabrication of thick cathodes. Firstly, the dough-like cathodes are manufactured at an extremely high thickness up to 1000 μm

without any crack formation and with decent consistency and flexibility. Secondly, the binder-less design reduces tortuosity and promotes electronic/ionic conductivity within the thick electrode structure. Besides, the binder space can be occupied by conductive agent and active material, which in return could further enhance the electronic conductivity and areal capacity, respectively. Thirdly, the dough-like cathode contains electrolyte in the structure which contributes to reducing tortuosity and providing enough ions to avoid the salt depletion effect at high power rates for thick electrodes. Lastly, NMP solvent processing is replaced by aqueous processing. Aqueous processing of dough-like cathodes is economically attractive since it results in the elimination of some manufacturing steps such as NMP recovery and is more eco-friendly than the NMP-processed electrode thanks to water-based chemistry. As a result of this unique electrode design, the thick dough-like cathode delivers a superb areal capacity of 10.5 mAh cm^{-2} with an extremely high active material loading of 74.5 mg cm^{-2} in zinc/$LiFePO_4$ battery. The above-mentioned values are the highest reported areal capacity and active material loading in ARZLBs.

In the current chapter, the method of binder-less and thick dough-like cathode fabrication is introduced. The dough-like cathodes are prepared at different weight ratios of active material and conductive agent and various electrode thicknesses. To take full advantage of the high specific-capacity zinc anode, the cathode thickness and active material loading are high enough to be paired with zinc metal. Furthermore, the electrochemical performance and rate capability of the ARZLBs constructed with dough-like cathodes at different thicknesses are evaluated. Finally, the energy density of the zinc/$LiFePO_4$ battery prepared by the dough-like cathode is compared with the battery fabricated by the slurry-cast cathode.

3.2. Experimental method

3.2.1 Fabrication of dough-like and slurry-cast cathode

The thick dough-like electrode was prepared by mixing the "solid phase powder" with "liquid phase electrolyte" according to the flowchart in Figure 3.1. In the first step, the "solid phase powder" was prepared by mixing and grinding carbon-coated $LiFePO_4$ (Tianjin STL Energy Technology) as active material with super P carbon black (abbreviated as SP-C; MTI) as a conductive agent. At the same time, the "liquid phase electrolyte" was prepared by dissolving $ZnSO_4.7H_2O$ (Sigma Aldrich) and Li_2SO_4. H_2O (Sigma Aldrich) in DDI water, forming a mixed solution of 2.0 mol L^{-1} $ZnSO_4$ and 1.5 mol L^{-1} Li_2SO_4. Then, the "liquid phase electrolyte" was added into the "solid phase powder" at a proper ratio, following by a continuous stirring in a planetary mixer (Thinky Mixer, AR100) at 2000 rpm for 15 mins to form a paste with a dough-like consistency. The obtained dough-like paste was then cast on a 200 μm thick graphite foil current collector at a designated thickness controlled by the rolling press machine. The diameter of the cathode was 24 mm (4.52 cm^2 surface area) with active material loading as high as 75 mg cm^{-2}. The electrode can be used directly inside the battery without drying and further processing.

The conventional slurry-cast cathode is prepared with the following procedure. First, the slurry was prepared by mixing and grinding carbon-coated $LiFePO_4$ active material, SP-C conductive agent, and Poly(vinylidenes fluoride) (PVDF, Sigma Aldrich) as the binder with a weight ratio of 85:7:8, respectively in NMP organic solvent (Sigma Aldrich). Then, the slurry was coated on a 200 μm thick graphite foil as the substrate by means of doctor blade technique and dried in a vacuum oven at 70 °C overnight to evaporate the organic solvent. After drying, the

electrodes were cut into a disk size of 24 mm diameter and it was used as the cathode inside the ARZLB.

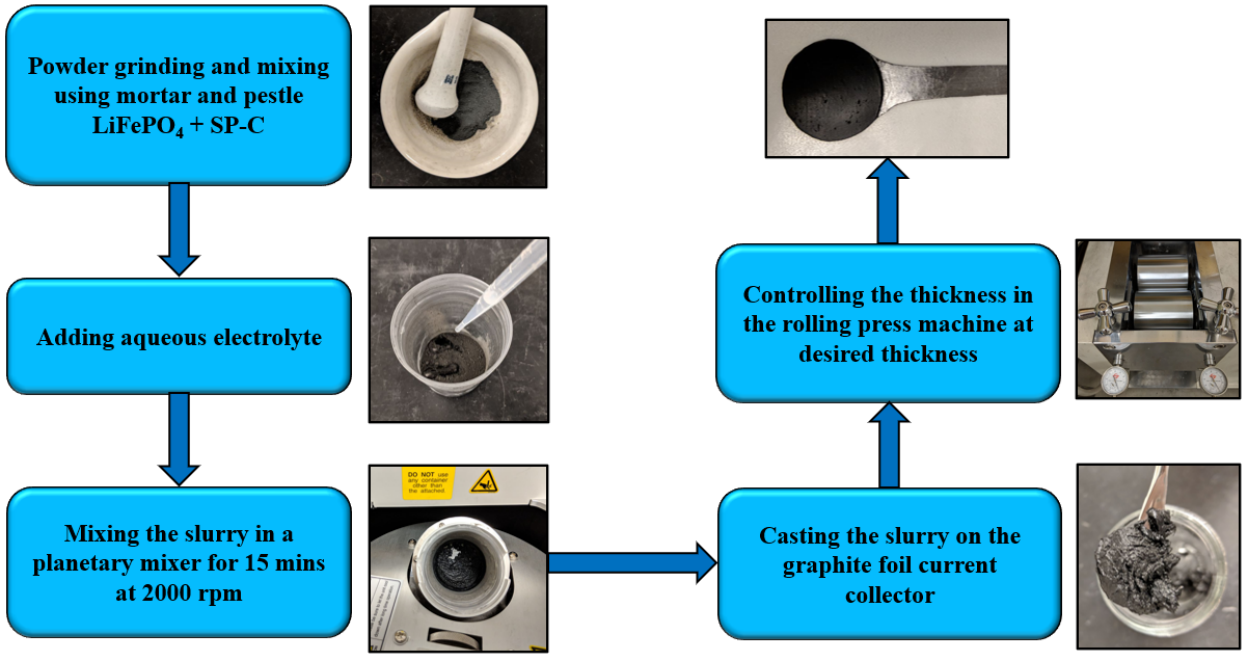

Figure 3.1 An illustration of dough-like cathode fabrication steps.

3.2.2 Preparation of aqueous rechargeable zinc/$LiFePO_4$ battery

The procedure for the preparation of zinc/$LiFePO_4$ battery is similar for dough-like and conventional cathodes. Zinc foil (Goodfellow) with 350 µm thickness was applied as the anode. The zinc foil was polished and sonicated in acetone solution and then rinsed with DDI water prior to experiments. The electrolyte was 2.0 mol L^{-1} $ZnSO_4$ and 1.5 mol L^{-1} Li_2SO_4 at adjusted pH of 5. The mild acidic electrolyte ensures high stability of zinc/$LiFePO_4$ battery with minimal water-splitting reaction [10,20]. Absorbent glass mat (AGM, NSG Group) and Celgard (5550) separators were soaked into the aqueous electrolyte. The AGM layer acts as the wetting layer to provide enough electrolyte for battery operation, while the Celgard layer serves as the barrier layer to prevent dendrite growth. After preparing the electrodes and aqueous electrolyte, the separator

layers were placed between the zinc foil anode and the dough-like cathode. The acrylic plates were used as supporting ends and fastened together using bolts and nuts, and the assembled batteries were sealed by applying parafilm-M self-sealing tape to minimize electrolyte loss upon cycling.

3.2.3 Electrochemical measurements

The cycling and rate capability performance of aqueous zinc/$LiFePO_4$ battery was investigated galvanostatically on a LAND battery tester (LANHE, CT2001A) at various current densities and C-rates (1 C corresponds to 170 mAh g^{-1}). The cut-off voltages were set at 0.8 V and 1.6 V. In this work, the specific capacity (mAh g^{-1}) measured based on the capacity of the electrode in mAh per total grams of active material; while the areal capacity (mAh cm^{-2}) calculated based on the capacity of the electrode in mAh per unit surface area of the electrode in cm^2. Electrochemical impedance spectroscopy (EIS) data of the full-cell zinc/$LiFePO_4$ battery was performed using zinc electrode as the reference and counter electrode and $LiFePO_4$ cathode as the working electrode. The scan rate was set from 1000 kHz to 0.1 Hz at 5 mV sinus amplitude using VSP-300 Biologic instrument.

3.2.4 Physiochemical characterization

Scanning electron microscopy (SEM, FESEM Zeiss Ultra Plus) images were taken with an acceleration voltage of 15 kV for a $LiFePO_4$ dough-like sample to characterize the morphology of the electrode. To scan the wet sample, SEM operated at a low vacuum mode by setting the chamber pressure at 1.3 mbar to reduce the evaporation and distortion of the hydrated sample. X-ray diffraction (XRD) patterns for dough-like $LiFePO_4$ cathode after drying were obtained using a Rigaku Miniflex 600 with a 2θ value from 10 to 80° to detect the peak change after battery cycling.

3.3. Results and discussion

3.3.1 Dough-like cathode vs. conventional cathode

In this chapter, $LiFePO_4$ was selected as the cathode active material because its plateau places in the safe zone of the electrochemical stability window of water to avoid oxygen generation. Moreover, $LiFePO_4$ belongs to the olivine group with a lattice structure and is a promising cathode material due to its high theoretical capacity (170 mAh g^{-1}), low material cost, abundant resources, and a flat charge/discharge profile [135,136]. The dough-like cathode, prepared by the $LiFePO_4$ active material, conductive carbon, and aqueous electrolyte, can be designed without any sign of cracking even at a very high thickness of 1000 μm (Figure 3.2a). The dough-like cathode paste can be formed into different shapes with flexible characteristics which could have potential applications in wearable electronic devices and smart packaging. For comparison, the $LiFePO_4$ cathode prepared with the slurry-cast method showed significant amounts of cracks even at 250 μm thickness as observed in Figure 3.2b.

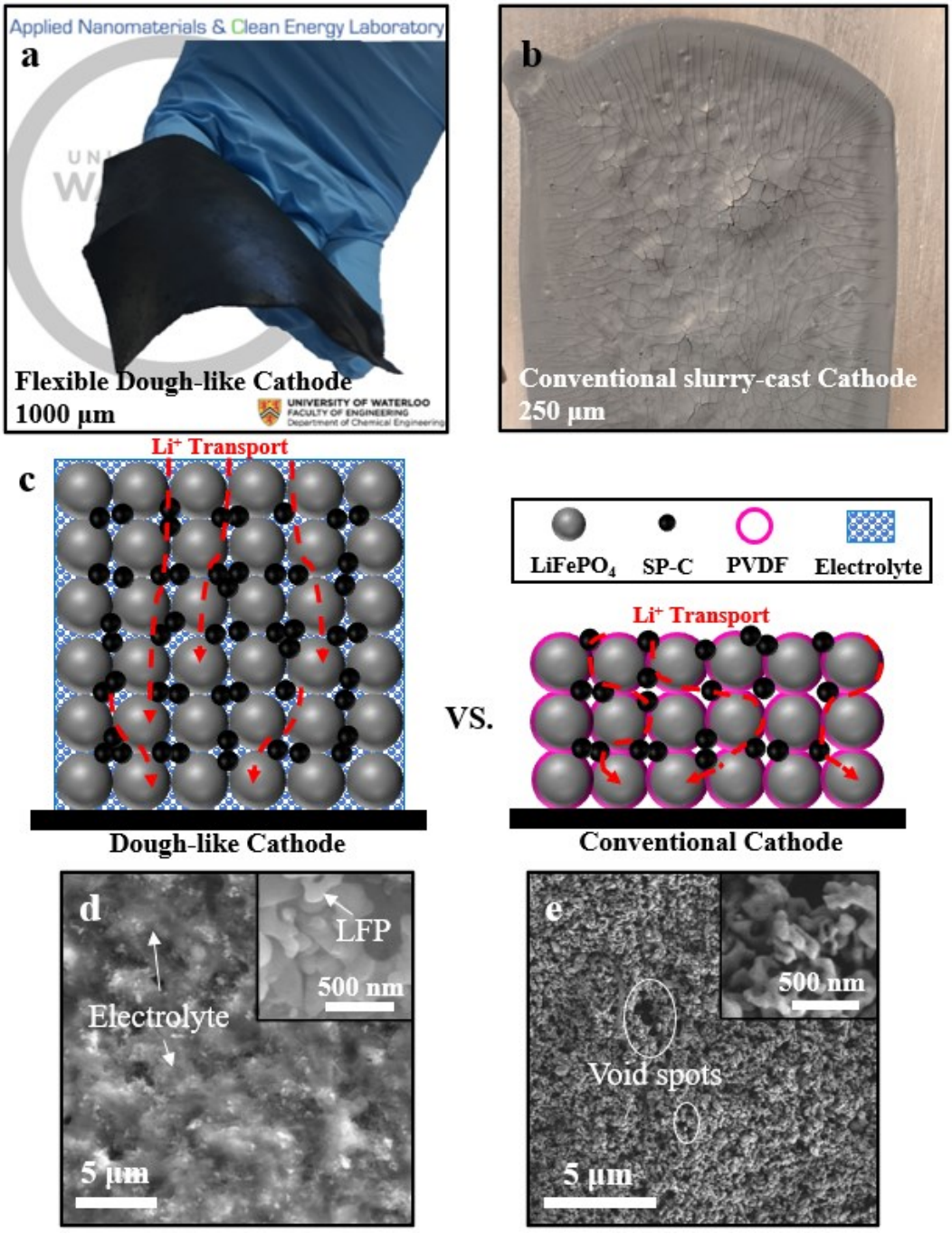

Figure 3.2 a) Image of a dough-like electrode having $LiFePO_4$, SP-C, and electrolyte within the structure with flexible characteristics at 1000 µm thickness. b) Image of slurry-cast conventional $LiFePO_4$ cathode at 250 µm thickness. c) Schematic comparison of dough-like cathode vs. conventional cathode. d) Surface SEM images of a dough-like electrode with 85 wt.% $LiFePO_4$ and 15 wt.% SP-C which dispersed in 2.0 mol L^{-1} $ZnSO_4$ and 1.5 mol L^{-1} Li_2SO_4 electrolyte. The inset is the high magnification SEM image. e) Surface SEM image of the conventional cathode with 85 wt.% $LiFePO_4$, 8 wt.% PVDF, and 7 wt.% SP-C. The inset is the high magnification SEM image.

As illustrated in the schematic in Figure 3.2c, compared to the conventional cathode the dough-like cathode facilitates a shorter distance for Li^+ ion transportation due to the reduced

tortuosity that arises from the binder-less design and abundant available Li^+ ions inside the dough-like composite. As seen in the SEM image of the dough-like cathode (Figure 3.2d), the $LiFePO_4$ nanoparticles (200-500 nm particle size) are uniformly dispersed in the electrode structure. The cloudy parts in the SEM image are attributed to the presence of electrolyte, forming a monolithic structure. The conventional cathode lacks electrolyte in its composite and forms some void spots inside its structure during the solvent drying process (Figure 3.2e). The deficiencies due to the cracks and void spots in the structure of conventional electrodes worsen the conductivity of the cathode.

3.3.2 Electrochemical performance of zinc/$LiFePO_4$ battery with dough-like cathode

The cycling and charge/discharge profiles of zinc/$LiFePO_4$ battery with 200 μm thick dough-like cathode at 85 wt.% are plotted in Figure 3.3a-b. For comparison, the electrochemical performance of zinc/$LiFePO_4$ battery with a conventional cathode at the same electrode thickness and weight percentage of $LiFePO_4$ is shown in Figure 3.3c-d. It is worth noting that 200 μm is the critical cracking thickness for the conventional $LiFePO_4$ cathode and the cathode confronts severe crack formation at higher thicknesses as previously observed in Figure 3.2b. The specific capacity in the first cycle for the battery with the dough-like cathode is 131 mAh g^{-1} at 1 mA cm^{-2}, which is 3.4 times higher than that for the battery with the conventional cathode (38 mAh g^{-1}). The superior specific capacity in the battery with dough-like cathode is attributed to improved electronic/ionic conductivity due to the binder-less and electrolyte-based structure with shorter Li-ion diffusion paths. More importantly, as seen in the inset images, the areal capacity of the battery with the dough-like cathode is 3.6 times higher than that for the battery with the conventional cathode (1.64 mAh cm^{-2} vs. 0.45 mAh cm^{-2}) in spite of the same electrode thickness and active material loading (12.5 vs. 12.9 mg cm^{-2}). The boosted areal capacity is due to the near-theoretical

specific capacity of the dough-like cathode at the same current density. Such enhanced specific and areal capacity is related to the binder-less and crack-free features of the thick dough-like cathode.

After 200 charge/discharge cycles, the battery with the dough-like cathode shows close to 80% capacity retention while the battery with the conventional cathode could only maintain 50% of its capacity. The significantly improved capacity retention is due to the crack-free and flexible structure of the dough-like cathode. The dough-like cathode can tolerate the severe stress of Li-ion intercalation/deintercalation during repeated battery cycling. However, this stress can accumulate in the conventional cathode, leading to crack formation and increased polarization. The cracks within the electrode laminate increase resistance of the electrode due to particle isolation which consequently leading to fade capacity.

The average coulombic efficiencies (CEs) were 99.9% and 99.6% in the battery with dough-like cathode and conventional cathode, respectively. The high value for CE represents constant coulombs at every single charge/discharge cycle and thus a low amount of irreversible side reactions. This means the battery with the dough-like cathode tends to have fewer side reactions and hence improved capacity retention. The charge/discharge profiles in Figure 3.3b showed 92% voltage efficiency (VE) in the initial cycle for the battery with the dough-like cathode, while its corresponding value with the conventional cathode in Figure 3.3d was less than 83%. The VE was measured based on the ratio of discharge to charge voltage at the median value for the specific capacity at each cycle number. The high VE is indirect evidence for better charge and ion transfer in the battery with the dough-like cathode. Consequently, the zinc/$LiFePO_4$ battery with the dough-like cathode at the same electrode thickness as the conventional cathode manifests superior areal capacity, enhanced cyclability, and improved VE.

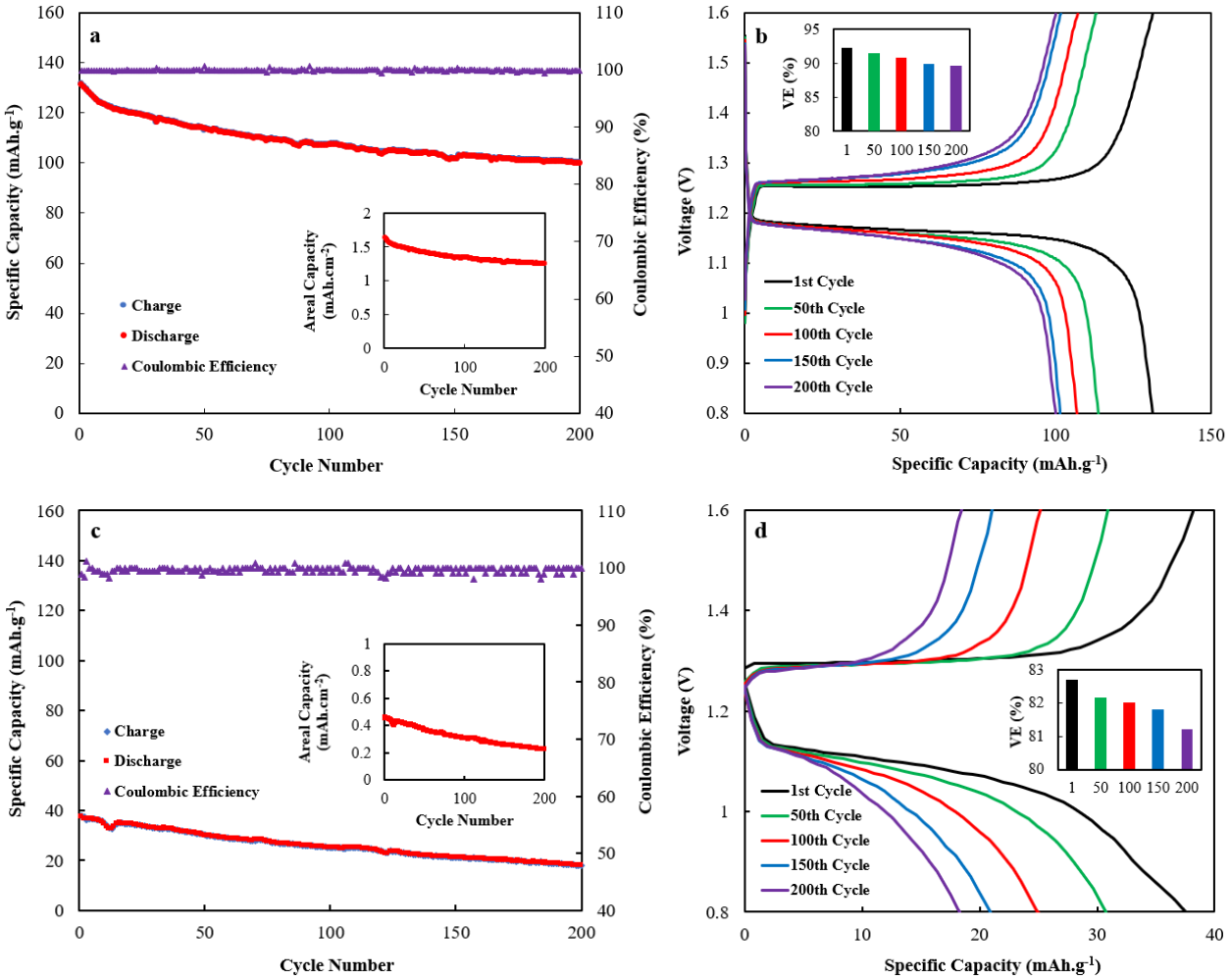

Figure 3.3 Electrochemical performance of zinc/$LiFePO_4$ battery at 1 mA cm^{-2} with: a-b) 200 µm thick dough-like cathode with 85 wt.% $LiFePO_4$, and c-d) 200 µm thick conventional cathode (highest possible thickness before critical cracking thickness) with 85 wt.% $LiFePO_4$. a, c) Specific capacity vs. cycle number. The insets are the discharge areal capacity vs. cycle number. b, d) Charge/discharge profiles of voltage vs. specific capacity. The insets are the histogram plots of VE at various cycle numbers.

3.3.3 Optimization of the dough-like cathode composition

The voltage/capacity profile of zinc/$LiFePO_4$ using 200 µm thick dough-like cathode design at different weight percentages of active material is plotted in Figure 3.4a. As seen, the specific capacity of the battery with 85, 90, and 95 wt.% $LiFePO_4$ is 131, 129, and 124 mAh g^{-1}, respectively. The inferior specific capacity with 95 wt.% $LiFePO_4$ is due to a lower amount of conductive material (only 5 wt.%) and hence a higher resistance in the electrode. Moreover, the gap between charge and discharge curves is the largest with 95 wt.% $LiFePO_4$ among these

batteries, showing the highest overpotential and the most severe polarization. As shown in the inset image of Figure 3.4a, the VEs of the batteries with 85, 90, and 95 wt.% $LiFePO_4$ are 92, 91 and 88%, respectively. The lower VE proves that the resistance of the battery is increasing as the conductive material is reduced.

As observed in Figure 3.4b, by increasing the weight percentage of $LiFePO_4$, the areal capacity was enhanced. The areal capacities of the batteries with 85, 90, and 95 wt.% $LiFePO_4$ is 1.64, 2.01, and 2.22 mAh cm^{-2}, respectively. However, the areal capacity increment brought by additional $LiFePO_4$ active material loading becomes less significant when the weight percentage of $LiFePO_4$ increases from 90% to 95%. Accordingly, the cathode with 90 wt.% $LiFePO_4$ active material and 10 wt.% SP-C conductive agent is considered as an optimal concentration for the dough-like cathode due to the combination of high specific capacity and areal capacity and decent VE.

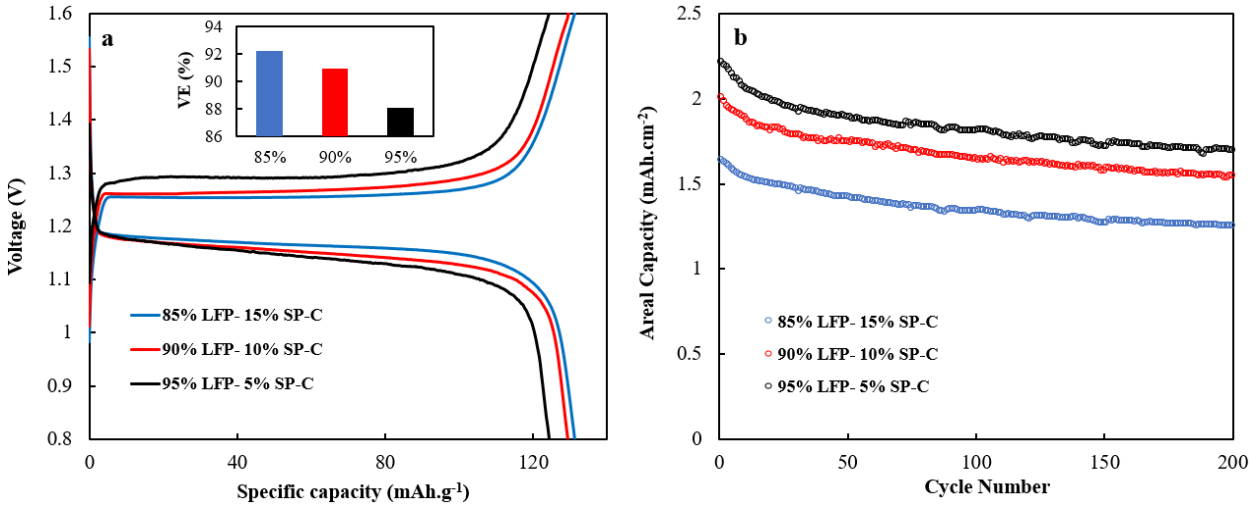

Figure 3.4 a) Voltage-capacity and b) areal capacity comparison of 200 µm thick dough-like cathodes at 85, 90, and 95 wt.% of $LiFePO_4$ active material. All tests were performed at 1 mA cm^{-2} current density.

3.3.4 High areal capacity zinc/$LiFePO_4$ battery with thick dough-like cathode

To further increase the areal capacity of the zinc/$LiFePO_4$ battery, dough-like cathodes with the thickness of 200 µm, 400 µm, 500 µm, 700 µm, and 1000 µm were fabricated and the associated zinc/$LiFePO_4$ batteries were assembled and evaluated. The rate capability performance of these zinc/$LiFePO_4$ batteries with different electrode thicknesses at various C-rates from C/15 to 2 C is illustrated in Figure 3.5. At C-rates of C/15, C/10, C/5, and C/2, all electrodes at a broad range of electrode thickness from 200 µm up to 1000 µm showed high discharge capacity and their capacity overlapped very closely. This electrochemical performance behavior means that the electrode thickness did not significantly affect the performance of the battery until 1 C-rate. At 1 C-rate, the cell with a high cathode thickness of 1000 µm delivered lower capacity compared to cells at lower thicknesses and its performance aggravated at 2 C-rate. This means that the polarization effect is enlarged when the applied current is increased to 1 and 2 C-rates, leading the battery to reach the cut-off voltage faster. At 700 µm electrode thickness, this effect was started to be noticed at only 2 C-rate. For 200 µm, 400 µm, and 500 µm electrode thicknesses, a sudden decrease in the discharge capacity of the batteries was not observed even at 2 C-rate. These results are highly desirable because $LiFePO_4$ with conventional electrode architecture at the thicknesses of more than 100 µm does not normally perform well at C-rates of equal or more than 1 C due to limited diffusivity through the thickness of electrode [137]. For the conventional cathode at 100 µm thickness, the highest specific capacity (i.e., 140 mAh g^{-1}) was achieved at C/15 and the capacity reduced substantially with an increase in the current density, reaching less than 65 mAh g^{-1} at 2 C. The poor rate performance is due to the presence of binders inside the conventional electrode structure, leading to increased tortuosity and thus cell polarization and active material underutilization. The

underutilization can be attributed to saturation of Li-ions in the surface layer of particle and/or Li-ion depletion in the electrolyte, which reduces the discharge capacity of the battery [124].

As seen, the rate performance of the battery constructed with thick dough-like cathodes was superior to the thin conventional cathode. Two main reasons explain this electrochemical performance behavior. First, the dough-like cathode is free from any binders. The binder-less design improves the electronic/ionic conductivity of the electrode due to reduced tortuous paths. The second reason lies in the presence of aqueous electrolyte in the electrode fabrication process. The innovative manufacturing process could increase ionic conductivity and contribute to lowering the underutilization negative effect by providing extra Li^+ ions inside the dough-like cathode structure. Moreover, the fabrication of electrolyte-based dough-like cathode does not require a drying step, which avoids the possible generation of cracks and void spots during solvent evaporation and hence further improves the electronic conductivity of the electrode. Accordingly, the binder-less and electrolyte-based electrode structure empower such monolithic electrode (free from any crack formation and void spots) with improved electronic/ionic conductivity.

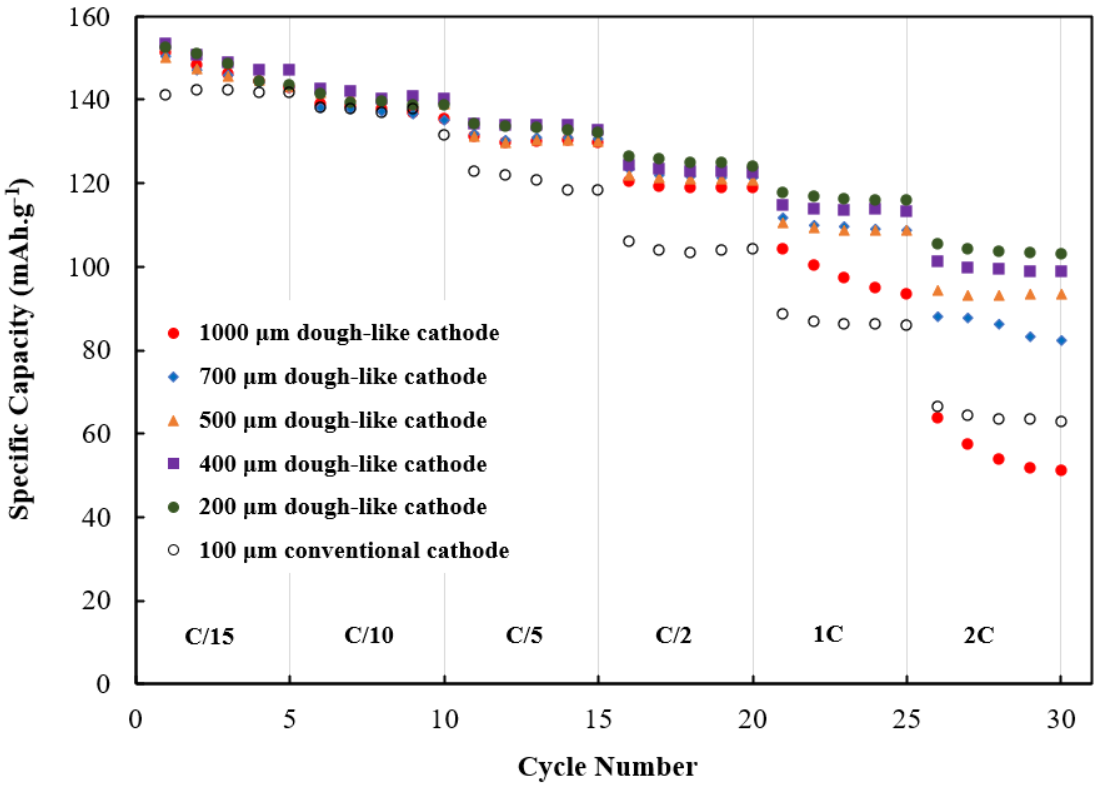

Figure 3.5 Rate capability of zinc/$LiFePO_4$ battery with 90 wt.% $LiFePO_4$ dough-like cathode at different electrode thicknesses and C-rates and its comparison with 100 µm conventional cathode.

The cycling stability of the battery at various cathode thicknesses is depicted in Figure 3.6. As seen, the zinc/$LiFePO_4$ batteries at 200 µm, 400 µm, 700 µm, and 1000 µm dough-like cathode delivered 2.0, 4.0, 6.5, and 10.1 mAh cm^{-2} areal capacity, respectively. The active material loading at 200 µm thickness was 14.9 mg cm^{-2}, while it reached an unprecedented value of 69.2 mg cm^{-2} at 1000 µm. For comparison, the active material loading and areal capacity of the battery with 100 µm thick conventional cathode was only 6.6 mg cm^{-2} and 0.7 mAh cm^{-2}. Therefore, the areal capacity of the battery with a 1000 µm dough-like cathode is at least 14 times higher than that with a 100 µm conventional cathode. The high areal capacity of the battery manufactured with the thick dough-like cathode is attributed to high active material loading and near-theoretical specific capacity performance.

As expected, by increasing the cathode thickness the capacity retention decreased. The zinc/$LiFePO_4$ battery with a 200 µm thick cathode showed 23.5% capacity loss over 200 cycles, whereas the corresponding value with a 700 µm cathode was 25.8%. The rate of capacity degradation is faster in initial cycles. If the first 10 cycles are not considered, the capacity retention at the 200^{th} cycle would be about 82%, 82%, and 80% at 200 µm, 400 µm, and 700 µm electrode thickness, respectively. The battery with a cathode thickness of 1000 µm lasted for 150 cycles; and after this breakpoint, the battery failed to operate due to short-circuiting. The earlier short-circuiting for the battery with 1000 µm thick cathode is due to the ultra-thick cathode design and high areal capacity. Yang et al. [138] revealed that the zinc dendrite might not be a problem at low cathode active material loading, but at high mass loading it will rapidly short circuit the battery. The batteries with a thicker electrode have a much higher capacity than thin electrodes. In other words, they deposit more zinc in every single cycle, which could lead to early short-circuiting. It is noted that the active material loading of 1000 µm thick dough-like cathode is significantly higher (about 10 times) than that of the conventional 100 µm thick cathode. Therefore, it is expected that the zinc/$LiFePO_4$ battery at high areal capacities delivers lower cycle life than the battery with a thin electrode architecture.

The higher capacity degradation with thicker electrodes is not specifically related to dough-like cathode structure. Generally, a higher capacity-fading rate is also observed for the cells with a thicker conventional electrode structure [128,139]. Zheng et al. [128] investigated two possible reasons for this effect for conventional electrodes. The first reason is due to the high internal resistance of thick electrodes, causing intensified polarization and thus overpotential. The overpotential can cause possible side reactions such as generating oxygen and irreversible phase transformation during cycling. The second reason is associated with the mechanical integrity of the electrode.

During intercalation and extraction of Li-ions into and from the lattice framework, the volume undergoes expansion and shrinkage, respectively. These changes in the volume impose severe stress within the thick electrode laminate in forthcoming cycling, leading to crack formation, increased resistance, and thus capacity fading [128]. In the proposed method, the first reason for the capacity fading of thick conventional electrodes, which is related to the increased polarization, may also be applied for thick dough-like electrodes. But the second reason which leads to crack formation inside the electrode laminate during repeated intercalation/extraction of Li-ions is not applicable to dough-like cathodes. Despite having high electrode thicknesses, the dough-like cathode possesses a flexible structure that assists the electrode to endure severe stresses within the structure during extended electrochemical cycling. As a cause of dough-like consistency, fracture in the structure of the electrode has not been observed even after 200 cycles.

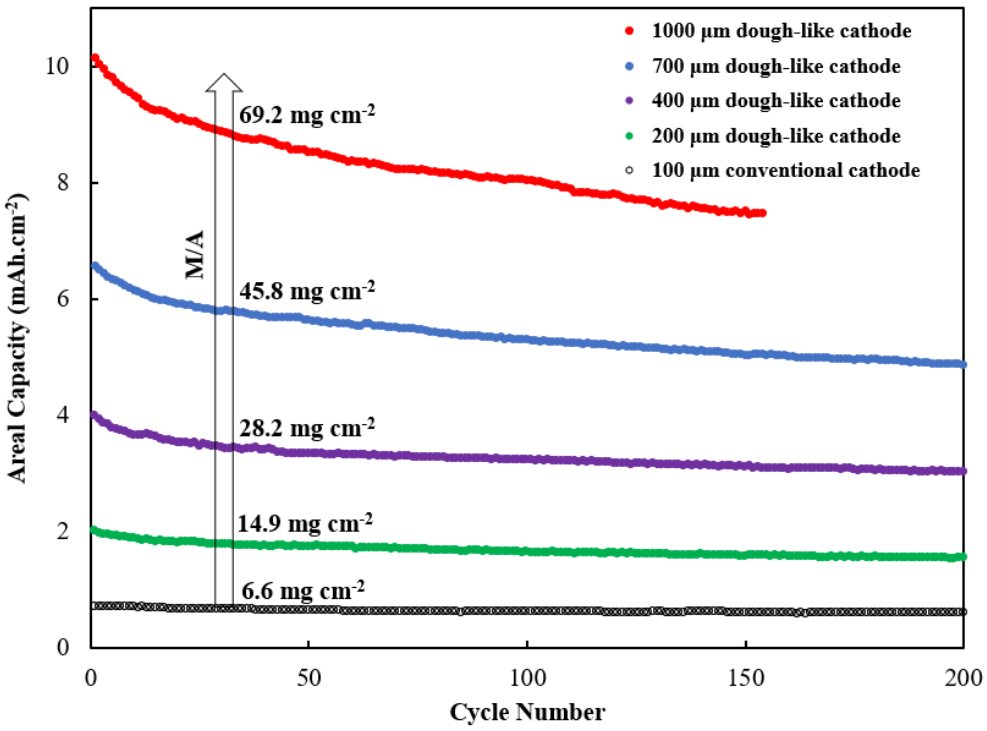

Figure 3.6 Areal capacity comparison of 90 wt.% $LiFePO_4$ dough-like electrode at various electrode thicknesses. All the tests were performed at 1 mA cm^{-2} current density. M/A: active material loading per unit surface area.

EIS profiles of zinc/$LiFePO_4$ battery manufactured with 700 μm thick dough-like cathode, zinc foil anode, and 2.0 mol L^{-1} $ZnSO_4$ and 1.5 mol L^{-1} Li_2SO_4 aqueous electrolyte is plotted in Figure 3.7a. Each plot consists of a single depressed semicircle at high to medium frequency zone followed by an inclined line in the low-frequency region. The semicircle represents the charge transfer resistance while the inclined line is attributed to the Li-ion diffusion inside the $LiFePO_4$ active material. The bulk resistance of the battery was 2.9 Ω at the initial cycle and raised to 4.0 Ω at the 200^{th} cycle. The bulk resistance indicates the total resistance of the battery including the resistance inside the electrodes, separator, electrolyte, and current collectors. A very small diameter of the semicircle shows a low charge transfer resistance. Since the dough-like electrode contains electrolyte in the structure the Li-ions can also be provided from the electrode composite, which contributes to faster transportation of Li-ions through the electrode with shorter diffusion paths. Therefore, a much lower charge transfer resistance in the battery with a dough-like cathode is consistent with its unique structure. EIS profile of the zinc/$LiFePO_4$ battery made with 100 μm conventional slurry-cast cathode is compared with 700 μm thick dough-like cathode (Figure 3.7b). As observed, the bulk resistance of the battery with the dough-like cathode was 3.7 Ω compared to 4.8 Ω in the battery with the conventional cathode. Besides, the battery constructed with the conventional cathode showed a large semicircle, indicating a much higher charge transfer resistance. Accordingly, the binder-less and electrolyte-based structure of the dough-like cathode improves the electronic/ionic conductivity of the cathode and lowers the resistance of the battery. This is another evidence that the rate performance of the battery with thick dough-like cathodes is superior to that of the conventional cathode.

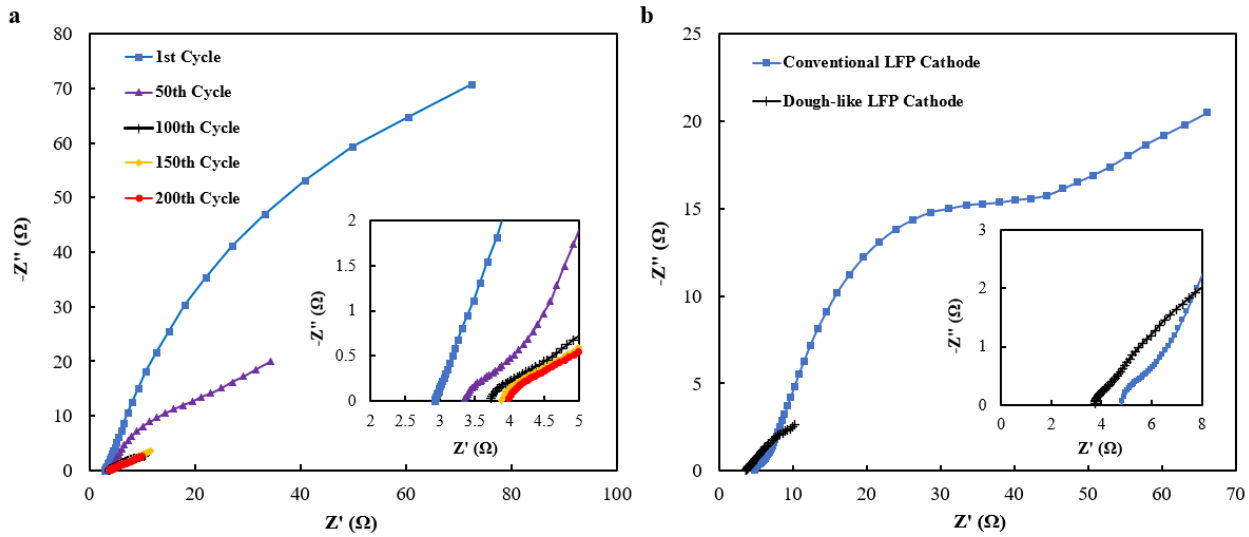

Figure 3.7 a) EIS profiles of zinc/$LiFePO_4$ battery manufactured with 700 µm thick dough-like cathode, zinc foil anode, and 2.0 mol L^{-1} $ZnSO_4$ and 1.5 mol L^{-1} Li_2SO_4 aqueous electrolyte. b) Comparison of EIS profiles of zinc/$LiFePO_4$ battery constructed with 700 µm thick dough-like $LiFePO_4$ cathode and 100 µm thick conventional cathode at the 100th cycle. The inset plots are EIS profiles at the high-frequency region.

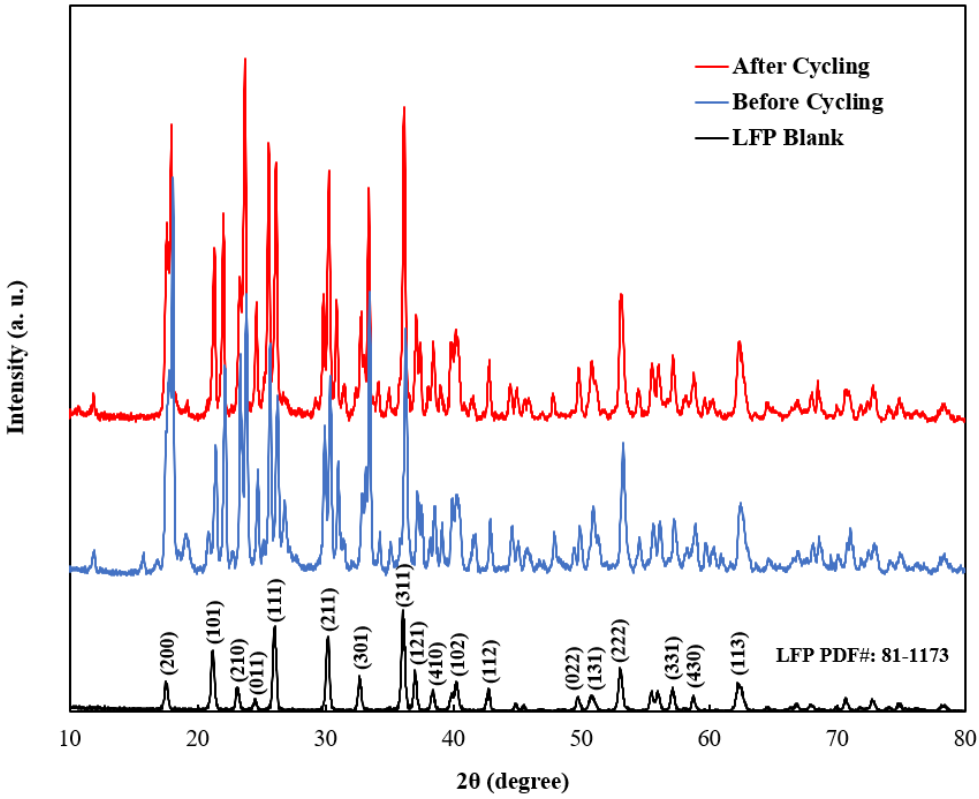

Figure 3.8 XRD patterns of 700 µm thick dough-like cathode with 90 wt.% $LiFePO_4$ and 10 wt.% SP-C dispersed into the aqueous electrolyte (2.0 mol L^{-1} $ZnSO_4$ and 1.5 mol L^{-1} Li_2SO_4) before and after 200 cycles. The XRD pattern of $LiFePO_4$ active material is denoted as LFP blank.

The XRD pattern of dough-like cathode before and after 200 cycles is plotted in Figure 3.8 to investigate the possible peak changes related to the dough-like cathode during battery cycling. Also, the diffraction peaks associated with the blank $LiFePO_4$ active material, such as 200, 101, 111, 211, and 311, are identified and labeled in this figure. As seen, all the major peaks related to the olivine structure of $LiFePO_4$ active material are indexed with the corresponding peaks in the dough-like cathode before and after battery cycling. Moreover, the peaks after cycling showed good overlaps with the original peaks before cycling, confirming the high stability of the dough-like cathode during battery cycling. This also indicates that the $LiFePO_4$ structure was not changed during multiple intercalation/deintercalation processes and Fe dissolution in the mildly acidic electrolyte was minimal.

3.3.5 Energy density comparison

To compare the energy density of zinc/$LiFePO_4$ with different electrode designs, a 700 μm thick dough-like electrode was selected and it is compared with a 100 μm thick conventional electrode. A 700 μm thick dough-like cathode was selected because it has a combination of high areal capacity and good rate performance. As previously observed in Figure 3.6, the zinc/$LiFePO_4$ battery with 700 μm thick cathode can deliver 6.5 mAh cm^{-2} areal capacity, while the battery with 100 μm thick conventional electrode can deliver only 0.7 mAh cm^{-2}. The schematic of zinc/$LiFePO_4$ battery with dough-like cathode design with all necessary inactive components such as current collectors and separators is illustrated in Figure 3.9a. It should be noted that the thickness of all components in the battery with the dough-like cathode is matched with the fabricated battery parameters. The schematic of zinc/$LiFePO_4$ battery cells with conventional cathode design in bipolar battery configuration is demonstrated in Figure 3.9b, which includes 9 battery cell units with an equivalent total capacity of the zinc/$LiFePO_4$ battery with the dough-like cathode design.

To minimize the inactive components in the battery cells, the bipolar configuration is selected. In the bipolar configuration, both sides of the cathode substrate are coated with the slurry and the zinc anode can be reduced and oxidized from both sides to reduce the battery size as much as possible. Besides, the thickness of the separator is half the size of the separator in the battery cell with the dough-like cathode design due to less dendrite growth in the thin electrode architecture. The zinc metal is also used at a lower thickness (150 μm) compared to zinc metal (350 μm) in the battery with a dough-like cathode to have a better material balance with the thin cathode. Since the dough-like cathode has roughly 9 times higher areal capacity than the conventional electrode, 9 cathodes and thus 9 battery cells were connected in parallel to deliver the same capacity as the battery with the dough-like cathode. As a result, the battery with the dough-like cathode has 1.85 mm in length, while the battery with conventional electrodes has 5.35 mm in length. Therefore, the practical volumetric energy density of the zinc/$LiFePO_4$ battery with the dough-like cathode is about 2.9 times higher than that of the battery with the conventional cathode design. This comparison was made with a 700 μm thick dough-like cathode and a higher energy density enhancement is expected at 1000 μm cathode thickness. It is worth noting that one of the most efficient battery configurations (bipolar) was selected for the battery with conventional electrodes, however, the energy density of the battery is still much lower than that of the battery with the dough-like cathode. This huge increase in the energy density of the battery with the dough-like cathode comes from successful thick electrode design with a near-theoretical specific capacity. In the thick electrode design, the ratio of active components (cathode active material) to inactive components such as separator, electrolyte, current collector, and substrate is higher than that of the battery with the thin electrode design. Furthermore, the cost of the battery cell pack with thick electrodes would be much lower than that of the battery with thin electrodes as a result of fewer

inactive components. A detailed processing cost study for the state-of-the-art Li-ion batteries states that a 50% reduction in the cost of current collectors and separators is attainable by doubling the electrode thickness [140]. Besides, more resistance is expected in a battery pack with a thin electrode design since additional necessary wiring is needed to connect multiple battery units in parallel to provide the same equivalent capacity as in the battery with thick electrode architecture.

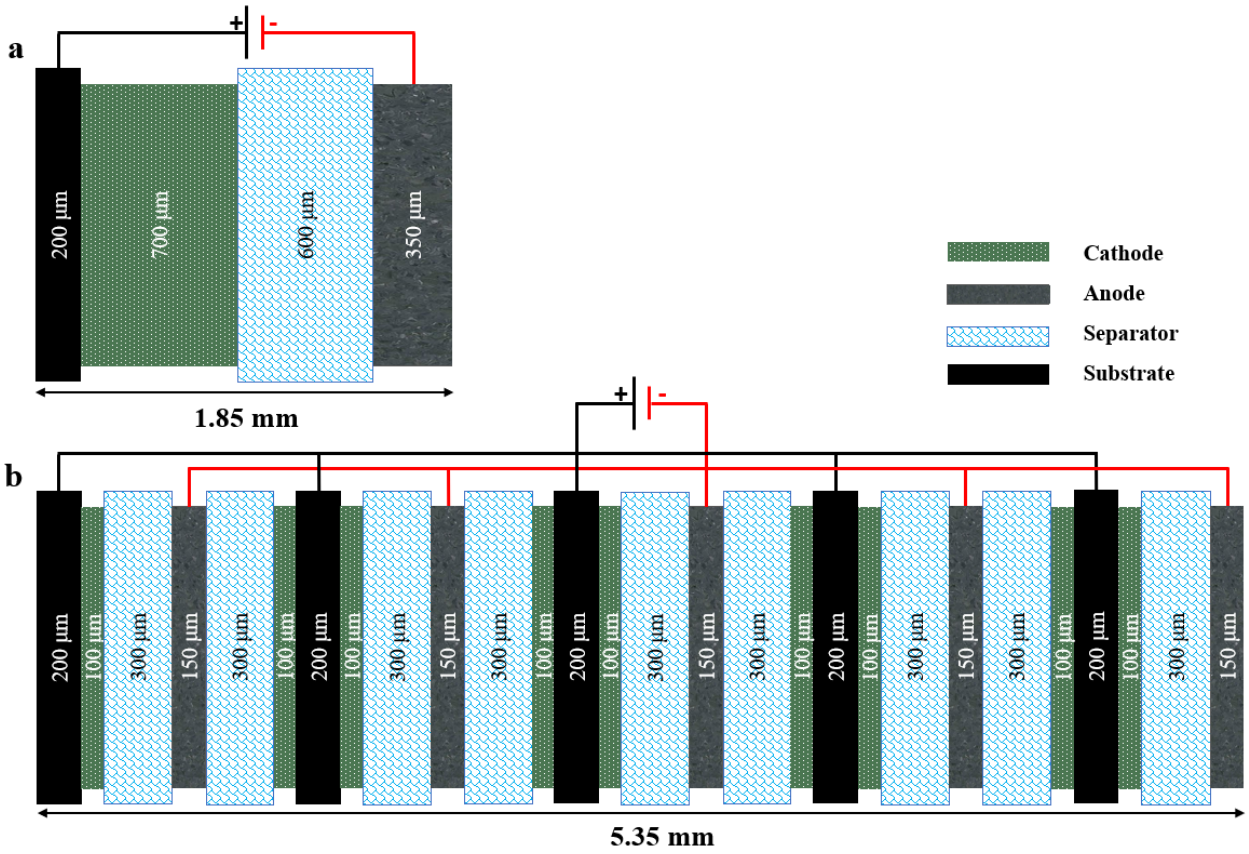

Figure 3.9 The schematic of zinc/$LiFePO_4$ battery with two different electrode architectures and an identical total capacity, a) 700 µm thick dough-like cathode, and b) 100 µm thick conventional cathode design (9 cells connected in parallel) in the bipolar battery cell configuration.

3.4. Summary

In summary, the areal capacity and active material loading of the zinc/$LiFePO_4$ batteries with dough-like and conventional cathodes at various thicknesses and active material loading are presented in Figure 3.10. The conventional cathode at 100 µm and active material loading of 6.6

mg cm^{-2} delivered a low areal capacity of 0.7 mAh cm^{-2}. The zinc/$LiFePO_4$ battery constructed with 1000 μm thick dough-like cathode delivers a record high areal capacity of 10.5 mAh cm^{-2} which is 15 times higher than the areal capacity of zinc/$LiFePO_4$ battery with a 100 μm conventional cathode. The enhancement in the areal capacity of the dough-like cathode results in at least a 190% increase in the energy density of the zinc/$LiFePO_4$ battery.

The proposed thick dough-like cathode design appears as a highly promising method to replace the conventional slurry-cast method in ARZLBs. The dough-like cathode manufacturing method is binder-less, aqueous processed, cost-effective, and scalable. The use of aqueous processed electrodes significantly cuts down the energy and material demands with a faster processing speed and a more straightforward manufacturing process compared to the slurry-cast electrodes. Aqueous processing compared to NMP-processing leads to the elimination of some manufacturing steps in the plant including drying and solvent recovery. Additionally, safety and environmental concerns associated with NMP solvent as a volatile organic compound can be resolved by water-based chemistry. More importantly, the use of thick dough-like electrodes reduces the inactive components in the battery pack such as current collectors and separators, resulting in tangible cost saving. The high areal-capacity dough-like cathodes provide new insight into developing high energy density and cost-effective ARZLBs toward practical applications that can compete with state-of-the-art aqueous batteries such as lead-acid batteries.

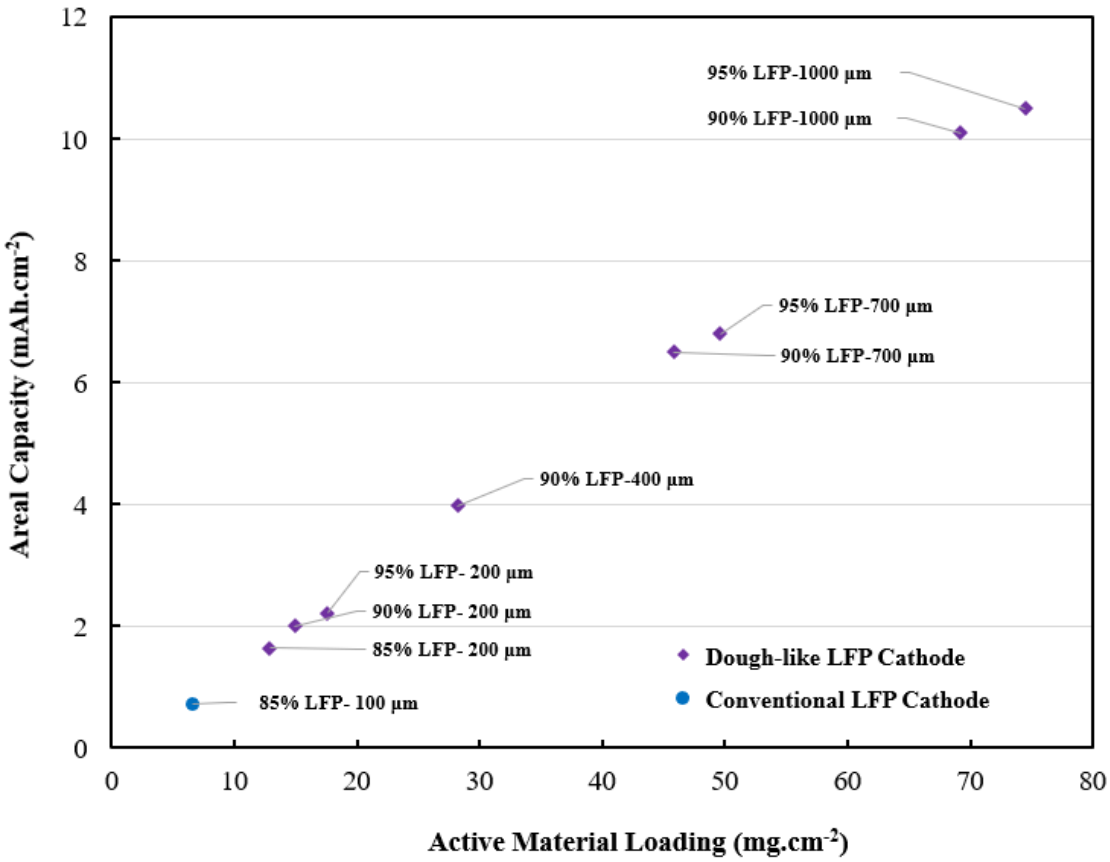

Figure 3.10 Comparison of areal capacity and active material loading of the zinc/$LiFePO_4$ battery with dough-like and conventional cathodes. All tests were performed at 1 mA cm^{-2} current density

4. Design of thick cathode enabled by 3D carbon nanotube networks for high areal-capacity zinc/$LiMn_2O_4$ battery

4.1. Introduction

As discussed in Chapter 3, the energy density of ARZLBs is limited by the cathode capacity. $LiFePO_4$ and $LiMn_2O_4$ as the common Li-ion cathode active materials have a theoretical capacity of 170 mAh g^{-1} and 148 mAh g^{-1}, respectively, while zinc metal as anode has a high theoretical capacity of 820 mAh g^{-1}. To increase the energy density of the battery, one effective strategy is to maximize the areal capacity. The areal capacity of the battery can be readily controlled by increasing the overall thickness of the cathode. However, increasing the thickness of the conventional electrode design while maintaining its theoretical specific capacity is a challenging approach. For example, the dispersion of the standard conductive additives such as carbon black in the structure of the conventional electrode becomes inhomogeneous throughout the thick electrode, leading to low and unstable electrode conductivity [141]. Also, polymeric binders enlarge the tortuosity and resistance of the electrode, making it impossible to prepare a thick electrode with a high specific capacity [129,130,132].

As a remedy, the proposed dough-like electrode design in Chapter 3 enables enhancing the areal capacity of the electrode to a record high value of 10.5 mAh cm^{-2} for zinc/$LiFePO_4$ to match with the high-capacity zinc anode. For comparison, the highest reported areal capacity of ARZLBs is 2.4 mAh cm^{-2} at 0.2 C-rate with the conventional cathode design [21]. Hence, the proposed dough-like cathode design can deliver at least 4 times higher areal capacity than the maximum areal capacity reported in the literature owing to ultra-thick electrode design.

To further enhance the energy density of ARZLB, the cell voltage can be tuned up by switching the cathode material from $LiFePO_4$ to $LiMn_2O_4$. $LiMn_2O_4$ active material has 1.8 V discharge voltage compared to 1.2 V discharge voltage for $LiFePO_4$ active material in ARZLBs. The higher output voltage results in at least 30% more energy density for the battery. Moreover, spinel-structured $LiMn_2O_4$ is non-toxic, inexpensive (earth-abundant manganese), and has better rate capability than $LiFePO_4$ cathode [142]. To take advantage of these features, a $LiMn_2O_4$ thick dough-like cathode was fabricated to further enhance the energy density of ARZLB. The zinc/$LiFePO_4$ battery with dough-like electrode architecture showed at least 200 cycle life before short-circuiting, while the durability of the zinc/$LiMn_2O_4$ battery with the dough-like cathode was limited to less than 40 cycles (Figure 4.1). The zinc/$LiMn_2O_4$ battery with the dough-like cathode design at 4.5 mAh cm^{-2} areal capacity was stable for roughly 40 cycles, but the battery showed a sudden capacity fading in subsequent cycles with only 50% capacity retention at the 60^{th} cycle. This sudden capacity fading is not linked to the short-circuiting issue. The main reason for the sudden capacity degradation of zinc/$LiMn_2O_4$ battery is almost certainly related to the high rate of destructive oxygen gas generation in the $LiMn_2O_4$ cathode laminate. It has been found that gas evolution rapidly decays the performance of Li-ion batteries over cycling, causing electrode degradation, increased cell resistance, shortened lifespan, and a significant distortion of battery [143–146]. Previous studies confirmed the presence of OER in aqueous zinc/$LiMn_2O_4$ batteries [10,20,21]. The production of oxygen gas is the direct effect of greater value of upper cut-off voltage in zinc/$LiMn_2O_4$ battery (2.1 V vs. Zn/Zn^{2+}) than that in zinc/$LiFePO_4$ battery (1.6 V vs. Zn/Zn^{2+}). It is noted that the OER is thermodynamically favorable at about 1.7 V vs. Zn/Zn^{2+} at pH=5. As shown in Figure 4.1b, evolved oxygen gas upon cycling in the $LiMn_2O_4$ dough-like cathode design could be trapped inside the electrode structure and create isolated regions. The accumulation of

oxygen gas and the expansion of isolated regions during forthcoming cycling would lead to sudden capacity fading in zinc/$LiMn_2O_4$ battery with thick dough-like cathode architecture. The sudden capacity fading was not observed in zinc/$LiFePO_4$ because the battery operates at a lower cut-off voltage, producing a very low amount of oxygen gas during cycling. Accordingly, the dough-like cathode is not a proper choice for the long-lasting operation of zinc/$LiMn_2O_4$ battery. Hence, a new cathode design to avoid the oxygen build-up within the electrode is required for the development of high areal-capacity zinc/$LiMn_2O_4$ batteries.

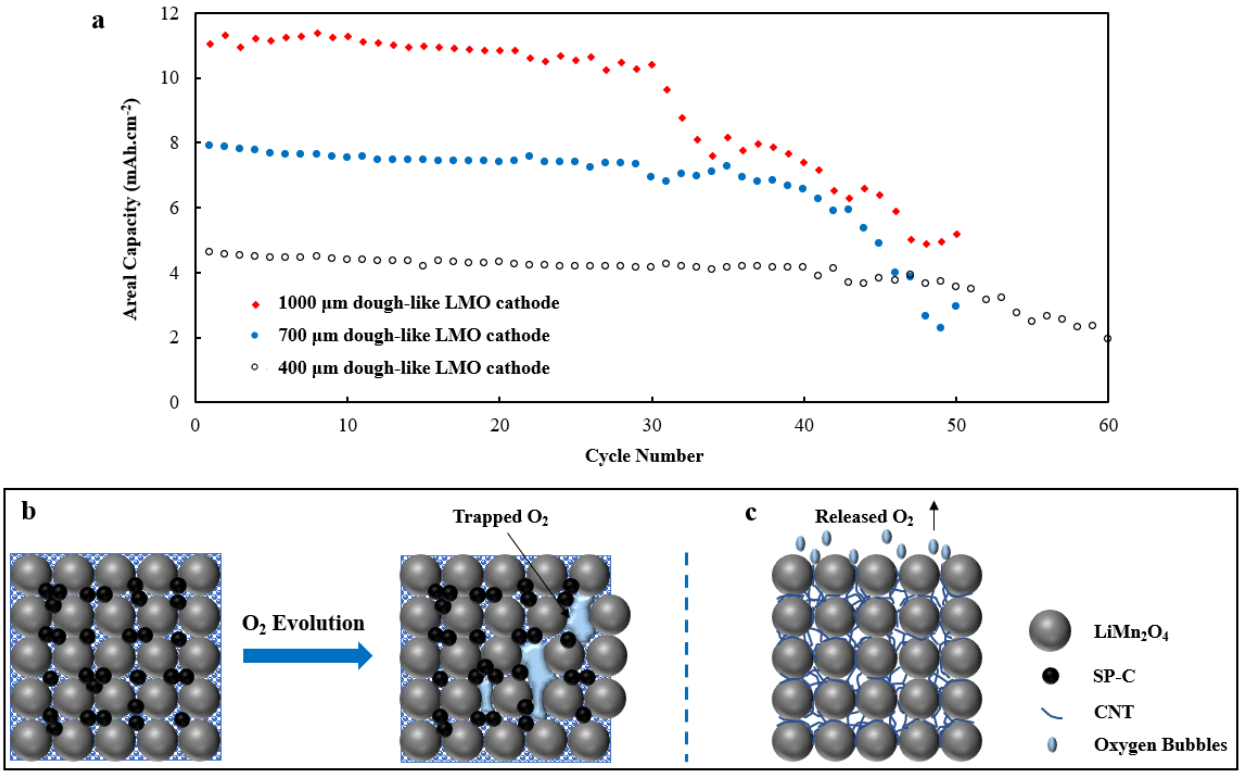

Figure 4.1 a) Cycle stability of zinc/$LiMn_2O_4$ battery manufactured with the dough-like cathode at different thicknesses, zinc foil anode, and 2.0 mol L^{-1} $ZnSO_4$ and 1.5 mol L^{-1} Li_2SO_4 aqueous electrolyte. The dough-like cathode comprised of 90% $LiMn_2O_4$ active material and 10 % SP-C which dispersed into the aqueous electrolyte. b) Schematic representation of dough-like electrode structure with $LiMn_2O_4$ active material before and after cycling. c) Schematic representation of $LiMn_2O_4$ electrode with a 3D CNT network during cycling.

In the current chapter, a unique three-dimensional carbon nanotube network (3D-CNT) thick cathode for high areal-capacity zinc/$LiMn_2O_4$ battery is introduced. The unique 3D-CNT electrode design brings fourfold advantages to the thick $LiMn_2O_4$ cathode. Firstly, as illustrated in

Figure 4.1c, the porous structure of the 3D-CNT electrode allows the release of generated oxygen gas during cycling while maintaining its structural stability during battery cycling. Secondly, similar to the promising thick electrodes (up to 800 μm) for non-aqueous silicon-$LiNi_xMn_yCo_zO_2$ (NMC) battery [147], this method is simple and fully scalable for thick electrode manufacturing. Thirdly, the 3D porous CNTs network not only enhances the electrical conductivity of electrode [148], but also interweaves $LiMn_2O_4$ particles in a 3D reinforced network without the assistance of additional polymeric binders to enhance the mechanical integrity of electrode and avoid the increased tortuosity and resistance brought by polymeric binders. Lastly, the eco-friendly aqueous processing resolves the environmental concerns of toxic NMP solvent and reduces the overall manufacturing cost related to NMP recovery facilities. As a result, the unique design of the 3D-CNT cathode allows the manufacturing of ultra-thick electrodes (up to 900 μm) with high areal capacity and active material loading of 13.5 mAh cm^{-2} and 113.5 mg cm^{-2}, respectively. A combination of a very thick electrode design with a specific capacity close to its theoretical value leads to extremely high areal capacity batteries. Therefore, by incorporating CNTs in the cathode's structure to form a 3D reinforced and conductive network, the areal capacity and the energy density of the aqueous zinc/$LiMn_2O_4$ batteries can be enhanced substantially without sacrificing the specific capacity.

4.2. Experimental method

4.2.1 Fabrication of 3D-CNT cathode

The 3D-CNT $LiMn_2O_4$ electrodes with interconnected networks were prepared with a simple and scalable method. The single-wall carbon nanotube (SWCNT) slurry (outer mean diameter: 1.6 nm, length: 5 μm) was purchased from OCSIAL company (Tuball BATT H_2O 0.4%).

The slurry is aqueous-based, entailing 99% H_2O, 0.4% CNT, and 0.6% carboxymethyl cellulose (CMC). The cathode consists of $LiMn_2O_4$ (MTI) active material, carbon fiber (Abbreviated as CF, length: 50 μm), CNT, and CMC, in which the CNT and CMC are added from the SWCNT aqueous solution. A typical fabrication procedure of the 3D-CNT $LiMn_2O_4$ cathode with 10 grams (dry-based weight) cathode slurry is illustrated in Figure 4.2 and described as follows. In the first step, the solid phase was prepared by grinding 9.45 gr $LiMn_2O_4$ and 0.425 gr CF using mortar and pestle. The CF was added for mechanical reinforcement of the electrode. Afterward, the solid phase was transferred to the mixer cup and then 12.5 gr of SWCNT aqueous solution was added to the solid phase mixture. Then, the slurry was blended in the planetary mixer (Thinky Mixer, AR100) for 30 mins at 2000 rpm to ensure homogenous mixing and to form a viscous slurry. The graphite foil was used as the cathode substrate due to its resistance to the acidic solution and it was roll-pressed before using to lower its thickness to 200 μm. In the next step, the slurry was cast on the graphite foil using doctor blade technique and the height of the doctor blade can be adjusted to achieve different desired active material loading. The coated electrodes were dried in the gravitational oven at 70 ºC for 2 hours. Eventually, the dried electrodes were cut into 24 mm disk size and then placed between rolling press machine to reduce 10% of their initial thickness. The calendering process can ensure good adhesion between the electrode composite film and the substrate and promote the rate performance of the electrode. In the 3D-CNT electrode design, only small amounts of conductive material and binder agents were used, thus giving more space for the active material. The extremely small number of inactive components in the electrode structure enables the fabrication of cathode with a high mass fraction of active material (>94 wt.%). The thick cathode demonstrated very high $LiMn_2O_4$ active materials loadings up to 114 mg cm^{-2}.

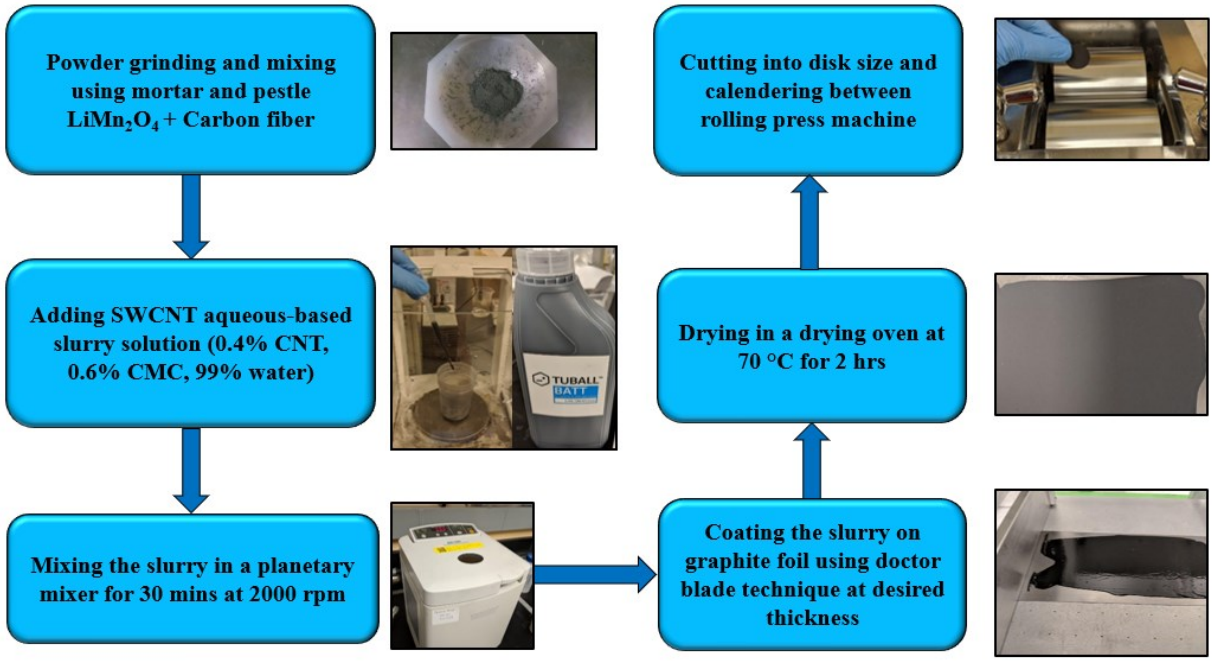

Figure 4.2 Fabrication procedure of thick 3D-CNT $LiMn_2O_4$ cathode

4.2.2 Preparation of aqueous rechargeable zinc/$LiMn_2O_4$ battery

The configuration of the zinc/$LiMn_2O_4$ battery is illustrated in Figure 4.3. As shown, the battery components are comprised of graphite foil substrate, thick $LiMn_2O_4$ cathode with high active material loading, zinc anode, and pre-soaked separator layers inside the aqueous electrolyte. The zinc anode was prepared by polishing 350 μm thick zinc foil (Goodfellow), ultrasonically treating in acetone, and then rinsing in DDI water. The electrolyte was a hybrid solution of 2.0 mol L^{-1} $ZnSO_4$ (Sigma Aldrich) and 1.5 mol L^{-1} Li_2SO_4 (Sigma Aldrich) at adjusted pH of 5. The cathode and anode were separated by the pre-soaked separator layers in between. The separator consists of AGM (NSG group) and Celgard (5550), where the AGM acts as the wetting layer to provide enough electrolyte for battery operation and Celgard is the barrier layer that can inhibit the dendrite growth. The Celgard was faced to the zinc anode and AGM was placed at top of Celgard. Finally, the battery was assembled using acrylic plates as supporting ends, fastened by bolt and nuts, and sealed by parafilm-M self-sealing films.

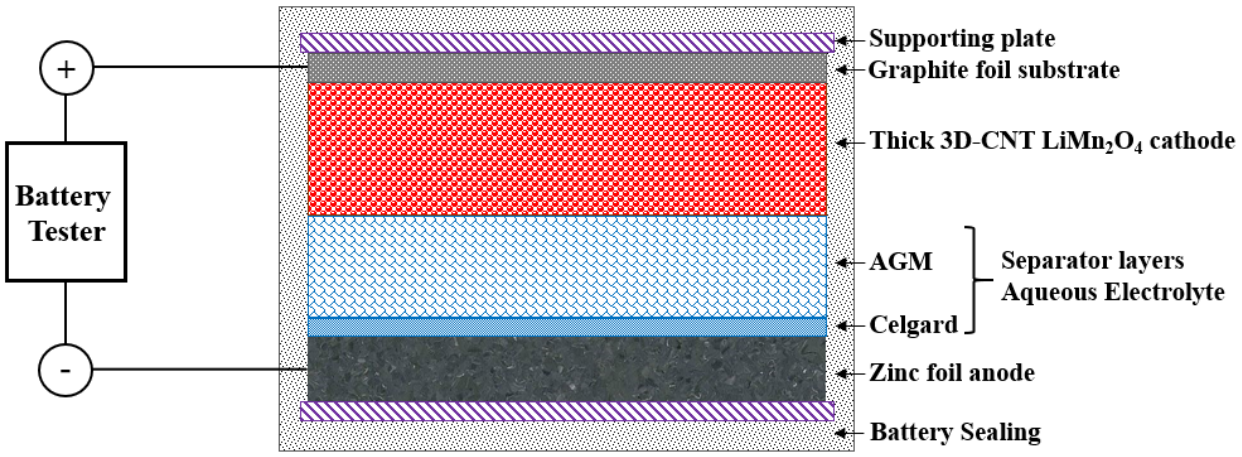

Figure 4.3 Configuration of zinc/$LiMn_2O_4$ battery comprising of a thick cathode, zinc anode, separator layers, substrate, and supporting ends.

4.2.3 Electrochemical measurements

The cycling performance of the fabricated zinc/$LiMn_2O_4$ battery was evaluated by a 3-step galvanostatic charge/discharge in the range of 1.5 V- 2.1 V vs. Zn/Zn^{2+} cut-off voltages in the LAND battery tester (LANHE, CT2001A). The 3-step galvanostatic charge/discharge was performed based on the following testing protocol: 1) charge/discharge at constant current and rest for 5 minutes, 2) charge/discharge at one-third of initial current and rest for 5 minutes, 3) charge/discharge at one-sixth of initial current. Table 4.1 shows the charge/discharge protocol for zinc/$LiMn_2O_4$ battery at 200 µm cathode thickness. The 3-step charge/discharge protocol can help to fully charge/discharge the battery at 100%- 0% state of charge (SOC). EIS of $LiMn_2O_4$ cathode as the working electrode was measured at potentiostat mode vs. open-circuit voltage (OCV) using VSP-300 Biologic instrument at scan rate from 1000 kHz to 0.1 Hz and at 5 mV sinus amplitude.

Table 4.1 Charge/discharge testing protocol for zinc/$LiMn_2O_4$ battery with 200 μm thick cathode

Steps	Charge	Discharge
1	Constant-current at 1C	Constant-current at 1C
2	Rest for 5 mins	Rest for 5 mins
3	Constant-current at C/3	Constant-current at C/3
4	Rest for 5 mins	Rest for 5 mins
5	Constant-current at C/6	Constant-current at C/6

4.2.4 Physiochemical characterization

The morphology of the cathode was imaged by SEM (LEO FESEM1530). Raman spectroscopy (Bruker Senterra, 532 nm laser) was used to evaluate the CNT defects inside the cathode before and after battery cycling. XRD (Rigaku MiniFlex 600) patterns were acquired with a 2θ value from 10 to 90° to analyze the peaks associated with $LiMn_2O_4$ active material and their changes during battery cycling.

4.3. Results and discussion

4.3.1 3D-CNT cathode fabrication and optimization

It is reported that the active material particle size must be micro-sized and preferably larger than CNTs' length to form a robust and conductive 3D network [149]. In this design, SWCNTs with a length of about 5 μm wrap the $LiMn_2O_4$ active material particles with an average particle size of 25 μm (D50= 23-27 μm), creating a uniform 3D reinforced and conductive structure as shown in Figure 4.4a. The SEM image shows that CNTs interconnect and wrap the $LiMn_2O_4$ active material particles. This unique structure allows the fabrication of very thick $LiMn_2O_4$ electrodes without any crack formation (Figure 4.4b). On the contrary, since the active material particle size of $LiFePO_4$ is in the range of nanosize and much smaller than CNTs length, such 3D reinforcement

networks are not formed. Hence, the 3D-CNT electrode design is not a suitable choice for manufacturing thick $LiFePO_4$ cathode. For example, the fabrication of 3D-CNT electrode with nanosized $LiFePO_4$ active material particles (200-500 nm) resulted in severe crack formation at 300 µm electrode thickness (Figure 4.4c). Figure 4.4b also shows that the mechanical property of the 3D-CNT $LiMn_2O_4$ electrode composite is so excellent that it is possible to fabricate crack-free electrodes even at extremely high thicknesses (up to 900 µm). It should be noted that it is not practical to fabricate an electrode thicker than 900 µm (dry thickness) due to crack formation after drying. Hence, 900 µm is considered as the critical cracking thickness for $LiMn_2O_4$ active material with the 3D-CNT electrode design. The mechanical reinforcement of the 3D conductive network enables the fabrication of ultra-thick electrodes with high active material loading. The CFs in the structure of the electrode composite increase the mechanical strength, while the CNTs provide a 3D reinforced and conductive network [150,151].

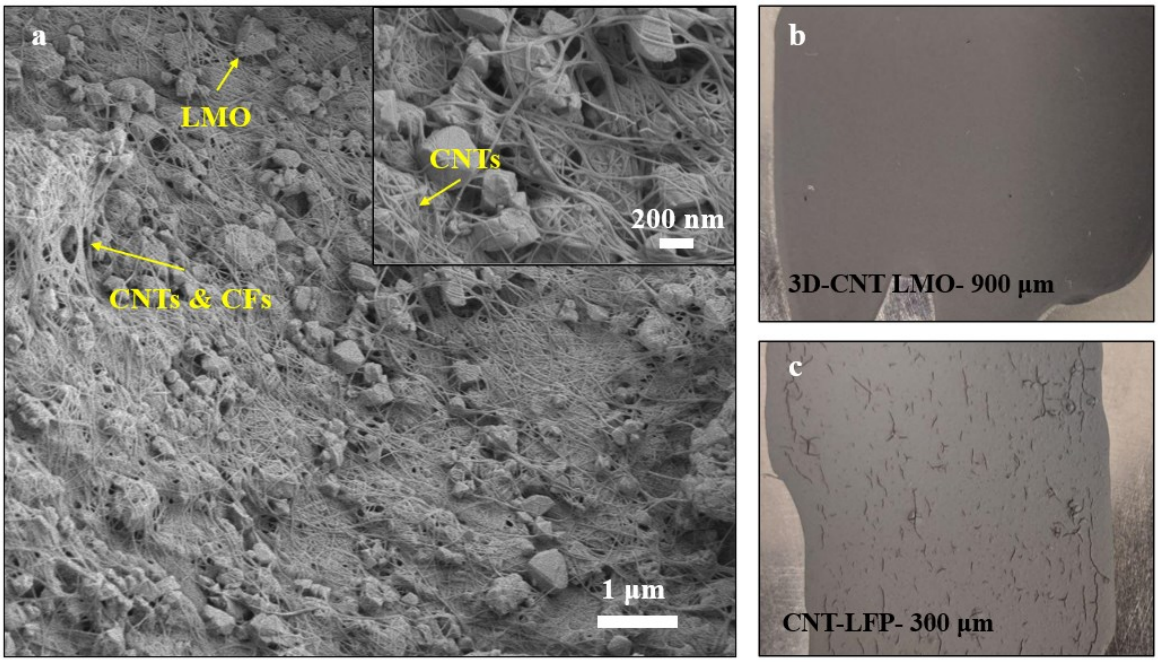

Figure 4.4 a) SEM image of 3D-CNT $LiMn_2O_4$ electrode having 0.5 wt.% CNT in the structure and the magnified SEM image. b) Optical image of 3D-CNT $LiMn_2O_4$ electrode (LMO) with 0.5 wt.% CNT coated on graphite foil at 900 µm (dried electrode thickness). c) Optical image of $LiFePO_4$ electrode (LFP) with 0.5 wt.% CNT coated on graphite foil at 300 µm (dried electrode thickness).

The cycling stability of zinc/$LiMn_2O_4$ battery manufactured with 400 μm thick cathodes at various mass fractions of CNTs was evaluated. As observed in Figure 4.5, the capacity loss of the battery with 0.25 wt.%, 0.5 wt.%, 1 wt.%, and 2 wt.% CNT is 10.4%, 5.5%, 5.9%, and 7.2% after 50 cycles. The capacity retention of the battery is at the highest with 0.5 wt.% CNT compared to other compositions due to adequate electronic/ionic conductivity and decent electrode structure. Besides, the areal capacity of the battery with 0.5 wt.% CNT cathode is also the highest among these batteries since it has a large amount of space for active material loading. However, the areal capacity of the battery with 0.25 wt.% CNT is about 6% lower than that of battery with 0.5 wt.% CNT cathode. This is likely due to the shortage of conductive material and low conductivity of the electrode. Moreover, as a result of low conductivity, the polarization could lead to faster capacity degradation. Therefore, 0.25 wt.% CNT is not an adequate amount for satisfactory battery performance. On the other hand, further increasing the weight percentage of CNTs in the composite to 1 wt.% and 2 wt.% slightly degraded the areal capacity and cycling performance of the battery. The areal capacity decreased due to a less loading of $LiMn_2O_4$ active material. As to the inferior capacity retention, it could be related to the structural changes at high weight percentages of CNTs. Since SWCNT solution contains 0.4 wt.% CNTs and 99% water, the addition of CNTs inside the composite is accompanied by a large amount of water inside the cathode slurry. The large amount of water may affect the composite structure due to the capillary forces while drying and relocation of binders in the course of the water removal process [132,152,153]. Therefore, formation of small cracks is expected during the drying process, causing active material particle isolation and capacity fading. Accordingly, the amount of CNT inside the $LiMn_2O_4$ cathode composite was set at 0.5 wt.% as an optimal amount for this work in terms of high areal capacity and cycling stability.

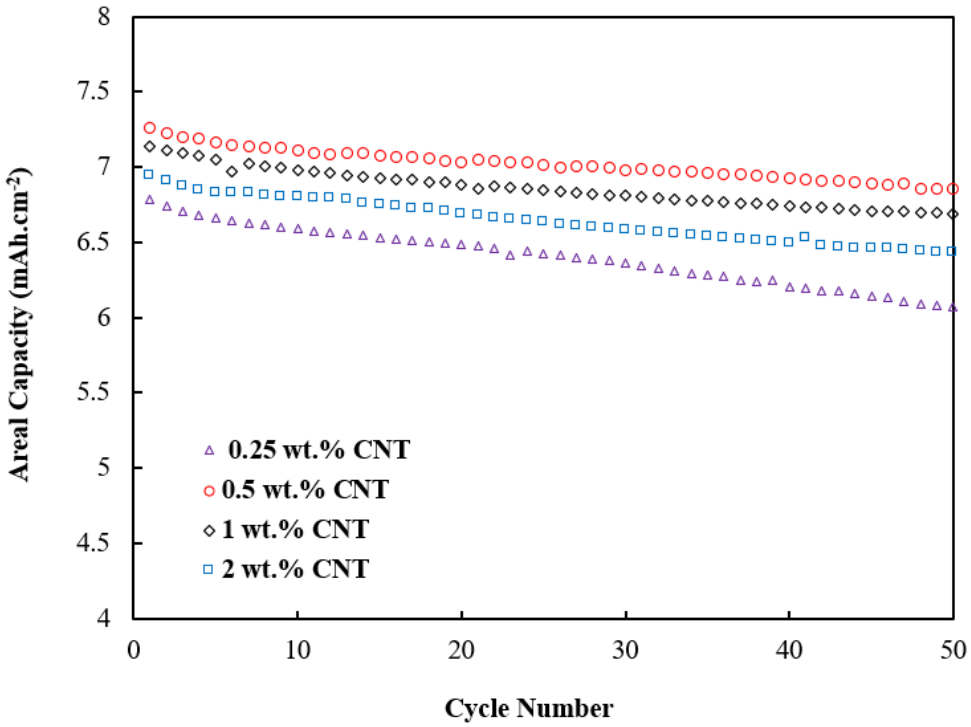

Figure 4.5 Cycling stability of zinc/$LiMn_2O_4$ battery with 0.25 wt.%, 0.5 wt.%, 1 wt.%, and 2 wt.% CNT.

4.3.2 3D-CNT $LiMn_2O_4$ cathode vs. dough-like $LiFePO_4$ cathode

$LiMn_2O_4$ active material has 148 mAh g^{-1} theoretical specific capacity and about 1.8 V discharge voltage while $LiFePO_4$ has 170 mAh g^{-1} theoretical specific capacity and 1.2 V discharge voltage in ARZLB. The higher operating voltage in the zinc/$LiMn_2O_4$ battery yields much better energy density than the zinc/$LiFePO_4$ battery. To compare the energy density between these two batteries in real operating conditions, the discharge voltage plateaus of zinc/$LiMn_2O_4$ with a 3D-CNT cathode and zinc/$LiFePO_4$ with a dough-like cathode are illustrated in Figure 4.6. In Figure 4.6a, the energy density of the batteries is compared in terms of the practical specific capacity of active material, while in Figure 4.6b, the energy density is compared based on the total capacity of the batteries with the same size and electrode thickness. In spite of the higher specific capacity for zinc/$LiFePO_4$, the zinc/$LiMn_2O_4$ battery has a superior average output voltage compared to the zinc/$LiFePO_4$ battery (1.8 V vs. 1.15 V). The area under the curve in Figure 4.6a represents the

energy density of the battery based on the unit weight of the cathode active material. Therefore, the battery manufactured with $LiMn_2O_4$ cathode can have at least 30% more energy density than zinc/$LiFePO_4$ battery based on the energy density per unit weight of active material. In another comparison, considering that both batteries are constructed with approximately the same size and electrode thickness, the volumetric energy density of the zinc/$LiMn_2O_4$ battery with the 3D-CNT cathode is at least 2.4 times the energy density of the zinc/$LiFePO_4$ with the dough-like cathode. The manufactured electrodes with the 3D-CNT cathode design are dry-based and have a higher ratio of active material compared to the dough-like cathode in which its space is partially occupied by the electrolyte. Hence, at the same electrode thickness, the 3D-CNT $LiMn_2O_4$ cathode delivers a higher areal capacity than the dough-like $LiFePO_4$ cathode because of higher active material loading. Apart from manufacturing feasible thick cathode architecture, utilizing $LiMn_2O_4$ with a higher electrochemical potential than $LiFePO_4$ active material is one step forward toward high energy density ARZLBs. As discussed in Chapter 3, the volumetric energy density of the zinc/$LiFePO_4$ batteries with a thick dough-like cathode is 190% more than the energy density of the zinc/$LiFePO_4$ batteries with a thin conventional cathode design. In the current chapter, $LiFePO_4$ active material was replaced with high-voltage $LiMn_2O_4$ active material in a new thick and high areal-capacity electrode architecture, resulting in a further 140% energy density enhancement. Therefore, the volumetric energy density of the zinc/$LiMn_2O_4$ battery manufactured with the thick 3D-CNT cathode is roughly 600% greater than the energy density of the zinc/$LiFePO_4$ battery with a thin conventional cathode. This significant improvement in the energy density of the batteries paves the way for the development of competent ARZLBs for commercialization.

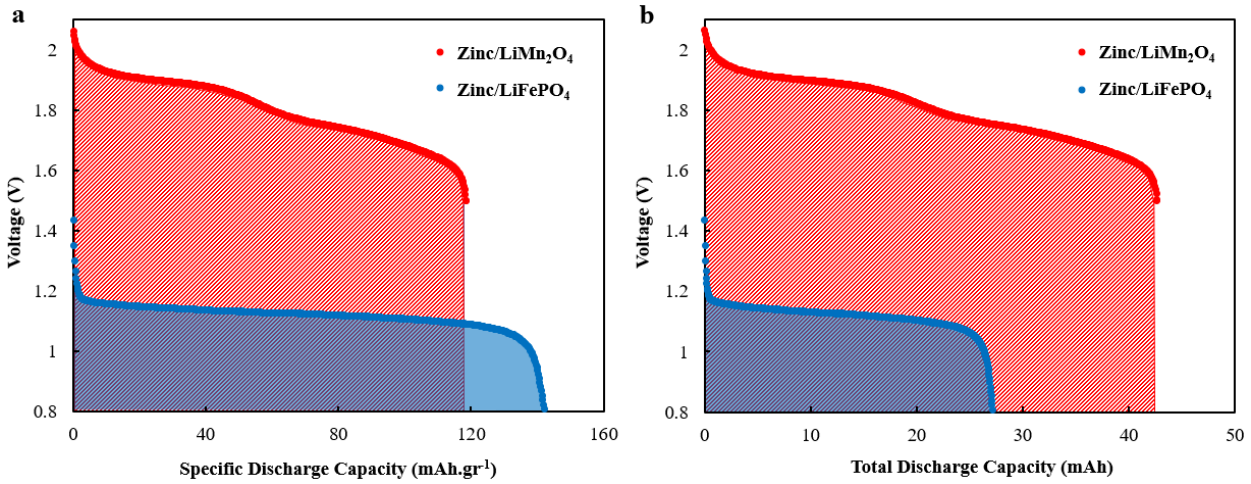

Figure 4.6 Energy density comparison of zinc/$LiMn_2O_4$ and zinc/$LiFePO_4$ batteries assembled by 3D-CNT and dough-like cathode design, respectively. The area under the curve represents a) the energy density of the battery per unit weight of active material, and b) the total energy of the battery in mWh. Both batteries are constructed with roughly the same size and electrode thickness.

On the other hand, the OCV values for the fully charged zinc/$LiMn_2O_4$ battery with 3D-CNT cathode and zinc/$LiFePO_4$ battery with dough-like cathode were recorded and compared in Figure 4.7. As shown, the zinc/$LiMn_2O_4$ was fully charged up to 2.1 V cut-off voltage at C/4 rate, followed by resting for 24 hours and then discharging down to 1.5 V at C/4 rate. The discharge capacity of the zinc/$LiMn_2O_4$ battery after the rest period was 96% of the charging capacity as a result of self-discharge. The HER is mainly responsible for the self-discharge of the battery. The zinc/$LiFePO_4$ battery showed better performance in terms of OCV stability with 99% CE after 24 hours of resting time. The lower value of OCV for the zinc/$LiFePO_4$ battery can alleviate the possible hydrogen generation. Although the OCV decay of zinc/$LiMn_2O_4$ battery is slightly higher than zinc/$LiFePO_4$ battery, a significantly higher output voltage and hence a much better energy density of the zinc/$LiMn_2O_4$ battery still make it an ideal candidate for ARZLBs.

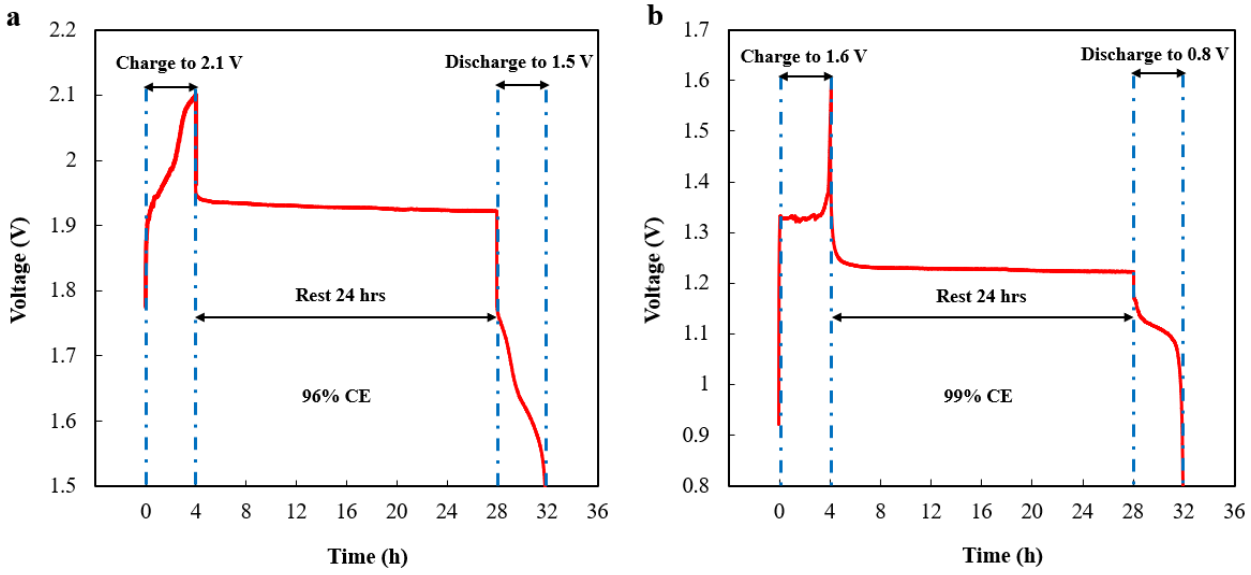

Figure 4.7 OCV stability comparison of two different ARZLBs in 2.0 mol L^{-1} $ZnSO_4$ and 1.5 mol L^{-1} Li_2SO_4 aqueous electrolyte: a) zinc/$LiMn_2O_4$ battery, and b) zinc/$LiFePO_4$ battery. The batteries were fully charged and discharged at C/4 rate.

4.3.3 Electrochemical performance of zinc/$LiMn_2O_4$ battery with 3D-CNT cathode

To investigate the rate performance of zinc/$LiMn_2O_4$ battery with 3D-CNT cathode and its comparison with the conventional cathode, the discharge specific capacity of the battery at various C-rates from C/15 to 2C is illustrated in Figure 4.8. The 3D-CNT cathodes were 200 µm and 400 µm thick with high active material loadings of 30 and 62 mg cm^{-2}. The fabricated conventional $LiMn_2O_4$ cathode was 200 µm thick with 22 mg cm^{-2} active material loading. The specific capacity of the zinc/$LiMn_2O_4$ battery with the 3D-CNT cathodes was as high as 100 mAh g^{-1} at C-rates up to C/2. At 1C and 2C rates, the specific capacity of the battery with 200 µm thick 3D-CNT cathode was decreased by roughly 30% and 50% of its value at C/15 due to the diffusion limitation during intercalation and deintercalation of lithium ions. The capacity of the battery with the conventional cathode at the same electrode thickness at 1C and 2C rates was substantially reduced by 50% and 80% of its initial value. This means that the polarization effect is raised more profoundly with the conventional cathode when the applied current is increased to 1C and 2C rates. The increase in the polarization of the battery can cause Li-ion saturation at the surface of the active material particles,

leading the battery to reach the cut-off voltage sooner [124]. This can cause underutilization of the active material because Li-ions do not have enough time to get through the depth of active material particles.

It has been observed that even the battery with 400 μm thick 3D-CNT cathode and high active material loading outperforms the battery with 200 μm conventional cathode. Generally, at high electrode thickness, the cell polarization and active material underutilization affect the performance of batteries by cause of an increase in the tortuosity and resistance of the electrode [124,137]. In the proposed design, the $LiMn_2O_4$ active material particles are interconnected by highly conductive CNTs that could improve electron transportation pathways and facilitate the movement of Li-ions even at high electrode thicknesses. Besides, a very low amount of binder (<1 wt.% CMC) in the structure of the 3D-CNT cathode reduces the electrode resistance. For comparison, because of the limitation in the electrode design, the conventional cathode needs a high amount of binder (8 wt.% PVDF) to effectively bind the particles together and eliminate the crack formation after drying. The binder in the structure of the electrode increases the tortuosity and resistance of the electrode by blocking the active material surface and creating isolated and non-conductive regions. The 400 μm thick 3D-CNT $LiMn_2O_4$ cathode with a high active material loading of 62 mg cm^{-2}, which is 3 times higher than the 200 μm thick conventional $LiMn_2O_4$ cathode, can deliver much of its capacity up to C/2 rate thanks to its unique electrode design.

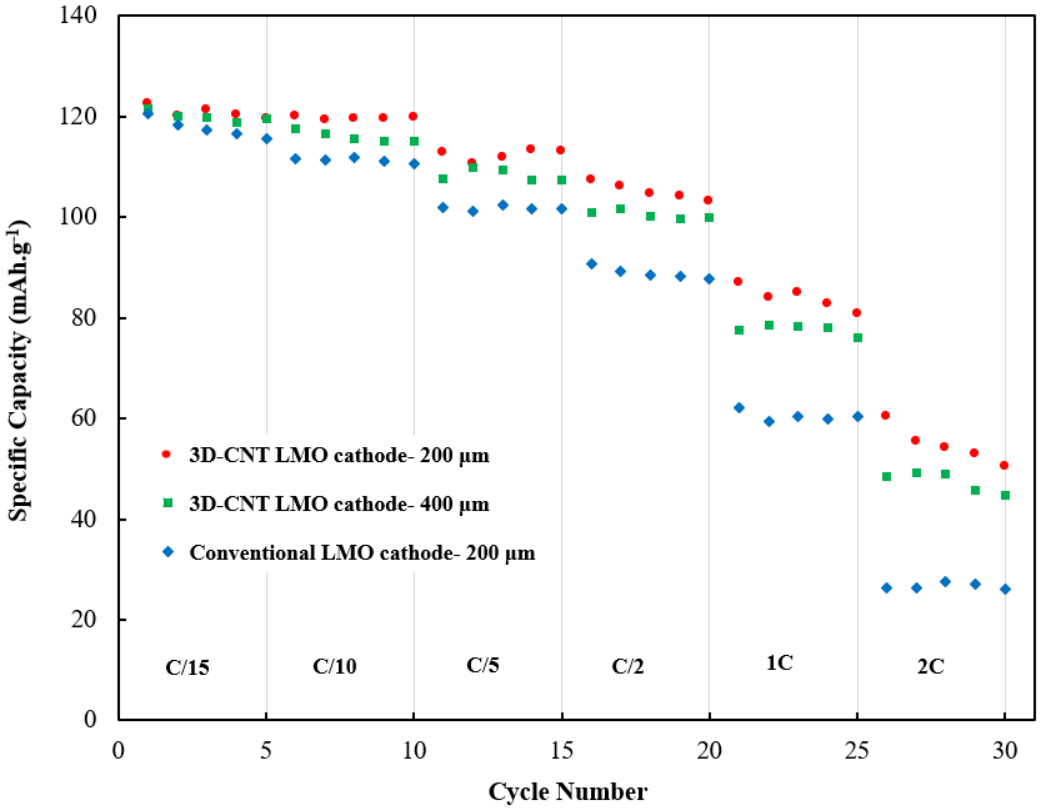

Figure 4.8 Rate capability of zinc/$LiMn_2O_4$ battery using zinc foil anode and 2.0 mol L^{-1} $ZnSO_4$ and 1.5 mol L^{-1} Li_2SO_4 electrolyte at two different electrode designs: 1) 200 µm and 400 µm thick 3D-CNT cathode, and 2) 200 µm thick conventional cathode.

The electrochemical performance of zinc/$LiMn_2O_4$ battery with 200 µm thick 3D-CNT cathode and 30.6 mg cm^{-2} active material loading for 100 cycles is shown in Figure 4.9a-b. The battery demonstrated a high specific capacity of around 121 mAh g^{-1} at the initial cycle which is almost equivalent to the practical specific capacity of $LiMn_2O_4$ active material. The practical specific capacity of $LiMn_2O_4$ active material is roughly 120 mAh g^{-1} [154]. As seen in the inset image of Figure 4.9a, the battery delivered 3.71 mAh cm^{-2} areal capacity. Despite having a relatively thick electrode design, the battery showed capacity retention as high as 93.5% at the 100th cycle. However, the cycle life of the battery with 200 µm thick cathode is restricted to roughly 100 cycles due to short-circuiting related to zinc dendrite formation. For comparison, the electrochemical performance of zinc/$LiMn_2O_4$ battery with the conventional cathode at 200 µm is plotted in Figure

4.9c-d. It is worth mentioning that 200 μm is the critical cracking thickness with the conventional cathode design. As seen, the battery showed a much lower specific capacity with only 78 mAh g^{-1} at the initial cycle. As a result of inferior specific capacity, the areal capacity of the battery was only 1.47 mAh cm^{-2} which is 60% lower than the areal capacity of the battery with the 3D-CNT cathode at the same electrode thickness. The inferior areal capacity is due to high electronic/ionic resistance in the cathode. The increased resistance also caused higher capacity fading in the battery with conventional cathode with 84% capacity retention over 100 cycles. The CE of the battery with the 3D-CNT cathode is found similar to that of the battery with the conventional cathode (98.6% vs. 98.5%). Therefore, the new electrode design does not affect the CE and the amount of possible side reactions (e.g., HER and OER) that can compete with the main electrochemical reaction is almost equivalent in both batteries.

The voltage-capacity curves of zinc/$LiMn_2O_4$ with the 3D-CNT cathode at different cycle numbers are plotted in Figure 4.9b. In these electrochemical performance tests, the cut-off voltage of the battery was controlled between 1.5 V- 2.1 V (vs. Zn/Zn^{2+}) which corresponds to 0%-100% SOC. To ensure full utilization of active material, the batteries were cycled at a three-step charge/discharge protocol. The VE of the battery decreased along with the cycle number, from 87% in the initial cycle to 85% at the 100^{th} cycle. In this work, the VE is defined by the ratio of discharge to charge voltage (first-step charge/discharge curves) at the median value for the specific capacity at each specific cycle number. The decrease in the VE of the battery can be attributed to the growing resistance as cycling progresses. As observed in the voltage-capacity curves of the battery with the conventional cathode (Figure 4.9d), the VE of the battery was roughly 83% due to high overpotential. Besides, a substantial amount of battery capacity was gained at lower C-rates (steps 2 and 3 of constant-current charge/discharge) due to high resistance. The significantly

higher VE of the battery with 3D-CNT cathode is due to the presence of a conductive network of CNTs and the absence of traditional polymeric binder in the electrode structure, leading to improved electronic/ionic conductivity.

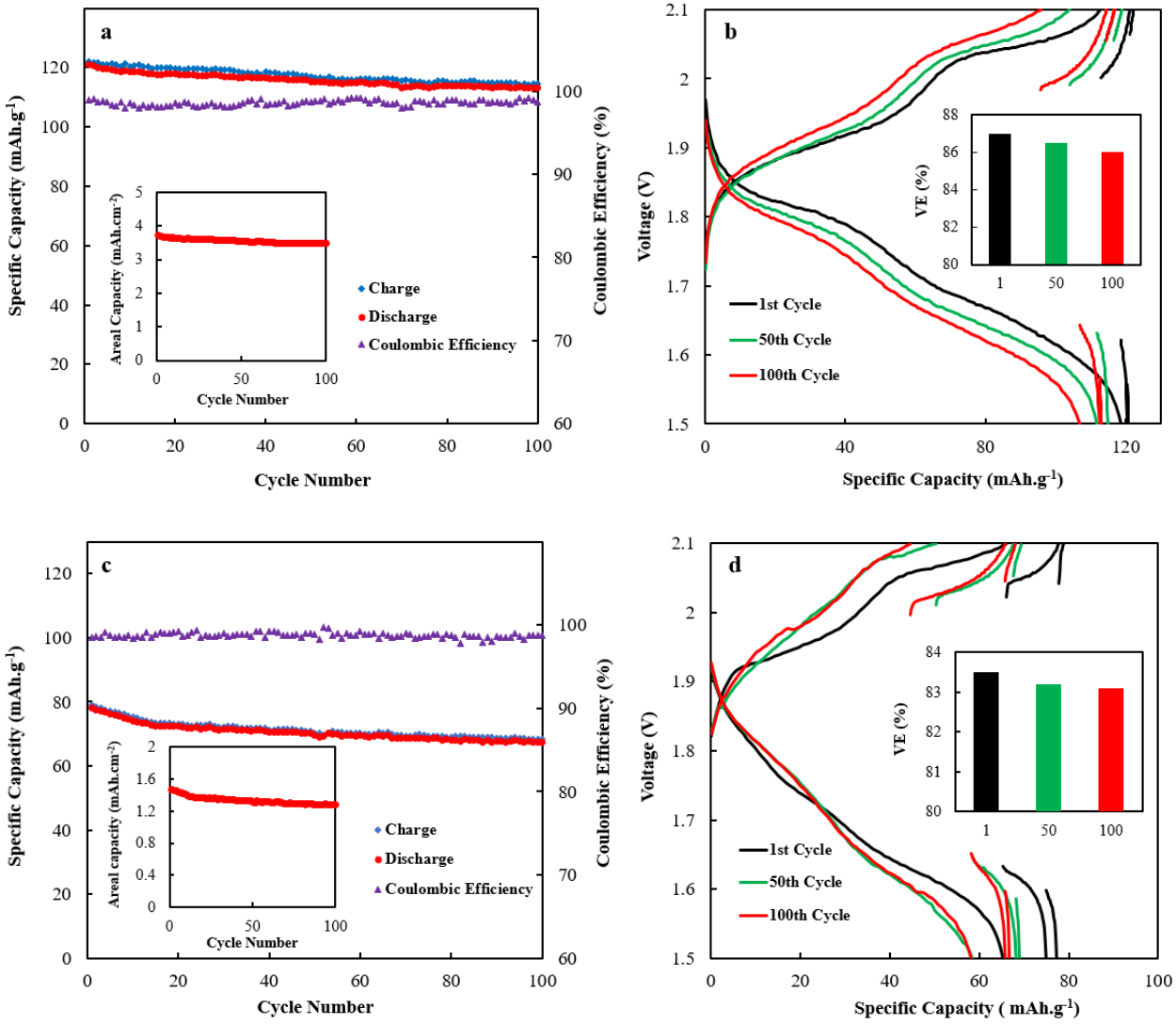

Figure 4.9 Electrochemical performance of the zinc/$LiMn_2O_4$ battery with: a-b) 200 µm thick 3D-CNT cathode, c-d) 200 µm thick conventional cathode (200 µm is the critical cracking thickness with conventional cathode design). a, c) Specific capacity vs. cycle number. The inset plot is areal capacity vs. cycle number. b, d) Charge/discharge profiles at various cycle numbers. The inset is the histogram plot of VE vs. cycle number.

To track changes in the cell resistance along with cycling, the impedance data of the zinc/$LiMn_2O_4$ battery fabricated with 200 µm thick 3D-CNT cathode was obtained at different cycles (Figure 4.10a). Each Nyquist plot is comprised of a semicircle at high to medium

frequencies, followed by an inclined line in the low-frequency region. The semicircle represents the charge transfer resistance, which its diameter defines the magnitude of the charge transfer resistance between the electrolyte and active material. The small semicircle in the Nyquist plots means low charge transfer resistance owing to the conductive network of CNTs. The sloping line is the Warburg impedance which attributes to the Li-ion diffusion inside $LiMn_2O_4$ particles. The intersection of the Nyquist plot with the coordinate axis defines the bulk resistance, which was 2.69 Ω at the first cycle and it surged as cycling progressed and reached 4.33 Ω at the 100^{th} cycle. The bulk cell resistance of the battery depends on the resistance in the current collectors, cathode, anode, and separator layers, and ionic conductivity of the electrolyte. The increase in the bulk resistance of the battery can link to the declining VE of the battery during battery cycling. EIS of zinc/$LiMn_2O_4$ battery fabricated with 200 μm thick conventional cathode was also measured and compared with 200 μm 3D-CNT cathode in Figure 4.10b. Benefiting from the high electronic/ionic conductivity of the 3D-CNT cathode, the battery showed much lower bulk and charge transfer resistance compared to the conventional cathode. The bulk resistance of the battery with the 3D-CNT cathode was 4.3 Ω, while the resistance of the battery with the conventional cathode was 7.7 Ω. Furthermore, the smaller diameter of the semicircle in the 3D-CNT cathode represents a much lower charge transfer resistance. This smaller bulk and charge transfer resistance are consistent with the higher rate performance of the battery with the 3D-CNT cathode compared to that with the conventional cathode.

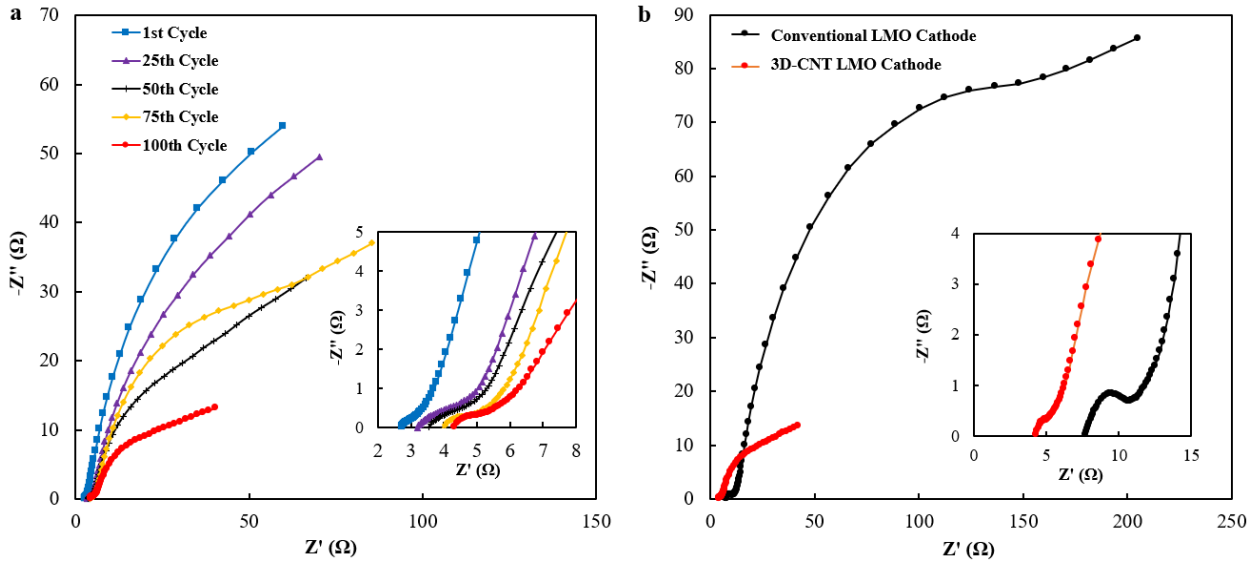

Figure 4.10 a) EIS measurement data of the zinc/$LiMn_2O_4$ battery made with zinc foil anode, 200 µm thick 3D-CNT cathode, and 2.0 mol L^{-1} $ZnSO_4$ and 1.5 mol L^{-1} Li_2SO_4 aqueous electrolyte. b) Comparison of EIS profiles of zinc/$LiMn_2O_4$ batteries fabricated with 200 µm thick 3D-CNT and conventional cathodes at the 100th cycle. The inset images are the enlarged area in the high-frequency region.

Characterization analyses were performed for the 200 µm 3D-CNT cathode before and after battery cycling. The cross-section and surface SEM images of the 3D-CNT cathode are presented in Figure 4.11. The cross-section images exhibited that the thickness of the cathode is 200 µm and the electrode coating showed decent mechanical integrity within its structure before and after battery cycling. It is worth mentioning that the expansion and shrinkage of active material during intercalation and deintercalation of Li-ions can impose severe stress on the cathode composite. This stress accumulates in thick electrodes and can cause crack formation during extended battery cycling [128]. However, the composite of the 3D-CNT cathode maintained its structural integrity even after multiple lithiation/de-lithiation steps. High magnification images disclosed that CNTs warped the $LiMn_2O_4$ active material particles in a 3D and reinforced structure, while its morphology was maintained intact after battery cycling. Such structure is highly desirable for manufacturing thick electrodes with high active material loading and areal capacity due to a combination of high conductivity and good mechanical toughness.

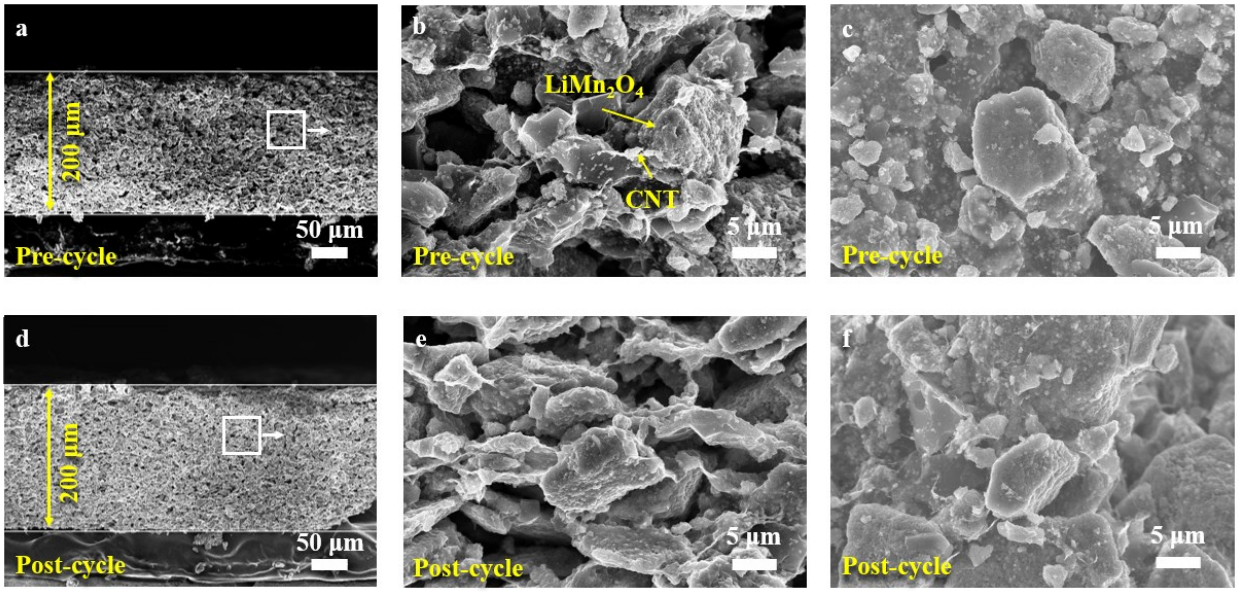

Figure 4.11 SEM images of 200 µm 3D-CNT cathode before battery cycling: a-b) cross-section image and the higher magnification image at the selected area, c) top-view SEM image. SEM images of 200 µm 3D-CNT cathode after 100 cycles: d-e) cross-section image and the higher magnification image at the selected area, f) top-view SEM image.

The XRD profiles of $LiMn_2O_4$ powder and 3D-CNT cathode before and after battery cycling are presented in Figure 4.12a. The peaks related to $LiMn_2O_4$ active material are labeled in this figure. All the major peaks in the pre-cycled cathode are indexed with the original $LiMn_2O_4$ peaks. Besides, the peak locations are not displaced after battery cycling. This implies the high stability of the cathode in the mildly acidic aqueous electrolyte after fully charged/discharged cycles. Although the peak intensity was changed during cycling, the difference in the ratio of peak intensity is insignificant. For example, the ratio of peak intensity at 111 to 311 planes was 1.7 before cycling and it reached 1.5 after battery cycling.

The Raman spectroscopy is conducted to distinguish the carbon nanomaterials' structural morphology and observe the defects of CNTs before and after battery cycling. The prominent bands related to SWCNTs are labeled in Figure 4.12b. The G and G′ bands that appeared at 1585 and 2665 cm^{-1} are indicators of the graphene since SWCNT is just a rolled-up sheet of graphene. The D (disorder) band indicates the presence of some defects in the graphene structure. The

intensity relative of the D to G (Graphene) band defines the quality of CNTs [155]. The peak intensities were obtained from their maximum counts. The ratio of D/G was 0.06 before cycling and slightly increased to 0.19 after battery cycling. As expected, as cycling progresses the disorder in the graphene structure will be increased. It has been revealed that the adsorption of Li-ion is favored inside SWCNTs and multiple attachments of Li-ions may affect the graphene structure [156]. However, as evidenced by the D/G peak intensity ratio, the change in the defect ratio is marginal.

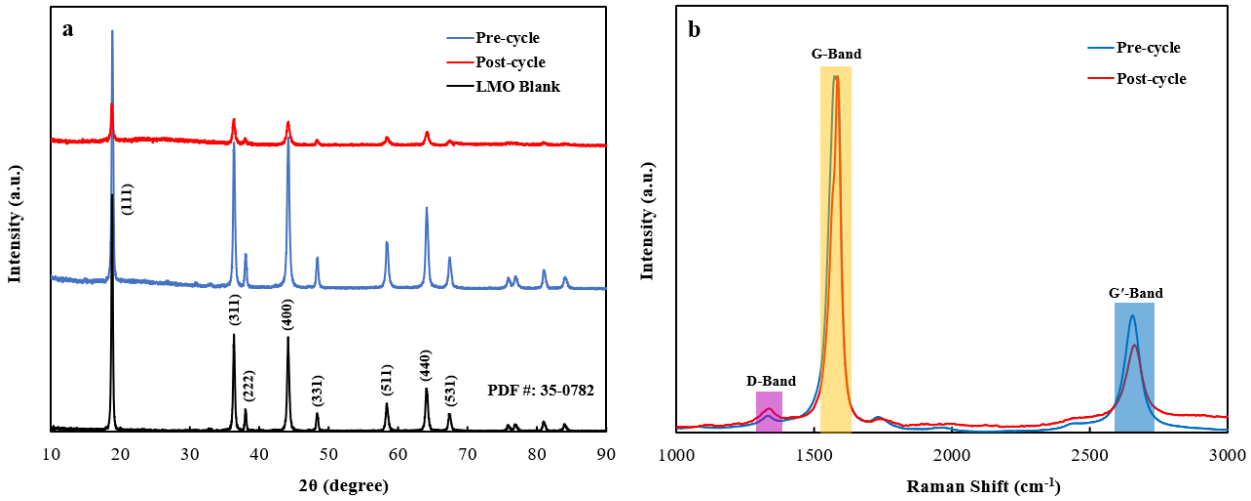

Figure 4.12 a) XRD analysis of 200 µm thick 3D-CNT cathode before and after 100 cycles. b) Raman spectroscopy of 200 µm thick 3D-CNT cathode before and after 100 cycles.

4.3.4 Thick 3D-CNT $LiMn_2O_4$ cathode

The cycling performance of the zinc/$LiMn_2O_4$ battery with thick 3D-CNT cathode was investigated at different electrode thicknesses from 200 µm to 900 µm and is plotted in Figure 4.13. By increasing the cathode thickness and thus active material loading, the areal capacity of batteries was boosted from 3.7 mAh cm^{-2} at 200 µm to 13.5 mAh cm^{-2} at 900 µm electrode thickness. Also, the active material loading was enhanced from 30.6 mg cm^{-2} at 200 µm to 113.5 mg cm^{-2} at 900 µm cathode thickness. The unique electrode design enables the manufacturing of ultra-thick cathodes with high specific capacity close to the practical specific capacity of $LiMn_2O_4$,

which is roughly 120 mAh g^{-1}. For example, the zinc/$LiMn_2O_4$ battery showed remarkable performance at 900 μm with 119 mAh g^{-1} specific capacity and 13.5 mAh cm^{-2} areal capacity. Therefore, the zinc/$LiMn_2O_4$ batteries with manufactured cathodes by a reinforced and conductive network of CNTs can deliver much higher areal capacities than conventional cathodes. For comparison, the areal capacity of the zinc/$LiMn_2O_4$ battery assembled with 120 μm thick conventional cathode (85 wt.% $LiMn_2O_4$, 7 wt.% SP-C, and 8 wt.% PVDF) was only 1.27 mAh cm^{-2}. Moreover, the zinc/$LiMn_2O_4$ battery fabricated with the 3D-CNT cathode shows a much more stable performance compared to the thick dough-like cathode. As previously mentioned, the battery with a dough-like $LiMn_2O_4$ cathode at 4.5 mAh cm^{-2} areal capacity showed only 50% capacity retention at the 60^{th} cycle (Figure 4.1). By contrast, the battery fabricated with a 3D-CNT cathode at roughly the same areal capacity exhibited more than 93% capacity retention over 100 cycles. Accordingly, the zinc/$LiMn_2O_4$ battery with a thick 3D-CNT cathode manifests a stable cycling performance even at high areal capacities.

As seen in Table 4.2, the areal capacity of the manufactured batteries in this work is much higher than the reported areal capacity of different ARLBs in the literature. The typical value for active material loading of ARLBs in scientific research is less than 10 mg cm^{-2}. A very low value of cathode mass loading and areal capacity in aqueous batteries impedes their development for the commercial stage. Despite the insignificant values in literature, the active material loading of zinc/$LiFePO_4$ with the dough-like cathode (74.5 mg cm^{-2}) and zinc/$LiMn_2O_4$ battery with the 3D-CNT cathode (113.5 mg cm^{-2}) is much superior to conventional electrodes. In conventional electrode design, a high amount of polymeric binder such as PVDF is required in electrode composite to maintain its structure at a thickness higher than 100 μm. Also, it is almost impossible to fabricate electrodes with a thickness of more than 200 μm, even by adding too much binder.

The binder in the structure increases the tortuosity and thereby leads to a longer path for Li-ion diffusion. The increased resistance in the electrode composite reduces the electronic/ionic conductivity of the electrode and results in active material underutilization. Due to the underutilization, the delivered capacity would be much lower than the practical specific capacity. However, in 3D-CNT cathode design, the binders account for less than 1 wt.% of the electrode composite, even at very high electrode thicknesses. Besides, CNTs build a reinforced and conductive network throughout the electrode composite.

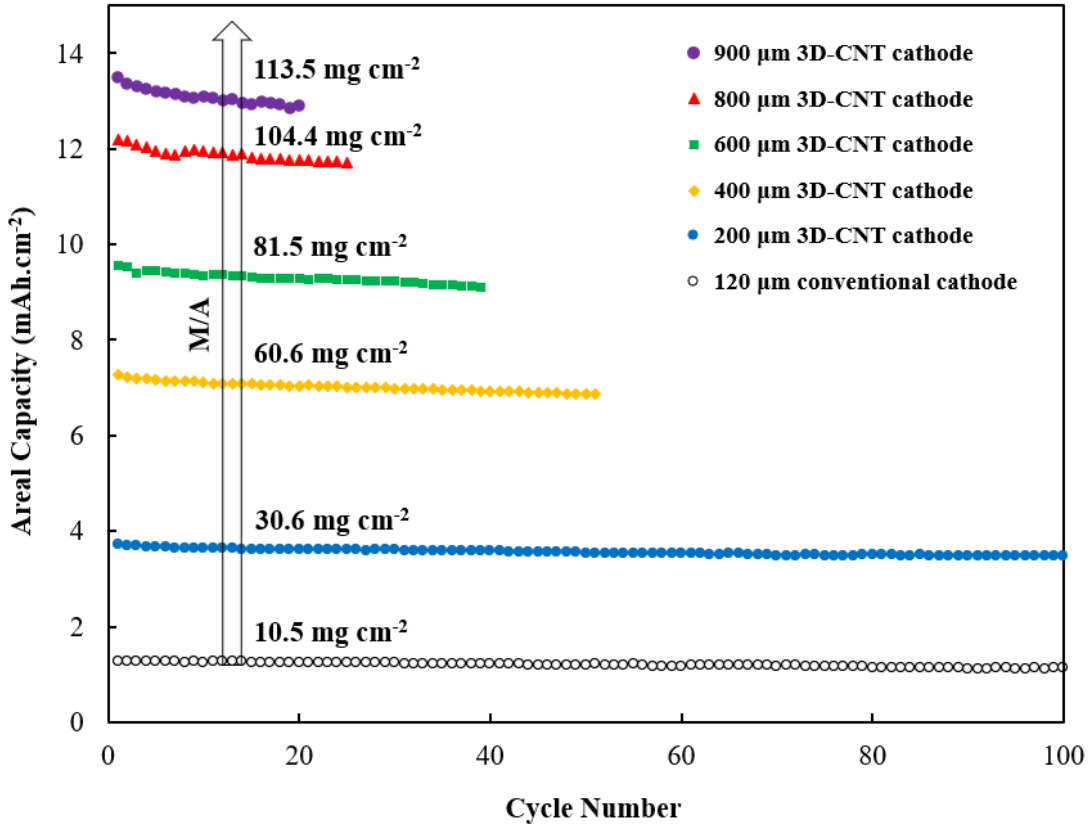

Figure 4.13 Areal capacity comparison of zinc/$LiMn_2O_4$ batteries at various thicknesses of the 3D-CNT cathode and with 120 µm thick conventional cathode. All batteries were tested at 4 mA cm^{-2} as the first step of the constant-current charge/discharge protocol.

Table 4.2 Reported areal capacity and active material loading of conventional electrodes and their comparison with this work.

Aqueous battery	Active material loading (mg cm^{-2})	Areal capacity (mAh cm^{-2})	Electrode design	Reference
zinc/$LiMn_2O_4$	2.4	0.3	Conventional	[10]
zinc/$LiFePO_4$	10	-	Conventional	[20]
zinc/$LiMn_2O_4$	-	0.65	Conventional	[85]
zinc/$LiMn_2O_4$	4-6	-	Conventional	[107]
zinc/$LiMn_2O_4$	4-6	-	Conventional	[111]
zinc/$LiMn_2O_4$	5	-	Conventional	[122]
zinc/$LiFePO_4$	3.2	-	Conventional	[64]
zinc/$LiFePO_4$	3-5		Conventional	[112]
TiS_2/$LiMn_2O_4$	4.2	-	Conventional	[157]
TiO_2/$LiMn_2O_4$	6-8		Conventional	[158]
$LiVPO_4F$/$LiVPO_4F$	5	0.58	Conventional	[159]
zinc/$LiMn_{0.8}Fe_{0.2}PO_4$	5	-	Conventional	[98]
zinc/$LiMn_2O_4$	-	2.4	Conventional	[21]
zinc/$LiFePO_4$	74.5	10.5	Dough-like	This work
zinc/$LiMn_2O_4$	113.5	13.5	3D-CNT	This work

As observed in Figure 4.13, the lifespan of the battery was shortened from 100 cycles at 200 μm to about 20 cycles at 900 μm due to short-circuiting. The early short-circuiting of the battery with a thicker electrode is because of extremely high active material loading and thereby high areal capacity. Yang et al. [138] revealed that zinc dendrite growth is not a concern in neutral/mild acidic electrolyte at small current density and/or low areal capacity. However, at high current density and/or high cathodic mass loading, the dendrites grow severely at every single cycle and short-circuit the battery rapidly. Two main reasons can explain this phenomenon. Firstly, since the total capacity of the battery at high areal capacity is much bigger than that in low areal capacity more zinc ions deposit in every single cycle. At a constant current density, the battery with a higher active material loading on the cathode side takes more time to complete one charge process, leading to more dendrite formation on the anode side. Secondly, more zinc ions are consumed in

the vicinity of the electrode surface at a high areal capacity, causing a concentration gradient. Subsequently, zinc depositions tend to grow toward the electrolyte depth, where more zinc ion is available for electrodeposition. In this chapter, conventional zinc foils were used as the anode. The flat and non-porous surface of the zinc foil anode does not provide enough space for zinc ion electrodeposition during charging. Moreover, the zinc electrode can be corroded by the HER, leading to shape change and inhomogenous electrodeposition. Therefore, the zinc foil anode is not a proper choice for a high areal capacity cathode. The strategies to prolong the cycle life of the battery and their implementation will be further discussed in the next chapters.

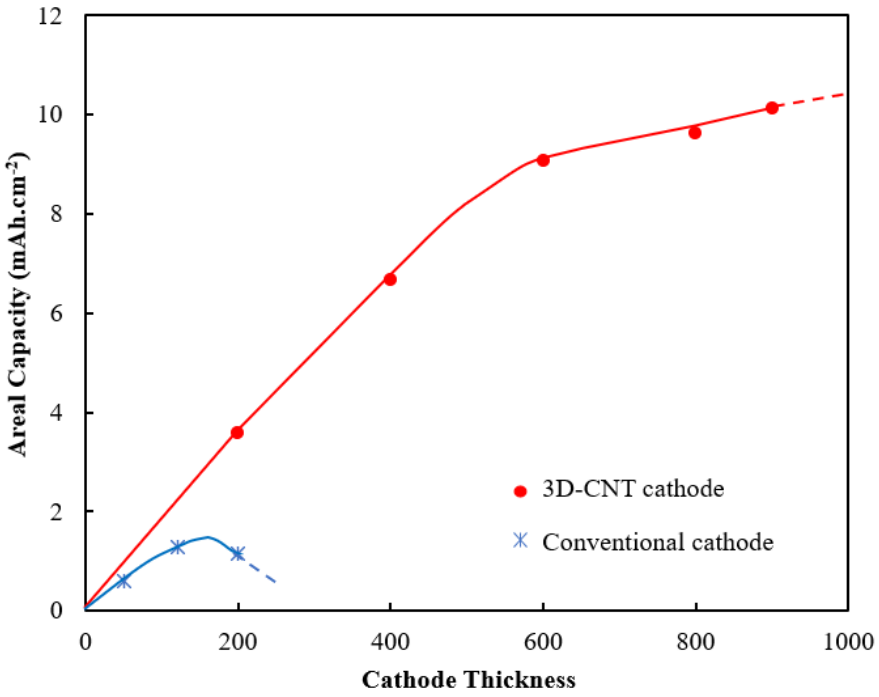

Figure 4.14 Effect of cathode thickness on the areal capacity of the zinc/$LiMn_2O_4$ battery with 3D-CNT and conventional electrode designs. All the tests were conducted at C/2 rate. The dashed lines represent the region after critical cracking thickness.

The areal capacity of batteries starts to decrease at the combination of high electrode thicknesses and high C-rates [124]. At a constant C-rate, thicker electrodes deliver a lower specific capacity than thinner electrodes. Therefore, there is an optimum point for the cathode thickness at each C-rate in which the areal capacity of the battery will be at the peak value [160]. After this

optimum point, the rate of loss in the specific capacity is too high that the total capacity of the battery will fall off sharply even by increasing the cathode thickness and active material loading. The polarization effect is responsible for the decrease in the areal capacity of the battery and is highly dependent on the discharge rate and electrode thickness. By increasing the electrode thickness, Li-ions have longer paths for diffusion and traveling through the depth of the electrode. Figure 4.14 compares the effect of electrode thickness on the areal capacity of the zinc/$LiMn_2O_4$ battery at C/2 rate (a single-step charge/discharge protocol was used). To better evaluate the effect of thickness on the areal capacity of the zinc/$LiMn_2O_4$ battery, the batteries were charged and discharged at a fixed C-rate (different current densities for each electrode thickness). As seen in Figure 4.14, the areal capacity of the battery with the conventional cathode was increased by the electrode thickness until it reached the maximum value at about 150 μm and the capacity thereupon fell off. The optimum point for the conventional electrode at C/2 rate was obtained at 150 μm, while at higher C/rates a lower optimum point is expected. For the 3D-CNT cathode, the areal capacity was increased sharply until about 600 μm and then its slope was dropped. It is observed that the areal capacity of the battery at C/2 rate was not decreased even at 900 μm thick electrode (900 μm is the critical cracking thickness). Therefore, the polarization effect for the 3D-CNT cathode is not as large as the conventional cathode. A conventional electrode needs too much polymeric binder in the structure to compose a crack-free electrode. For example, at 200 μm electrode thickness, 8 wt.% PVDF was used. However, in the 3D-CNT cathode design, $LiMn_2O_4$ particles are interconnected with highly conductive CNTs and only 0.75 wt.% CMC as a cellulose binder was used in the structure even at 900 μm thick electrode. Therefore, 3D-CNT cathode with highly conductive, 3D reinforced, and improved structure enables the manufacturing of ultra-thick electrodes with high deliverable areal capacity.

4.4. Summary

In this chapter, a unique 3D-CNT ultra-thick cathode design has been proposed for the zinc/$LiMn_2O_4$ battery with unprecedented active material loading and areal capacity. The CNTs network in the electrode structure reinforces the mechanical integrity of the composite and enhances the electronic/ionic conductivity of the electrode, leading to near-theoretical specific capacity performance. Furthermore, the toxic and expensive NMP-solvent processing of the electrode is replaced by inexpensive and eco-friendly aqueous processing. The areal capacity and active material loading of 3D-CNT thick cathodes at various electrode thicknesses are compared with dough-like and conventional cathodes in Figure 4.15. The areal capacity of zinc/$LiMn_2O_4$ battery with the 3D-CNT cathode at 200 μm is almost similar to the areal capacity of the battery with the dough-like cathode at 400 μm due to the dry-based and compact electrode composite structure. Therefore, apart from using $LiMn_2O_4$ with a higher output voltage than $LiFePO_4$, the compact composite and the high ratio of active material to inactive materials in 3D-CNT cathode design could contribute to yield a better energy density than zinc/$LiFePO_4$ battery with the dough-like cathode design. The zinc/$LiMn_2O_4$ battery manufactured with the 3D-CNT thick cathode design manifested 140% more energy density than the zinc/$LiFePO_4$ battery fabricated with the dough-like cathode at the same electrode thickness. It is worth noting that the cost per energy in the high energy-density ARZLBs would be much more economical than that in low energy-density batteries. The active material loading and areal capacity of the zinc/$LiMn_2O_4$ battery with the 3D-CNT cathode reach 113.5 mg cm^{-2} and 13.5 mAh cm^{-2} respectively, which is 10 times higher than the areal capacity of zinc/$LiMn_2O_4$ battery with the conventional cathode design. Consequently, the ultra-thick cathode design with a high ratio of active material to inactive components (e.g.,

separators and current collectors) in zinc/$LiMn_2O_4$ battery pack can promote energy density and cut the cost of ARZLBs for commercialization.

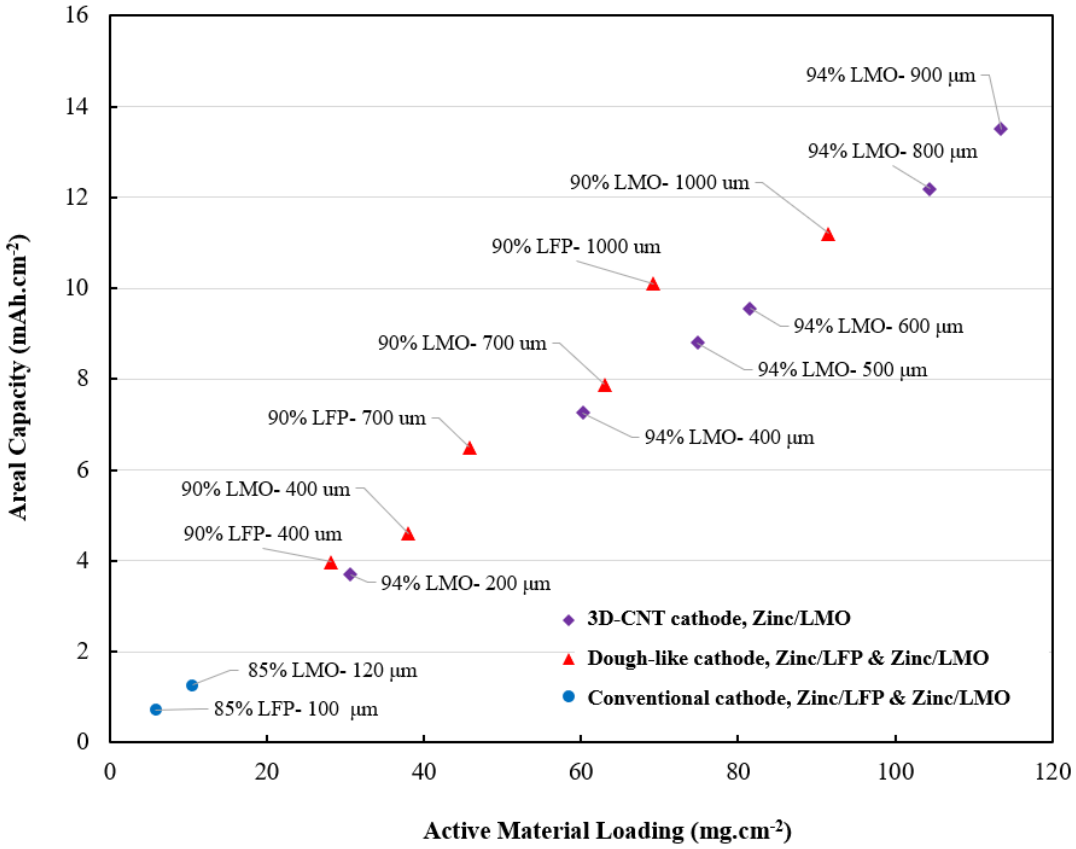

Figure 4.15 Comparison of areal capacity for zinc/$LiMn_2O_4$ and zinc/$LiFePO_4$ batteries using different cathode designs at various electrode thicknesses and active material loadings.

5. Development of porous zinc paste composite anode for high areal-capacity zinc/$LiMn_2O_4$ battery

5.1. Introduction

For aqueous Li-ion batteries, zinc is a promising anode due to its abundant resources, high specific capacity (820 mAh g^{-1}), low redox potential (-0.762 V vs. SHE), and non-toxicity [21,22]. ARZLBs are potential alternatives to commercial batteries, e.g., lead-acid and Li-ion batteries in some application areas that require safe, eco-friendly, and low-cost energy storage. However, the cycle life of this type of battery is strongly limited by the zinc anode. During the charging process, zinc deposits near the nucleation sites of the zinc electrode and on top of the protuberance tips where the zinc ions can easily migrate. Uneven zinc deposition during extended battery cycling forms sharp and need-like protrusions, known as zinc dendrites, which can cause short-circuiting and disastrous failure of the battery [38–40]. The dendrite formation hinders the application of zinc anode in ARZLBs for long-term cycling behavior.

Specifically, the formation of zinc dendrite is much more severe for ARZLBs with thick cathodes as opposed to the common ARZLBs with thin cathodes. The main reason is behind the fact that batteries with large cathodic mass and high areal capacity will deposit more zinc during every single charge step, leading to the accelerated formation of zinc dendrites [138]. Moreover, due to the shortage of zinc ions on the proximity of electrode surface and hence a pronounced concentration gradient, zinc deposits preferably on top of protuberances and consequently causing a progressive intensification of zinc dendrites. Accordingly, zinc dendrites propagate extremely in high areal-capacity batteries. As discussed in Chapter 4, the zinc/$LiMn_2O_4$ battery with a high areal

capacity of 13.5 mAh cm^{-2} showed only about 20 cycles before short-circuiting, while the battery with an areal capacity of 3.7 mAh cm^{-2} lasted for at least 100 cycles. Consequently, conventional zinc anode is not a proper choice to be paired with thick cathodes.

The limited cycle life of ARZLBs with conventional zinc electrodes is originated from three main reasons. First, the surface of conventional zinc electrodes such as zinc foil and zinc plate is flat and non-porous and hence it does not provide much surface to accommodate enough zinc deposition during the charging process [38]. Second, the uneven current distribution throughout the conventional zinc electrode tends to construct inhomogeneous protrusions during zinc deposition. These protrusions can attract more zinc ions at the tips compared to the rest of the zinc surface owing to the possession of the high electric field, leading to progressive intensification of the zinc surface heterogeneities [39]. Finally, the zinc anode can be consumed by the hydrogen evolution-induced corrosion during the charging process and resting time, causing low reversibility of the zinc electrode and shape change [40]. All of these limitations trigger the zinc dendrite growth and consequently shorten the cycle life of ARZLBs.

To suppress the detrimental dendrite formation and improve the durability of high areal-capacity zinc/$LiMn_2O_4$ batteries, a newly designed porous zinc paste composite (PZPC) electrode is developed in this chapter to replace the conventional zinc foil. The PZPC anode is comprised of zinc dust, CNTs, CFs, and functional additives. Such unique formula empowers the PZPC anode to 1) provide more surface for zinc deposition, 2) optimize the current distribution, 3) inhibit the HER, and 4) alleviate the zinc corrosion. The small-sized and high surface area zinc dust particles (<10 μm) can be effectively wrapped by CNTs in a 3D porous and conductive network to provide more surface for zinc deposition and regulate the current distribution at the same time. The CF is added to strengthen the mechanical integrity of the electrode composite and further increase the

electrode conductivity. The selected functional additives (tin, bismuth, and lead metal ions or metal oxide) are aimed to improve the corrosion resistance of the zinc and increase the hydrogen evolution overpotential to promote the lifespan of the battery [85,97].

5.2. Experimental method

5.2.1 Preparation of PZPC anode

The PZPC anode is prepared with a highly porous structure to accommodate more surface for zinc deposition compared to the zinc foil anode. The following recipe is for the fabrication of 10 grams of dried-based PZPC electrode. First, 8.9 grams of zinc dust powders with an average particle size <10 μm (Sigma Aldrich) and 0.6 grams of CF (length: 50 μm) were blended with 12.5 grams of aqueous-based SWCNT solution (OCSIAL, Tuball BATT H_2O, 0.4%) in the planetary mixer (Thinky Mixer, AR100) at 2000 rpm for 15 mins. The SWCNT solution is comprised of 0.4% SWCNT, 0.6% CMC, and 99% H_2O. Then, 335 milligrams polytetrafluoroethylene (PTFE) suspension solution (60 wt.% dispersion in DDI water, Sigma Aldrich) was added to the zinc powder slurry as a binding agent and mixed for another 15 mins. The additives solution consisted of 100 milligrams tin(II) sulfate (95%, Acros Organics), 50 milligrams bismuth(III) oxide (99.9%, Acros Organics), and 25 milligrams lead(II) acetate (99%, Alfa Aesar) in DDI water. The prepared additive solution was added to the zinc powder slurry and the whole mixture was blended in the planetary mixer at 2000 rpm for 30 mins to form the zinc paste slurry. The zinc paste slurry was cast on a thin zinc foil (Goodfellow) with 150 μm thickness as the substrate, and the thickness of the coating was controlled using the doctor blade technique at 800 μm as shown in Figure 5.1. The casted zinc paste slurry was dried at ambient temperature for 4 hours and had a thickness of around 300 μm after drying. The resultant PZPC contains 89 wt.% zinc dust, 6 wt.% CF, 0.5 wt.% CNT,

0.75 wt.% CMC, 2 wt.% PTFE, 1 wt.% tin sulfate, 0.5 wt.% bismuth oxide, and 0.25 wt.% lead acetate. The additives were added to reduce corrosion of the zinc electrode and promote the cycle life of the battery. The mass ratio of additives inside PZPC has been selected in accordance with prior works in the literature [161–163]. The range of bismuth oxide as an additive to effectively suppress the zinc dendrites is 0.5 wt.%- 2 wt.% [161,162]. Moreover, tin sulfate is in the range between 0.5 wt.% to 1 wt.% to reduce hydrogen gassing on the zinc electrode [163]. Lead is a toxic material and the restriction of the hazardous substances directive (RoHS) specifies the maximum lead content below 0.1% (1000 ppm) under RoHS 3 (EU 2015/863) or below 0.4% (4000 rpm) under RoHS Annex III lead exemption when it is used as an alloying element [164]. Therefore, the lead content in the PZPC anode complies with the RoHS criteria.

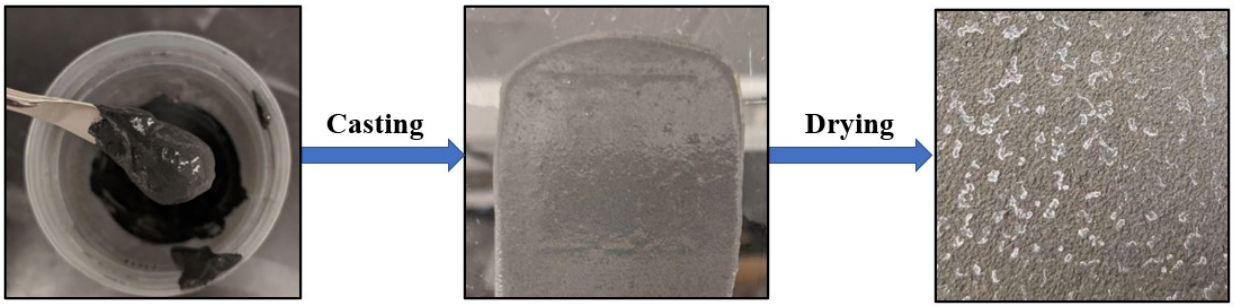

Figure 5.1 Experimental steps of casting the zinc paste slurry on a zinc foil substrate.

5.2.2 Preparation of zinc/$LiMn_2O_4$ battery

The construction of the zinc/$LiMn_2O_4$ battery is similar to the previously described battery in section 4.2.2. The 3D-CNT $LiMn_2O_4$ cathode at different thicknesses was fabricated with the same procedure as explained in section 4.2.1. The prepared PZPC was employed as the anode with a thin zinc foil (150 µm, Goodfellow) as its substrate. Zinc foil with a thickness of 350 µm was also used as the anode to compare its performance with the PZPC anode. The electrolyte was a mixed solution of 2.0 mol L^{-1} $ZnSO_4$ (Sigma Aldrich) and 1.5 mol L^{-1} Li_2SO_4 (Sigma Aldrich) at

adjusted pH of 5. The cathode and anode were separated by separator layers in between which were previously soaked inside the aqueous electrolyte.

5.2.3 Electrochemical measurements

Chronoamperometry (CA) measurements were conducted to study the deposition of zinc on the surface of PZPC and zinc foil electrodes using a three-electrode setup on a VSP-300 Biologic workstation. The working, reference, and counter electrodes were zinc, saturated calomel electrode (SCE), and Platinum (Pt) wire, respectively; and an overpotential of -120 mV vs. Zn^{2+}/Zn in an aqueous electrolyte of 2.0 mol L^{-1} $ZnSO_4$ and 1.5 mol L^{-1} Li_2SO_4 was applied when the current density was recorded. Symmetric zinc battery cells were assembled in a CR2032 coin cell case using a pre-soaked AGM separator in an aqueous electrolyte of 2.0 mol L^{-1} $ZnSO_4$ and 1.5 mol L^{-1} Li_2SO_4 to evaluate the cycling lifespan and overall voltage hysteresis of the battery with PZPC and zinc foil electrodes. The voltage-time curves for the symmetric zinc battery were recorded at 1 mA cm^{-2} and a constant capacity of 0.5 mAh cm^{-2}. The cycling performance of the fabricated zinc/$LiMn_2O_4$ battery was evaluated by a 3-step galvanostatic charge/discharge protocol in the range of 1.5 V-2.1 V vs. Zn/Zn^{2+} cut-off voltages as already explained in section 4.2.3 using a LAND battery tester (LANHE, CT2001A). EIS data were obtained with 5 mV amplitude and frequency range from 1 MHZ to 0.1 HZ to study the resistance of zinc/$LiMn_2O_4$ battery with PZPC anode and 3D-CNT cathode.

5.2.4 Physiochemical characterization

The SEM and XRD characterization methods were conducted with the same equipment explained in 4.2.4. The morphology of the PZPC electrode before and after battery cycling was studied using SEM images. The XRD patterns in the range from 5 to 90° were obtained to detect

the peak change related to zinc metal during battery cycling. The energy dispersive X-ray (EDX) mapping was conducted to analyze the elemental distribution of PZPC. N_2 adsorption-desorption measurement (Micromeritics-ASAP 200) was used to investigate the surface area and pore size distribution of the PZPC according to the Brunauer-Emmett-Teller (BET) theory and Barrett-Joyner-Halenda (BJH) model, respectively.

5.3. Results and discussion

5.3.1 Characterization of PZPC electrode

CF, CNT, and binder are the essential constituents of the PZPC architecture. The CF strengthens the mechanical integrity of the composite and its combination with binder and CNTs leads to the successful manufacturing of crack-free PZPC electrode. The images of PZPC with and without CF and PTFE binder are shown in Figure 5.2a. As seen, the PZPC without CF and PTFE binder displayed severe crack formation, while the addition of CF and binder resolves this issue. The crack-free PZPC electrode is further characterized by both cross-section and surface SEM to discover its morphology in Figure 5.2b-e. Clearly, the cross-sectional SEM image in Figure 5.2b displays that a highly porous PZPC with a thickness of 280 μm is coated on a zinc foil substrate. In contrast, the zinc foil beneath PZPC has a dense and non-porous structure. The zinc dust particles are found to be smaller than 10 μm in both cross-sectional and surface SEM images (Figure 5.2c-e), providing a high surface area for zinc deposition. More importantly, zinc dust particles are wrapped and interconnected by the porous conductive networks of CNTs and CFs (Figure 5.2e), which can regulate zinc deposition/dissolution at high current density. By contrast, the surface of commercial zinc foil is nearly flat with large dents and defects (Figure 5.2f) and more visible small dents as seen in the magnified image (Figure 5.2g). Due to the limited surface

area of the zinc foil, those dents and defects are likely to trigger the growth of zinc dendrites. Furthermore, the existence of PZPC additives including lead, bismuth, and tin is evidenced visually in EDX mapping in Figure 5.3. The presence of the PTFE binder is also validated by the fluorine in the sample. Notedly, the elemental mapping discloses the distribution of bismuth, lead, tin, and fluorine within PZPC, indicating the well-distribution of all the additives and binder in the PZPC electrode.

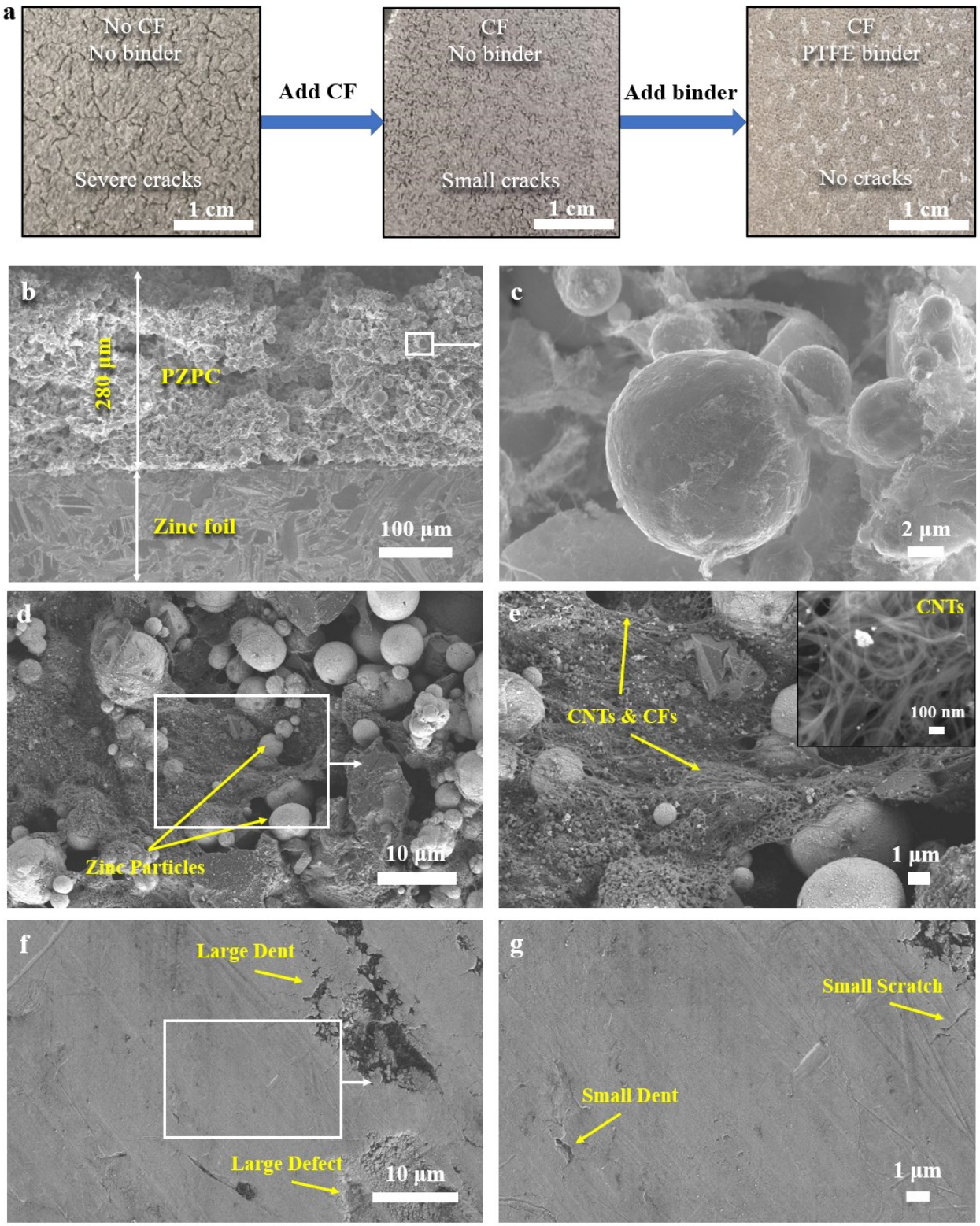

Figure 5.2 a) Image of PZPC with and without CF and PTFE binder. All electrodes contain zinc dust and 0.5 wt.% CNT. b) Cross-section SEM image of PZPC coated on a zinc foil substrate, and c) Cross-section SEM image of PZPC at high magnification for the selected region. d-e) Surface SEM images of PZPC and the magnified image for the selected area. f-g) Surface SEM image of zinc foil and the magnified image for the selected area.

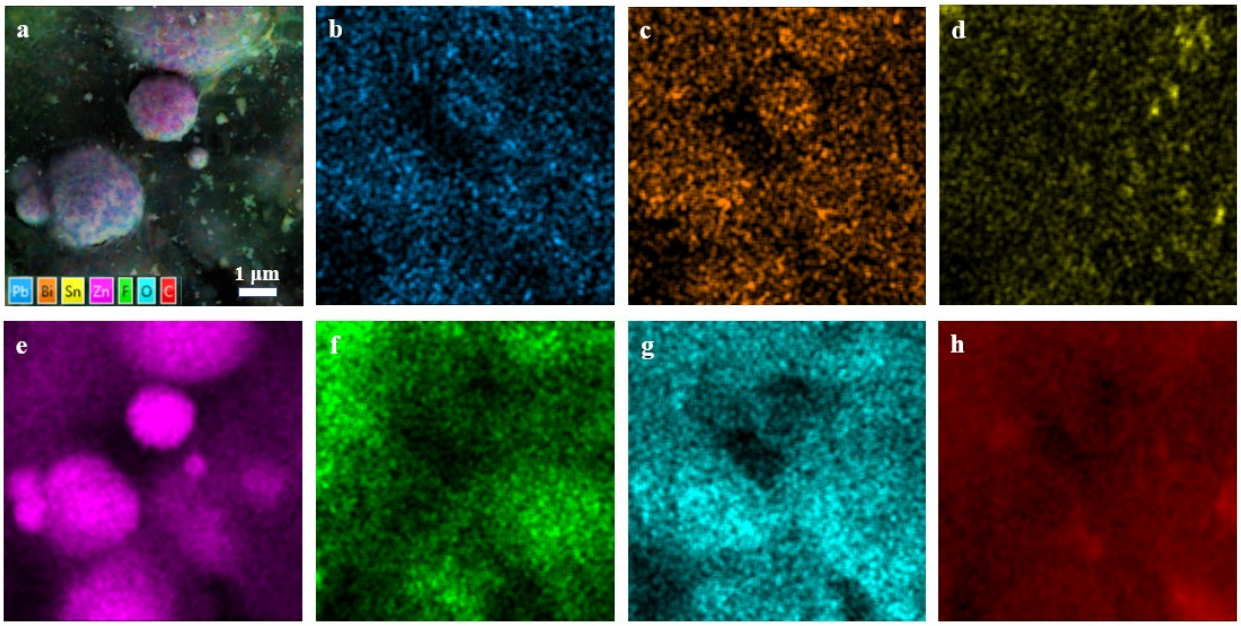

Figure 5.3 EDX mapping of PZPC (a); and the elemental mapping distribution of lead (b), bismuth (c), tin (d), zinc (e), fluorine (f), oxygen (g), and carbon (h).

To determine the porosity of the PZPC electrode, the saturation method is applied. The porosity is a property that defines the total volume of empty or pore space in a sample and is a fraction of void volume over the bulk volume. In this method, the PZPC was weighted before saturation (W_{dry}) and after full saturation with water as a wetting fluid (W_{sat}). The bulk volume of the PZPC (V_{bulk}) was determined by the thickness and the dimensions of the sample. By knowing the density of the DDI water, the pore volume can be estimated from the following equation.

$$\emptyset = \frac{V_{bulk} - V_{matrix}}{V_{bulk}} = \frac{(W_{sat} - W_{dry})/\rho_{fluid}}{V_{bulk}} = \frac{0.304g/1.00\,\frac{g}{cm^3}}{(4cm \times 4cm \times 0.031cm)} = 0.61 \pm 0.02$$

The porosity of the PZPC is estimated to be 61% and even a higher porosity measurement is expected if the test has been conducted in vacuum mode. Accordingly, in comparison with the rigid and non-porous zinc foil electrode, the highly porous PZPC has enough room for zinc deposition, especially for high areal-capacity ARZLBs.

N_2 adsorption-desorption measurement was conducted to investigate the pore structure and surface area of the PZPC based on BET theory. The existence of mesopores is confirmed by a typical hysteresis loop in a type-IV N_2 adsorption-desorption isotherm in Figure 5.4a. The shape of the hysteresis loop (type H3) indicates the existence of large amounts of slit-shaped pores. The pore size distribution (Figure 5.4b) reveals the dominance of large mesopores (> 10 nm) and macropores within the structure of PZPC. An average pore size of 18.05 nm and a total pore volume of 0.038 $cm^3\ g^{-1}$ were calculated for the PZPC (Table 5.1). These large mesopores and macropores in PZPC can promote the diffusion of zinc ions from the bulk electrolyte to the nucleation sites of zinc deposition at the electrode-electrolyte interface. Furthermore, the PZPC possesses a BET surface area of 8.41 $m^2\ g^{-1}$, which is 1.62×10^4 times higher than the surface area of the conventional zinc foil anode (0.00052 $m^2\ g^{-1}$, calculated by its weight and dimension). Therefore, the dramatic increase in surface area of the PZPC can provide abundant sites for zinc deposition during charging. The high surface area is also favorable for enhancing the contact area at the electrode-electrolyte interface and thus reducing the polarization effect.

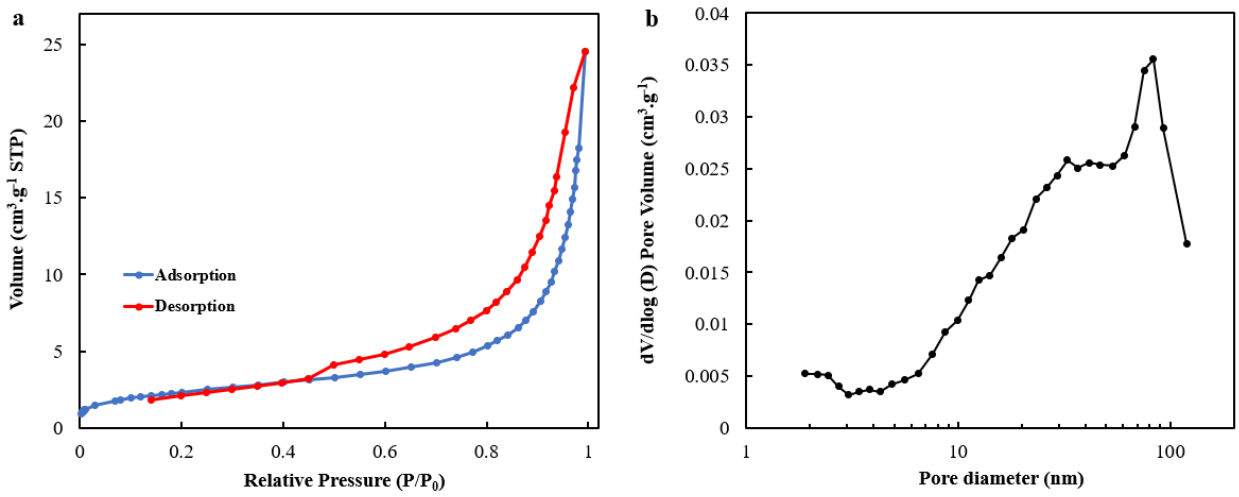

Figure 5.4 a) N_2 adsorption-desorption isotherm data and b) Pore size distribution for PZPC.

Table 5.1 The obtained data from N_2 adsorption-desorption isotherm for PZPC.

BET Surface area ($m^2 g^{-1}$)	Pore volume ($cm^3 g^{-1}$)	Adsorption average pore width (nm)
8.41	0.038	18.05

Consequently, these unique morphological features of PZPC not only significantly boost up the surface area for zinc deposition and the electrode-electrolyte interfacial area, but also can potentially regulate the current distribution and hence shorten the distance for ion and electron transfer. Therefore, the PZPC anode with a high surface area and porous structure can be a good replacement for conventional zinc anodes in high areal-capacity zinc/$LiMn_2O_4$ batteries for plentiful zinc depositions in every single cycle.

5.3.2 Half-cell study of the PZPC

To study the deposition of zinc on the surface of the PZPC electrode, a CA test was performed in a typical three-electrode setup, where PZPC and zinc foil electrodes with a geometric area of 2 cm^2 were used as the working electrode, and Pt wire and SCE were the counter and reference electrodes, respectively [43]. The current densities collected at -1.11 V vs SCE for both PZPC and zinc foil electrodes and are plotted against time in Figure 5.5. The current density for zinc foil anode was dropped rapidly to -9.3 mA cm^{-2} for 90 seconds and then the rate of decrease was reduced until the current density tends to be stable at -11.4 mA cm^{-2} after about 1000 seconds. The deposition current density for the PZPC was declined quickly for 5 seconds and reached -6.0 mA cm^{-2} and then it slowly approached -7.6 mA cm^{-2} after 20 minutes of monitoring. The rate of decrease in the current was much lower than that in the zinc foil electrode with a lower absolute value for the deposition current. It has been reported that a higher rate of decrease in the current density implies more dendrite growth on the surface of electrode [77]. Moreover, the higher absolute value of the deposition current density suggests fast nucleation and more dendrite growth for the

zinc foil electrode as a result of non-uniform zinc depositions and planar surface [77,109]. The PZPC electrode exhibited a much lower absolute value for deposition current which indicates its ability to suppress zinc dendrite formation. This is because the electrode has a higher surface area for zinc deposition and thereby provides more nucleation sites for zinc. Furthermore, the conductive network of CNTs and CFs inside the electrode can facilitate the homogenous current distribution in the zinc electrode, leading to less dendrite growth.

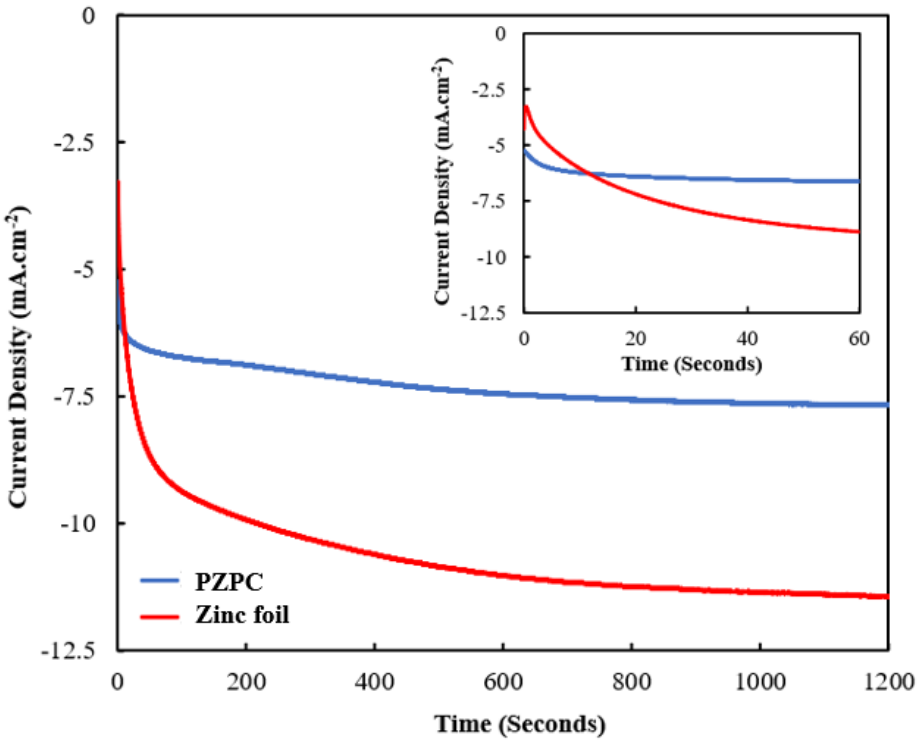

Figure 5.5 CA test of the PZPC and zinc foil electrodes in an aqueous electrolyte and using a three-electrode setup. Zinc, SCE, and Pt wire were used as the working, reference, and counter electrodes with an applied overpotential of -120 mV vs. zinc electrode.

The stability of zinc foil and PZPC was investigated using symmetric zinc battery cells in 2.0 mol L^{-1} $ZnSO_4$ and 1.5 mol L^{-1} Li_2SO_4 aqueous electrolyte (Figure 5.6). The symmetric zinc battery with zinc foil electrode was short-circuited in less than 50 hours of constant-current cycling, while the battery with PZPC showed an over three-fold lifespan, lasting for 158 hours. As seen in the inset images of Figure 5.6, the shortened lifespan of the battery is accompanied by the

enlarged voltage-time curves due to the sluggish kinetics of Zn^{2+} and high polarization effect [138]. The improved cycling performance is associated with the highly porous structure of the PZPC. Besides, the much lower voltage hysteresis at the same current density for the battery with PZPC compared to zinc foil (23 mV vs. 79 mV) is attributed to a considerably higher contact area at the electrode-electrolyte interface and thus improved diffusion kinetics of Zn^{2+} from the electrolyte into the interface layer. Also, a drastic reduction of polarization at the discharge platform from 19.2 mV with zinc foil to 8.6 mV with PZPC electrode is observed. The lower overall voltage hysteresis and reduced polarization at the discharge curve confirm the stable and homogenous zinc plating [138].

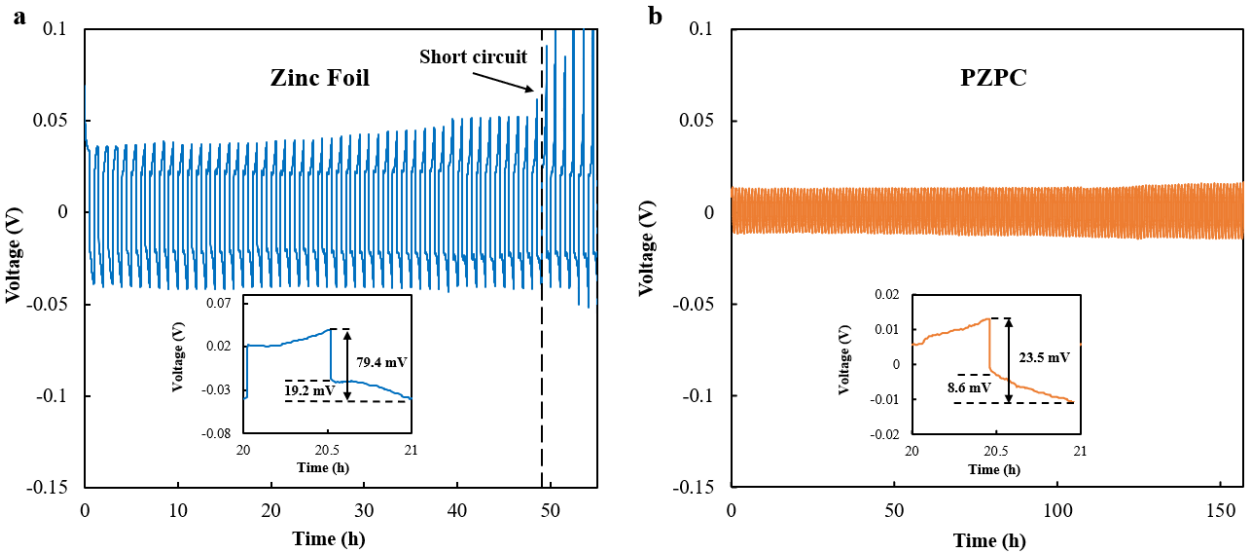

Figure 5.6 Galvanostatic zinc plating/stripping at 1 mA cm^{-2} using symmetric zinc battery cell constructed with: a) zinc foil, and b) PZPC. The electrolyte was an aqueous solution of 2.0 mol L^{-1} $ZnSO_4$ and 1.5 mol L^{-1} Li_2SO_4. The inset figures are the magnified voltage-time curves with labeling the voltage hysteresis and the polarization potential for the discharge curve. The dashed line represents the region after short-circuiting.

5.3.3 Electrochemical performance of zinc/$LiMn_2O_4$ battery using PZPC anode

After the assembly of zinc/$LiMn_2O_4$ battery with PZPC anode and 3D-CNT cathode, the OCV profile of a fully charged cell up to 2.1 V at 0.2 C-rate with respect to time for 24 hours is plotted in Figure 5.7. A higher OCV value is corresponding to less self-discharge for battery [109].

OCV value of 1960 mV is observed for the battery after 24 hours with PZPC compared to 1940 mV with zinc foil anode, suggesting lower self-discharge and better storage property with the PZPC anode due to corrosion reduction additives.

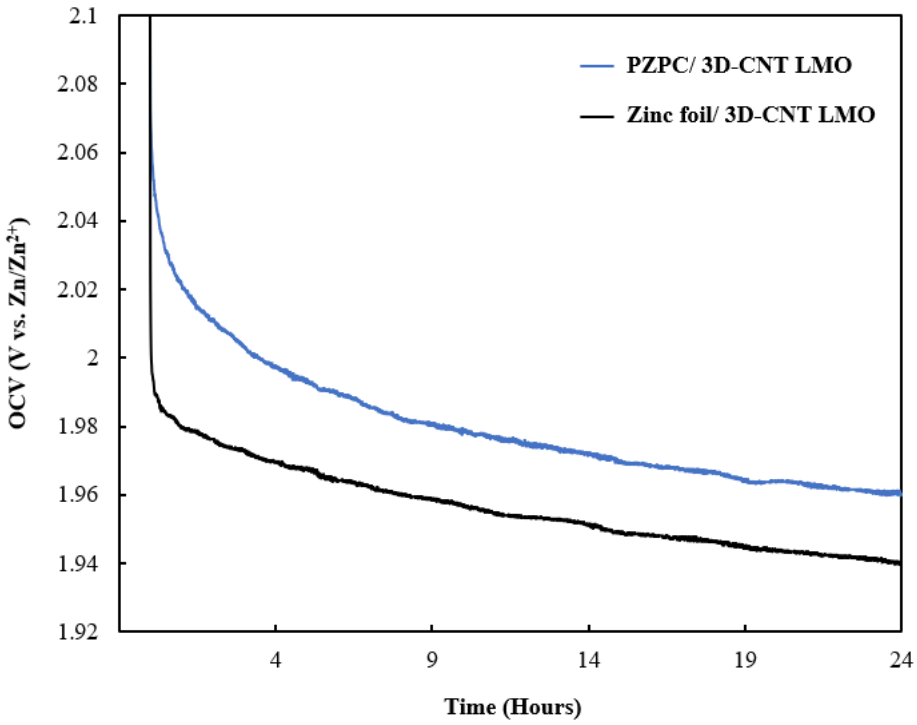

Figure 5.7 OCV comparison of fully charged zinc/$LiMn_2O_4$ battery using PZPC anode and zinc foil anode during 24 hours rest period. The cathode was a 200 µm thick 3D-CNT electrode.

The rate capability of the zinc/$LiMn_2O_4$ battery using PZPC and zinc foil anodes from C/15 to 2C rate is shown in Figure 5.8. The 3D-CNT electrodes with 200 µm and 400 µm thickness and high active material loadings (32 mg cm^{-2} and 63 mg cm^{-2}) were used as the cathode. The discharge capacity at C/15 up to C/2 for the battery using the PZPC anode was almost the same as that of the battery using the zinc foil anode. However, at 1C and 2C rates, the battery with PZPC anode outperformed the battery with zinc foil anode in terms of rate capability. For example, the discharge capacity of the battery at 1C rate with 400 µm thick cathode and using PZPC anode is approximately 86 mAh g^{-1}, which is 10.2% higher than that for the zinc foil anode (78 mAh g^{-1}).

Such superior rate performance is attributed to the high contact area of the PZPC anode with electrolyte, relatively low local current density, and hence the facilitated zinc plating/stripping process. Local current density can be reduced on a porous zinc electrode with a high surface area compared to zinc foil with a planar surface, assisting in applying higher surface current densities on the PZPC anode [38].

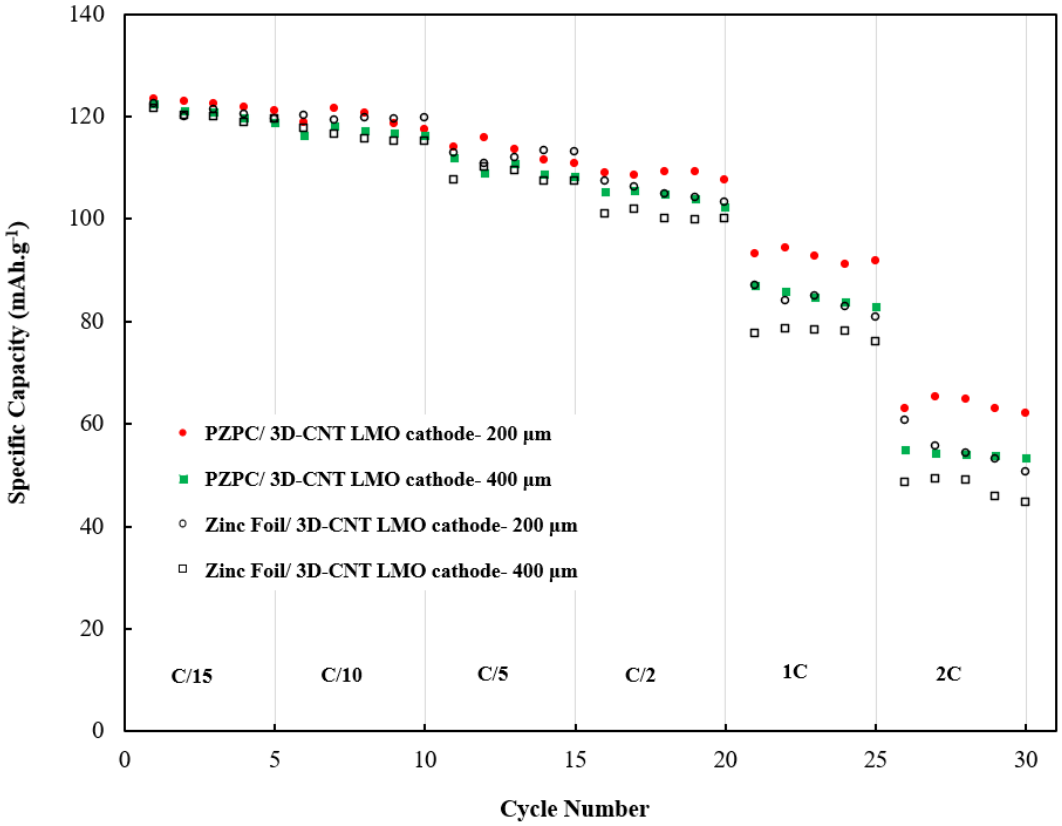

Figure 5.8 Rate capability of the zinc/$LiMn_2O_4$ battery using PZPC and zinc foil anode. The cathodes were 200 µm and 400 µm thick 3D-CNT electrodes. The electrolyte was an aqueous solution of 2.0 mol L^{-1} $ZnSO_4$ and 1.5 mol L^{-1} Li_2SO_4.

The electrochemical performance of zinc/$LiMn_2O_4$ battery with PZPC anode and 200 µm thick 3D-CNT cathode is illustrated in Figure 5.9. The battery with the PZPC anode exhibited a high specific capacity of 122.5 mAh g^{-1} at the 1st cycle. More importantly, the battery lasted for 500 cycles before short-circuiting and still maintained 73% of its capacity after 500 cycles. The average for CE was 99.3% when PZPC anode was employed (Figure 5.9a), while it was roughly

98.6% for the zinc/$LiMn_2O_4$ battery with zinc foil anode (Figure 4.9a). The improved CE can be attributed to the mitigated hydrogen gassing on the anode side via employing the corrosion reduction additives in the structure of the PZPC [85]. The charge/discharge profiles of the zinc/$LiMn_2O_4$ battery at different cycle numbers are plotted in Figure 5.9b. By increasing the cycle number, the VE of the battery was declined from 94% in the initial cycles to 91% and 88% at 400th and 500th cycles, which is likely to be related to the growing resistance as cycling progressed.

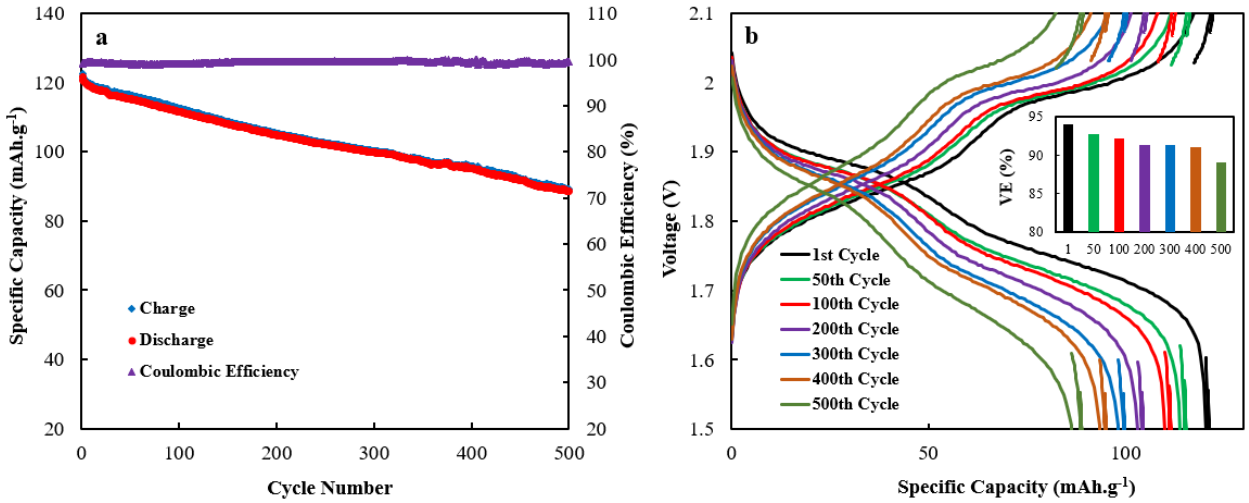

Figure 5.9 Electrochemical performance of zinc/$LiMn_2O_4$ battery using 200 µm thick 3D-CNT cathode, PZPC anode, and 2.0 mol L^{-1} $ZnSO_4$ and 1.5 mol L^{-1} Li_2SO_4 aqueous electrolyte: a) Specific capacity vs. cycle number, b) Charge/discharge profiles at various cycle numbers. The inset is the histogram plot of VE vs. cycle number.

The electrochemical performance of the PZPC anode was compared with the zinc foil anode in the zinc/$LiMn_2O_4$ battery (Figure 5.10). As observed in the charge/discharge profiles, the VE of the battery with the PZPC anode enhanced significantly compared to that with the zinc foil anode. For comparison, the VE with the PZPC anode was 94% and 92% at the initial and the 100th cycle, while the corresponding values with the zinc foil anode were 87% and 86%. The high VE of the battery means that the gap between charge and discharge profiles is small due to low resistivity. EIS data was obtained to elucidate the difference between the resistance of the batteries using PZPC and zinc foil anodes (Figure 5.10c-d). As seen, the bulk resistance of the battery with PZPC

anode was remarkably lower than the zinc foil anode at the 1st (1.97 Ω vs. 2.69 Ω) and the 100th cycle (3.50 Ω vs. 4.33 Ω). Besides, the smaller diameter of the semicircle in the battery with the PZPC anode indicates lower charge transfer resistance. Therefore, the results are in agreement with the higher VE of the battery with the PZPC compared to the zinc foil anode. The superior VE and the lower resistance of the battery with PZPC anode can be due to the highly conductive zinc electrode and the large area of accessible electrode-electrolyte interface as a result of 3D and highly porous structure [40].

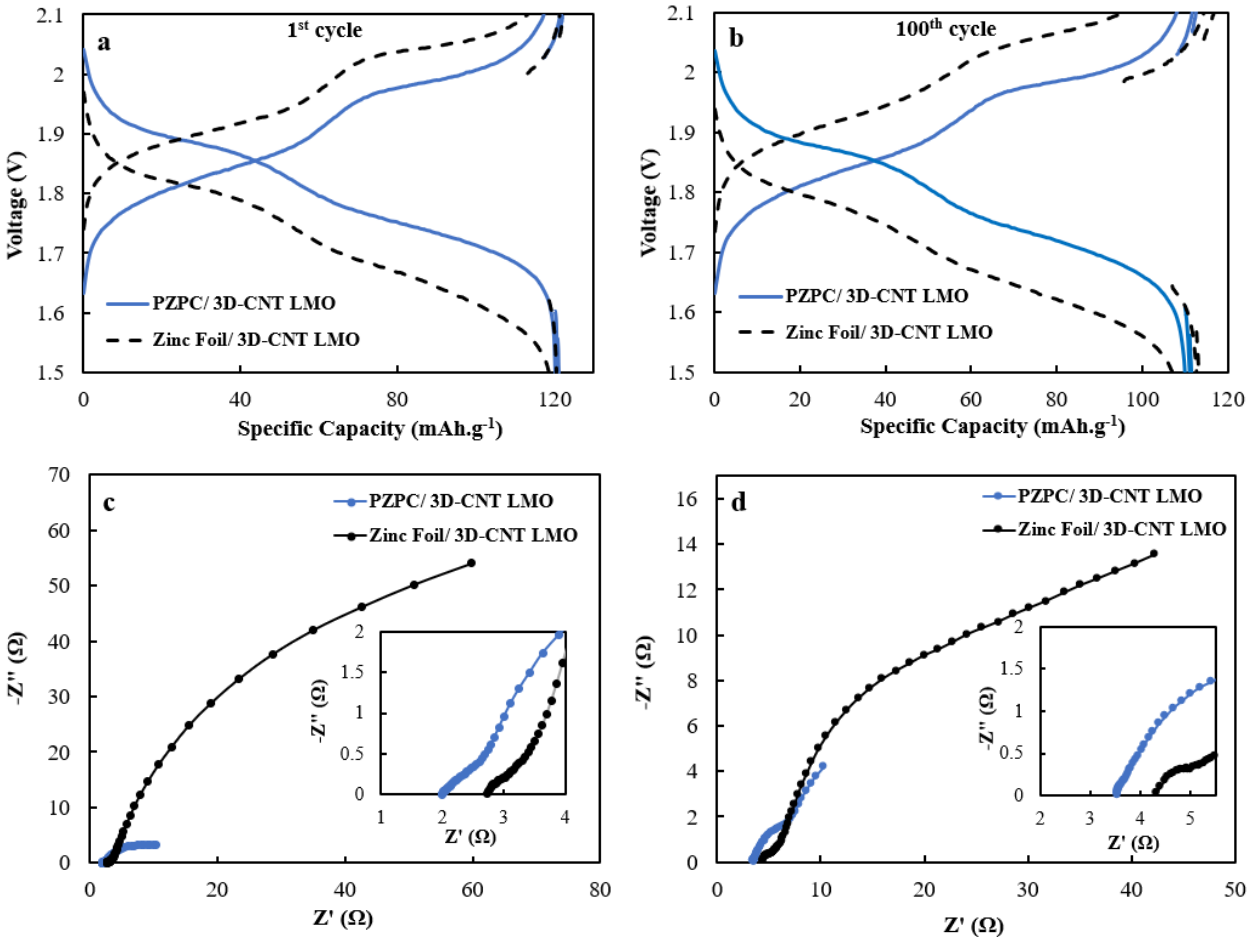

Figure 5.10 a-b) Voltage-capacity profile comparison of zinc/$LiMn_2O_4$ battery using PZPC and zinc foil anodes and 200 µm thick 3D-CNT cathode at the initial cycle (a) and the 100th cycle (b). c-d) Comparison of EIS profiles of zinc/$LiMn_2O_4$ battery with PZPC and zinc foil anodes and using 200 µm thick 3D-CNT cathode at the initial cycle (c) and the 100th cycle (d). The insets are EIS data of the battery at the high-to-medium frequency region.

Similar to the zinc/$LiMn_2O_4$ battery with zinc foil anode and 3D-CNT cathode, the batteries with PZPC anode and 3D-CNT cathodes (200 µm and 400 µm) also delivered high areal capacities of 3.6 mAh cm^{-2} and 7.2 mAh cm^{-2}, respectively (Figure 5.11). However, the durability of zinc/$LiMn_2O_4$ batteries is substantially extended from 100 cycles with zinc foil anode to 500 cycles with PZPC anode for 200 µm 3D-CNT cathode and from 50 cycles to over 220 cycles before short-circuiting for 400 µm 3D-CNT cathode. Accordingly, the lifespan of high areal-capacity zinc/$LiMn_2O_4$ batteries with PZPC anode can be improved by up to 5 times compared to that with the conventional zinc foil anode.

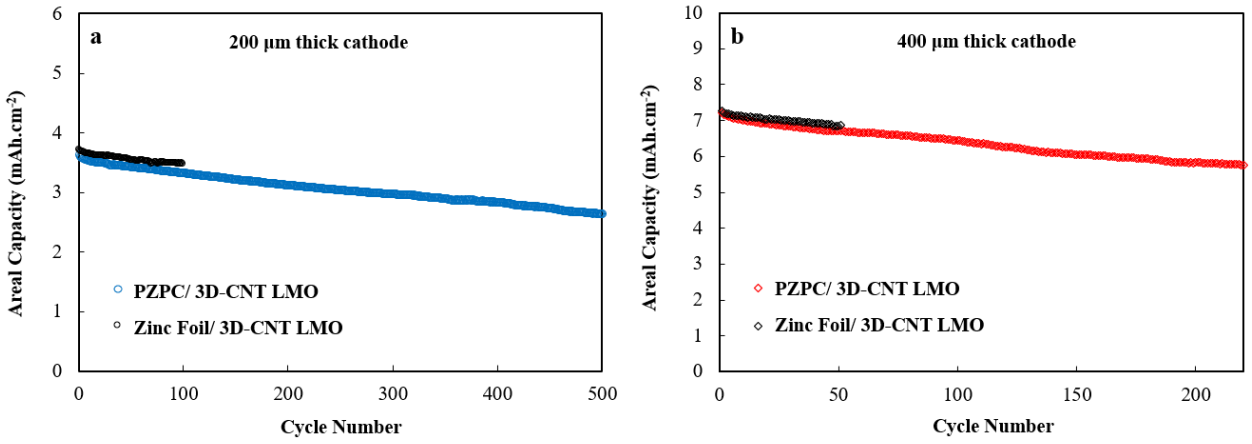

Figure 5.11 Cycle life comparison of zinc/$LiMn_2O_4$ battery using PZPC and zinc foil anodes with: a) 200 µm thick 3D-CNT cathode, and b) 400 µm thick 3D-CNT cathode.

The morphology of PZPC and conventional zinc foil electrode before and after battery cycling are also characterized and compared in Figure 5.12. As seen, the surface of the zinc foil anode is planar and non-porous, while the PZPC anode has a high surface area suitable for ample zinc deposits. The morphology of zinc deposits after only 100 cycles showed sharp and needle-like tips that can penetrate through the separator, while zinc deposits in PZPC after 500 cycles have a dense and layered structure with flattened edges. The high surface area of the PZPC can reduce the local current density, leading to slower zinc deposition. Accordingly, a more

homogenous and compact zinc deposition is realized with 3D and porous structured zinc anode [165]. Benefiting from this improved morphology, the durability of the battery was prolonged significantly compared to the battery with zinc foil anode.

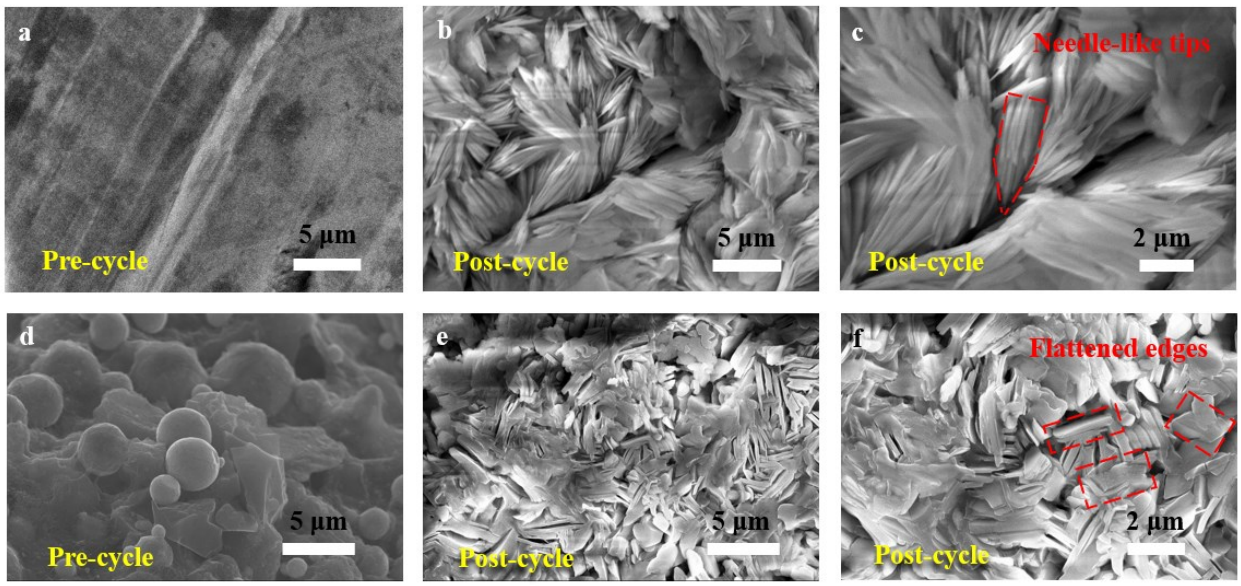

Figure 5.12 a-c) Surface SEM image of zinc foil before cycling and after 100 cycles in zinc/$LiMn_2O_4$ battery with 200 µm thick 3D-CNT cathode. d-f) Surface SEM images of PZPC before cycling and after 500 cycles in zinc/$LiMn_2O_4$ battery with 200 µm thick 3D-CNT cathode.

Pre-cycled and post-cycled zinc foil and PZPC electrodes were also analyzed by XRD and the obtained profiles are shown in Figure 5.13. The XRD data of the pre-cycled zinc foil and PZPC confirms the presence of peaks associated with the zinc metal. After battery cycling, several new peaks evolved in the zinc foil which is related to the formation of ZnO, $Zn(OH)_2$, $ZnSO_4.7H_2O$, and $Zn_4SO_4(OH)_6$. The peaks corresponding to 002, 004, and 006 planes of $Zn_4SO_4(OH)_6.3H_2O$ are located at 9.6, 19.1, and 28.6 degrees, respectively. $Zn_4SO_4(OH)_6$ forms on the surface of the zinc electrode as a side reaction between Zn^{2+}, SO_4^{2-} and OH^-, which could block the efficient diffusion of Zn^{2+} [166]. The following reactions can lead to the formation of $Zn_4SO_4(OH)_6$.

$$2H_2O + 2e^- \leftrightarrow H_2 \uparrow + 2\,OH^- \quad (5.1)$$

$$4Zn^{2+} + 6OH^- + SO_4^{2-} + xH_2O \leftrightarrow Zn_4SO_4(OH)_6.xH_2O \quad (5.2)$$

The unwanted HER is accompanied by the production of OH^-. Since HER can be suppressed by the corrosion reduction additives inside the PZPC, the production of OH^- and hence the peak intensities related to the formation of $Zn_4SO_4(OH)_6$ was minimal. For PZPC anode, several new peaks including peaks associated with ZnO at 33.7 and 58.7 degrees are observed after battery cycling. Furthermore, the different peak intensity of metallic zinc in the post-cycled zinc foil and PZPC reflects different development of zinc during battery cycling. The peaks at 100 and 110 planes of zinc surface support vertical zinc dendrite growth, while the peak at 002 surface supports flat zinc depositions [109]. For the zinc foil anode, the relative peak intensity of 002 to 100 was 0.93 before cycling and it declined to 0.76 after 100 cycles, indicating the development of zinc dendrite growth. As to the PZPC anode, the peak intensity ratio of 002 to 100 planes was 1.12 before cycling and it increased to 1.72 after extensive 500 cycles. This is very clear evidence that zinc dendrite is suppressed by using the PZPC anode, leading to prolonged cycle life.

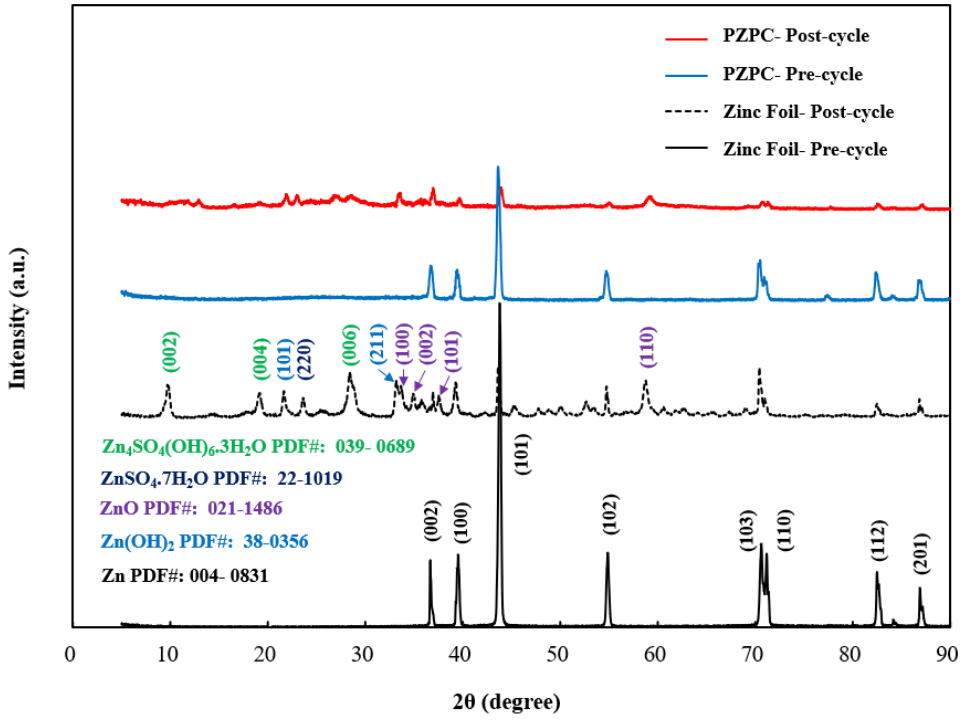

Figure 5.13 XRD patterns of pre-cycled and post-cycled zinc foil and PZPC electrodes. The post-cycled XRD profiles for zinc foil and PZPC anodes are after 100 and 500 cycles, respectively.

5.3.4 Mechanism of PZPC

To help understand the mechanism of zinc deposition, the schematic of PZPC and conventional zinc electrodes in an aqueous electrolyte is illustrated in Figure 5.14. As observed in the schematic of the conventional zinc electrode (Figure 5.14a), the zinc dendrites tend to grow through the electrolyte depth where the concentration of zinc ions is high enough. Besides, the zinc deposition is not homogenous as a result of non-uniform current distribution throughout the zinc electrode. The inhomogeneous electric current distribution can intensify the zinc dendrite growth during extended battery cycling [39]. Another performance-limiting problem is the hydrogen generation on the electrode surface. As discussed in Chapter 2, hydrogen evolution is thermodynamically favorable in aqueous electrolytes. The electrochemical potential of the HER is higher than the zinc metal. Consequently, the electrons can be consumed by protons rather than participating in the main electrochemical reaction, affecting the CE and reversibility of the zinc anode. Furthermore, hydrogen evolution can cause zinc corrosion and shape change of the zinc electrode, worsening the topography of the zinc surface and zinc electrodeposition.

The water-zinc reactions that occur in an acidic electrolyte during zinc corrosion were previously expressed in Equation 2.15. The zinc electrode can be corroded and the released electrons are consumed in the parasitic side reaction, resulting in hydrolysis of water and low reversibility of the zinc electrode. The competitive water-zinc reactions can also occur during rest periods which is referred to as self-discharge. The hydrogen generation from hydrolysis of water molecules can cause water depletion and build up internal pressure in a sealed battery, leading to swelling and blow-out [43]. Furthermore, consumption of protons increases the electrolyte pH, altering the optimal environment for the zinc/$LiMn_2O_4$ battery.

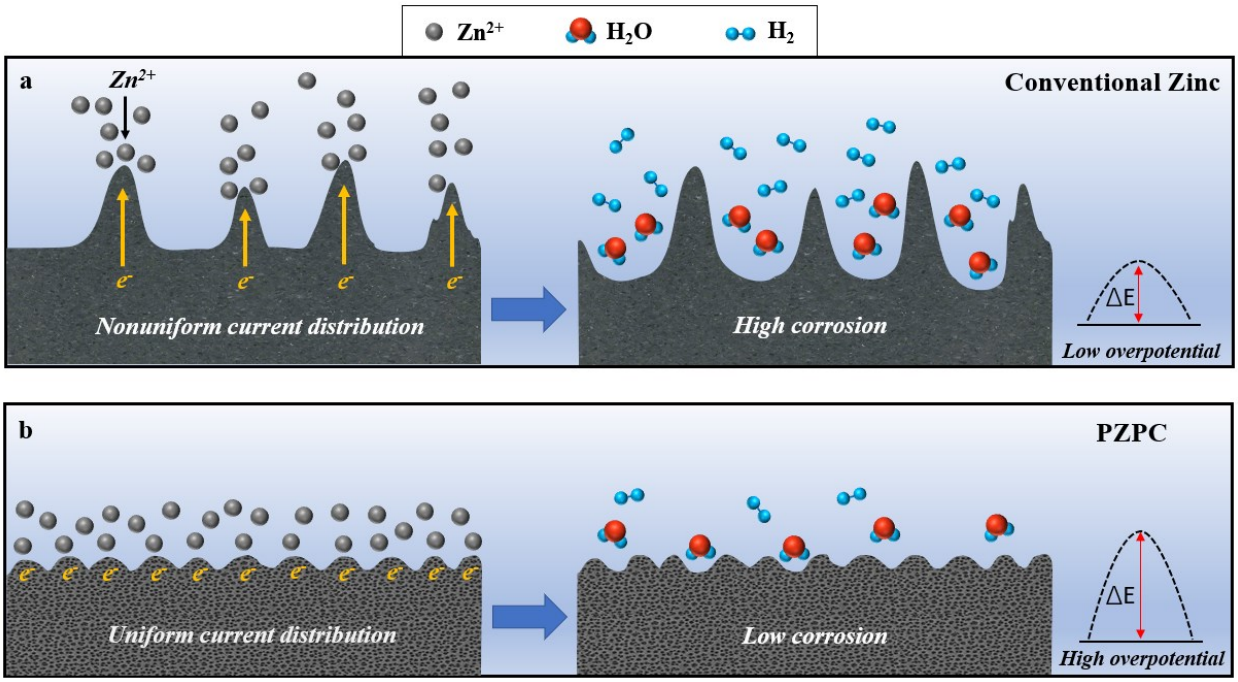

Figure 5.14 Schematic illustration of the two different zinc electrodes in an acidic aqueous electrolyte: a) conventional zinc, and b) PZPC.

Figure 5.14b represents the schematic of the PZPC electrode in an aqueous electrolyte. The conductive network of the PZPC facilitates uniform current distribution and thus homogenous zinc electrodeposition [165]. Furthermore, the highly porous structure accommodates further space for zinc deposition. The incorporation of tin sulfate, lead acetate, and bismuth oxide additives inside the PZPC increases the hydrogen evolution overpotential and improves the corrosion resistance of the electrode. Therefore, these additives are aimed to reduce hydrogen gassing and facilitate the long shelf life of the battery. To evaluate the effect of each component on the battery performance, the cycling stability of the PZPC with and without CF, PTFE binder, and additives is compared in Figure 5.15. The zinc/$LiMn_2O_4$ battery fabricated with 400 µm thick 3D-CNT cathode and PZPC anode without having any CF, binder, and additives lasted for roughly 50 cycles, while the addition of CF or binder increased the durability to nearly 75 and 90 cycles. Moreover, the battery with both CF and biner inside the PZPC structure lasted for 110 cycles. The shortened cycle life of

PZPC without binder and CF is due to the poor mechanical integrity of the electrode composite as previously observed in Figure 5.2a. Furthermore, the additive included PZPC anode doubled the cycle life of the battery compared to the non-additive one, reaching roughly 220 cycles. The effect of corrosion reduction additives is the main reason for the improved lifespan. Tin sulfate, lead acetate, and bismuth oxide increase the overpotential for HER [85,96,97]. Consequently, the rate of water-induced corrosion reaction can be reduced substantially, leading to improved zinc reversibility and topography.

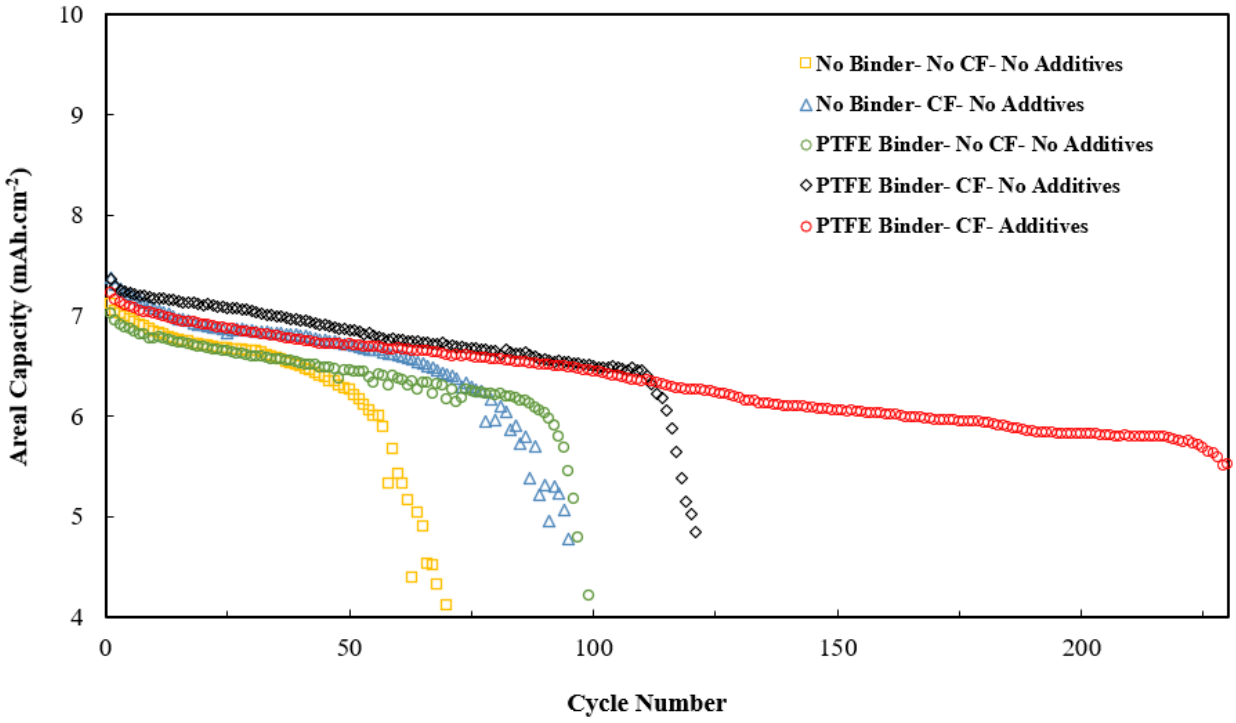

Figure 5.15 Cycle life comparison of zinc/$LiMn_2O_4$ battery with 400 µm thick 3D-CNT cathode and using different types of zinc electrodes including PZPC with and without binder, CF, and additives. The battery with a PZPC anode containing binder, CF, and additives exhibited the highest cycle life.

Overall, the PZPC has several advantages over the conventional zinc electrode. First, the highly porous and 3D skeleton of the PZPC induces the zinc ions to plate within the void space. The porous structure also allows the release of unwanted produced hydrogen gas. Second, the interconnected and reinforced networks of CNTs and CFs retain the mechanical integrity of the

composite during battery cycling and improve the electrical conductivity. Third, the functional additives inside the composite are aimed to increase the hydrogen evolution overpotential, thereby reducing the corrosion rate and shape change of the zinc electrode.

5.4. Summary

The areal capacity of the zinc/$LiMn_2O_4$ battery improved significantly with ultra-thick 3D-CNT cathode by as high as 13.5 mAh cm^{-2}. However, the cycle life of the battery is limited due to severe dendrite formation and fatal short-circuiting stemming from the zinc anode. The zinc dendrite could be a serious problem at high areal capacity and active material loading due to pronounced zinc deposition and large concentration gradient. For example, the cycle life of zinc/$LiMn_2O_4$ battery using zinc foil anode was only about 50 cycles at 7.3 mAh cm^{-2} areal capacity, which offsets the application of high areal capacity zinc/$LiMn_2O_4$ battery for commercialization. In this study, the zinc foil electrode was replaced by a novel PZPC anode to extend the cycle life of the battery. The enlarged electroactive surface area of the PZPC anode ensures uniform distribution of electric current and minimizes the zinc nuclei size effectively, facilitating homogenous zinc deposition and hence reducing dendrite growth. Moreover, the functional additives inside the PZPC increase the overpotential of HER and improve the corrosion resistance of the electrode. Consequently, zinc/$LiMn_2O_4$ battery cells manufactured by the PZPC electrodes exhibit a much longer cycle life, by up to 5 times, compared to zinc foil anode. For example, the durability of zinc/$LiMn_2O_4$ battery using PZPC at a high areal capacity of 7.2 mAh cm^{-2} is extended to 220 cycles. Therefore, the construction of the highly porous and conductive PZPC anode offers the opportunity to effectively prolong the lifespan of ARZLBs, even at high areal capacities. Besides significant achievement in the cycle life, the use of PZPC also improves

the rate capability and VE and lowers the self-discharge of the battery due to the high electrode-electrolyte contact area and corrosion reduction additives.

6. Development of gel electrolyte for high areal-capacity zinc/$LiMn_2O_4$ battery

6.1. Introduction

As discussed in Chapter 5, the use of PZPC anode prolongs the cycle life of high areal-capacity zinc/$LiMn_2O_4$ battery by up to 5 times compared to the zinc foil anode. Although the incorporation of PZPC is an effective approach to suppress the dendrite formation, the water-zinc reactions in conventional aqueous electrolyte systems will inevitably induce the corrosion of the zinc electrode. As explained in Chapter 2, zinc metal can be corroded in aqueous electrolytes by the competitive HER, worsening the reversibility of the zinc electrode. Furthermore, the generated hydrogen gas leads to increased internal pressure and resistance in a sealed battery pack or water depletion in an open-cell configuration [43]. More importantly, the high corrosion rate of the zinc electrode causes shape change and electrode densification, leading to inhomogeneous current distribution and intensified dendrite growth. Accordingly, the hydrogen evolution-induced corrosion reaction negatively affects the durability of aqueous zinc-based batteries.

According to the literature [110,119,122], the conventional electrolyte system can be improved for aqueous batteries by adding gelling agent into the liquid electrolyte to form a gel-type electrolyte. There are various types of gelling agents including xanthan gum [116], polyvinyl alcohol [117,118], gelatin [119], cross-linked CMC [115], and silica [103,110], all of which showed promising results in aqueous batteries. Gel electrolytes inherit the advantage of high ionic conductivity from aqueous electrolytes and high safety from solid-state electrolytes [109]. Although gel electrolytes improve the water retention, flexibility, and safety of the battery [111,113,115,123], their effect on the durability of

zinc-based aqueous batteries specifically at high areal capacities with high loading of cathodic active materials still remains unexplored.

In the present chapter, a low-cost gel-type electrolyte system is developed for high-areal capacity zinc/$LiMn_2O_4$ battery by incorporation of fumed silica (FS) gelling agent inside aqueous electrolyte to effectively suppress the corrosion rate of the zinc and prolong the lifespan of the battery. The unique properties of the FS-gel electrolyte bring several advantages for aqueous zinc/$LiMn_2O_4$ batteries. Firstly, FS can immobilize water molecules through strong chemical bonding with water molecules [110,111], restraining the water-zinc reactions. Secondly, benefiting from mitigated water-induced corrosion reactions and higher mechanical strength of thixotropic FS-gel electrolyte, zinc dendrite growth is suppressed. Thirdly, the electrolyte contributes to lower the energy runway from the battery by improving the OCV stability and reducing the float charge current. Lastly, the water retention capability of the electrolyte system is improved with immobilized FS-gel electrolyte [109,111], providing an opportunity for leak-proof and maintenance-free ARZLBs for commercialization.

The high areal-capacity zinc/$LiMn_2O_4$ batteries were assembled with the FS-gel electrolyte to evaluate its effects on zinc dendrite formation and durability of the battery. The corrosion rate of the zinc metal decreases by almost half as compared to the aqueous electrolyte system. Moreover, the FS-gel electrolyte prolongs three-fold the cycle life of a high areal capacity zinc/$LiMn_2O_4$ battery compared to the aqueous electrolyte system. It is also investigated that the combination of FS-gel- electrolyte and PZPC anode can even further extend the lifespan of high areal capacity zinc/$LiMn_2O_4$ by at least six times compared to that with aqueous electrolyte and zinc foil anode. Accordingly, the proposed FS-gel electrolyte is a low-cost and scalable solution

to effectively protect zinc anode from corrosion and prolong the cycle life of high areal-capacity zinc/$LiMn_2O_4$ batteries.

6.2. Experimental method

6.2.1 Preparation of FS-gel electrolyte

The electrolyte was prepared by mixing FS with a conventional aqueous electrolyte system. Typically, an aqueous electrolyte was firstly prepared by dissolving $ZnSO_4.7H_2O$ (Sigma Aldrich) and $Li_2SO_4.H_2O$ (Sigma Aldrich) salts inside the DDI water and adjusting the pH at 5. The prepared aqueous electrolyte contains 2.0 mol L^{-1} $ZnSO_4$ and 1.5 mol L^{-1} Li_2SO_4. Then, a certain amount of FS powder (Sigma Aldrich) with a particle size of 14 nm was added into the aqueous electrolyte, reaching a designed FS concentration of 2-6 wt.%. The electrolyte was vigorously stirred for 2 hours at 60 °C to form the thixotropic FS-gel electrolyte. Then, the AGM (NSG Group) separator with the porosity over >90% and the thickness of 400 μm and the Celgard (5550) separator with the average pore size of 0.064 μm and the porosity of 55% were impregnated in such FS-gel electrolyte. After the degassing of the electrolyte under the vacuum, the separators were stayed for 12 hours prior to the cell assembly to guarantee the full absorption of gel electrolyte into the separators.

6.2.2 Preparation of zinc/$LiMn_2O_4$ battery

For zinc/$LiMn_2O_4$ battery fabrication, thick 3D-CNT cathode, zinc foil or PZPC anode, and FS-gel electrolyte were used. Preparation of 3D-CNT $LiMn_2O_4$ cathode and PZPC anode were followed as previously reported procedures in experimental sections 4.2.1 and 5.2.1, respectively. AGM and Celgard were used as separator layers (pre-soaked inside the FS-gel) in between the cathode and anode. The current collectors for the cathode and anode were graphite foil and thin

zinc foil (150 μm), respectively. Eventually, the prepared battery cells were fastened by bolts and nuts and sealed using parafilm-M self-sealing films.

6.2.3 Electrochemical measurements

Linear polarization data was obtained to plot the Tafel curves and to measure the corrosion current of the zinc in different electrolyte systems. The data were recorded in a three-electrode setup using SCE, Pt wire, and zinc foil as the reference, counter, and working electrodes, respectively. The linear potential was applied from -0.02 V to +0.02 V vs. OCV with a scan rate of 0.1 mV s^{-1} using VSP-300 Biologic instrument. The conductivity values for different electrolyte solutions were measured using the Oakton conductivity meter (COND 6+ model). Cyclic voltammetry (CV) of zinc redox reaction in different electrolyte systems was conducted using a three-electrode setup to investigate the reversibility of zinc deposition/dissolution in different electrolyte systems. Glassy carbon electrode (GCE), Pt wire, and SCE were employed as the working, counter, and reference electrodes. The static GCE was used to deposit zinc on its surface at a scan rate of 10 mV s^{-1} and a potential sweep from 0 to -1.3 V (vs. SCE). CV of zinc/$LiMn_2O_4$ battery using $LiMn_2O_4$ cathode as the working electrode and zinc anode as the reference and counter electrodes was obtained on VSP-300 Biologic potentiostat at 0.1 mV s^{-1} scan rate and between 1.5 V and 2.1 V (vs. zinc). The test was conducted to identify the reduction and oxidation peaks of the 3D-CNT $LiMn_2O_4$ cathode in FS-gel and aqueous electrolyte systems. The float charge current performance of the zinc/$LiMn_2O_4$ battery was performed by a LAND battery tester (LANHE, CT2001A) at constant-current mode from 1.5 V to 2.1 V (vs. Zn/Zn^{2+}) at 0.2 C-rate, followed by constant-voltage charging at 2.1 V for 24 hours, and finally constant-current discharging the battery to 1.5 V at 0.2 C-rate. 1C is defined as 120 mAh g^{-1}, which is the practical specific capacity of $LiMn_2O_4$ active material. The float charge current is used to evaluate the

battery functioning in terms of energy retention at nearly full SOC. The stability of OCV was monitored for 24 hours (without charging and discharging) after the battery was charged by the constant-current mode at 0.2 C-rate. After 24 hours of the rest period, the battery was constant-current discharged to 1.5 V at 0.2 C-rate. The cycling performance of assembled zinc/$LiMn_2O_4$ battery cells was evaluated by a 3-step galvanostatic charge/discharge testing protocol as explained in 4.2.3 using a LAND battery tester. The cut-off voltage of the battery was set between 1.5 V to 2.1 V. The EIS data of the zinc/$LiMn_2O_4$ battery was recorded in a two-electrode setup consisting of the zinc electrode as the reference and counter electrode and $LiMn_2O_4$ cathode as the working electrode at potentiostat mode. The scan rate was set from 1000 kHz to 0.1 Hz at 5 mV sinus amplitude using VSP-300 Biologic instrument. All tests were performed at room temperature.

6.2.4 Physiochemical characterization

The morphology of the 3D-CNT cathode and PZPC anode inside zinc/$LiMn_2O_4$ battery with FS-gel electrolyte after battery cycling and washing with DDI water were imaged using LEO FESEM1530 SEM. The XRD patterns of the post-cycled 3D-CNT cathode and PZPC anode were obtained using Rigaku MiniFlex 600 (40 kV, 25 mA) to analyze the peak change after battery cycling with FS-gel electrolyte.

6.3. Results and discussion

6.3.1 Optimization of FS-gel electrolyte

To optimize the FS concentration in the gel electrolyte, linear polarization data of zinc foil electrodes in different FS-gel electrolytes were collected to investigate the corrosion behavior of the electrodes. The corresponding Tafel curves were plotted in Figure 6.1a. The corrosion current

densities of the zinc foil electrodes in the different electrolyte systems were calculated from Tafel curves and compared in Figure 6.1b. The corrosion current density of the zinc foil significantly decreased from 18.75 μA cm^{-2} in the aqueous electrolyte to 9.24 μA cm^{-2} in the 2 wt.% FS-gel electrolyte. Therefore, the addition of the FS thickening agent effectively reduces the corrosion reaction on the zinc surface. The corrosion current further decreased to 7.86 μA cm^{-2} and 7.38 μA cm^{-2} when FS increased to 4 wt.% and 6 wt.% in gel electrolyte, respectively. It is noted that the further increase of FS from 4 wt.% to 6 wt.% leads to only a slight reduction in the corrosion current (~ 6.1%). This suggests that 4 wt.% FS is sufficient enough to alleviate zinc corrosion. On the other hand, the ionic conductivities of the gel electrolyte were also measured and plotted in Figure 6.1b. Clearly, the introduction of FS gradually reduced the conductivity of the electrolyte, decreasing from 73.7 to 68.1 mS cm^{-1} for the aqueous electrolyte and 6 wt.% FS-gel electrolytes. Given the fact that 4 wt.% FS-gel electrolyte still maintains over 95% conductivity of the aqueous electrolyte, 4 wt.% FS was selected as the optimum concentration for the gel electrolyte.

The zinc redox reaction in the aqueous electrolyte and 4 wt.% FS-gel electrolytes were further investigated by CV and the obtained curves were compared in Figure 6.1c. The zinc deposits at the surface of GCE below -1.04 V (vs. SCE) in the aqueous electrolyte and before -1.01 V (vs. SCE) in the FS-gel electrolyte. A nucleation loop was formed at the end of the cathodic scan. Anodic peaks at the reverse scan represent zinc stripping from the deposited zinc on the GCE and appeared at -0.71 V and -0.70 V vs. (SCE) in the aqueous and FS-gel electrolytes, respectively. The nucleation overpotential (NOP) was measured by the difference between the potential at the initial cathodic current and the cross-over potential at which the current switches from cathodic to anodic. The NOP was significantly decreased in the FS-gel electrolyte with 14 mV compared to

45 mV in the aqueous electrolyte. The lower value of NOP explains better reversibility of the zinc plating and stripping in the FS-gel electrolyte.

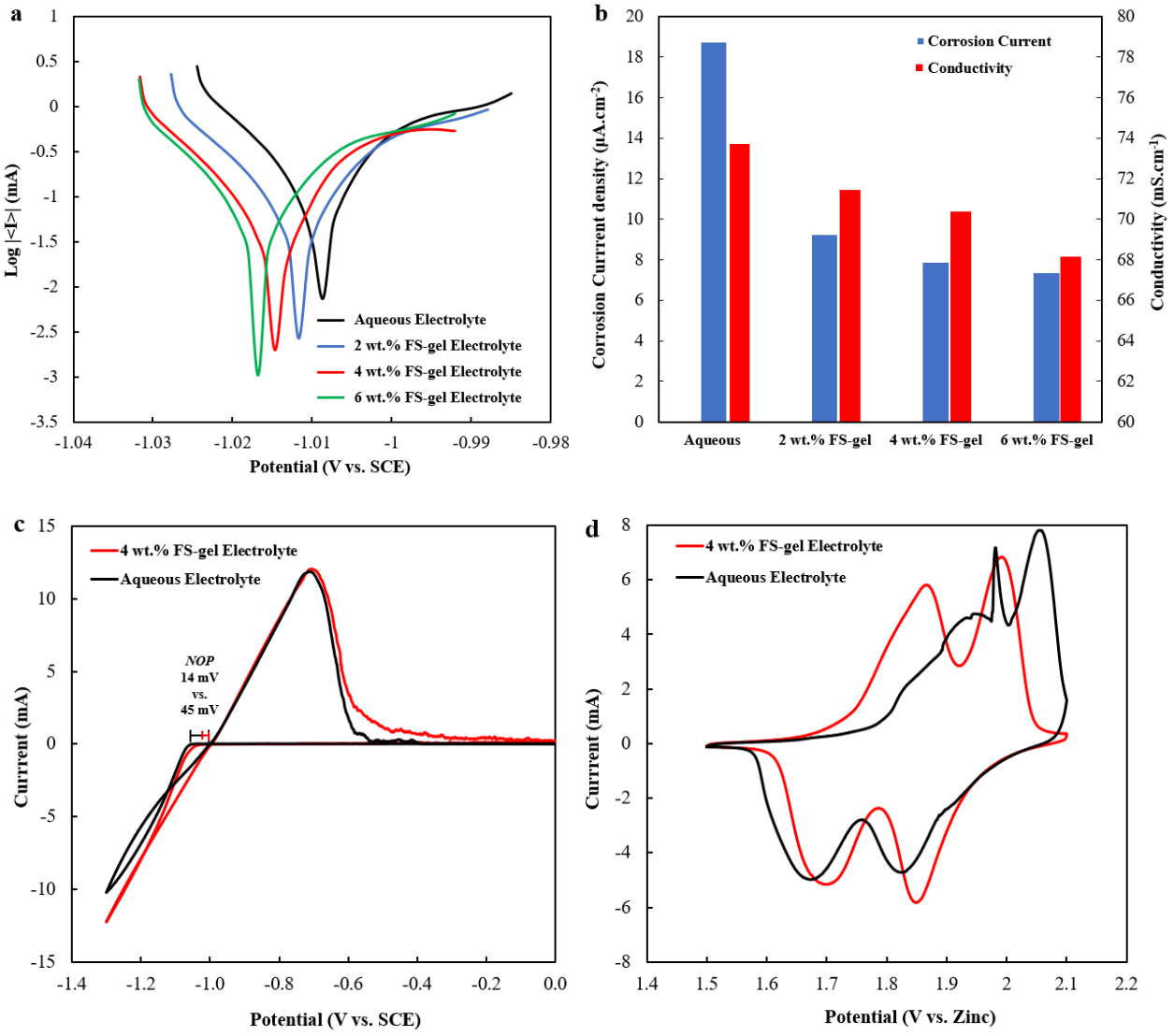

Figure 6.1 a) Tafel curves of zinc foil in different electrolyte systems with a three-electrode setup using zinc foil as the working electrode, Pt wire as the counter electrode, and SCE as the reference electrode, b) histogram plot of zinc corrosion current densities and conductivity measurements in different electrolyte systems. c) CV of zinc redox reaction in aqueous and 4 wt.% gel electrolyte on a GCE at a scan rate of 10 mV s^{-1}. NOP is the nucleation overpotential. d) CV of zinc/$LiMn_2O_4$ battery with 3D-CNT $LiMn_2O_4$ as the working electrode and zinc foil as the counter and reference electrode in different electrolyte systems.

The schematic of zinc plating in aqueous electrolyte and FS-gel electrolyte is illustrated in Figure 6.2 to understand the effect of FS in zinc corrosion protection. Since Li_2SO_4 salts are not involved in the electrochemical reactions on the zinc side they are removed from the schematic. In

the aqueous electrolyte, the water molecules move through the electrode surface, hydrolyze via gaining electrons from the zinc electrode, and induce hydrogen evolution (Figure 6.2a). The zinc electrode will be corroded by HER, causing shape change on its surface. Therefore, the electric current distributes non-uniformly on densified zinc surface and zinc ions have a tendency to be deposited on top of protuberance tips, worsening the zinc dendrite growth. In the FS-gel electrolyte system as seen in Figure 6.2b, the silica molecules form hydrogen bonds with water molecules through OH groups and mitigate the parasitic water-zinc reactions. As a result of the reduced rate of zinc corrosion, the topography of the electrode surface is more homogenous and thus a uniform zinc deposition is expected. Besides, the zinc electrode surface can be mechanically protected from dendrite growth in the FS-gel electrolyte. Hence, the zinc electrode in the FS-gel electrolyte has the advantages of less corrosion and uniform zinc deposition, outperforming the conventional aqueous electrolyte system.

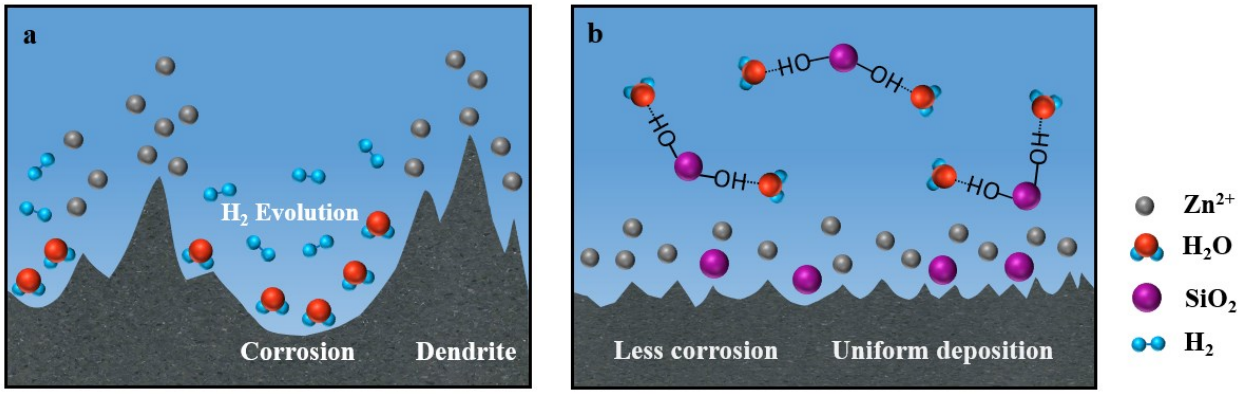

Figure 6.2 Schematic illustration of zinc deposition on a typical zinc electrode in a) aqueous electrolyte and b) FS-gel electrolyte.

The CV of zinc/$LiMn_2O_4$ battery using $LiMn_2O_4$ cathode as the working electrode and zinc anode as the counter and reference electrodes is presented in Figure 6.1d to investigate the 3D-CNT $LiMn_2O_4$ cathode reduction and oxidation peaks in different electrolyte systems. The two sets of redox peaks are related to two phases of lithium intercalation/deintercalation in $LiMn_2O_4$

active material [10]. As seen, the anodic peaks, which are responsible for Li-ion deintercalation from $LiMn_2O_4$, appeared at a lower potential in the FS-gel electrolyte than in the aqueous electrolyte. The anodic peaks in the FS-gel electrolyte shifted down (-120 mV and -70 mV) and appeared at 1.86 and 1.99 V (vs. zinc). Also, the cathodic peaks are situated at 1.70 and 1.85 V (vs. zinc), showing +30 mV movement in their peaks' positions. The decreased gap between anodic and cathodic peaks as a result of the shift in their peaks' positions in the FS-gel electrolyte is attributed to better kinetics of Li-ion intercalation/deintercalation and lower polarization. Moreover, the more symmetric behavior of the CV curve in the FS-gel electrolyte means better reversibility of Li-ion intercalation/deintercalation into/from the active material.

6.3.2 Electrochemical performance of zinc/$LiMn_2O_4$ battery with FS-gel electrolyte

The float charge current has been used in the literature to monitor battery performance at a full SOC. The lower and more stable charging current corresponds to better performance since the battery requires less energy to compensate for the energy loss [77,109]. The float charge current for 24 hours at a constant voltage of 2.1 V and its partial magnification is illustrated in Figure 6.3a. The floating current dropped rapidly only a few minutes after the test started and it became stable after about 4 hours. The floating current for the battery with the FS-gel electrolyte was 0.04 mA, while its value for the battery with the aqueous electrolyte was roughly 0.07 mA. Therefore, the float charge current was about 40% lower for the battery with the FS-gel electrolyte. The superior performance of the battery with FS-gel electrolyte in terms of float charge current explains lower energy runaway compared to that with the aqueous electrolyte. The oxygen generation from the decomposition of water at high voltage is responsible for the higher float charge current in the aqueous electrolyte. Another important tool to evaluate the energy run-away in the battery is by monitoring the OCV decay over time. The OCV of the fully charged batteries with FS-gel and the

aqueous electrolyte is plotted for 24 hours (Figure 6.3b). The batteries were fully charged up to 2.1 V at 0.2 C-rate, and then the OCV was monitored without charging/discharging. The battery with FS-gel electrolyte showed a higher OCV value which is attributed to lower self-discharge and less hydrogen generation. The voltage of the battery with the aqueous electrolyte dropped more than that with the FS-gel electrolyte. After 24 hours of the rest period, the OCV of the battery with FS-gel electrolyte was at 1956 mV compared to 1940 mV for the battery with aqueous electrolyte, indicating the advantage of FS-gel electrolyte in improving the OCV. Therefore, the battery with gel electrolyte is better at holding the charge capacity and can offer better storage capability.

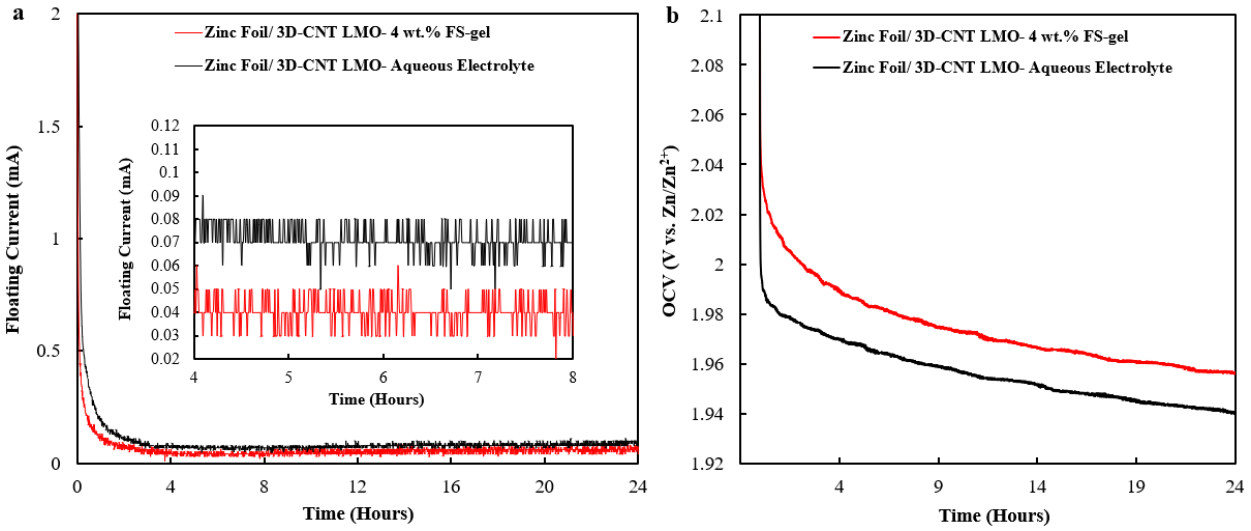

Figure 6.3 Float charge current of zinc/$LiMn_2O_4$ battery by a constant voltage at 2.1 V for 24 hours with aqueous and 4 wt.% FS-gel electrolytes. b) OCV monitoring of the fully charged zinc/$LiMn_2O_4$ battery for 24 hours with aqueous and 4 wt.% FS-gel electrolytes.

The electrochemical performance of zinc/$LiMn_2O_4$ battery using 4 wt.% FS-gel electrolyte, 3D-CNT cathode, and zinc foil anode is presented in Figure 6.4. Both batteries at 200 µm and 400 µm cathode thicknesses delivered a high specific capacity close to 120 mAh g^{-1} at initial cycles. The durability of the battery at 200 µm was 280 cycles with 72% capacity retention, while the battery at 400 µm cathode thickness lasted for 180 cycles before short-circuiting with 80% capacity retention. The lower lifespan of the battery with 400 µm thick cathode is due to further zinc

depositions and dendrite formations as a result of higher battery capacity and more concentration gradient. The CE of the batteries at 200 µm and 400 µm was 99.2 and 99.0%, showing minimal side reaction. The slightly lower CE at 400 µm can be due to higher polarization and overpotential, which can induce possible side reactions.

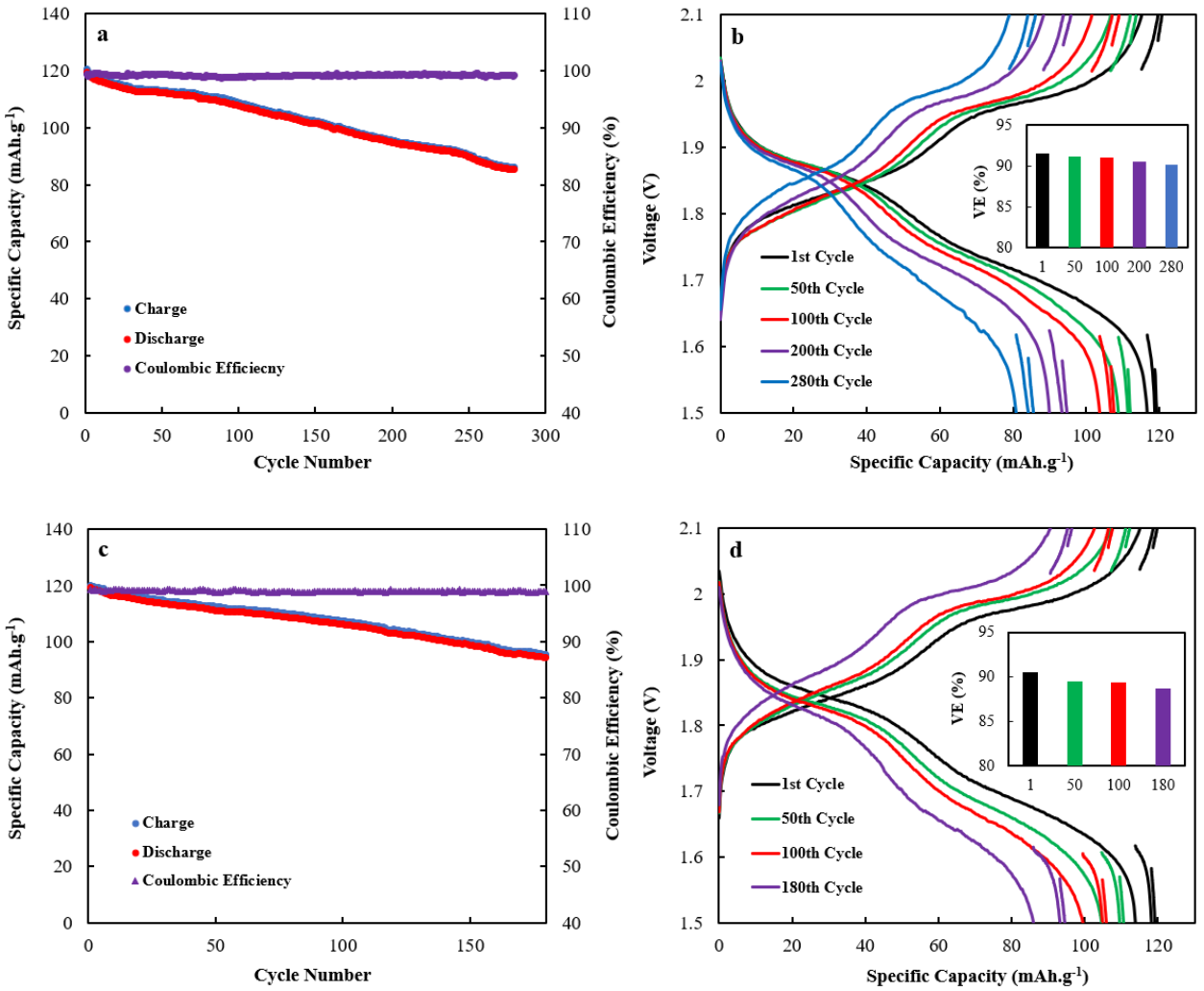

Figure 6.4 Specific capacity vs. cycle number and voltage-capacity profiles at various cycle numbers for the zinc/$LiMn_2O_4$ battery using 4 wt.% FS-gel electrolyte, zinc foil anode, and 3D-CNT cathode at two different electrode thickness: a-b) 200 µm 3D-CNT cathode, c-d) 400 µm thick 3D-CNT cathode. The insets are the histogram plots of VE vs. cycle number.

The voltage-capacity profiles of the battery at various cycle numbers were obtained between 1.5 V- 2.1 V (vs. Zn/Zn^{2+}) cut-off voltage and using a three-step constant-current charge/discharge protocol (Figure 6.4 b, d). The VE of the battery was close to 92% and gradually decreased to 90%

at the 280th cycle. Besides, the battery with 400 μm thick cathode delivered slightly lower VE due to the thicker electrode design and hence a higher electronic/ionic resistance.

The voltage-capacity curves of the battery using FS-gel electrolyte and aqueous electrolyte at 200 μm and 400 μm cathode thickness are compared in Figure 6.5. The comparison is made for the initial and the last cycle of the battery with the aqueous electrolyte. As seen, the battery using FS-gel electrolyte displayed a lower overpotential for charge and discharge curves and thus superior performance in terms of VE. For example, the VE of the battery with 200 μm thick 3D-CNT cathode and using FS-gel electrolyte was roughly 92% compared to 87% with the aqueous electrolyte in the initial cycle. The higher VE suggests a lower electronic/ionic resistance for the battery using the FS-gel electrolyte. The batteries using FS-gel and aqueous electrolyte showed roughly similar specific capacity at both cathode thicknesses. Furthermore, the CE of the battery with FS-gel electrolyte was greater than the aqueous electrolyte (99.2% vs. 98.6%). The better CE can be attributed to mitigated hydrogen evolution-induced corrosion and lower self-discharge in the battery using FS-gel electrolyte.

The durability of zinc/$LiMn_2O_4$ battery constructed with FS-gel electrolyte is compared with the aqueous electrolyte in Figure 6.6. At 3.8 mAh cm^{-2} areal capacity, the zinc/$LiMn_2O_4$ battery with 4 wt.% FS-gel electrolyte exhibited 280 cycles, which is 2.8 times longer than the cycle life of the battery with the aqueous electrolyte. Moreover, the durability of the battery at 7.4 mAh cm^{-2} areal capacity and 62 mg cm^{-2} active material loading using FS-gel electrolyte was boosted from 50 cycles to roughly 180 cycles. Accordingly, the use of FS-gel electrolyte successfully extends the cycle life of high areal-capacity zinc/$LiMn_2O_4$ battery by almost 3 times the lifespan of the battery with the aqueous electrolyte system via effectively suppressing the zinc corrosion and dendrite growth. FS can immobilize the water molecules via hydrogen bonding. As a result of the

decrease in the activity of water-induced reactions, the corrosion of the zinc metal electrode can be suppressed and homogenous zinc deposition is expected [109–111]. Consequently, the lifespan of the battery using FS-gel electrolyte is significantly longer than the aqueous electrolyte system.

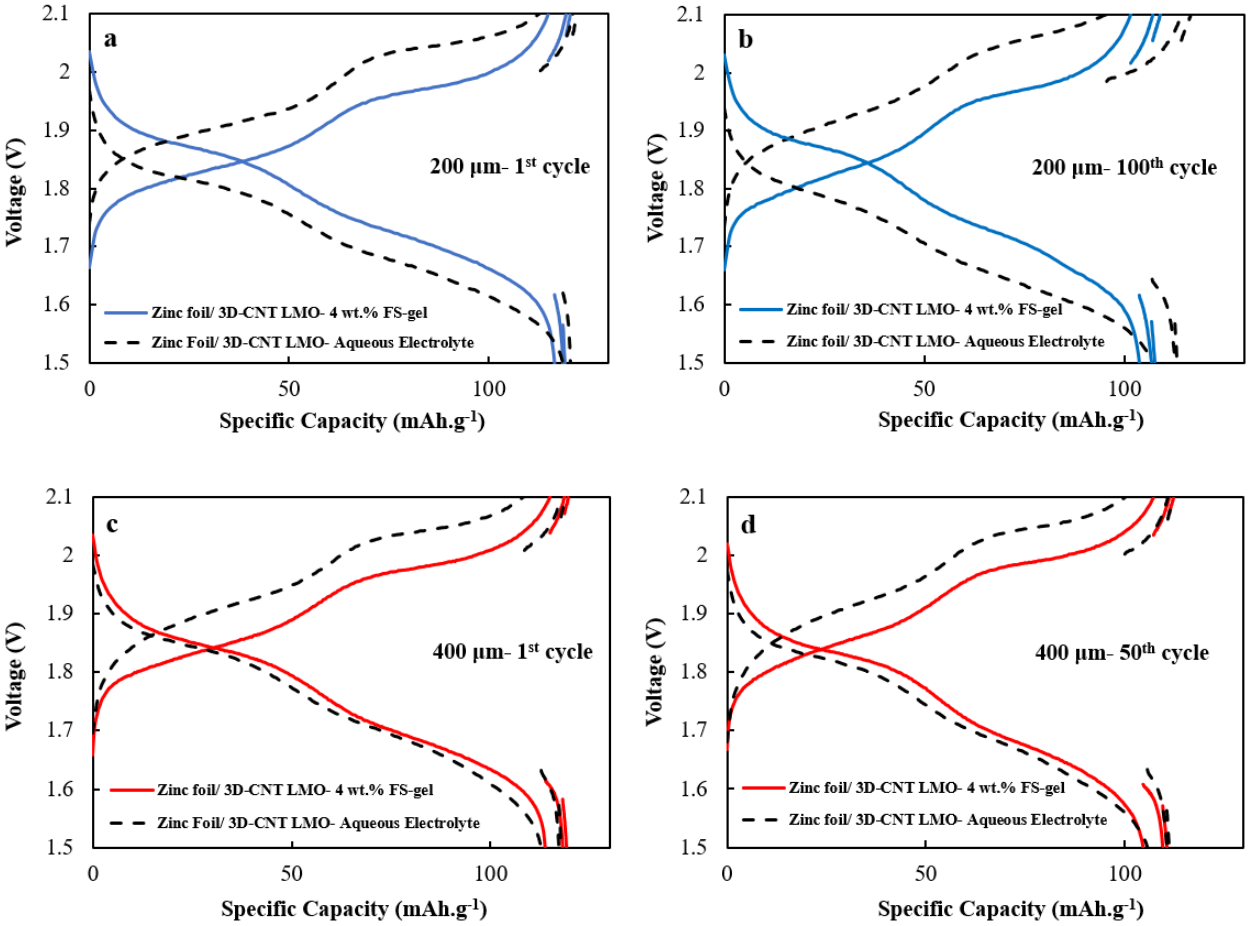

Figure 6.5 Voltage-capacity comparison of zinc/$LiMn_2O_4$ battery using 4 wt.% FS-gel electrolyte and aqueous electrolyte (2.0 mol L^{-1} $ZnSO_4$ and 1.5 mol L^{-1} Li_2SO_4) at two different thicknesses of 3D-CNT cathode: a-b) 200 µm 3D-CNT cathode, and c-d) 400 µm 3D-CNT cathode.

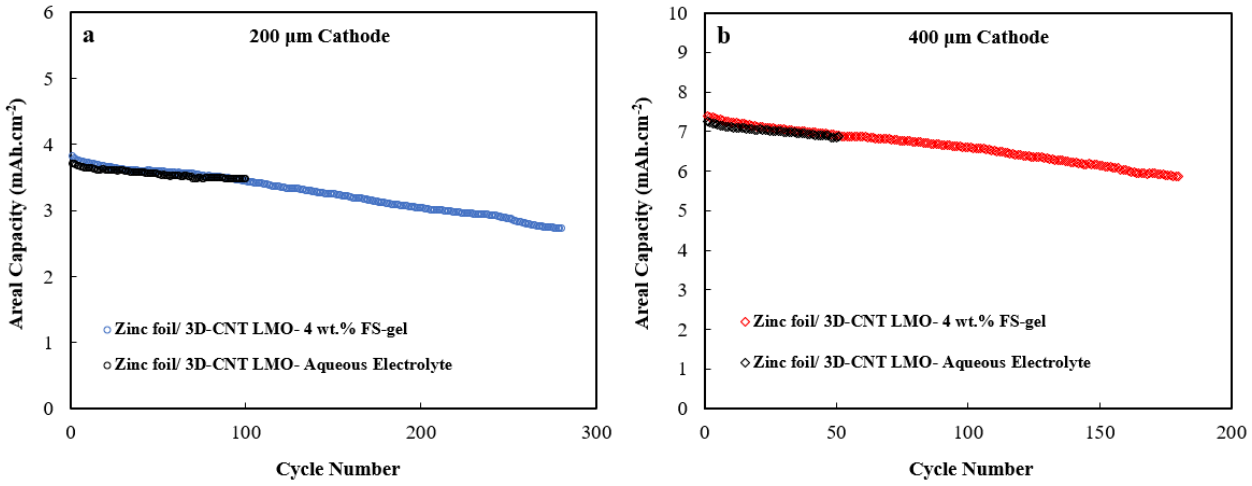

Figure 6.6 Cycle life comparison of zinc/$LiMn_2O_4$ battery using 4 wt.% FS-gel electrolyte and aqueous electrolyte (2.0 mol L^{-1} $ZnSO_4$ and 1.5 mol L^{-1} Li_2SO_4) at two different thicknesses of 3D-CNT cathode: a) 200 µm thick 3D-CNT cathode, b) 400 µm thick 3D-CNT cathode.

6.3.3 Electrochemical performance of zinc/$LiMn_2O_4$ battery with PZPC anode and FS-gel electrolyte

Taking the advantages of PZPC anode and FS-gel electrolyte, the high areal-capacity zinc/$LiMn_2O_4$ batteries were assembled with them. The rate capability performance of zinc/$LiMn_2O_4$ battery using 3D-CNT cathode, PZPC anode, and FS-gel electrolyte is depicted in Figure 6.7. The 3D-CNT cathodes were at two different thicknesses of 200 µm and 400 µm with 31 mg cm^{-2} and 63 mg cm^{-2} active material loading, respectively. As observed in Figure 6.7, the battery showed decent rate performance from C/15 to C/2 rate with a slight decrease in the capacity, delivering more than 100 mAh g^{-1} specific capacity. The major capacity drop occurred at 1C and 2C rates, in which the specific capacity of the battery with 200 µm thick cathode was reduced to around 95 and 68 mAh g^{-1}. For 400 µm thick cathode, the corresponding specific capacity was lower and delivered 85 and 57 mAh g^{-1} at 1C and 2C rates. The high discharge capacity of the battery with these thick cathodes suggests the advantage of FS-gel electrolyte and PZPC anode in improving the rate performance of the battery. The porous and 3D structured PZPC

anode embodies a complementary role with FS-gel electrolyte to facilitate the ionic movement [103]. The porous structure of the anode enhances the contact area in the electrode-electrolyte interface and promotes ionic transportation flux [40].

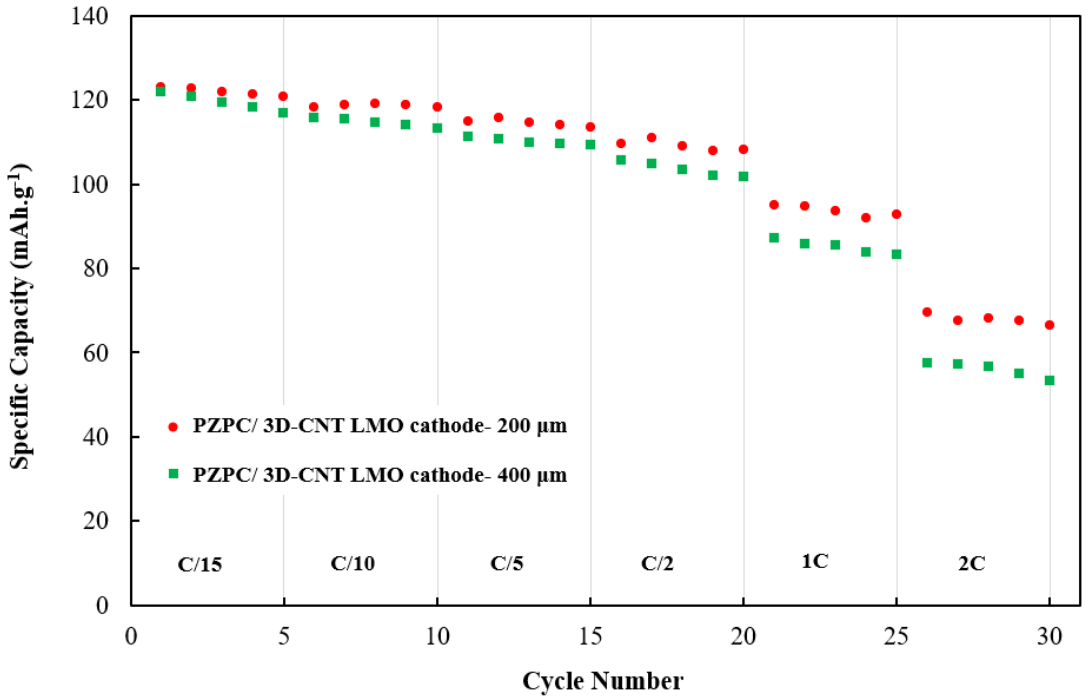

Figure 6.7 Rate capability performance of zinc/$LiMn_2O_4$ battery with 200 µm and 400 µm thick 3D-CNT cathodes, PZPC anode, and 4 wt.% FS-gel electrolyte from C/15 to 2C rate.

The electrochemical performance of zinc/$LiMn_2O_4$ battery with 200 µm thick 3D-CNT cathode, PZPC anode, and 4 wt.% FS-gel electrolyte is plotted in Figure 6.8. As shown, the discharge capacity of the battery was 123 mAh g^{-1} at the 1st cycle. More importantly, the durability of the battery was 600 cycles before short-circuiting with only 0.047% capacity loss per cycle. Therefore, the combination of FS-gel electrolyte and PZPC anode makes the battery last longer compared to the aqueous electrolyte with PZPC anode (500 cycles, Figure 5.9). The average for CE was 99.5% which corresponds to a very little amount of side reaction during cycling. For comparison, the CE of the battery with zinc foil and PZPC anodes in the aqueous electrolyte was 98.6% (Figure 4.9) and 99.3% (Figure 5.9), respectively. The significantly improved

electrochemical performance of the battery is related to the highly porous and conductive PZPC anode combined with additional corrosion protection for the zinc electrode via FS-gel electrolyte.

As observed in Figure 6.8b, the cut-off voltage of the battery was controlled between 1.5 V-2.1 V (vs. Zn/Zn^{2+}) and the battery was galvanostatically tested using a three-step charge/discharge protocol. As cycling proceeds, the contribution of steps 2 and 3 (charge/discharge at a lower C-rate than step 1) to the total capacity is increasing. The battery can be charged and discharged better at lower C-rates since its resistance is escalating during battery cycling. Furthermore, the VE of the battery declined from 92% at the initial cycle to 89% at the 600th cycle. The decrease in the VE of the battery is also due to the growing resistance inside the battery upon cycling.

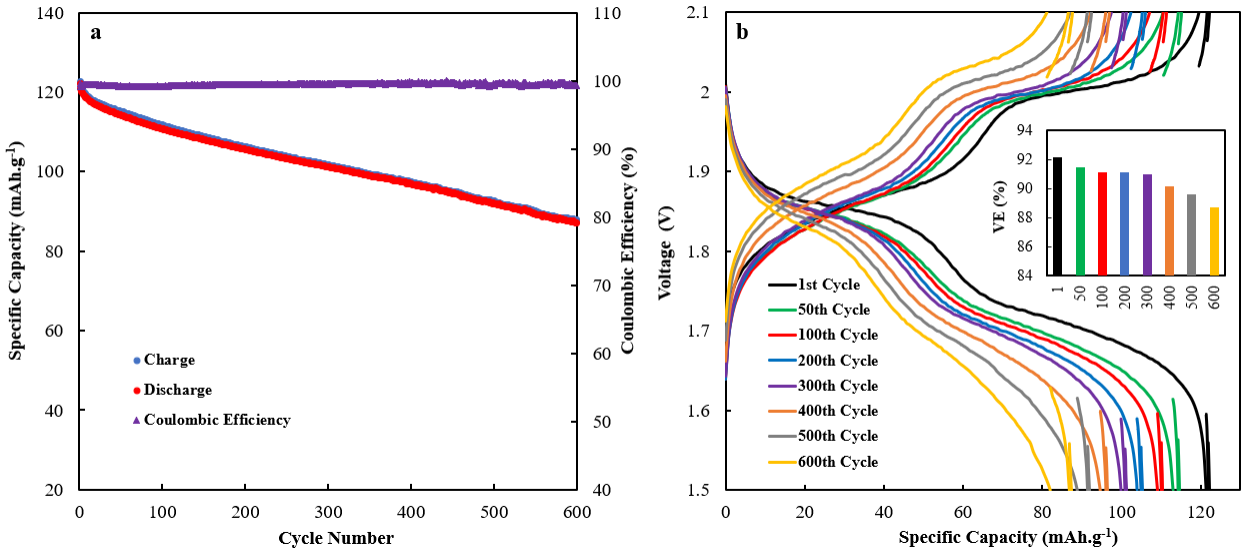

Figure 6.8 Electrochemical performance of zinc/$LiMn_2O_4$ battery using 200 µm thick 3D-CNT cathode, PZPC anode, and 4 wt.% FS-gel electrolyte at 1C rate (1st step of constant-current charge/discharge protocol): a) Specific capacity vs. cycle number. b) Charge/discharge profiles at various cycle numbers. The inset is the histogram plot of VE vs. cycle number.

To evaluate the effect of resistance, EIS data of the zinc/$LiMn_2O_4$ battery constructed with 3D-CNT cathode, PZPC anode, and 4 wt.% FS-gel electrolyte was obtained (Figure 6.9a). The bulk resistance of the battery, which is indicated by the intercept of real impedance at the high-frequency region, was 2.21 Ω at the initial cycle and the resistance was increased gradually by the

cycle number, reaching 4.73 Ω at the 600th cycle. Moreover, the diameter of charge transfer resistance is also increasing during battery cycling. Therefore, this result is in agreement with decreasing VE as cycling proceeds. The Nyquist plots of batteries using different zinc electrodes and electrolyte systems are compared in Figure 6.9b. The bulk resistance and charge transfer resistance of the battery with PZPC anode and FS-gel electrolyte was significantly reduced compared to that of the batteries with zinc foil anode in FS-gel electrolyte and zinc foil or PZPC anode in the aqueous electrolyte system. The bulk resistance of the battery with PZPC and FS-gel at the 100th cycle was 3.17 Ω, while the corresponding values with zinc foil and PZPC anode in the aqueous electrolyte and zinc foil in gel electrolyte were 4.33, 3.50, and 3.59 Ω, respectively. Furthermore, the battery with PZPC and FS-gel electrolyte showed a much lower charge transfer resistance due to the very small diameter of the semicircle in the Nyquist plot. The improved conductivity of the battery can be attributed to the enhanced contact area in the electrode-electrolyte interface [40]. The PZPC has a much higher surface area than zinc foil and facilitates ionic transportation. Moreover, the hydrophilic silica in the electrolyte is in good contact with PZPC anode at the electrode/electrolyte interphase and may provide enhanced pathways for the zinc ion diffusion, contributing to reduce the polarization [167].

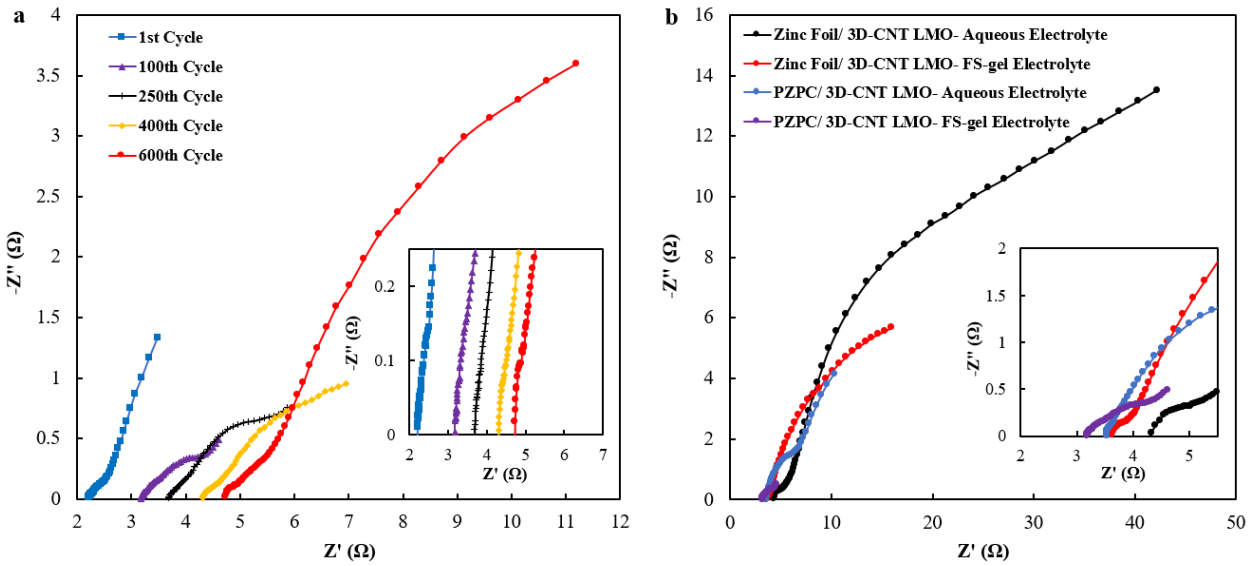

Figure 6.9 a) EIS measurement data of the zinc/$LiMn_2O_4$ battery made with 200 µm thick 3D-CNT cathode, PZPC anode, and 4 wt.% FS-gel electrolyte at different cycle numbers. b) Comparison of Nyquist plots of zinc/$LiMn_2O_4$ batteries at the 100th cycle using different zinc anodes and electrolyte systems. The inset plots are the enlarged area in the high-to-medium frequency region.

The SEM images of PZPC anode before and after battery cycling are presented in Figure 6.10a-f. The zinc particles are interconnected with CNTs in a highly porous structure (Figure 6.10a-c) to provide a conductive matrix with good mechanical strength. This structure is suitable for high amounts of zinc deposition within its void space. The morphology of PZPC after 600 full charge/discharge cycles using FS-gel electrolyte is shown in Figure 6.10d-f. The zinc deposits are compact and have irregular shapes with flat and smooth edges rather than sharp tips and mossy-like structures as previously observed in the zinc foil anode (Figure 5.12b-c). Besides, the cross-section image of the PZPC anode revealed that the zinc can grow within its highly porous structure (Figure 6.10f). Therefore, zinc dendrite can be delayed due to the highly porous structure of the PZPC anode and the low rate of zinc corrosion in the FS-gel electrolyte to ultimately prolong the cycle life of high areal-capacity zinc/$LiMn_2O_4$ batteries.

The XRD pattern of the PZPC anode as observed in Figure 6.11a exhibited a decrease in the peaks' intensity of zinc element after cycling; however, no significant peak shift is detected after battery cycling. Moreover, new peaks of ZnO, $Zn(OH)_2$, $ZnSO_4.7H_2O$, and $Zn_4SO_4(OH)_6.3H_2O$

are distinguished for the anode after cycling. The change in the peak intensity reflects different development of the zinc electrode during cycling. For example, the zinc surface containing peaks at 100 and 110 planes can support vertical zinc dendrite growth, while the peak at 002 plane supports flat zinc deposition [109]. As observed, the peak intensity at 100 and 110 was substantially reduced. This is additional evidence that zinc dendrite growth was suppressed successfully as also confirmed by the SEM images.

The SEM images of the 3D-CNT $LiMn_2O_4$ cathode before and after 600 full charge/discharge cycles are shown in Figure 6.10g-i. As observed in the cross-section images (Figure 6.10g-h), the cathode is supported by CNTs and retained its structural integrity without the formation of cracks inside its composite even after 600 repeated intercalation and deintercalation of lithium inside active material particles. It should be pointed out that the intercalation/deintercalation process is associated with volume change for active material and causes severe stress inside thick cathodes. This accumulation of stress can be more problematic inside thick cathodes and can lead to crack formations [128]. However, the 3D-CNT cathode composite can still retain its structure after extensive battery cycling. Besides, the morphology of $LiMn_2O_4$ particles remained intact after 600 full charge/discharge cycles (Figure 6.10i). It is also observed that there are some traces of FS in the post-cycled cathode even after washing with DDI water.

The XRD patterns of the 3D-CNT cathode before and after 600 charge/discharge cycles are shown in Figure 6.11b. All major peaks after cycling fitted well with the original pattern before cycling and the peak locations were not displaced significantly, indicating the high stability of the 3D-CNT cathode and unchanged crystallinity of $LiMn_2O_4$ after more than 600 cycles. This could be indirect evidence that manganese dissolution was minimal.

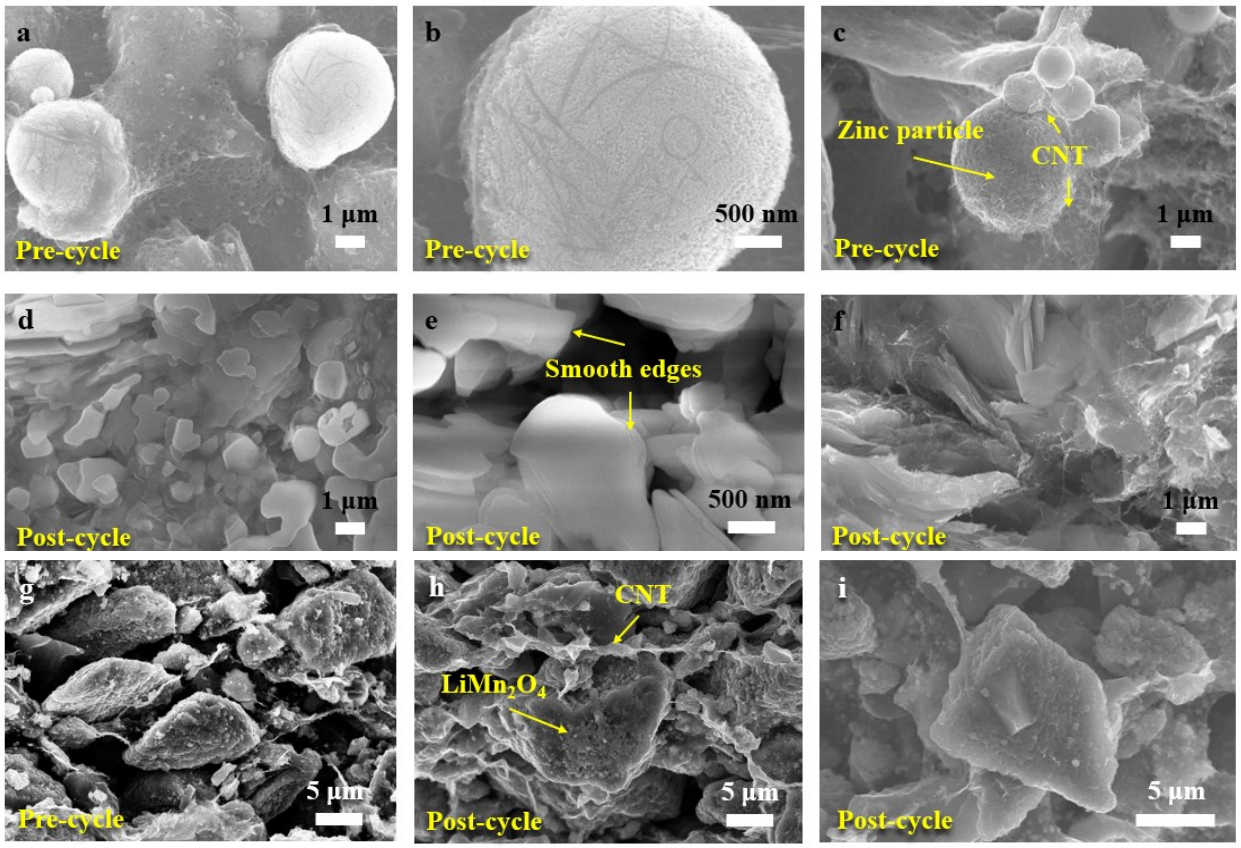

Figure 6.10 Morphology of pre-cycled PZPC: a-b) Surface SEM images at different magnification, c) cross-section SEM. Morphology of PZPC after 600 cycles: d-e) Surface SEM images at different magnification, f) cross-section SEM observation. Morphology of 3D-CNT cathode before and after 600 cycles: g-h) cross-section SEM images, i) Surface SEM image.

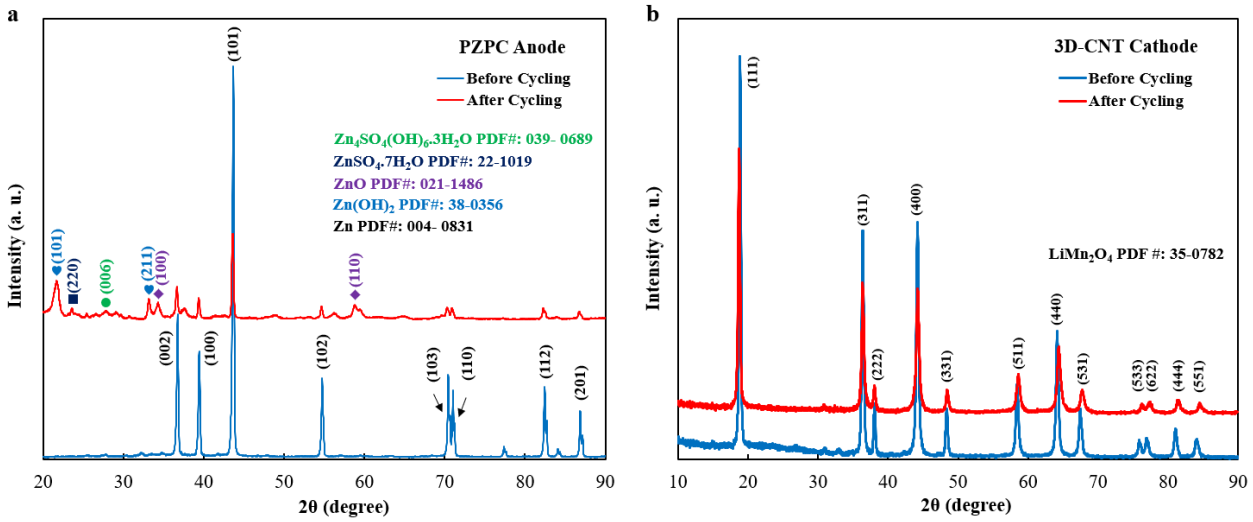

Figure 6.11 XRD patterns of a) PZPC anode before and after 600 cycles and b) 3D-CNT $LiMn_2O_4$ cathode before and after 600 cycles in zinc/$LiMn_2O_4$ battery using 4 wt.% FS-gel electrolyte.

6.3.4 Durability of high areal-capacity zinc/$LiMn_2O_4$ battery

The cycle life of zinc/$LiMn_2O_4$ batteries manufactured with FS-gel electrolyte, PZPC anode, and thick 3D-CNT cathode at various electrode thicknesses is shown in Figure 6.12. The durability of the battery was reduced upon increasing the cathode thickness and active material loading. The lifespan of the battery with a 500 μm thick cathode was 270 cycles, while another battery lasted for 600 cycles with a 200 μm thick cathode. The zinc/$LiMn_2O_4$ battery fabricated with the ultra-thick cathode, having 8.8 mAh cm^{-2} areal capacity and 74.9 mg cm^{-2} active material loading, manifested a much higher areal capacity (at least 10 times) than the reported areal capacity for the zinc/$LiMn_2O_4$ battery in the literature [10,85,107,111,122]. Moreover, it is observed that the battery at lower electrode thickness displayed a much more stable performance. The capacity loss of the zinc/$LiMn_2O_4$ battery at 200 μm, 270 μm, 340 μm, 400 μm, and 500 μm was 0.047%, 0.051%, 0.056%, 0.077%, and 0.083% per cycle. As expected, as areal capacity increases the capacity degrades faster. This is because the internal resistance of the electrode surges at higher electrode thicknesses, leading to intensified polarization and capacity fading [128]. Besides, the rate of slow-kinetics oxygen evolution generation would be greater in the battery with a higher areal capacity since its charging time is longer at a constant current-density battery testing.

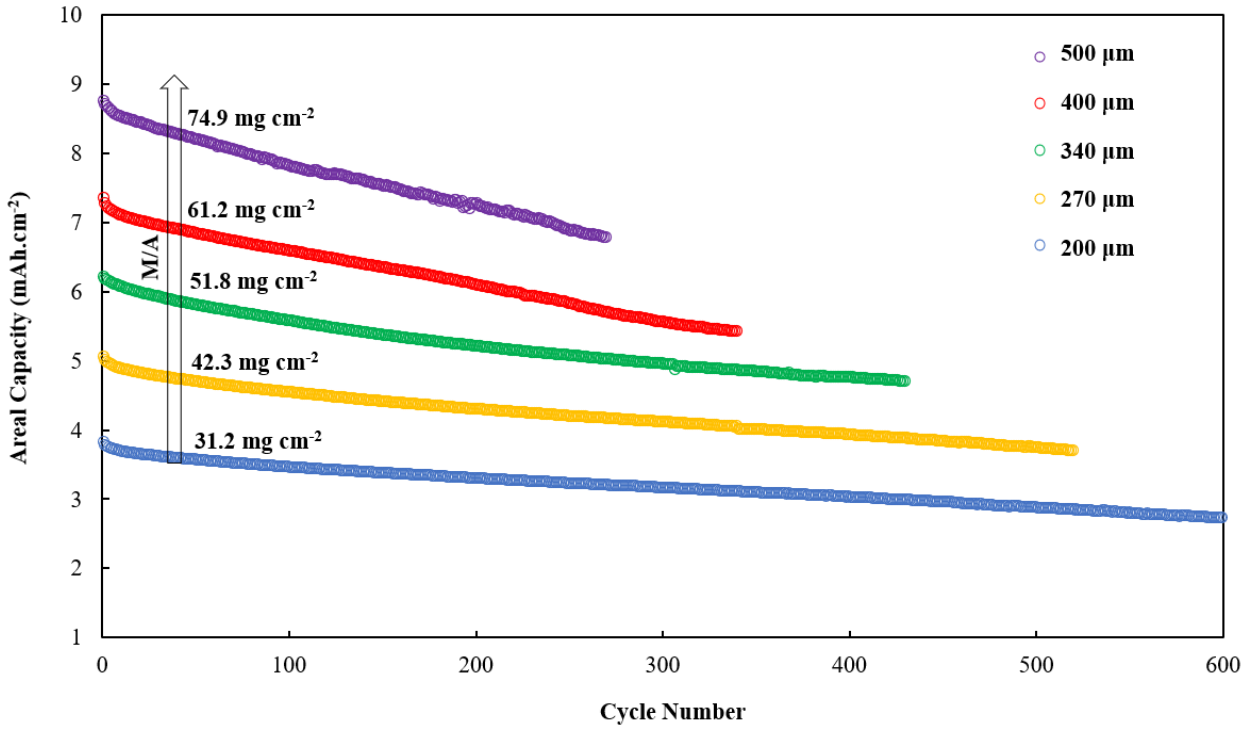

Figure 6.12 Cycle life comparison of zinc/$LiMn_2O_4$ battery using PZPC anode and 4 wt.% FS-gel electrolyte at various 3D-CNT cathode thicknesses. M/A: active material loading per unit surface area.

6.4. Summary

In this study, a low-cost FS-gel electrolyte was developed for high areal-capacity zinc/$LiMn_2O_4$ battery to mitigate the several issues related to water-induced electrochemical side reactions such as corrosion and dendrite growth. These problems can be alleviated in the FS-gel electrolyte by lowering the high reactivity of water through hydrogen bonding with water molecules and mechanically protecting the zinc surface. Moreover, the FS-gel electrolyte improves the reversibility of oxidation and reduction reactions on both cathode and anode sides. The lifespan of the zinc/$LiMn_2O_4$ battery using the FS-gel electrolyte is compared with the aqueous electrolyte at two different thicknesses of the cathode in Figure 6.13. The combination of FS-gel electrolyte and PZPC anode manifests a remarkable cycle life increment in the high areal-capacity zinc/$LiMn_2O_4$ battery compared to that with aqueous electrolyte and zinc foil anode. For 200 µm

thick cathode, the lifespan of the zinc/$LiMn_2O_4$ battery was 100 cycles with aqueous electrolyte and zinc foil and prolonged to 280 cycles using FS-gel electrolyte and further extended to 600 cycles using both FS-gel electrolyte and PZPC anode. The durability of the zinc/$LiMn_2O_4$ battery at 7.3 mAh cm^{-2} areal capacity with PZPC anode and FS-gel electrolyte was significantly extended to 340 cycles compared to only 50 cycles with aqueous electrolyte and zinc foil anode. Therefore, the cycle life of high areal-capacity zinc/$LiMn_2O_4$ battery prolongs by at least 6 times the lifespan of the battery with zinc foil anode and aqueous electrolyte system via using PZPC anode and FS-gel electrolyte. Such significant improvement is made by effectively suppressing the dendrite growth using highly porous PZPC anode and mitigating the water-induced corrosion by means of FS-gel electrolyte. Apart from prolonged cycle life, the battery manufactured with FS-gel electrolyte demonstrates better VE and lower energy runaway compared to that with aqueous electrolyte due to smaller resistance and reduced rate of HER. Consequently, the high-performance zinc/$LiMn_2O_4$ battery system with high areal capacity 3D-CNT cathode, PZPC anode, and FS-gel electrolyte can be a proper replacement for high demand lead-acid batteries.

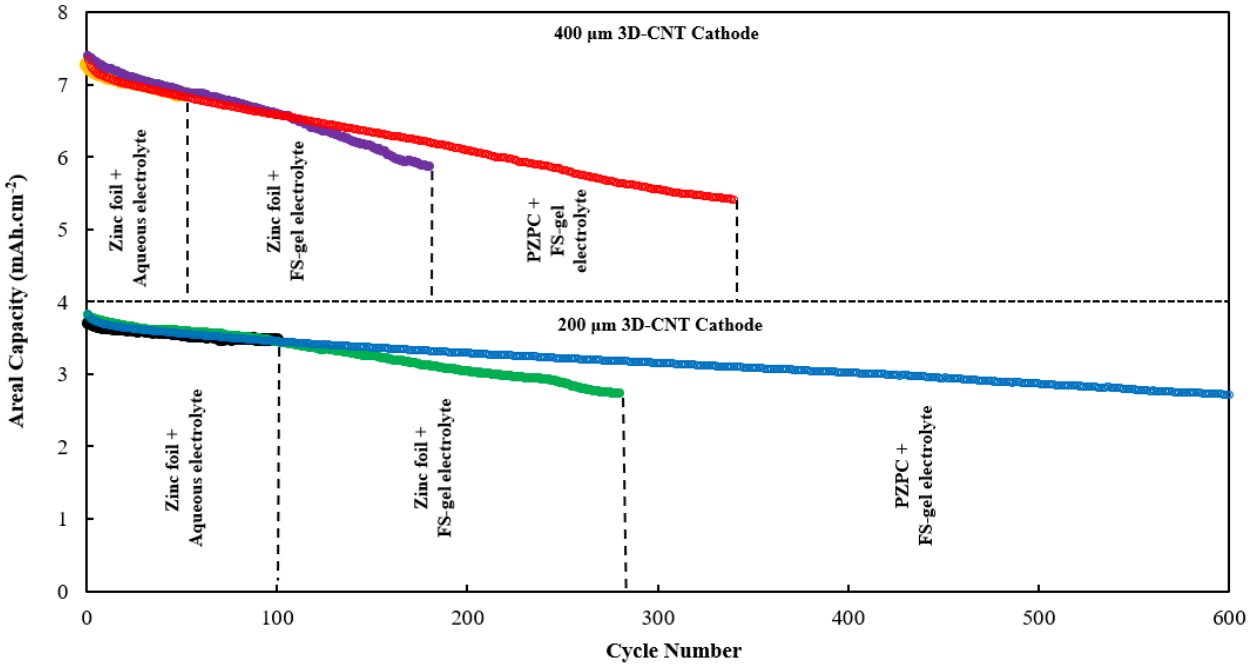

Figure 6.13 Durability comparison of zinc/$LiMn_2O_4$ batteries with 200 µm and 400 µm 3D-CNT cathode and different zinc electrodes and electrolyte systems.

7. Conclusions and future works

7.1. Conclusions

ARZLBs are unique for EES applications due to numerous potential benefits including i) low cost, ii) safe operation, iii) low environmental impacts, and iv) high ionic conductivity. However, their commercialization is plagued by inadequate energy density and cycle life. One feasible strategy to increase the energy density of ARZLBs is by enhancing the areal capacity via thick cathode design to match with the high specific-capacity zinc anode and to promote the ratio of active to inactive components. The fabrication of thick cathodes using conventional methods imposes certain limitations. The proposed electrode designs for ARZLBs in the published literature are limited to thin cathodes (typically <100 μm) with low active material loadings (<10 mg cm^{-2}), bounding their practical energy density. Moreover, the cycle life of the ARZLBs drastically reduces by increasing the areal capacity of the battery due to the severe zinc dendrite growth upon cycling and hydrogen evolution-induced corrosion. In the current research, innovative methods have been presented to manufacture a practical ARZLB with high areal capacity as well as addressing challenges associated with the battery including zinc dendrite formation and inadequate cycle life.

In Chapter 3, a binder-less thick cathode design with dough-like consistency has been proposed. High areal-capacity ARZLBs with record high values of 10.5 mA cm^{-2} for zinc/$LiFePO_4$ and 11.2 mA cm^{-2} for zinc/$LiMn_2O_4$ battery using dough-like cathode structure at extremely high thicknesses (up to 1000 μm thick) were demonstrated. In this innovative method, the electrodes are manufactured more straightforwardly, cheaper, faster, and safer than conventional fabrication methods, providing a binder-less and flexible structure. For comparison, the areal capacity of a

dough-like $LiFePO_4$ cathode at 1000 μm is 15 times higher than that in conventional $LiFePO_4$ cathode at 100 μm. The enhancement in the areal capacity of the battery using a 700 μm thick dough-like cathode successfully increases the energy density of the zinc/$LiFePO_4$ battery by 190% compared to that with a 100 μm conventional cathode. Besides, the use of thick cathodes cuts the cost of battery manufacturing by lowering the ratio of inactive components such as current collectors and separators in the battery stack. However, the zinc/$LiMn_2O_4$ batteries fabricated with dough-like electrodes showed high capacity degradation and limited cycle life by cause of oxygen generation and creation of isolated regions within the electrode structure, resulting in fast capacity degradation.

In Chapter 4, the cathode structure for zinc/$LiMn_2O_4$ is redesigned using a 3D reinforced and conductive CNT-supported composite. The 3D-CNT cathode can be manufactured up to 900 μm thick, manifesting unprecedented areal capacity and active material loading for zinc/$LiMn_2O_4$ battery by as much as 13.5 mAh cm^{-2} and 113.5 mg cm^{-2}, respectively. Furthermore, the energy density of the zinc/$LiMn_2O_4$ with the 3D-CNT cathode design is 140% higher than a zinc/$LiFePO_4$ with the dough-like electrode at the same thickness due to a higher discharge voltage (1.8 V compared to 1.2 V) and a higher mass fraction of active material in 3D-CNT electrode structure. However, by increasing the areal capacity, the cycle life of the battery is restricted to less than 100 cycles due to severe dendrite growth on a conventional zinc anode, leading to fatal short-circuiting. The zinc foil anode has a flat and non-porous structure, triggering zinc dendrite formation as a result of uneven zinc depositions and inhomogeneous electric current distribution. Accordingly, the problems associated with the typical zinc anode were addressed in Chapter 5.

In Chapter 5, the typical zinc metal anode was replaced by a novel PZPC with a highly porous and conductive structure. The enlarged electroactive surface area of the PZPC anode

ensures the homogenous current distribution and thus uniform zinc deposition, minimizing the zinc nuclei size and dendrite growth. The PZPC is manufactured using zinc dust, CFs, CNTs, PTFE, and functional additives. The functional additives are comprised of tin sulfate, bismuth oxide, and lead acetate and they promote the corrosion resistance of the zinc by imposing high overpotential for the HER. The cycle life of zinc/$LiMn_2O_4$ battery using PZPC anode is dramatically improved by up to 5 times the lifespan of the battery with a typical zinc anode. The cycle life of zinc/$LiMn_2O_4$ battery with PZPC anode was prolonged to 500 cycles at 3.6 mAh cm^{-2} areal capacity and 220 cycles at 7.2 mAh cm^{-2} areal capacity. The improved cycle life is attributed to the high surface area, uniform zinc deposition, and the effect of corrosion reduction additives in PZPC. Furthermore, the high surface area and increased electrode-electrolyte contact area provides enhanced pathways for zinc deposition and promotes the rate capability of the battery by 10%.

Finally, in Chapter 6, the cycle life of the high areal-capacity zinc/$LiMn_2O_4$ battery was further improved by reducing the corrosion rate of zinc and dendrite growth using FS as a gelling agent inside the aqueous electrolyte. The FS-gel electrolyte mitigates the parasitic water-zinc reactions through hydrogen bonding and mechanically protects the zinc surface. Besides, the reversibility of zinc deposition/dissolution at the anode and Li-ion intercalation/deintercalation at the cathode improves in the FS-gel electrolyte. The lifespan of zinc/$LiMn_2O_4$ battery with a thick 3D-CNT cathode at 3.8 mAh cm^{-2} areal capacity using PZPC anode and FS-gel electrolyte is further extended to 600 cycles. Moreover, the battery manufactured with the FS-gel electrolyte exhibits better VE, higher OCV retention, and lower float charge current compared to the aqueous electrolyte.

A summary of this work is presented in Figure 7.1 with more provided detailed information in Table 7.1. As shown, the areal capacity of the zinc/$LiMn_2O_4$ reaches an unprecedented value of

13.5 mAh cm^{-2} with a 3D-CNT thick cathode; however, the cycle life is limited with the conventional zinc anode and aqueous electrolyte system. By employing PZPC and FS-gel electrolyte, the durability of the battery is enhanced six-fold, even at very high areal capacity values. Consequently, high areal-capacity and durable aqueous rechargeable zinc/$LiMn_2O_4$ batteries developed in this work with thick 3D-CNT cathode design, PZPC anode, and FS-gel electrolyte can be an ideal candidate for EES applications with intrinsically safe, eco-friendly, and low-cost privileges.

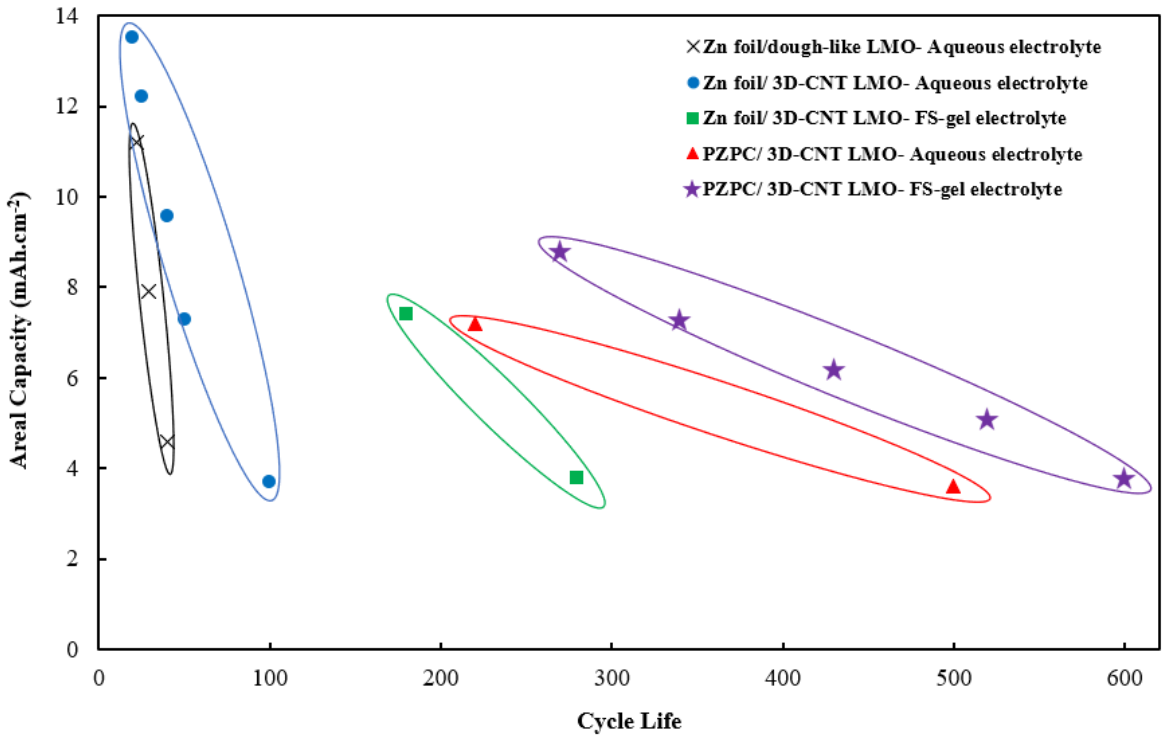

Figure 7.1 Areal capacity vs. cycle life of zinc/$LiMn_2O_4$ with thick $LiMn_2O_4$ cathodes and using different zinc anodes and electrolyte systems.

Table 7.1 Comparison of areal capacity and cycle life of aqueous rechargeable zinc/$LiMn_2O_4$ batteries at various thicknesses of 3D-CNT $LiMn_2O_4$ cathode and using different zinc electrodes and electrolyte systems.

Cathode thickness (μm)	Anode type	Electrolyte	Active material loading (mg cm^{-2})	Areal capacity (mAh cm^{-2})	Cycle life	Capacity retention (%)
200	Zinc foil	Aqueous	30.6	3.7	100	94
400	Zinc foil	Aqueous	60.6	7.3	50	95
600	Zinc foil	Aqueous	81.5	9.6	40	95
800	Zinc foil	Aqueous	104.4	12.2	25	96
900	Zinc foil	Aqueous	113.5	13.5	20	96
200	PZPC	Aqueous	29.1	3.6	500	73
400	PZPC	Aqueous	60.0	7.2	220	80
200	Zinc foil	FS-gel	31.1	3.8	280	72
400	Zinc foil	FS-gel	61.9	7.4	180	80
200	PZPC	FS-gel	31.2	3.8	600	72
270	PZPC	FS-gel	42.3	5.1	520	74
340	PZPC	FS-gel	51.8	6.2	430	76
400	PZPC	FS-gel	61.2	7.3	340	74
500	PZPC	FS-gel	74.9	8.8	270	78

7.2. Future works

Besides the achievements developed in this work for high-performance ARZLB, there is still room for further improvement of the battery for commercialization. Based on the results of this thesis, the following recommendations are provided for future research.

I. Additives inside aqueous electrolytes are an essential component to tune the performance of ARZLBs and protect the zinc electrode. The underlying mechanism of additive behavior is based on the substrate effect or adsorption on the electrode surface to optimize the current distribution or to block the formation sites of zinc dendrites and slow down the rate of zinc deposition. However, additives can also increase the resistance of the electrolyte and the zinc electrode which subsequently affects the overall performance of aqueous batteries. There are vast numbers of organic and inorganic additives with proven track records of success in ARZLBs and other zinc-based batteries as reviewed in Chapter 2. Attention should be paid to the exploration and optimization of various additives and examination of a combination of additives for the current system. The selected additives can be added to the FS-gel electrolyte to further optimize the zinc deposition during the charging process and to extend the durability of the battery.

II. The current performance evaluation of the battery has been conducted at room temperature. For the commercialization of the proposed system, a detailed experimental study is required for the performance evaluation of the zinc/Li-ion battery at various temperatures including freezing and sub-zero temperatures. This kind of investigation would reveal the actual performance of the battery in the harsh weather conditions that should meet the requirements for Canadian winters before commercialization.

III. For battery scale-up, the battery cells can be connected in series or/and in parallel to expand the discharge voltage or/and total capacity of the battery pack, respectively. As the size of the battery increases, a high amount of hydrogen and oxygen can be generated as a result of water-splitting reactions upon cycling. Therefore, detailed engineering is required for investigation on the battery pack design to ensure maximum safety during battery operation. For instance, the battery pack can be equipped with safety valves to allow the release of excess generated gasses as can be seen in the valve-regulated lead-acid batteries. A proper battery pack design may also facilitate the recombination of generated hydrogen and oxygen gas inside a sealed battery to prevent it from drying out during cycling. Moreover, the long-term performance evaluation of the prototype battery is an important step before commercialization. During the long-term performance evaluation, some valuable information including battery maintenance criteria (e.g., DDI water refilling in a specific period) can be obtained. This information is beneficial for designing a proper battery pack with good sealing to minimize the maintenance of the battery or even introducing a maintenance-free prototype design.

References

(1) International Energy Outlook 2019 with Projections to 2050; Washington, DC, **2019**.

(2) Chen, H.; Cong, T. N.; Yang, W.; Tan, C.; Li, Y.; Ding, Y. Progress in Electrical Energy Storage System: A Critical Review. *Prog. Nat. Sci.* **2009**, *19* (3), 291–312.

(3) Amin, S. M.; Wollenberg, B. F. Toward a Smart Grid: Power Delivery for the 21st Century. *IEEE Power Energy Mag.* **2005**, *3* (5), 34–41.

(4) Phuangpornpitak, N.; Tia, S. Opportunities and Challenges of Integrating Renewable Energy in Smart Grid System. *Energy Procedia* **2013**, *34*, 282–290.

(5) Abbas A. Akhil, Georgianne Huff, Aileen B. Currier, Benjamin C. Kaun, D. M. R.; Stella Bingqing Chen, Andrew L. Cotter, Dale T. Bradshaw, and W. D. G. *DOE/EPRI Electricity Storage Handbook in Collaboration with NRECA*; 2015.

(6) Dunn, B.; Kamath, H.; Tarascon, J.-M. Electrical Energy Storage for the Grid: A Battery of Choices. *Science (80-.).* **2011**, *334* (6058), 928 LP – 935.

(7) Pan, H.; Shao, Y.; Yan, P.; Cheng, Y.; Han, K. S.; Nie, Z.; Wang, C.; Yang, J.; Li, X.; Bhattacharya, P.; et al. Reversible Aqueous Zinc/Manganese Oxide Energy Storage from Conversion Reactions. *Nat. Energy* **2016**, *1*, 16039.

(8) Perry, M. L.; Weber, A. Z. Advanced Redox-Flow Batteries: A Perspective. *J. Electrochem. Soc.* **2016**, *163* (1), A5064–A5067.

(9) Gubler, L. Membranes and Separators for Redox Flow Batteries. *Curr. Opin. Electrochem.* **2019**, *18*, 31–36.

(10) Yan, J.; Wang, J.; Liu, H.; Bakenov, Z.; Gosselink, D.; Chen, P. Rechargeable Hybrid Aqueous Batteries. *J. Power Sources* **2012**, *216*, 222–226.

(11) Zhu, W. H.; Zhu, Y.; Tatarchuk, B. J. Self-Discharge Characteristics and Performance Degradation of Ni-MH Batteries for Storage Applications. *Int. J. Hydrogen Energy* **2014**, *39* (34), 19789–19798.

(12) Tanabe, E. H.; Schlemmer, D. F.; Aguiar, M. L.; Dotto, G. L.; Bertuol, D. A. Recovery of Valuable Materials from Spent NIMH Batteries Using Spouted Bed Elutriation. *J. Environ. Manage.* **2016**, *171*, 177–183.

(13) Liu, Z.; Huang, Y.; Huang, Y.; Yang, Q.; Li, X.; Huang, Z.; Zhi, C. Voltage Issue of Aqueous Rechargeable Metal-Ion Batteries. *Chem. Soc. Rev.* **2020**, *49* (1), 180–232.

(14) Huang, S.; Zhu, J.; Tian, J.; Niu, Z. Recent Progress in the Electrolytes of Aqueous Zinc-

Ion Batteries. *Chem. – A Eur. J.* **2019**, *25* (64), 14480–14494.

(15) Tarascon, J.-M.; Armand, M. Issues and Challenges Facing Rechargeable Lithium Batteries. *Nature* **2001**, *414* (6861), 359–367.

(16) Alias, N.; Mohamad, A. A. Advances of Aqueous Rechargeable Lithium-Ion Battery: A Review. *J. Power Sources* **2015**, *274*, 237–251.

(17) Li, W.; Dahn, J. R.; Wainwright, D. S. Rechargeable Lithium Batteries with Aqueous Electrolytes. *Science (80-.).* **1994**, *264* (5162), 1115 LP – 1118.

(18) Kim, H.; Hong, J.; Park, K.-Y.; Kim, H.; Kim, S.-W.; Kang, K. Aqueous Rechargeable Li and Na Ion Batteries. *Chem. Rev.* **2014**, *114* (23), 11788–11827.

(19) Chang, Z.; Li, C.; Wang, Y.; Chen, B.; Fu, L.; Zhu, Y.; Zhang, L.; Wu, Y.; Huang, W. A Lithium Ion Battery Using an Aqueous Electrolyte Solution. *Sci. Rep.* **2016**, *6*, 28421.

(20) Yesibolati, N.; Umirov, N.; Koishybay, A.; Omarova, M.; Kurmanbayeva, I.; Zhang, Y.; Zhao, Y.; Bakenov, Z. High Performance Zn/LiFePO4 Aqueous Rechargeable Battery for Large Scale Applications. *Electrochim. Acta* **2015**, *152*, 505–511.

(21) Wang, F.; Borodin, O.; Gao, T.; Fan, X.; Sun, W.; Han, F.; Faraone, A.; Dura, J. A.; Xu, K.; Wang, C. Highly Reversible Zinc Metal Anode for Aqueous Batteries. *Nat. Mater.* **2018**.

(22) Xu, W.; Wang, Y. Recent Progress on Zinc-Ion Rechargeable Batteries. *Nano-Micro Lett.* **2019**, *11* (1), 90.

(23) Suo, L.; Oh, D.; Lin, Y.; Zhuo, Z.; Borodin, O.; Gao, T.; Wang, F.; Kushima, A.; Wang, Z.; Kim, H.-C.; et al. How Solid-Electrolyte Interphase Forms in Aqueous Electrolytes. *J. Am. Chem. Soc.* **2017**, *139* (51), 18670–18680.

(24) Suo, L.; Borodin, O.; Gao, T.; Olguin, M.; Ho, J.; Fan, X.; Luo, C.; Wang, C.; Xu, K. "Water-in-Salt" Electrolyte Enables High-Voltage Aqueous Lithium-Ion Chemistries. *Science (80-.).* **2015**, *350* (6263), 938 LP – 943.

(25) Trudgeon, D. P.; Qiu, K.; Li, X.; Mallick, T.; Taiwo, O. O.; Chakrabarti, B.; Yufit, V.; Brandon, N. P.; Crevillen-Garcia, D.; Shah, A. Screening of Effective Electrolyte Additives for Zinc-Based Redox Flow Battery Systems. *J. Power Sources* **2019**, *412*, 44–54.

(26) Xu, K. Electrolytes and Interphases in Li-Ion Batteries and Beyond. *Chem. Rev.* **2014**, *114* (23), 11503–11618.

(27) Zhi, J.; Yazdi, A. Z.; Valappil, G.; Haime, J.; Chen, P. Artificial Solid Electrolyte Interphase for Aqueous Lithium Energy Storage Systems. *Sci. Adv.* **2017**, *3* (9), e1701010.

(28) Robinson, D. M.; Go, Y. B.; Greenblatt, M.; Dismukes, G. C. Water Oxidation by λ-MnO2: Catalysis by the Cubical Mn4O4 Subcluster Obtained by Delithiation of Spinel LiMn2O4. *J. Am. Chem. Soc.* **2010**, *132* (33), 11467–11469.

(29) Reddy, T. B. *Linden's Handbook of Batteries, Fourth Edition*, 4th ed.; McGraw-Hill Education: New York, 2011.

(30) Li, W.; McKinnon, W. R.; Dahn, J. R. Lithium Intercalation from Aqueous Solutions. *J. Electrochem. Soc.* **1994**, *141* (9), 2310–2316.

(31) Luo, J.-Y.; Cui, W.-J.; He, P.; Xia, Y.-Y. Raising the Cycling Stability of Aqueous Lithium-Ion Batteries by Eliminating Oxygen in the Electrolyte. *Nat Chem* **2010**, *2* (9), 760–765.

(32) Zhou, Z.; Xiang, A.; Xia, M.; Zhou, N. Advanced LiTi2(PO4)3 Anode with High Performance for Aqueous Rechargeable Lithium Battery. *Ceram. Int.* **2018**, *44* (17), 21599–21606.

(33) Ao, H.; Zhao, Y.; Zhou, J.; Cai, W.; Zhang, X.; Zhu, Y.; Qian, Y. Rechargeable Aqueous Hybrid Ion Batteries: Developments and Prospects. *J. Mater. Chem. A* **2019**, *7* (32), 18708–18734.

(34) Pei, W.; Hui, Y.; Huaquan, Y. Electrochemical Behavior of Li□Mn Spinel Electrode Material in Aqueous Solution. *J. Power Sources* **1996**, *63* (2), 275–278.

(35) Manickam, M.; Singh, P.; Thurgate, S.; Prince, K. Redox Behavior and Surface Characterization of LiFePO4 in Lithium Hydroxide Electrolyte. *J. Power Sources* **2006**, *158* (1), 646–649.

(36) He, P.; Liu, J.-L.; Cui, W.-J.; Luo, J.-Y.; Xia, Y.-Y. Investigation on Capacity Fading of LiFePO4 in Aqueous Electrolyte. *Electrochim. Acta* **2011**, *56* (5), 2351–2357.

(37) Li, H.; Ma, L.; Han, C.; Wang, Z.; Liu, Z.; Tang, Z.; Zhi, C. Advanced Rechargeable Zinc-Based Batteries: Recent Progress and Future Perspectives. *Nano Energy* **2019**, *62*, 550–587.

(38) Khor, A.; Leung, P.; Mohamed, M. R.; Flox, C.; Xu, Q.; An, L.; Wills, R. G. A.; Morante, J. R.; Shah, A. A. Review of Zinc-Based Hybrid Flow Batteries: From Fundamentals to Applications. *Mater. Today Energy* **2018**, *8*, 80–108.

(39) Fu, J.; Cano, Z. P.; Park, M. G.; Yu, A.; Fowler, M.; Chen, Z. Electrically Rechargeable Zinc–Air Batteries: Progress, Challenges, and Perspectives. *Adv. Mater.* **2017**, *29* (7), 1604685.

(40) Han, C.; Li, W.; Liu, H. K.; Dou, S.; Wang, J. Principals and Strategies for Constructing a

Highly Reversible Zinc Metal Anode in Aqueous Batteries. *Nano Energy* **2020**, *74*, 104880.

(41) Mainar, A. R.; Iruin, E.; Colmenares, L. C.; Kvasha, A.; de Meatza, I.; Bengoechea, M.; Leonet, O.; Boyano, I.; Zhang, Z.; Blazquez, J. A. An Overview of Progress in Electrolytes for Secondary Zinc-Air Batteries and Other Storage Systems Based on Zinc. *J. Energy Storage* **2018**, *15*, 304–328.

(42) Krężel, A.; Maret, W. The Biological Inorganic Chemistry of Zinc Ions. *Arch. Biochem. Biophys.* **2016**, *611*, 3–19.

(43) Mitha, A.; Yazdi, A. Z.; Ahmed, M.; Chen, P. Surface Adsorption of Polyethylene Glycol to Suppress Dendrite Formation on Zinc Anodes in Rechargeable Aqueous Batteries. *ChemElectroChem* **2018**, *5* (17), 2409–2418.

(44) Cui, Y.; Yuan, Z.; Zhuang, Q.; Sun, Z. Investigation of Lithium Ion Kinetics through LiMn2O4 Electrode in Aqueous Li2SO4 Electrolyte. *J. Appl. Electrochem.* **2012**, *42*.

(45) Hlongwa, N.; Ikpo, C.; Ross, N.; Nzaba, M.; Ndipingwi, M.; Baker, P.; Iwuoha, E. Electrochemical Studies on Novel LiMnPO4 Coated with Magnesium Oxide-Gold Composite Thin Film in Aqueous Electrolytes. *J. Nano Res.* **2016**, *44*, 90–99.

(46) Ruffo, R.; La Mantia, F.; Wessells, C.; Huggins, R. A.; Cui, Y. Electrochemical Characterization of LiCoO2 as Rechargeable Electrode in Aqueous LiNO3 Electrolyte. *Solid State Ionics* **2011**, *192* (1), 289–292.

(47) Wang, F.; Xiao, S.; Chang, Z.; Yang, Y.; Wu, Y. Nanoporous LiNi1/3Co1/3Mn1/3O2 as an Ultra-Fast Charge Cathode Material for Aqueous Rechargeable Lithium Batteries. *Chem. Commun.* **2013**, *49* (80), 9209–9211.

(48) Han, M.; Zhi, J.; Hoang, T. K. A.; Li, Y.; Li, L.; Chen, P. Artificial Solid Electrolyte Interphase for Thermally Stable Rechargeable Aqueous Zinc Batteries. *J. Power Sources* **2019**, *441*, 227171.

(49) Shao, M.; Deng, J.; Zhong, F.; Cao, Y.; Ai, X.; Qian, J.; Yang, H. An All-Vanadium Aqueous Lithium Ion Battery with High Energy Density and Long Lifespan. *Energy Storage Mater.* **2019**, *18*, 92–99.

(50) Ndipingwi, M. M.; Ikpo, C. O.; Hlongwa, N. W.; Dywili, N.; Djoumessi Yonkeu, A. L.; Iwuoha, E. I. Crystal Chemistry and Lithium-Ion Intercalation Properties of Lithium Manganese Silicate Cathode for Aqueous Rechargeable Li-Ion Batteries. *J. Appl. Electrochem.* **2019**, *49* (5), 465–474.

(51) Zhu, X.; Hoang, T.; Chen, P. Novel Carbon Materials in the Cathode Formulation for High Rate Rechargeable Hybrid Aqueous Batteries. *Energies* **2017**, *10*, 1844.

(52) Yuan, G.; Geng, M.; Zhang, P.; Li, B. Hybrids of LiMn2O4 Nanoparticles Anchored on Carbon Nanotubes/Graphene Sheets as Long-Cycle-Life Cathode Material for Rechargeable Hybrid Aqueous Batteries. *J. Solid State Electrochem.* **2020**, *24* (3), 601–607.

(53) Tang, W.; Tian, S.; Liu, L. L.; Li, L.; Zhang, H. P.; Yue, Y. B.; Bai, Y.; Wu, Y. P.; Zhu, K. Nanochain LiMn2O4 as Ultra-Fast Cathode Material for Aqueous Rechargeable Lithium Batteries. *Electrochem. commun.* **2011**, *13* (2), 205–208.

(54) Tang, W.; Hou, Y.; Wang, F.; Liu, L.; Wu, Y.; Zhu, K. LiMn2O4 Nanotube as Cathode Material of Second-Level Charge Capability for Aqueous Rechargeable Batteries. *Nano Lett.* **2013**, *13* (5), 2036–2040.

(55) Chen, L.; Li, D.; Zheng, X.; Chen, L.; Zhang, Y.; Liang, Z.; Feng, J.; Si, P.; Lou, J.; Ci, L. Integrated Nanocomposite of LiMn2O4/Graphene/Carbon Nanotubes with Pseudocapacitive Properties as Superior Cathode for Aqueous Hybrid Capacitors. *J. Electroanal. Chem.* **2019**, *842*, 74–81.

(56) Qu, Q.; Fu, L.; Zhan, X.; Samuelis, D.; Maier, J.; Li, L.; Tian, S.; Li, Z.; Wu, Y. Porous LiMn2O4 as Cathode Material with High Power and Excellent Cycling for Aqueous Rechargeable Lithium Batteries. *Energy Environ. Sci.* **2011**, *4* (10), 3985–3990.

(57) Zhi, J.; Bertens, K.; Yazdi, A. Z.; Chen, P. Acrylonitrile Copolymer/Graphene Skinned Cathode for Long Cycle Life Rechargeable Hybrid Aqueous Batteries at High-Temperature. *Electrochim. Acta* **2018**, *268*, 248–255.

(58) Köhler, J.; Makihara, H.; Uegaito, H.; Inoue, H.; Toki, M. LiV3O8: Characterization as Anode Material for an Aqueous Rechargeable Li-Ion Battery System. *Electrochim. Acta* **2000**, *46* (1), 59–65.

(59) Ding, M.; Zhao, M.; Gong, H.; Zheng, Q.; Song, X. Novel High-Rate Performance of Dual Carbon-Coated Li3V2(PO4)3 Materials Used in an Aqueous Electrolyte. *Ind. Eng. Chem. Res.* **2019**, *58* (2), 790–797.

(60) Geng, L.; Foley, S. B.; Dong, H.; Koenig Jr., G. M. LiFePO4-Accelerated Change in Surface and Electrochemical Properties in Aqueous Systems Induced by Mechanical Agitation. *Energy Technol.* **2019**, *7* (3), 1801116.

(61) Zhang, Y.; Xin, P.; Yao, Q. Electrochemical Performance of LiFePO4/C Synthesized by

Sol-Gel Method as Cathode for Aqueous Lithium Ion Batteries. *J. Alloys Compd.* **2018**, *741*, 404–408.

(62) Fu, Y.; Wei, Q.; Zhang, G.; Zhong, Y.; Moghimian, N.; Tong, X.; Sun, S. $LiFePO_4$-Graphene Composites as High-Performance Cathodes for Lithium-Ion Batteries: The Impact of Size and Morphology of Graphene. *Mater. (Basel, Switzerland)* **2019**, *12* (6), 842.

(63) Noerochim, L.; Yurwendra, A. O.; Susanti, D. Effect of Carbon Coating on the Electrochemical Performance of LiFePO4/C as Cathode Materials for Aqueous Electrolyte Lithium-Ion Battery. *Ionics (Kiel).* **2016**, *22* (3), 341–346.

(64) Tron, A.; Jo, Y. N.; Oh, S. H.; Park, Y. D.; Mun, J. Surface Modification of the LiFePO4 Cathode for the Aqueous Rechargeable Lithium Ion Battery. *ACS Appl. Mater. Interfaces* **2017**, *9* (14), 12391–12399.

(65) Duan, W.; Zhao, M.; Mizuta, Y.; Li, Y.; Xu, T.; Wang, F.; Moriga, T.; Song, X. Superior Electrochemical Performance of a Novel LiFePO4/C/CNTs Composite for Aqueous Rechargeable Lithium-Ion Batteries. *Phys. Chem. Chem. Phys.* **2020**, *22* (4), 1953–1962.

(66) Wang, F.; Suo, L.; Liang, Y.; Yang, C.; Han, F.; Gao, T.; Sun, W.; Wang, C. Spinel LiNi0.5Mn1.5O4 Cathode for High-Energy Aqueous Lithium-Ion Batteries. *Adv. Energy Mater.* **2017**, *7* (8), 1600922.

(67) Yang, C.; Chen, J.; Ji, X.; Pollard, T. P.; Lü, X.; Sun, C.-J.; Hou, S.; Liu, Q.; Liu, C.; Qing, T.; et al. Aqueous Li-Ion Battery Enabled by Halogen Conversion–Intercalation Chemistry in Graphite. *Nature* **2019**, *569* (7755), 245–250.

(68) Yan, Z.; Wang, E.; Jiang, L.; Sun, G. Superior Cycling Stability and High Rate Capability of Three-Dimensional Zn/Cu Foam Electrodes for Zinc-Based Alkaline Batteries. *RSC Adv.* **2015**, *5* (102), 83781–83787.

(69) Parker, J. F.; Chervin, C. N.; Nelson, E. S.; Rolison, D. R.; Long, J. W. Wiring Zinc in Three Dimensions Re-Writes Battery Performance-Dendrite-Free Cycling. *Energy Environ. Sci.* **2014**, *7* (3), 1117–1124.

(70) Parker, J. F.; Nelson, E. S.; Wattendorf, M. D.; Chervin, C. N.; Long, J. W.; Rolison, D. R. Retaining the 3D Framework of Zinc Sponge Anodes upon Deep Discharge in Zn–Air Cells. *ACS Appl. Mater. Interfaces* **2014**, *6* (22), 19471–19476.

(71) Parker, J.; Pala, I.; Chervin, C.; Long, J.; Rolison, D. Minimizing Shape Change at Zn Sponge Anodes in Rechargeable Ni–Zn Cells: Impact of Electrolyte Formulation. *J.*

Electrochem. Soc. **2016**, *163*, A351–A355.

(72) Parker, J. F.; Chervin, C. N.; Pala, I. R.; Machler, M.; Burz, M. F.; Long, J. W.; Rolison, D. R. Rechargeable Nickel–3D Zinc Batteries: An Energy-Dense, Safer Alternative to Lithium-Ion. *Science (80-.).* **2017**, *356* (6336), 415 LP – 418.

(73) Wang, Z.; Huang, J.; Guo, Z.; Dong, X.; Liu, Y.; Wang, Y.; Xia, Y. A Metal-Organic Framework Host for Highly Reversible Dendrite-Free Zinc Metal Anodes. *Joule* **2019**, *3* (5), 1289–1300.

(74) Kang, Z.; Wu, C.; Dong, L.; Liu, W.; Mou, J.; Zhang, J.; Chang, Z.; Jiang, B.; Wang, G.; Kang, F.; et al. 3D Porous Copper Skeleton Supported Zinc Anode toward High Capacity and Long Cycle Life Zinc Ion Batteries. *ACS Sustain. Chem. Eng.* **2019**, *7* (3), 3364–3371.

(75) Molkenova, A.; Belgibayeva, A.; Ibrayeva, D.; Sultanov, M.; Zhumagali, S.; Akhmetova, N.; Hara, T.; Bakenov, Z. A New Step in the Development of Zn/LiFePO4 Aqueous Battery. *Mater. Today Proc.* **2017**, *4* (3, Part A), 4452–4457.

(76) Akhmetova, N.; Orazbekova, G.; E.Kenzhegaliyeva; Mentbayeva, A.; Molkenova, A.; Bakenov, Z. Development of a Novel Gel-like Composite Polymer Separator for 3D Zn/LiFePO4 Aqueous Hybrid Ion Battery. *Mater. Today Proc.* **2018**, *5* (11, Part 1), 22871–22876.

(77) Ahmed, M.; Yazdi, A. Z.; Dayani, S. B.; Jahed, H.; Chen, P. Fabrication of Zinc Anodes for Aqueous Lithium-Ion Batteries by Supersonic Cold Spraying. *ChemElectroChem* **2019**, *6* (5), 1333–1337.

(78) Tao, H.; Tong, X.; Gan, L.; Zhang, S.; Zhang, X.; Liu, X. Effect of Adding Various Carbon Additives to Porous Zinc Anode in Rechargeable Hybrid Aqueous Battery. *J. Alloys Compd.* **2016**, *658*, 119–124.

(79) Zhao, Z.; Zhao, J.; Hu, Z.; Li, J.; Li, J.; Zhang, Y.; Wang, C.; Cui, G. Long-Life and Deeply Rechargeable Aqueous Zn Anodes Enabled by a Multifunctional Brightener-Inspired Interphase. *Energy Environ. Sci.* **2019**, *12* (6), 1938–1949.

(80) Li, W.; Wang, K.; Zhou, M.; Zhan, H.; Cheng, S.; Jiang, K. Advanced Low-Cost, High-Voltage, Long-Life Aqueous Hybrid Sodium/Zinc Batteries Enabled by a Dendrite-Free Zinc Anode and Concentrated Electrolyte. *ACS Appl. Mater. Interfaces* **2018**, *10* (26), 22059–22066.

(81) Kang, L.; Cui, M.; Jiang, F.; Gao, Y.; Luo, H.; Liu, J.; Liang, W.; Zhi, C. Nanoporous

CaCO3 Coatings Enabled Uniform Zn Stripping/Plating for Long-Life Zinc Rechargeable Aqueous Batteries. *Adv. Energy Mater.* **2018**, *8* (25), 1801090.

(82) Zhao, K.; Wang, C.; Yu, Y.; Yan, M.; Wei, Q.; He, P.; Dong, Y.; Zhang, Z.; Wang, X.; Mai, L. Ultrathin Surface Coating Enables Stabilized Zinc Metal Anode. *Adv. Mater. Interfaces* **2018**, *5* (16), 1800848.

(83) Liang, P.; Yi, J.; Liu, X.; Wu, K.; Wang, Z.; Cui, J.; Liu, Y.; Wang, Y.; Xia, Y.; Zhang, J. Highly Reversible Zn Anode Enabled by Controllable Formation of Nucleation Sites for Zn-Based Batteries. *Adv. Funct. Mater.* **2020**, *30* (13), 1908528.

(84) Sun, K. E. K.; Hoang, T. K. A.; Doan, T. N. L.; Yu, Y.; Zhu, X.; Tian, Y.; Chen, P. Suppression of Dendrite Formation and Corrosion on Zinc Anode of Secondary Aqueous Batteries. *ACS Appl. Mater. Interfaces* **2017**, *9* (11), 9681–9687.

(85) Sun, K. E. K.; Hoang, T. K. A.; Doan, T. N. L.; Yu, Y.; Chen, P. Highly Sustainable Zinc Anodes for a Rechargeable Hybrid Aqueous Battery. *Chem. – A Eur. J.* **2018**, *24* (7), 1667–1673.

(86) Huang, J.; Guo, Z.; Ma, Y.; Bin, D.; Wang, Y.; Xia, Y. Recent Progress of Rechargeable Batteries Using Mild Aqueous Electrolytes. *Small Methods* **2019**, *3* (1), 1800272.

(87) Zhang, X. SECONDARY BATTERIES – ZINC SYSTEMS | Zinc Electrodes: Overview. In *Encyclopedia of Electrochemical Power Sources*; 2009; pp 454–468.

(88) Wang, Y.; Yang, S.-Z.; You, Y.; Feng, Z.; Zhu, W.; Gariépy, V.; Xia, J.; Commarieu, B.; Darwiche, A.; Guerfi, A.; et al. High-Capacity and Long-Cycle Life Aqueous Rechargeable Lithium-Ion Battery with the FePO4 Anode. *ACS Appl. Mater. Interfaces* **2018**, *10* (8), 7061–7068.

(89) Yuan, X.; Wu, X.; Zeng, X.-X.; Wang, F.; Wang, J.; Zhu, Y.; Fu, L.; Wu, Y.; Duan, X. A Fully Aqueous Hybrid Electrolyte Rechargeable Battery with High Voltage and High Energy Density. *Adv. Energy Mater.* **2020**, *10* (40), 2001583.

(90) Li, H.; Weng, G.; Li, C. Y. V.; Chan, K.-Y. Three Electrolyte High Voltage Acid–Alkaline Hybrid Rechargeable Battery. *Electrochim. Acta* **2011**, *56* (25), 9420–9425.

(91) Zhang, J.; Jiang, G.; Xu, P.; Ghorbani Kashkooli, A.; Mousavi, M.; Yu, A.; Chen, Z. An All-Aqueous Redox Flow Battery with Unprecedented Energy Density. *Energy Environ. Sci.* **2018**, *11* (8), 2010–2015.

(92) Li, M.; Luo, S.; Qian, Y.; Zhang, W.; Jiang, L.; Shen, J. Effect of Additives on

Electrodeposition of Nanocrystalline Zinc from Acidic Sulfate Solutions. *J. Electrochem. Soc.* **2007**, *154*, D567–D571.

(93) Hao, J.; Long, J.; Li, B.; Li, X.; Zhang, S.; Yang, F.; Zeng, X.; Yang, Z.; Pang, W. K.; Guo, Z. Toward High-Performance Hybrid Zn-Based Batteries via Deeply Understanding Their Mechanism and Using Electrolyte Additive. *Adv. Funct. Mater.* **2019**, *29* (34), 1903605.

(94) Wu, X.; Li, Y.; Li, C.; He, Z.; Xiang, Y.; Xiong, L.; Chen, D.; Yu, Y.; Sun, K.; He, Z.; et al. The Electrochemical Performance Improvement of LiMn2O4/Zn Based on Zinc Foil as the Current Collector and Thiourea as an Electrolyte Additive. *J. Power Sources* **2015**, *300*, 453–459.

(95) Tron, A.; Jeong, S.; Park, Y. D.; Mun, J. Aqueous Lithium-Ion Battery of Nano-LiFePO4 with Antifreezing Agent of Ethyleneglycol for Low-Temperature Operation. *ACS Sustain. Chem. Eng.* **2019**, *7* (17), 14531–14538.

(96) Kim, H.-I.; Shin, H.-C. SnO Additive for Dendritic Growth Suppression of Electrolytic Zinc. *J. Alloys Compd.* **2015**, *645*, 7–10.

(97) Otani, T.; Fukunaka, Y.; Homma, T. Effect of Lead and Tin Additives on Surface Morphology Evolution of Electrodeposited Zinc. *Electrochim. Acta* **2017**, *242*, 364–372.

(98) Zhao, J.; Li, Y.; Peng, X.; Dong, S.; Ma, J.; Cui, G.; Chen, L. High-Voltage Zn/LiMn0.8Fe0.2PO4 Aqueous Rechargeable Battery by Virtue of "Water-in-Salt" Electrolyte. *Electrochem. commun.* **2016**, *69*, 6–10.

(99) Zhong, X.; Wang, F.; Ding, Y.; Duan, L.; Shi, F.; Wang, C. Water-in-Salt Electrolyte Zn/LiFePO4 Batteries. *J. Electroanal. Chem.* **2020**, *867*, 114193.

(100) Wang, L.; Zhang, Y.; Hu, H.; Shi, H.-Y.; Song, Y.; Guo, D.; Liu, X.-X.; Sun, X. A Zn(ClO4)2 Electrolyte Enabling Long-Life Zinc Metal Electrodes for Rechargeable Aqueous Zinc Batteries. *ACS Appl. Mater. Interfaces* **2019**, *11* (45), 42000–42005.

(101) Cheng, X.; Pan, J.; Zhao, Y.; Liao, M.; Peng, H. Gel Polymer Electrolytes for Electrochemical Energy Storage. *Adv. Energy Mater.* **2018**, *8* (7), 1702184.

(102) Wang, Z.; Li, H.; Tang, Z.; Liu, Z.; Ruan, Z.; Ma, L.; Yang, Q.; Wang, D.; Zhi, C. Hydrogel Electrolytes for Flexible Aqueous Energy Storage Devices. *Adv. Funct. Mater.* **2018**, *28* (48), 1804560.

(103) Lu, C.; Hoang, T. K. A.; Doan, T. N. L.; Acton, M.; Zhao, H.; Guan, W.; Chen, P. Influence of Different Silica Gelling Agents on the Performance of Aqueous Gel Electrolytes. *J. Ind.*

Eng. Chem. **2016**, *42*, 101–106.

(104) Banik, S.; Akolkar, R. Suppressing Dendrite Growth during Zinc Electrodeposition by PEG-200 Additive. *J. Electrochem. Soc.* **2013**, *160*, D519–D523.

(105) Ballesteros, J. C.; Díaz-Arista, P.; Meas, Y.; Ortega, R.; Trejo, G. Zinc Electrodeposition in the Presence of Polyethylene Glycol 20000. *Electrochim. Acta* **2007**, *52* (11), 3686–3696.

(106) Xiong, W.; Hoang, T. K. A.; Yang, D.; Liu, Y.; Ahmed, M.; Xu, J.; Qiu, X.; Chen, P. Electrolyte Engineering for a Highly Stable, Rechargeable Hybrid Aqueous Battery. *J. Energy Storage* **2019**, *26*, 100920.

(107) Hoang, T. K. A.; Doan, T. N. L.; Cho, J. H.; Su, J. Y. J.; Lee, C.; Lu, C.; Chen, P. Sustainable Gel Electrolyte Containing Pyrazole as Corrosion Inhibitor and Dendrite Suppressor for Aqueous Zn/LiMn2O4 Battery. *ChemSusChem* **2017**, *10* (13), 2816–2822.

(108) Hoang, T. K. A.; Acton, M.; Chen, H. T. H.; Huang, Y.; Doan, T. N. L.; Chen, P. Sustainable Gel Electrolyte Containing Pb2+ as Corrosion Inhibitor and Dendrite Suppressor for the Zinc Anode in the Rechargeable Hybrid Aqueous Battery. *Mater. Today Energy* **2017**, *4*, 34–40.

(109) Xiong, W.; Yang, D.; Hoang, T. K. A.; Ahmed, M.; Zhi, J.; Qiu, X.; Chen, P. Controlling the Sustainability and Shape Change of the Zinc Anode in Rechargeable Aqueous Zn/LiMn2O4 Battery. *Energy Storage Mater.* **2018**, *15*, 131–138.

(110) Huang, J.; Chi, X.; Han, Q.; Liu, Y.; Du, Y.; Yang, J.; Liu, Y. Thickening and Homogenizing Aqueous Electrolyte towards Highly Efficient and Stable Zn Metal Batteries. *J. Electrochem. Soc.* **2019**, *166*, A1211–A1216.

(111) Hoang, T. K. A.; Doan, T. N. L.; Lu, C.; Ghaznavi, M.; Zhao, H.; Chen, P. Performance of Thixotropic Gel Electrolytes in the Rechargeable Aqueous Zn/LiMn2O4 Battery. *ACS Sustain. Chem. Eng.* **2017**, *5* (2), 1804–1811.

(112) Pan, J. L.; Yin, Y.; Wen, Y. H.; Bai, S. L.; Cheng, J.; Cao, G. P.; Yang, Y. S. A Silica-Based Gel Electrolyte System for Improving the Cycle Performance of LiFePO4 Batteries in an Aqueous Medium. *RSC Adv.* **2016**, *6* (3), 2176–2182.

(113) Zhu, M.; Wang, X.; Tang, H.; Wang, J.; Hao, Q.; Liu, L.; Li, Y.; Zhang, K.; Schmidt, O. G. Antifreezing Hydrogel with High Zinc Reversibility for Flexible and Durable Aqueous Batteries by Cooperative Hydrated Cations. *Adv. Funct. Mater.* **2020**, *30* (6), 1907218.

(114) Wang, X.; Hou, Y.; Zhu, Y.; Wu, Y.; Holze, R. An Aqueous Rechargeable Lithium Battery

Using Coated Li Metal as Anode. *Sci. Rep.* **2013**, *3* (1), 1401.

(115) Zhao, Y.; Zhang, Y.; Sun, H.; Dong, X.; Cao, J.; Wang, L.; Xu, Y.; Ren, J.; Hwang, Y.; Son, I. H.; et al. A Self-Healing Aqueous Lithium-Ion Battery. *Angew. Chemie Int. Ed.* **2016**, *55* (46), 14384–14388.

(116) Zhang, S.; Yu, N.; Zeng, S.; Zhou, S.; Chen, M.; Di, J.; Li, Q. An Adaptive and Stable Bio-Electrolyte for Rechargeable Zn-Ion Batteries. *J. Mater. Chem. A* **2018**, *6* (26), 12237–12243.

(117) Zeng, Y.; Zhang, X.; Meng, Y.; Yu, M.; Yi, J.; Wu, Y.; Lu, X.; Tong, Y. Achieving Ultrahigh Energy Density and Long Durability in a Flexible Rechargeable Quasi-Solid-State Zn–MnO2 Battery. *Adv. Mater.* **2017**, *29* (26), 1700274.

(118) He, B.; Zhang, Q.; Li, L.; Sun, J.; Man, P.; Zhou, Z.; Li, Q.; Guo, J.; Xie, L.; Li, C.; et al. High-Performance Flexible All-Solid-State Aqueous Rechargeable Zn–MnO2 Microbatteries Integrated with Wearable Pressure Sensors. *J. Mater. Chem. A* **2018**, *6* (30), 14594–14601.

(119) Han, Q.; Chi, X.; Liu, Y.; Wang, L.; Du, Y.; Ren, Y.; Liu, Y. An Inorganic Salt Reinforced Zn2+-Conducting Solid-State Electrolyte for Ultra-Stable Zn Metal Batteries. *J. Mater. Chem. A* **2019**, *7* (39), 22287–22295.

(120) SAITO, M.; NISHIMURA, T.; YANAGIDA, D.; SATOH, S.; NISHIUMI, K.; AKUTA, R.; OKAMOTO, K. Suppression of Dendrite Formation by Using a Hydrogel Separator for Zinc Alkaline Battery. *Electrochemistry* **2017**, *85* (10), 637–639.

(121) Zhao, J.; Sonigara, K. K.; Li, J.; Zhang, J.; Chen, B.; Zhang, J.; Soni, S. S.; Zhou, X.; Cui, G.; Chen, L. A Smart Flexible Zinc Battery with Cooling Recovery Ability. *Angew. Chemie Int. Ed.* **2017**, *56* (27), 7871–7875.

(122) Chen, S.; Lan, R.; Humphreys, J.; Tao, S. Perchlorate Based "Oversaturated Gel Electrolyte" for an Aqueous Rechargeable Hybrid Zn–Li Battery. *ACS Appl. Energy Mater.* **2020**, *3* (3), 2526–2536.

(123) Han, Q.; Chi, X.; Zhang, S.; Liu, Y.; Zhou, B.; Yang, J.; Liu, Y. Durable, Flexible Self-Standing Hydrogel Electrolytes Enabling High-Safety Rechargeable Solid-State Zinc Metal Batteries. *J. Mater. Chem. A* **2018**, *6* (45), 23046–23054.

(124) Du, Z.; Wood, D. L.; Daniel, C.; Kalnaus, S.; Li, J. Understanding Limiting Factors in Thick Electrode Performance as Applied to High Energy Density Li-Ion Batteries. *J. Appl.*

Electrochem. **2017**, *47* (3), 405–415.

(125) Armand, M.; Axmann, P.; Bresser, D.; Copley, M.; Edström, K.; Ekberg, C.; Guyomard, D.; Lestriez, B.; Novák, P.; Petranikova, M.; et al. Lithium-Ion Batteries – Current State of the Art and Anticipated Developments. *J. Power Sources* **2020**, *479*, 228708.

(126) Shi, B.; Shang, Y.; Pei, Y.; Pei, S.; Wang, L.; Heider, D.; Zhao, Y. Y.; Zheng, C.; Yang, B.; Yarlagadda, S.; et al. Low Tortuous, Highly Conductive, and High-Areal-Capacity Battery Electrodes Enabled by Through-Thickness Aligned Carbon Fiber Framework. *Nano Lett.* **2020**, *20* (7), 5504–5512.

(127) Wu, T.; Zhao, Z.; Zhang, J.; Zhang, C.; Guo, Y.; Cao, Y.; Pan, S.; Liu, Y.; Liu, P.; Ge, Y.; et al. Thick Electrode with Thickness-Independent Capacity Enabled by Assembled Two-Dimensional Porous Nanosheets. *Energy Storage Mater.* **2021**.

(128) Zheng, H.; Li, J.; Song, X.; Liu, G.; Battaglia, V. S. A Comprehensive Understanding of Electrode Thickness Effects on the Electrochemical Performances of Li-Ion Battery Cathodes. *Electrochim. Acta* **2012**, *71*, 258–265.

(129) Doherty, T.; Limthongkul, P.; Butros, A.; Duduta, M.; Cross, J. C. Electrochemical Slurry Compositions and Methods for Preparing the Same. Google Patents December 19, 2013.

(130) Ludwig, B.; Zheng, Z.; Shou, W.; Wang, Y.; Pan, H. Solvent-Free Manufacturing of Electrodes for Lithium-Ion Batteries. **2016**, *6*, 23150.

(131) Singh, M.; Kaiser, J.; Hahn, H. Thick Electrodes for High Energy Lithium Ion Batteries. *J. Electrochem. Soc.* **2015**, *162* (7), A1196–A1201.

(132) Chiang, Y. M.; Duduta, M.; Holman, R.; Limthongkul, P.; Tan, T. Semi-Solid Electrodes Having High Rate Capability. Google Patents June 19, 2014.

(133) Gomez, J.; Kalu, E. E.; Nelson, R.; Akpovo, C.; Weatherspoon, M. H.; Zheng, J. P. Binder-Free Electrode Fabrication by Electroless-Electrolytic Method. *ECS Electrochem. Lett.* **2012**, *1* (6), D25–D28.

(134) Kremer, L. S.; Hoffmann, A.; Danner, T.; Hein, S.; Prifling, B.; Westhoff, D.; Dreer, C.; Latz, A.; Schmidt, V.; Wohlfahrt-Mehrens, M. Manufacturing Process for Improved Ultra-Thick Cathodes in High-Energy Lithium-Ion Batteries. *Energy Technol.* **2020**, *8* (2), 1900167.

(135) Cho, Y.-D.; Fey, G. T.-K.; Kao, H.-M. The Effect of Carbon Coating Thickness on the Capacity of LiFePO4/C Composite Cathodes. *J. Power Sources* **2009**, *189* (1), 256–262.

(136) Liu, Y.; Zhang, M.; Li, Y.; Hu, Y.; Zhu, M.; Jin, H.; Li, W. Nano-Sized LiFePO4/C Composite with Core-Shell Structure as Cathode Material for Lithium Ion Battery. *Electrochim. Acta* **2015**, *176*, 689–693.

(137) Yu, D. Y. W.; Donoue, K.; Inoue, T.; Fujimoto, M.; Fujitani, S. Effect of Electrode Parameters on LiFePO4 Cathodes. *J. Electrochem. Soc.* **2006**, *153* (5), A835–A839.

(138) Yang, Q.; Liang, G.; Guo, Y.; Liu, Z.; Yan, B.; Wang, D.; Huang, Z.; Li, X.; Fan, J.; Zhi, C. Do Zinc Dendrites Exist in Neutral Zinc Batteries: A Developed Electrohealing Strategy to In Situ Rescue In-Service Batteries. *Adv. Mater.* **2019**, *31* (43), 1903778.

(139) Park, K.-Y.; Park, J.-W.; Seong, W. M.; Yoon, K.; Hwang, T.-H.; Ko, K.-H.; Han, J.-H.; Jaedong, Y.; Kang, K. Understanding Capacity Fading Mechanism of Thick Electrodes for Lithium-Ion Rechargeable Batteries. *J. Power Sources* **2020**, *468*, 228369.

(140) Wood, D. L.; Li, J.; Daniel, C. Prospects for Reducing the Processing Cost of Lithium Ion Batteries. *J. Power Sources* **2015**, *275*, 234–242.

(141) Danner, T.; Singh, M.; Hein, S.; Kaiser, J.; Hahn, H.; Latz, A. Thick Electrodes for Li-Ion Batteries: A Model Based Analysis. *J. Power Sources* **2016**, *334*, 191–201.

(142) Dai, Y.; Cai, L.; White, R. E. Capacity Fade Model for Spinel LiMn2O4Electrode. *J. Electrochem. Soc.* **2012**, *160* (1), A182–A190.

(143) Strauss, F.; Teo, J. H.; Schiele, A.; Bartsch, T.; Hatsukade, T.; Hartmann, P.; Janek, J.; Brezesinski, T. Gas Evolution in Lithium-Ion Batteries: Solid versus Liquid Electrolyte. *ACS Appl. Mater. Interfaces* **2020**, *12* (18), 20462–20468.

(144) Kim, Y. Mechanism of Gas Evolution from the Cathode of Lithium-Ion Batteries at the Initial Stage of High-Temperature Storage. *J. Mater. Sci.* **2013**, *48*.

(145) Rowden, B.; Garcia-Araez, N. A Review of Gas Evolution in Lithium Ion Batteries. *Energy Reports* **2020**, *6*, 10–18.

(146) Mao, C.; Ruther, R. E.; Geng, L.; Li, Z.; Leonard, D. N.; Meyer, H. M.; Sacci, R. L.; Wood, D. L. Evaluation of Gas Formation and Consumption Driven by Crossover Effect in High-Voltage Lithium-Ion Batteries with Ni-Rich NMC Cathodes. *ACS Appl. Mater. Interfaces* **2019**, *11* (46), 43235–43243.

(147) Elango, R.; Demortière, A.; De Andrade, V.; Morcrette, M.; Seznec, V. Thick Binder-Free Electrodes for Li–Ion Battery Fabricated Using Templating Approach and Spark Plasma Sintering Reveals High Areal Capacity. *Adv. Energy Mater.* **2018**, *8* (15), 1703031.

(148) Guoping, W.; Qingtang, Z.; Zuolong, Y.; MeiZheng, Q. The Effect of Different Kinds of Nano-Carbon Conductive Additives in Lithium Ion Batteries on the Resistance and Electrochemical Behavior of the LiCoO2 Composite Cathodes. *Solid State Ionics* **2008**, *179* (7), 263–268.

(149) Park, S.-H.; King, P. J.; Tian, R.; Boland, C. S.; Coelho, J.; Zhang, C. (John); McBean, P.; McEvoy, N.; Kremer, M. P.; Daly, D.; et al. High Areal Capacity Battery Electrodes Enabled by Segregated Nanotube Networks. *Nat. Energy* **2019**, *4* (7), 560–567.

(150) Jacques, E.; Kjell, M. H.; Zenkert, D.; Lindbergh, G.; Behm, M.; Willgert, M. Impact of Electrochemical Cycling on the Tensile Properties of Carbon Fibres for Structural Lithium-Ion Composite Batteries. *Compos. Sci. Technol.* **2012**, *72* (7), 792–798.

(151) Zhu, X.; Doan, T. N. L.; Yu, Y.; Tian, Y.; Sun, K. E. K.; Zhao, H.; Chen, P. Enhancing Rate Performance of LiMn2O4 Cathode in Rechargeable Hybrid Aqueous Battery by Hierarchical Carbon Nanotube/Acetylene Black Conductive Pathways. *Ionics (Kiel).* **2016**, *22* (1), 71–76.

(152) Tan, T.; Chiang, Y. M.; Ota, N.; Wilder, T.; Duduta, M. Asymmetric Battery Having a Semi-Solid Cathode and High Energy Density Anode. Google Patents September 6, 2016.

(153) Singh, M.; Kaiser, J.; Hahn, H. A Systematic Study of Thick Electrodes for High Energy Lithium Ion Batteries. *J. Electroanal. Chem.* **2016**, *782*, 245–249.

(154) Rao, M. C. LiMn2O4 Cathodes for Solid State Lithium-Ion Batteries-Energy Storage and Conversion. *J. Optoelectron. Biomed. Mater.* **2013**, *5*.

(155) Yasumitsu, M.; Kohei, M.; Hiromichi, K. Purity and Defect Characterization of Single-Wall Carbon Nanotubes Using Raman Spectroscopy. *J. Nanomater.* **2011**, *2011*.

(156) de las Casas, C.; Li, W. A Review of Application of Carbon Nanotubes for Lithium Ion Battery Anode Material. *J. Power Sources* **2012**, *208*, 74–85.

(157) Sun, W.; Suo, L.; Wang, F.; Eidson, N.; Yang, C.; Han, F.; Ma, Z.; Gao, T.; Zhu, M.; Wang, C. "Water-in-Salt" Electrolyte Enabled LiMn2O4/TiS2 Lithium-Ion Batteries. *Electrochem. commun.* **2017**, *82*, 71–74.

(158) Suo, L.; Borodin, O.; Sun, W.; Fan, X.; Yang, C.; Wang, F.; Gao, T.; Ma, Z.; Schroeder, M.; von Cresce, A.; et al. Advanced High-Voltage Aqueous Lithium-Ion Battery Enabled by "Water-in-Bisalt" Electrolyte. *Angew. Chemie Int. Ed.* **2016**, *55* (25), 7136–7141.

(159) Yang, C.; Ji, X.; Fan, X.; Gao, T.; Suo, L.; Wang, F.; Sun, W.; Chen, J.; Chen, L.; Han, F.;

et al. Flexible Aqueous Li-Ion Battery with High Energy and Power Densities. *Adv. Mater.* **2017**, *29* (44), 1701972.

(160) Horváth, D. V; Coelho, J.; Tian, R.; Nicolosi, V.; Coleman, J. N. Quantifying the Dependence of Battery Rate Performance on Electrode Thickness. *ACS Appl. Energy Mater.* **2020**, *3* (10), 10154–10163.

(161) Park, D.-J.; Aremu, E. O.; Ryu, K.-S. Bismuth Oxide as an Excellent Anode Additive for Inhibiting Dendrite Formation in Zinc-Air Secondary Batteries. *Appl. Surf. Sci.* **2018**, *456*, 507–514.

(162) Xiao, Y.; Shi, J.; Zhao, F.; Zhang, Z.; He, W. Effects of Electrolyte Additives on the Properties of Zinc-Bismuth Electrodes in Zinc-Air Batteries. *J. Electrochem. Soc.* **2018**, *165*, A47–A54.

(163) Phillips, J.; Mohanta, S.; Maske, C.; Bose, D. C.; Wu, J. J.; McKinney, B. L. PASTED ZINC ELECTRODE FOR RECHARGEABLE NICKEL-ZINC BATTERIES, 2010.

(164) RoHS Guide; www.rohsguide.com/rohs-lead-exemptions.htm

(165) Lu, W.; Xie, C.; Zhang, H.; Li, X. Inhibition of Zinc Dendrite Growth in Zinc-Based Batteries. *ChemSusChem* **2018**, *11* (23), 3996–4006.

(166) Hao, J.; Li, X.; Zhang, S.; Yang, F.; Zeng, X.; Zhang, S.; Bo, G.; Wang, C.; Guo, Z. Designing Dendrite-Free Zinc Anodes for Advanced Aqueous Zinc Batteries. *Adv. Funct. Mater.* **2020**, *30* (30), 2001263.

(167) Lu, C.; Hoang, T. K. A.; Doan, T. N. L.; Zhao, H.; Pan, R.; Yang, L.; Guan, W.; Chen, P. Rechargeable Hybrid Aqueous Batteries Using Silica Nanoparticle Doped Aqueous Electrolytes. *Appl. Energy* **2016**, *170*, 58–64.